Mathematical Modelling of Cereal Extrusion

Michael McPhail

Mansfield College

University of Oxford

A thesis submitted for the degree of

Doctor of Philosophy

Trinity 2019

Acknowledgements

I would like to thank my academic supervisors Ian Griffiths and Jim Oliver, and my industrial supervisor Ritchie Parker for their time, effort and expertise. The opportunity to work with, and learn from each of you has been invaluable. No quantity of chocolate would be enough to express my gratitude. I would also like to thank the InFoMM CDT directors Chris Breward and Colin Please for making this thesis possible. I am grateful to Nestlé and the EPSRC for their financial support of this project. I would like to thank Endre Süli and Patrick Farrell for their valuable discussion on the numerical component of this thesis.

On a personal level I would like to thank all of my friends who have enriched my time in Oxford. In particular, my frequent coffee and dinner companions including Florian, Tino, Bogdan, Thomas, Ian, and Abi; my housemates for the past year Caoimhe and Jess; Davin, for being the perfect office mate; and Tori, for being an invaluable support and friend.

I would also like to thank those in OCIAM for providing a great environment within which this work could take place.

Finally, I would like to thank my family for their continued love and support.

Abstract

In this thesis we analyse a mathematical model for an industrial process known as extrusion, and develop techniques for finding solutions to this model. The model for extrusion describes the evolution of a viscous liquid containing small vapour bubbles. The lengthscales corresponding to different features in this model can differ by orders of magnitude; so, we first distinguish a macroscale and a microscale. The parameters governing the dynamics of the system also vary over orders of magnitude. We exploit the asymptotic structure of the model to develop reduced systems of equations that are easier to solve, and give physical insight more readily.

In Chapter 1 we describe extrusion, and existing models for extrusion. In Chapter 2 we describe the model for extrusion used throughout this thesis. This model is decomposed into a macroscale model, describing the flow of a viscous, compressible fluid on lengthscales comparable to the extruder; and a microscale model, describing the evolution of vapour bubbles in the mixture. In Chapter 3 we consider the microscale model. We develop reduced models in different parameter regimes and estimate a macroscopic lengthscale for bubble growth, from which we predict parameter regimes for which the extruded product is long and thin. In Chapter 4 we exploit the slenderness of the product to construct reduced macroscale models, similar to the Trouton model for incompressible flows. In Chapter 5 we develop a numerical scheme capable of solving the full system described in Chapter 2, and compare these solutions to those of the reduced models developed in Chapters 3 and 4. Finally, in Chapter 6 we provide some concluding remarks on the model for extrusion we have considered, and on the key findings of Chapters 3, 4, and 5.

Contents

Chapter 1

Introduction

1.1 Extrusion in manufacturing

Extrusion is a technique used to manufacture a range of products including cereal, pet food, polymer foams, artificial wine corks, and optical fibres. At Nestlé, extrusion is used to produce expanded cereals and snack foods. The global extruded snack food market was valued at $80.6 billion USD in 2018, and is growing as the demand for ready-to-eat food products increases [2]. While extrusion is in widespread use in the manufacture of snack foods, mathematical models for extrusion are not; innovation is often driven by experiment. This is because modelling and simulation of extrusion is difficult. A particularly challenging case to model is extrusion with vapour-driven expansion, where a vapour-phase forms within the product. The overarching aim of the work in this thesis is to gain a better understanding of the vapour-driven expansion of extruded products using mathematical modelling.

An extruder, the device used for extrusion, is shown in figure 1.1. It comprises a screw system, where the product is mixed and cooked, and a die, through which the product is pushed into the atmosphere. Raw ingredients, which for cereal would include a powdered starch mix and water, are fed into one end of the extruder, the product is mixed and cooked, and then the product is forced through a die, changing its shape and texture. The temperature and pressure difference between inside and outside of the extruder leads to vapourisation of the more volatile ingredients of the mixture—in the case of cereal this means the water (moisture) in the mixture evaporates—as the product is pushed through the die. The result is small, internal cavities within the final product, which can be seen in figure 1.2a. Moreover, changing the shape of the die will change the shape of the final product. A variety of extruded-snack-food shapes are shown in 1.2b. These two properties, the internal

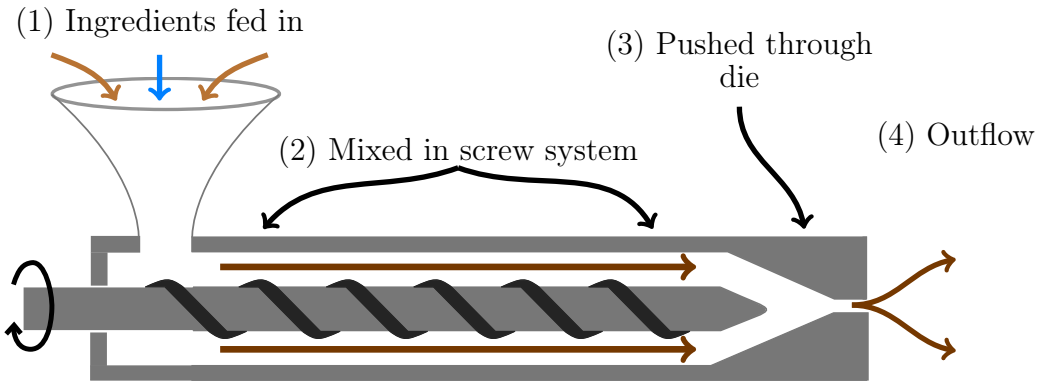

Figure 1.1: *A schematic illustration of a single-screw extruder. Ingredients are* (1) *fed in, and then* (2) *mixed and cooked as they are pushed through the screw system,* (3) *pushed out of the die,* (4) *into the atmosphere.*

structure and the shape, determine the quality of the final product. A mathematical model for how these properties of the final product depend on the initial state and the extruder configuration will aid in the design of new products.

During extrusion, there is a complicated interplay of many different mechanical and thermodynamic processes, all of which depend on the composition of the mixture, as well as the geometry and setup of the extruder. This means that understanding this process requires exploring a high-dimensional parameter space. Improvements and changes to products are currently experimentally driven; however, these experiments can be expensive and time consuming.

A model of extrusion, and a method of finding solutions to this model, can reduce the dependency on performing experiments, and broaden the type of studies that can be performed to better understand the process. Being able to simulate extrusion would make a comprehensive exploration of parameter space feasible, and, depending on the simplicity of the underlying model, offer direct insights through analysis of the governing equations. In this thesis we present a mathematical model for extrusion and describe methods by which solutions to this model can be found. Through both analytic and numerical analysis, we study this model in order to better understand extrusion and provide industrially relevant insight.

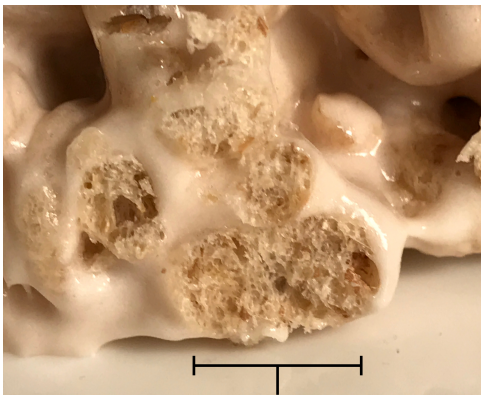

(a)

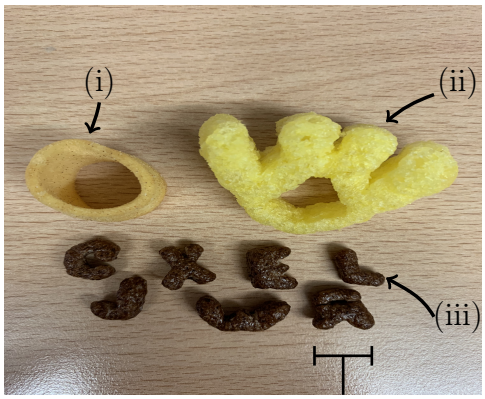

(b)

Figure 1.2: (a) *The interior of an extruded cereal product. The macroscale, which in this case is on the order of 1cm, is comparable to the size of the product, and the microscale is on the order of the internal bubbles, in this case down to 1/100th of the macroscale.* (b) *An assortment of extruded snack products:* (ii) *and* (iii) *are both vapour driven,* (i) *is not.*

1.2 Overview

In this chapter we introduce extrusion and review literature on the different aspects of extrusion that we will subsequently study in later chapters. In Chapter 2 we present a model for extrusion based on those common in the literature. A key feature of this model is the distinction between macroscale evolution, on the length scale of the product, and microscale evolution, on the length scale of the bubbles in the product. The evolution on each of these length scales is described by a *macroscale model* and a *microscale model* respectively. These models are coupled to each other to describe the evolution of the product.

In Chapter 3 we analyse the microscale model. We describe a numerical method for finding solutions to this model and use asymptotic analysis to derive reduced microscale models that are valid in different parameter regimes. From this microscale model, we identify parameter regimes for which the extruded mixture is long and thin outside of the die. Motivated by this insight, in Chapter 4 we consider the macroscale model in the long–thin limit outside of the extruder. By only considering flow outside of the extruder, we derive reduced models similar to the Trouton model for incompressible flow [76]. With the simplicity of this reduced model, we study the evolution of the shape of the product and the effect of accounting for more complicated thermodynamics; both of these studies are currently infeasible using the full model.

In Chapter 5 we consider flow in the two-dimensional (2D) and axisymmetric cases, and construct a numerical method for finding solutions to the full model for extrusion. We then apply this method to a number of cases of interest: the stick-slip flow of an incompressible fluid, to verify the accuracy of the scheme; extrusion in 2D using realistic parameters; in the long–thin limit, in order to verify the analysis of Chapter 4; and the stick-slip flow of a compressible fluid, in order to investigate local properties of the solution near the end of the outlet. In Chapter 6 we summarise our findings and make some concluding remarks.

1.3 Literature review

In this section we review the literature relevant to the construction and analysis of a model for extrusion. The goal of this review is to put into context, and thereby motivate, the model of Chapter 2 and the analysis in subsequent chapters. We first consider a general statement of the problem in a multiphase flow framework. Namely, we discuss various approaches to modelling the flow of bubbly mixtures in the literature concerned with a range of applications. Then, in Section 1.3.2, we discuss the most common models of cereal extrusion. These models comprise a macroscale model and a microscale model, each capturing the evolution of the product on different length scales. The microscale model describes the evolution of a bubble surrounded by a liquid. There is a large body of literature on this problem, which we discuss in Section 1.3.3. The macroscale model concerns the flow of a fluid out of the die. This problem has been studied for many fluids with different properties, and we discuss some of this literature in Section 1.3.4. In Section 1.3.5 we make some concluding remarks on the literature we have considered in order to motivate the work contained in the rest of this thesis.

1.3.1 Multiphase flow models

The most general model for extrusion must account for the presence of multiple phases to describe the dynamics of a solid–liquid–gas mixture. The liquid and solid phases are well mixed; thus, we consider these two components to behave like a single liquid. So, the first simplification to the most general model is to only consider the flow of a liquid–gas mixture. We briefly discuss multiphase flow approaches to studying liquid–gas flows, specifically when the gas phase is dispersed, before making further simplifications in later sections based on typical characteristics of extrusion.

Drew and Passman [21], and Ishii and Hibiki [39] present mathematical formulations of general two-phase flow problems. The appropriate formulation depends on the details of the system being modelled. Rouhani and Sohal [61] review literature on two-phase flow patterns. Brennen [15] describes the classification of different flow patterns depending on the extent of separation between phases. At the two ends of the spectrum are *separated* flows and *disperse* flows. Separated flows consist of separate, parallel streams of multiple fluids. Dispersed flows, the flow pattern observed during extrusion [42], consist of one phase that is distributed in the form of drops, bubbles, or particles within the other *continuous* phase. Here, we are interested in a *multicomponent mixture*, as introduced by Drew and Passman [21], for which the dispersed phase, in this case gas, is distributed throughout the continuous phase, in this case the liquid mixture, where the two phases are immiscible.

Because of the complexity of the internal structure of the mixture, using the pointwise equations for conservation of mass and momentum to model the dynamics of each component is not a feasible approach. Instead, Drew and Passman [21] detail averaging procedures from which *effective* conservation equations can be derived. These effective equations describe the conservation of mass, momentum, and energy for each phase within a representative volume surrounding each point. The interactions between phases, such as the transfer of mass and momentum, are captured by jump conditions, which arise due to integration over phase boundaries. Thus, the resulting averaged equations describe the conservation of mass, momentum, and energy of each phase in the mixture, with each equation containing interaction terms corresponding to the transfer of that quantity across the inter-phase boundaries.

There are two common methods of modelling a multiphase flow of a two-phase mixture using effective conservation equations: use experimentally based constitutive laws to describe the interaction terms; or sum together the effective conservation equations of each quantity over the phases, cancelling out many of the interaction terms, and close the resulting equations using appropriate constitutive laws. The former is the most common approach, and examples of systems modelled this way can be found in pipe flow [15], coffee-bean roasting [25], the baking of bread [82], wastewater management [41], and blood flow [45] to name a few. The latter method can be applied to fewer systems; however, when this method can be used, there can be considerable advantages. One such advantage is the possibility of a model for the evolution of the system

without constitutive laws specific to particular cases. This is the approach commonly taken when modelling for extrusion, and the approach we will take throughout this thesis.

When a sum is taken over the equations for the transport of each quantity, the resulting system of equations describes the evolution of an effective, single-phase, compressible fluid. This system of equations must be closed by relating the density to the pressure. This can be achieved directly, by way of a constitutive law, or, in place of a constitutive law, by constructing a model for the interaction between the phases; this second approach we discuss further in the next section. For a constitutive law to be effective, the interaction between the phases must be well studied, at least experimentally, and these interactions must be such that they can sensibly be captured by a relationship between the independent variables describing the state of each phase. We now discuss a number of examples where this approach is appropriate

Many of the features present during extrusion will also be present during a volcanic eruption. To model eruptions featuring a continuous liquid phase and a dispersed gas phase, a constitutive law is often used to relate the volume fraction of gas, and hence the density of the mixture, to the pressure in the liquid [32, 40, 77]. The dynamics of an *effusive* volcanic eruption are very similar to those of an extruded mixture just after the onset of bubble nucleation. A key feature of this process is the formation and growth of vapour bubbles due to the exsolution of volatiles. This exsolution is driven by the high temperatures and drop in pressure in the mixture [32]. One of the simplest, physically sensible constitutive laws used in models for volcanic eruptions, proposed by Turcotte *et al.* [77], is given by

$$\frac{\phi}{\phi_0} + \left(\frac{p}{p_0}\right)^n = 1, \tag{1.1}$$

where ϕ is the volume fraction of gas at fluid pressure p, ϕ_0 is a known volume fraction of gas at some reference pressure p_0, and n is an experimentally determined exponent. We note that (1.1) is taken directly from [77]; however, the right hand side should be 2 so that the equation is satisfied when $\phi = \phi_0$ and $p = p_0$.

An example of a constitutive law used in a model for the extrusion of a compressible fluid [30, 29, 80], is to assume that the density is proportional to the fluid pressure, *i.e.*

$$\rho = \rho_0 + B\left(p - p_0\right), \tag{1.2}$$

where ρ is the fluid density, p is the pressure of the fluid, ρ_0 is the density of the fluid at a reference pressure p_0, and B is a constant of proportionality. This type of constitutive law is typically employed when the fluid is weakly compressible, so that the change in density is small. To consider strongly compressible Newtonian fluids, Taliadorou *et al.* [71] compared this linear relationship to an exponential dependence give by

$$\rho = \rho_0 \exp\left(\beta\left(p - p_0\right)\right), \tag{1.3}$$

where β is constant. In each of these examples, the parameters n, B, and β incorporate the physical properties of the fluid, capturing the response of the fluid to changes in pressure. Equations (1.1), (1.2), and (1.3) suppose the existence of an effective barotropic relationship for the mixtures.

There are cases when supposing that the mixture is effectively barotropic, as a means of closing the governing equations, is insufficient. A review on the acoustic properties of liquids containing gas bubbles was given by van Wijngaarden [81]. Early interest in this topic was driven by the need to design quieter propellers for ships and submarines during World War II. These mixtures have complex dispersion relationships; the speed of an acoustic wave depends on the natural frequency of the bubbles [56, 65, 81]. The properties of these mixtures are too complex to be captured by supposing the mixture is effectively barotropic [15, 55], more detailed accounts of the behaviour of the bubbles is necessary.

Prescribing a reasonable constitutive law is a clean way to close the governing system of equations compared to alternative approaches (such as those described in the following section). Using this approach to construct an extrusion model is not feasible for two reasons: prescribing an appropriate constitutive law is heavily dependent on experimental results, which are not readily available and can be costly and difficult to perform; and the complexity of the mixtures we consider means that a single constitutive law cannot capture the wide array of physical processes that must be accounted for in a model for extrusion. For this reason, we outline a more realistic modelling approach in the next section.

1.3.2 Mathematical models of extrusion

In general, models for extrusion exploit two key properties of the extruded products: the high drag between the phases, and a clear discrepancy between the length scale

of microscopic features (*i.e.* bubbles) and the length scale of macroscopic evolution. The high viscosity of the liquid phase typically means that the bubbles are advected by the fluid [42]. As both the gas and liquid phases move with the same velocity, the equations governing the transport of each phase can be combined to give equations governing the transport of an effective fluid. Brennen describes this procedure for a dispersed mixture [15] and Drew describes this process in a more general framework [21].

Alavi *et al.* [3, 4] present a model for the extrusion of a starch-based microcellular foam produced by supercritical carbon dioxide, which comprises a macroscale model and a microscale model. The formulation of the model is as follows: the macroscale model describes expansion during the axisymmetric flow of the product, and the microscale model informs this expansion by determining the size of the entrained bubbles. In the macroscale model of Alavi *et al.* [3], the fluid domain is discretised into a finite number of concentric cylinders, where the properties of each cylinder are assumed to be radially uniform. The transmission of moisture between cylinders is accounted for by the prescription of fluxes based on the different states of each cylinder. The axial expansion of each cylinder is determined by combining the conservation of mass of the effective fluid and the change in density of the effective fluid, which depends on the microscale model. The microscale model describes the evolution of a bubble surrounded by a finite quantity of liquid subject to the macroscopic pressure.

Lach [42] presents an extension of the model presented by Alavi *et al.* [3] that accounts for temperature change. Rather than using the concentric cylinder formulation of Alavi *et al.*, Lach employs the finite element method (FEM) to solve the macroscale model. Due to numerical difficulties, solutions were only found to a one-dimensional (1D) approximation to the full model. These solutions, although they must suppose the pressure profile *a priori*, offer a number of experimentally verifiable insights. The most notable finding was the non-monotonic dependence of the final diameter of the product on the moisture content.

Lach [42] encountered numerical convergence issues for two-dimensional (2D) simulations, and suggested that the complexity of the microscale–macroscale coupling was to blame. Moreover, the limitations of the software that this model was implemented in, the commercial solver ANSYS Fluent, as well as restricted access to the source code, meant that these obstacles were insurmountable. Experiments performed by

Lach found significant cross-sectional variation in the properties of the final product, which cannot be predicted by 1D simulations. The addition of calcium phosphate, to promote uniform nucleation, reduced this variation and brought the experimental conditions more in line with the assumptions required to construct a 1D model.

Due to the complexity of modelling extrusion, a number of assumptions are commonly made. The most notable assumption is that there is no, or limited interaction between bubbles on the microscale. This significantly simplifies both the microscale and macroscale models, but neglects a number of key processes like coalescence, and Otswald ripening. The assumption that bubbles do not interact is likely to be accurate soon after nucleation, when the bubbles are smaller, but break down as the bubbles get larger. Lach [42], having observed a clear experimental correlation between early-time dynamics and the final state, suggests that a model without these processes is still practically useful. That is, if trends in the early-time dynamics are well understood, these will likely hold in the late-time dynamics as well.

In Chapter 2 we present a model that incorporates the same physical processes as Lach [42] in a more general, three-dimensional formulation. Previous models, namely those of Alavi *et al.* [3] and Lach [42], encode the numerical discretisation into the formulation of the model. Because of the expected complexity of the governing equations and the numerical difficulties encountered by Lach *et al.*, we do not want to be limited to any particular discretisation. Instead we first present a continuum formulation of the model, and then later discretise when we wish to solve these governing equations numerically. This approach has two benefits: it is more flexible in overcoming numerical difficulties, and, perhaps more importantly, asymptotic methods can be used to interrogate the continuum formulation. In addition, by starting from the continuum formulation, we can consider non-axisymmetric shapes, overcoming an inherent limitation of Alavi *et al.*'s approach [3].

1.3.3 Models for bubble growth

The framework of a macroscale–microscale coupling employed by Alavi *et al.* [3] and Lach [42] allows for each component to be replaced by models of varying complexity. In the most general formulation, the microscale model describes the evolution of a bubble surrounded by a viscous liquid; a well-studied problem for which there is a large body of literature. An early model for bubble dynamics was discussed by Lord Rayleigh in 1917 [57], who considered the collapse of a spherical cavity at constant

pressure, as well as the collapse of a gas-filled cavity when the gas pressure is given by Boyle's law. As we shall now describe, this early model has since been extended by incorporating additional physical effects relevant to the particular application. Plesset and Prosperetti [54], and later Brennen [14], present comprehensive reviews of the literature concerning the growth and collapse of bubbles.

The first extension to this model was the incorporation of the viscosity of the liquid to give the well-known Rayleigh–Plesset equation [54]. The three key quantities that control the rate of bubble growth are as follows: the pressure in the bubble at the liquid–bubble interface, the stress in the liquid at the liquid–bubble interface, and the surface tension. Any process that modifies any of these quantities, or the dependence of these quantities on growth rate, will change the bubble dynamics. For example, more complex liquid properties, like a yield stress [79] or a viscoelastic rheology [7], have been incorporated to modify the momentum balance at the surface of the bubble.

The simplest assumption that can be made about the bubble pressure, employed by Rayleigh [57], is that it is constant; however, the complex nature of the thermodynamics of extrusion results in a changing bubble pressure. A number of authors account for the diffusion of some volatile component through the liquid, and the subsequent vapourisation of this component into the bubble, resulting in an increase in bubble pressure [10, 24, 53, 68]. These models neglect temperature changes as they are concerned with processes that are approximately isothermal. Scriven [64] considered the growth of a gas bubble in an infinite medium controlled by the transport of heat and matter; however, he employed a simplified description of the fluid mechanics, ignoring viscous and inertial effects, which limit the applicability if this work to models of extrusion.

The bubble-growth model most commonly used for cereal extrusion is the *cell model*, originally proposed by Amon and Denson [5]. In this model, the bubble is assumed to be surrounded by a finite envelope of liquid, as opposed to an infinite body of liquid supposed in the derivation of the Rayleigh–Plesset equation. The motivation for introducing a finite body of liquid is to account for limited bubble–bubble interactions; namely, the competition for heat and moisture between neighbouring bubbles. A comparison between the cell model and the model with an infinite body of liquid was made by Elshereef *et al.* [23]. They conclude that the two models agree at early times, and then diverge for later times. We will generally consider the model with

an infinite body of liquid throughout this work; however, we discuss both models in Chapter 2, as well as our reasoning for not focussing on the cell model.

1.3.4 Macroscopic flow

The macroscale model describes the flow of a compressible fluid from inside the die to outside. Even though the compressibility of this fluid is described by a complicated microscale model, we still expect to observe similar features to those of simpler compressible, or incompressible fluids. This type of problem is commonly referred to as a die-swell problem, and is characterised by two key features: the change in boundary condition from no-slip to a free boundary as the fluid exits the die, and the fact that the fluid domain must be determined as a part of the solution.

Considering just the free boundary component of the domain, models for the extensional flow of an incompressible fluid (which are valid in the limit in which the fluid is long and thin) have been successfully applied to glass-drawing [17, 33, 37, 66, 67]. These models describe the evolution of some key quantities along the axis of flow, as well as the change in shape of the cross-section [17]. In addition, these models can describe deflection of the axis of flow, as well as twisting; two effects that are commonly observed in practice during the extrusion of irregular shapes. Moreover, these models can be extended to account for temperature dependent viscosities, and more complicated cross-sectional domains that are not simply connected. In Chapter 4, we discuss these models for extensional flow in more detail.

A common industrial problem is the extrusion of a viscoelastic fluid [73]. Models for this process contain many of the same features as models for extrusion; namely, complicated constitutive laws must be evaluated along the particle paths. As a result of the complexity in the governing equations, the associated computational difficulty of these problems is high. A commercial solver, ANSYS Polyflow, is dedicated to solving problems of this type. Polyflow uses the finite element method to solve the governing equations, and an Arbitrary Lagrangian–Eulerian (ALE) method to deform the mesh and account for the free boundary [1]. Because Polyflow is closed source, and the extrusion of a bubbly mixture is not already part of the suite of models available, this software cannot be used in this work. Instead, we develop a solver using open-source software.

Studies on the extrusion of a compressible fluid are limited. Georgiou [29] considered

the extrusion of a weakly compressible fluid in two dimensions. To solve the governing equations with a free boundary, a bespoke scheme was constructed using the finite element method. The position of the free boundary must be determined at the same time as the field variables. In this case the pressure–density relationship is simple enough for the density to be eliminated from the governing equations; the density is replaced by an expression containing the pressure. A fluid of this nature is not as complex as the mixtures that we consider. The pressure–density relationship that we are interested in must be determined by solving the microscale model on each particle path. Therefore, we will develop a numerical method distinct from those found in the literature.

1.3.5 Concluding remarks on available literature

There is a large body of literature concerned with bubbly, liquid–gas flow. A conventional multiphase flow approach would be to consider the effective conservation-of-mass and conservation-of-momentum equations of each phase, and then close the governing equations by prescribing experimentally motivated constitutive laws wherever necessary. Models for extrusion, in cases where the liquid phase is very viscous, exploit the absence of a drift velocity between the phases to combine the governing equations of each phase. The result is conservation-of-mass and conservation-of-momentum equations for a single-phase fluid, which is referred to as the macroscale model. A microscale model is constructed to close the macroscale model.

The microscale model describes the evolution of a bubble surrounded by a viscous liquid. This problem has been extensively studied; however, limited attention has been given to cases for which the temperature and composition of the surrounding liquid both vary and are both important. Moreover, when the composition of the surrounding liquid is important, it is often due to some dissolved gas species, not a liquid phase that is evaporating at the surface of the bubble. This distinction modifies the thermodynamics at the interface: a significant amount of energy is used to vapourise the liquid, and the thermodynamic equilibrium relationship between a dissolved gas and the gas in the bubble is different to the relationship between a liquid and the gas in the bubble. So, while we can take inspiration from the analysis found in the literature, the specific properties of our system will be different; thus, our analysis will be different as well.

Finally, we considered literature relevant to the macroscale system; namely, literature on the extrusion of both non-Newtonian and compressible flows. In the available literature, systems of equations with similar properties have been solved (*e.g.* [31, 29, 30, 71, 47]); however, none of these methods can be readily extended to account for the unique properties of the microscale–macroscale coupling required to model extrusion. The complexity of the microscale model used to close our macroscale model necessitates the development of a new method for finding solutions.

Chapter 2

A model of extrusion

In this chapter we present a model to describe the extrusion of cereal. The remaining chapters in this thesis will be dedicated to analysing this model. In Section 2.1 we describe the properties of the cereal mixture, particularly for the stage of extrusion that we are interested in, during which the mixture comprises a viscous liquid that contains bubbles. The model we describe in this chapter assumes that the bubbly mixture can be represented by a single-phase, viscous, compressible fluid. This model is composed of a macroscale model, which describes evolution on the length scale of the product, coupled to a microscale model, which describes evolution on the length scale of the bubbles in the mixture.

In Section 2.2 we present the macroscale model. We consider a fluid that begins inside (and is bounded by) the extruder, and flows out of the extruder, where it is free to expand. The partial differential equations (PDEs) governing mass and momentum transfer are the compressible Navier–Stokes equations. These equations must be closed by incorporating an additional relationship between the state variables; this relationship is given by the microscale model.

In Section 2.3 we present the microscale model, which describes the evolution of bubbles subject to conditions imposed by the macroscale. The microscale model describes the evolution of the size of a bubble surrounded by a fluid of infinite extent. This model accounts for most of the physical and thermodynamic properties of the gas and liquid phases, so that on the macroscale we need only consider effective properties of the mixture. We also present the cell model for bubble growth [5], which is commonly utilised in models of extrusion [3, 42].

In Section 2.5 we present the dimensionless macroscale model, and in Section 2.6

we present the dimensionless microscale model. The system of equations, as presented in these sections, forms the model for extrusion that we consider in this thesis. We refer back to these equations in subsequent chapters when we analyse components of the model, or when we consider the full model comprising both the microscale and macroscale models.

2.1 Extrusion of a two-phase mixture

2.1.1 What is cereal?

The transition from raw cereal ingredients into the final product takes place over a number of distinct stages. During each stage, the product undergoes physical and chemical changes. We will call the four main stages: mixing, cooking, the flash, and post-processing; these are illustrated in figure 2.1. The raw ingredients include a starchy dry-mix and a wet component, such as water. During the first stage, mixing, these ingredients are combined as they are pushed along a screw system. The resulting mixture behaves like a highly viscous liquid. The complex microstructure of the dry-mix gives this mixture a complex rheology [49]. We neglect many details of this complex rheology throughout this work; instead, we consider Newtonian liquids. As the mixture is pushed further down the screw system, the high shear stress in the fluid induces significant viscous heating, which initiates the cooking stage. The resulting temperature increase, by up to 100 Kelvin, cooks the product, changing both its chemical and physical properties. Near the end of the screw system, the mixture is at a high temperature, around 400 Kelvin, and a high pressure, up to 3 bar [42]. The wet component, which is at this stage dissolved in the liquid mixture, is well above its boiling point at atmospheric pressure. At the end of the screw system, the mixture is pushed through a device known as *the die*, which is fitted onto the end of the extruder. Dies with different shapes and diameters are used to change the shape and texture of the final product.

The rapid pressure drop as the mixture is pushed through the die results in the supersaturation of the wet component of the mixture. When the pressure in the mixture drops below the vapour pressure of the wet component of the mixture, bubbles will nucleate. The onset of vaporisation of the wet component of the mixture marks the start of the flash stage. The flash can be characterised by three features: the rapid expansion of the product due to the nucleation and growth of bubbles, a cooling of the product due to the enthalpy of vaporisation of the wet component, and the drying

of the product as the concentration of the wet component of the mixture decreases. The flash usually begins just before the outlet of the die, and ends after any of the components required for ongoing vaporisation, such as heat or moisture, have been depleted. Inside the die, the wet component can only evaporate into the bubbles. Outside the die, as well as evaporating into the bubbles, the wet component near the edge of the mixture can evaporate into the atmosphere. At some point downstream of the flash, the mixture can either be supported by a conveyor belt so that it can be transported for processing, or, more commonly, it will be cut into bite-size pieces by a fast moving blade.

In this thesis we investigate the flash stage. Specifically, we are interested in the behaviour of the mixture after bubbles have nucleated, and prior to the post-processing stage. The components of this system include the wet and dry ingredients as well as the gas phase; each of these components must be accounted for. For simplicity we suppose that the mixture comprises a liquid phase, within which the wet component is dissolved, and a gas phase. We adopt a nomenclature so that the various components do not get confused. We refer to the wet component of the liquid as *moisture*, and we are interested in the concentration of moisture, in kg of moisture per kg of liquid mixture, or the moisture content. The dry ingredients we refer to as *dry-mix*. We capture the effect of the dry-mix on the dynamics indirectly; not by considering its physical properties, but instead through experimentally-motivated constitutive laws. The gas in the two-phase mixture is confined in bubbles, and is the vapourised form of the wet component of the product. This phase will be referenced interchangeably by *gas*, *vapour*, or *bubbles*. By considering the system as a two-phase, gas–liquid flow, we can reduce the problem formulation into a simple expression: we are interested in the dynamics of a viscous, bubbly flow from the point of bubble nucleation inside the die until bubble growth is arrested downstream.

2.1.2 Effective conservation equations

The conventional approach for treating multi-phase flows is to consider the transport equations for the mass, momentum, and energy of each phase. In this approach, transmission of each quantity (mass, momentum, and energy) between phases is accounted for by incorporating experimentally-motivated constitutive laws. When using this approach, it can be difficult to find constitutive laws that are applicable across the spectrum of expected parameter values. We will show in Chapter 3 that the microscale dynamics associated with this problem lead to parameter regimes for which

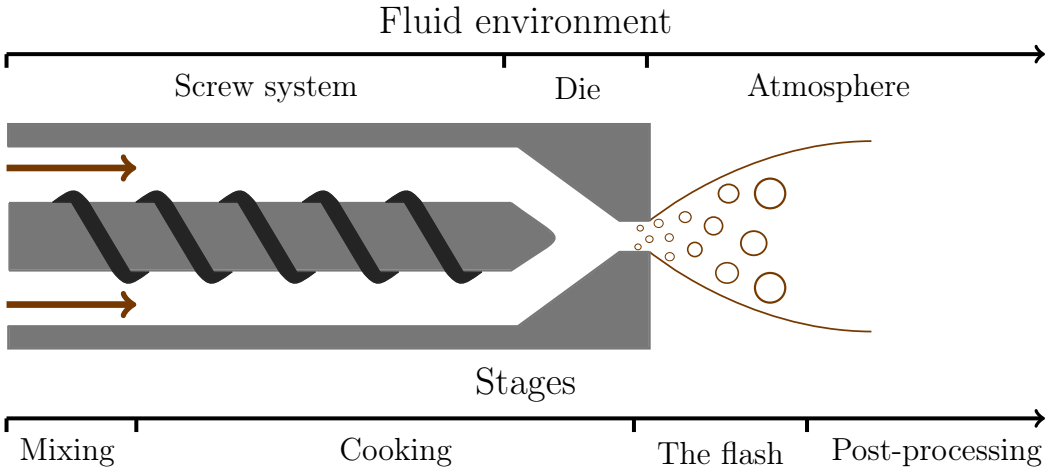

Figure 2.1: *A schematic illustration of the exit of a single-screw extruder. Ingredients are fed in from the left, and are then processed through the various stages as they move to the right.*

fundamentally different behaviours occur. Capturing all of these behaviours with a single macroscale constitutive law is infeasible. This challenge is compounded by the difficulty in performing experiments, and in measuring the state of the product during the flash stage. Difficulties associated with a multi-phase, constitutive law approach motivate the development of an alternative, physics-based approach.

The general principle underlying the design of a physics-based model is to consider a single *effective fluid* that behaves like the mixture. A representative volume taken from within the mixture, containing both liquid and gas, will inherit properties from each phase. Such a volume will be highly viscous due to the liquid phase, and compressible due to the gas phase. We will use the compressible Navier–Stokes equations to describe the behaviour of a single fluid that represents the two-phase mixture.

A systematic derivation of a model for an effective fluid representing the mixture is described by Drew and Passman [22], Ishii and Hibiki [39], and Fowler [27]. The effective conservation equations generated in this manner capture macroscopic dynamics by averaging over representative volumes larger than the microscopic features in this system. By averaging over the microscale features, we have lost some information. To close the macroscopic model governed by the equations of compressible, viscous flow, we must recover this information by coupling these equations to a microscopic model. This microscopic model describes the growth rate of bubbles, which depends on the macroscopic field variables. In its simplest form, the microscale model relates

the growth of bubbles to the macroscopic pressure. More complicated variants of the microscale model incorporate more detailed thermodynamics relating the bubble size to the local temperature and moisture content in the liquid phase.

A key assumption that we make throughout this work, in order to derive a mathematically tractable model, is that the mixture is in the *disperse limit*. In this limit, the bubbles are small and well dispersed, so that they do not interact through the microscale model. This assumption is commonly used to understand systems with bubbly flows [15]. For example, bubble–bubble interactions are neglected when studying the acoustic properties of dilute bubbly mixtures [6, 16, 81]. Assuming that we are in the disperse limit simplifies the relationship between the properties of the two phases in the mixture and the single fluid representing them. We expect the disperse limit assumption to be valid for earlier times, just after bubble nucleation, and to break down as the bubbles grow larger.

Alternative microscale models have been proposed that attempt to account for bubble–bubble interactions through the microscale model. We discuss one such model, proposed by Amon and Denson [5], in Section 2.3.6. Because of the modularity of the microscale–macroscale framework we employ, an alternative microscale model, such as Amon and Denson's, can be substituted in for the disperse limit model we consider. We choose to present and use the simplest model, one valid in the disperse limit, aware of the fact that the disperse limit assumption may break down when larger bubbles are present in our system.

The model we use throughout this work is composed of a macroscale model, capturing the dynamics on a length scale typical of the entire mixture, coupled to a microscale model, capturing dynamics on a length scale typical of the size of bubbles in the mixture. The macroscale model describes the evolution of the variables that determine the state of the fluid: the density, ρ, in kg/m^3; the velocity, $\boldsymbol{u}$, in m/s; the pressure, p, in Pa; the temperature, T, in K; and the moisture concentration, c, in kg/kg_{liquid}. Outside of the die the fluid boundary is free, so the shape of the fluid must also be determined as part of the macroscale model. The properties of the fluid should reflect the properties of the mixture that it represents. These mixture properties—such as the coefficients of viscosity, the specific heat capacity, thermal conductivity *etc.*—will depend on the composition of the mixture. For simplicity we will generally assume that these properties are equal to those of the liquid phase. An

exception to this rule will be the second coefficient of viscosity, which is associated with viscous resistance to expansion. This will be clarified at the introduction of each property.

The microscale model describes the evolution of a spherically symmetric gas bubble surrounded by a liquid. We denote microscale state variables with hats in order to distinguish them from their macroscale counterparts. For example, $\hat{p}$ denotes the pressure within the liquid phase of our microscale model, where as p denotes the fluid pressure on the macroscale. Both of these quantities appear in the microscale model, but they both refer to different things, making this distinction necessary. The state of the microscale system is characterised by both the liquid and gas states. The state of the liquid is determined by its radial velocity, $\hat{u}$; its pressure, $\hat{p}$; its temperature, $\hat{T}$; and the moisture concentration, $\hat{c}$. The state of the bubble is determined by its radius, $\hat{R}$, in m; its pressure, $\hat{p}_{\mathrm{B}}$; its temperature, $\hat{T}_{\mathrm{B}}$; and the number of moles of gas in the bubble, $\hat{N}_{\mathrm{B}}$, in mol. The units of the microscale variables are the same as their macroscale counterparts unless otherwise stated.

To construct a coupled microscale–macroscale model we make a number of assumptions. We assume that there is no further nucleation after an initial nucleation event. We also neglect any bubble–bubble interactions that may produce or destroy bubbles; we do not account for bubble coalescence or break-up. In our model, the number of bubbles per unit volume of liquid is fixed. We assume that the bubble radius is uniform within each representative volume. So, in the continuum limit there is a single bubble radius at each point in the fluid, which is equal to the radius of bubbles in a representative volume containing this point. We will assume that the liquid is a Newtonian fluid, unless otherwise stated, and that the gas is ideal.

2.2 Macroscale model

2.2.1 Conservation of mass and momentum

We consider the extrusion of a viscous, compressible fluid. In this section we present the equations governing conservation of mass and momentum of the fluid. In Section 2.2.2 we consider conservation of energy, and conservation of mass of the moisture. In a full model of extrusion, all of these quantities—mass, momentum, energy, and moisture concentration—must be determined. Throughout the work detailed in this thesis, we predominately focus on finding solutions to only the conservation of mass

and momentum components of the macroscale model. While the temperature and moisture concentration may have an impact on mass and momentum transfer, we will generally only consider reduced models in which this is not the case (with the exception of Chapter 4, Section 4.4). Within these reduced models, the equations governing conservation of energy and moisture concentration tend to act in an auxiliary manner, dependent on, but not influencing, the transfer of mass and momentum within the system. For this reason, the equations governing conservation of mass and momentum are presented separately here, and will form the core of the macroscale model we consider in this thesis.

We consider a fluid bounded by the surfaces $G_1(x, y, z) = 0$, while inside the die, and $G_2(x, y, z, t) = 0$, while outside the die, where (x, y, z) denote Cartesian coordinates and t denotes time, as illustrated in figure 2.2. We define $z = 0$ to coincide with the end of the die. We suppose that bubble nucleation occurs at $z = -\ell$, which is inside the die; therefore, $G_1(x, y, z) = 0$ defines the surface of the die between $-\ell \leq z \leq 0$ with fluid flowing into the volume enclosed by this surface through $z = -\ell$. At some point the mixture will be cut into pieces. The flash, however, has generally finished before cutting occurs. So, the appropriate length scale along the axis of flow will be the length scale over which bubble growth occurs, which depends on the microscale dynamics. Discussion of this length scale is deferred until we discuss the microscale model in Chapter 3. For now we denote the length by l_e and define the fluid surface for $0 < z \leq l_e$ by $G_2(x, y, z, t) = 0$. The region corresponding to a cross-section of the extruded product at some point along the axis of flow (*i.e.* the z-axis) is denoted by $\Omega(z, t)$. The equations governing conservation of mass and momentum are given respectively by

$$\frac{\partial \rho}{\partial t} + \nabla \cdot (\rho \boldsymbol{u}) = 0, \tag{2.1}$$

$$\rho \frac{\mathrm{D}\boldsymbol{u}}{\mathrm{D}t} = \nabla \cdot \boldsymbol{\sigma} + \rho \boldsymbol{g}, \tag{2.2}$$

where ρ is the mixture density; the liquid velocity $\boldsymbol{u} = (u, v, w)$ in Cartesian coordinates; the stress tensor is given by

$$\boldsymbol{\sigma} = (-p + \lambda \nabla \cdot \boldsymbol{u})\mathbb{I} + \mu \left(\nabla \boldsymbol{u} + (\nabla \boldsymbol{u})^T \right), \tag{2.3}$$

where $\mathbb{I}$ is the identity tensor; μ is the dynamic viscosity of the mixture; λ is the second coefficient of viscosity of the mixture; and $\boldsymbol{g}$ is the acceleration due to gravity

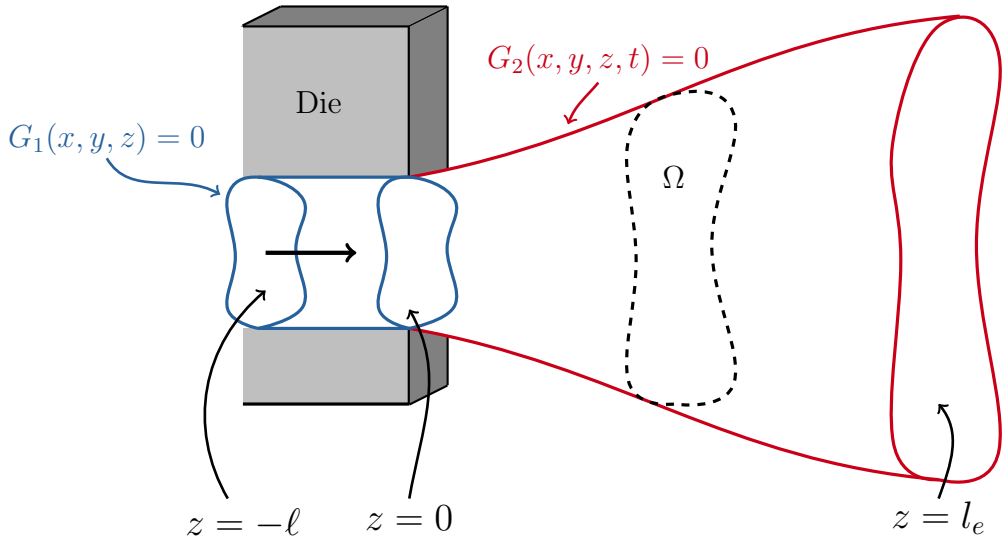

Figure 2.2: *Schematic of a three-dimensional flow of a compressible fluid. For* $-\ell < z < 0$ *the fluid is inside the die; bounded by a rigid impermeable surface given by* $G_1(x,y,z)=0$*. Outside the die, for* $0 < z < l_e$*, the fluid is free to expand, and is bounded by the surface* $G_2(x,y,z,t)=0$*. The domain* $\Omega = \Omega(z,t)$ *refers to a cross-section of the extruded product at a particular* z *position.*

(acting in the y direction). For short-hand we have used the material derivative, which is defined to be

$$\frac{\mathrm{D}}{\mathrm{D}t} = \frac{\partial}{\partial t} + \boldsymbol{u}\cdot\nabla\,. \tag{2.4}$$

The equations for conservation of mass and momentum, (2.1)–(2.3), do not form a closed system. In order to capture the dynamics of a compressible fluid, this system must be closed by relating the density of the product to its pressure. Often the equations of compressible flow are closed using an equation of state, see, for example, [30, 29, 71, 80]. The complexity of the mixture we consider necessitates the construction of a microscale model to close the system.

The macroscopic density depends on the volume fraction of gas in the mixture. The volume fraction of gas, α_g, is related to the number of bubbles per unit volume of liquid, η, and the bubble volume, $\hat{V}$, by

$$\alpha_g = \alpha_l \eta \hat{V}, \tag{2.5}$$

where α_l is the volume fraction of liquid. The volume fraction of liquid is given by $\alpha_l = 1 - \alpha_g$, and, using (2.5), can be expressed in terms of η and $\hat{V}$ by

$$\alpha_l = \frac{1}{1+\eta\hat{V}}. \tag{2.6}$$

The density of the mixture is given by

$$\rho = \rho_l \alpha_l + \rho_g \alpha_l, \tag{2.7}$$

where ρ_l is the density of the liquid component and ρ_g is the density of the gas component. When the density of the gas contained in the bubbles is negligible, the density of the mixture is given by

$$\rho = \frac{\rho_l}{1 + \eta \hat{V}}, \tag{2.8}$$

which is the result presented by Brennan [15]. The bubble volume is related to the radius of the bubbles, $\hat{R}$, according to $\hat{V} = 4\pi\hat{R}^3/3$. The macroscale model is closed by coupling it to a microscale model that determines $\hat{R}$. For a simple example of a microscale model consider the isothermal growth of a gas bubble with a fixed quantity of an ideal gas surrounded by a viscous fluid. In this case, the growth rate of the bubble depends on the pressure in the liquid surrounding the bubbles, which is coupled to the macroscopic pressure. In more complicated variants, such as the model we describe in Section 2.3, the microscale model also accounts for the impact of macroscopic temperature and moisture content on bubble growth. The microscale model returns the bubble radius, as well as the rate at which heat and moisture are being consumed as the bubbles grow. We consider parameter regimes in Chapter 4 for which heat consumption on the microscale can influence the macroscale. In these cases, we introduce a source term in our macroscale conservation of energy equation that captures the microscopic consumption of heat.

To solve the time-dependent problem, appropriate initial conditions must be prescribed. This requires prescribing the density and velocity as well as the fluid domain by prescribing $G_2(x, y, z, 0)$. In Chapter 4 we consider reductions of the time-dependent macroscale model; however, we do not try and find time-dependent solutions. We are interested in the state of the product after the extruder has been running for some time. Thus, we only look for time-steady solutions, which do not require knowledge of the initial state. For this reason, as well as the fact that the physically appropriate initial conditions for an extruder are not obvious, we do not prescribe initial conditions in this thesis.

The appropriate boundary condition will depend on whether the fluid is inside or

outside of the die. Inside the die we impose no slip between the fluid and the die, which is given by

$$\boldsymbol{u} = \boldsymbol{0} \quad \text{on} \quad G_1(x, y, z) = 0. \tag{2.9}$$

Outside the die, the respective kinematic and dynamic boundary conditions on the fluid surface are given by

$$\frac{\partial G_2}{\partial t} + \boldsymbol{u} \cdot \nabla G_2 = 0, \quad \text{and} \quad \boldsymbol{\sigma} \cdot \nabla G_2 = -\gamma \varkappa \nabla G_2 \quad \text{on} \quad G_2(x, y, z, t) = 0, \tag{2.10}$$

where $\varkappa = \nabla \cdot \boldsymbol{n}$ is the curvature of the surface, $\boldsymbol{n}$ is the outward pointing unit normal to the surface, and γ is the surface tension of the mixture, which we take to be constant.

We assume that, at $z = -\ell$, bubbles nucleate uniformly throughout the cross-section so that the mixture density is uniform. We prescribe the velocity and density by

$$\boldsymbol{u} = (0, 0, w_0(x, y)) \qquad \text{and} \qquad \rho = \rho_0 \quad \text{at} \quad z = -\ell, \tag{2.11}$$

respectively, where w_0 depends on the flow prior to flashing, and ρ_0 is a constant. We suppose that there is nothing pulling or pushing on the mixture downstream, so we impose that there is no stress, *i.e.*

$$\boldsymbol{\sigma} \cdot \boldsymbol{e}_z = 0 \quad \text{at} \quad z = l_e, \tag{2.12}$$

where $\boldsymbol{e}_z = (0, 0, 1)$ is the unit vector in the z-direction.

In summary, the equations governing mass and momentum transport on the macroscale are given by (2.1)–(2.8). The macroscale field variables are the density, ρ, the pressure, p, and the velocity, $\boldsymbol{u}$. The boundary conditions are given by (2.9)–(2.12). The macroscale governing equations are closed by a microscale model that determines the size of bubbles in the mixture, captured by the bubble radius $\hat{R}$.

2.2.2 Conservation of energy and moisture

The equations of conservation of energy and moisture concentration, c, in the fluid are given respectively by

$$\rho \frac{\mathrm{D}}{\mathrm{D}t}(c_v T) = \nabla \cdot (k \nabla T) + \mu \left(\nabla \boldsymbol{u} + (\nabla \boldsymbol{u})^T \right) : \nabla \boldsymbol{u} - (p - \lambda \nabla \cdot \boldsymbol{u}) \nabla \cdot \boldsymbol{u}, \tag{2.13}$$

$$\frac{\partial c}{\partial t} + \nabla \cdot (c \boldsymbol{u}) = \nabla \cdot (D \nabla c), \tag{2.14}$$

where T is the temperature of the mixture, c_v is the specific heat capacity of the mixture, k is the thermal conductivity of the mixture, and D is the coefficient of diffusion for moisture in the mixture. The last two terms on the right hand side of (2.13) correspond to heat generated by viscous heating and work done by the fluid respectively, where the double dot product is defined by

$$\mathbf{A} : \mathbf{B} = \sum_i \sum_j A_{ij} B_{ij}. \tag{2.15}$$

We discuss the effect of the microscale on the conservation-of-energy and conservation-of-moisture equations when we present the microscale model in Section 2.3. Inside the die, we impose the boundary conditions given by

$$T = T_{\text{die}} \qquad \text{and} \qquad \boldsymbol{n} \cdot \nabla c = 0 \quad \text{on} \quad G_1(x, y, z) = 0, \tag{2.16a,b}$$

so that the temperature of the fluid equals that of the die, T_{die}, and the die is impermeable to moisture. Outside of the die, we impose Newton's law of cooling [12] and a condition of thermodynamic equilibrium, which are respectively given by

$$\boldsymbol{n} \cdot \nabla T = h(T - T_{\text{atm}}) \quad \text{and} \quad \mathcal{P}(c, T) = p_{\text{atm}} \quad \text{on} \quad G_2(x, y, z, t) = 0, \tag{2.17a,b}$$

where h is a constant that determines how fast heat is transported away from the product, T_{atm} is the temperature of the atmosphere, p_{atm} is the atmospheric pressure, and $\mathcal{P}(c, T)$ is a condition of thermodynamic equilibrium between moisture dissolved in the liquid and the atmosphere. This equilibrium condition, which is given by a constitutive law, is discussed more in Section 2.3. At the point of nucleation we impose the temperature and moisture concentration to be

$$T = T_0, \qquad \text{and} \qquad c = c_0 \quad \text{at} \quad z = -\ell, \tag{2.18a,b}$$

respectively, where T_0 and c_0 are constants. Downstream we assume that there is no diffusive flux of heat or concentration along the direction of flow. That is, we impose the conditions given by

$$\frac{\partial T}{\partial z} = 0 \qquad \text{and} \qquad \frac{\partial c}{\partial z} = 0 \quad \text{at} \quad z = l_e. \tag{2.19a,b}$$

We omit the prescription of initial conditions because we shall be concerned with only time-steady solutions.

2.3 Microscale model

The macroscale model describes a fluid that represents a bubbly mixture. We have supposed that this representative fluid is compressible; however, we must look to the microscale structure to understand this compressibility. The microscale model for the mixture relates the pressure in the liquid and gas phases to the evolution of the mixture density, closing the equations describing the macroscale flow. For a bubbly mixture in which no bubbles are created or destroyed, the closure relation describes the evolution of the size of the bubbles, as well as the rate at which moisture and heat are consumed during bubble growth. The complexity of this relationship can vary significantly depending on how detailed a description of the thermodynamics is used. In this section we describe the microscale model, as well as the modelling assumptions commonly used in literature that make these models mathematically tractable.

We model the behaviour of a single spherically-symmetric bubble surrounded by a viscous fluid, as illustrated in figure 2.3. We develop the microscale model in the Lagrangian reference frame of the bubble; the result is a model for the time-evolution of a bubble subject to macroscale forcing terms (such as the macroscale pressure). When mapped into the Eulerian reference frame in which the macroscale model is posed, the microscale model describes the evolution of bubbles along the particle paths of the mixture. We suppose that the liquid surrounding the bubble is infinite in extent. By using this model, we are implicitly assuming that we are in the disperse limit; the bubbles in the mixture are far enough away from each other that they do not interact. This is not the only bubble-growth model that has been incorporated into extrusion models. In Section 2.3.6 we discuss a model in which a bubble is surrounded by a finite envelope of fluid. This model, presented as the *cell model* by Amon and Denson [5], is often used in extrusion models to account for some bubble-bubble interaction [3, 42, 44, 78]. In order to distinguish it from the cell model, we refer to the model that considers an infinite body of liquid surrounding a bubble as the *disperse model* for the remainder of this work. We will use the disperse model throughout this work unless otherwise stated. We use this model for a number of reasons: it is more consistent with the disperse-limit assumption we have made on the macroscale; from it we can derive leading-order approximations to the solutions, which are not found when there is a finite body of liquid; the microscale–macroscale coupling is more straightforward, and more physically well-grounded compared to the cell model.

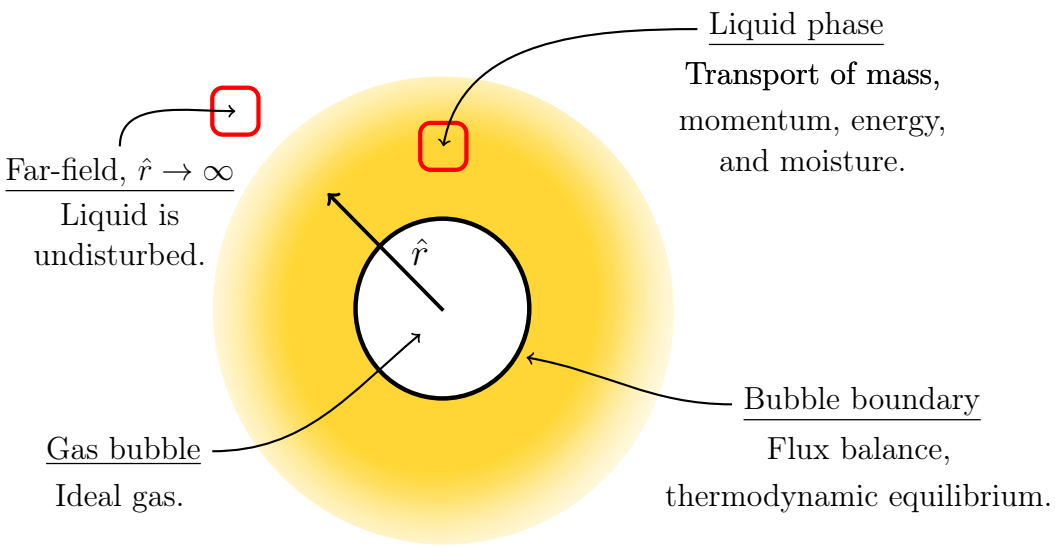

Figure 2.3: *Schematic of an ideal-gas bubble surrounded by a liquid of infinite extent. In the liquid phase we must account for the transport of mass, momentum and energy; as well as moisture transport. At the interface between phases we impose boundary conditions associated with conservation of mass, conservation of momentum, and thermodynamic equilibrium, as stated in Section 2.3.2.*

We make a number of assumptions regarding the microscale structure, in line with other authors who have constructed extrusion models [3, 42, 44, 78], to ensure a tractable final model. We have assumed that all bubbles are spherical; so their size is captured by a single variable, $\hat{R}$, the radius. We assume that temperature and pressure are uniform throughout the bubble, but not necessarily in the liquid. We assume that the liquid surrounding the bubble is incompressible and Newtonian, and that the density and viscosity of the liquid are independent of the moisture content and temperature. We will assume that the moisture in the liquid is water.

2.3.1 Liquid continuum equations

We denote the distance from the centre of the bubble to a point in the fluid by $\hat{r}$, and the elapsed time since bubble nucleation by $\hat{t}$. For a bubble surrounded by a liquid, we model the fluid variables in the domain $\hat{r} > \hat{R}(\hat{t})$. The radial velocity and pressure fields within the liquid surrounding the gas bubble are denoted by $\hat{u}(\hat{r}, \hat{t})$ and $\hat{p}(\hat{r}, \hat{t})$, and are assumed to be governed by the spherically-symmetric, incompressible

Navier–Stokes equations [11], namely,

$$\frac{1}{\hat{r}^2}\frac{\partial\left(\hat{r}^2\hat{u}\right)}{\partial\hat{r}} = 0, \tag{2.20}$$

$$\rho_l\left(\frac{\partial\hat{u}}{\partial\hat{t}} + \hat{u}\frac{\partial\hat{u}}{\partial\hat{r}}\right) = -\frac{\partial\hat{p}}{\partial\hat{r}} + \mu_l\left(\frac{1}{\hat{r}^2}\frac{\partial}{\partial\hat{r}}\left(\hat{r}^2\frac{\partial\hat{u}}{\partial\hat{r}}\right) - \frac{2\hat{u}}{\hat{r}^2}\right), \tag{2.21}$$

in $\hat{r} > \hat{R}(\hat{t})$, where μ_l is the liquid's dynamic viscosity.

Assuming that there is no heat generated within the liquid cereal, conservation of energy results in an advection–diffusion equation,

$$\frac{\partial\hat{T}}{\partial\hat{t}} + \hat{u}\frac{\partial\hat{T}}{\partial\hat{r}} = \frac{\kappa_l}{\hat{r}^2}\frac{\partial}{\partial\hat{r}}\left(\hat{r}^2\frac{\partial\hat{T}}{\partial\hat{r}}\right) \quad \text{in} \quad \hat{r} > \hat{R}(\hat{t}), \tag{2.22}$$

for the temperature, $\hat{T}(\hat{r},\hat{t})$, in the liquid, where κ_l is the thermal diffusivity of the liquid given by

$$\kappa_l = \frac{k_l}{\rho_l(c_v)_l}; \tag{2.23}$$

here k_l is the thermal conductivity and $(c_v)_l$ the specific heat capacity of the liquid.

An advection–diffusion equation is used to model moisture transport. That is, the water concentration, $\hat{c}(\hat{r},\hat{t})$, in the liquid obeys

$$\frac{\partial\hat{c}}{\partial\hat{t}} + \hat{u}\frac{\partial\hat{c}}{\partial\hat{r}} = \frac{D_l}{\hat{r}^2}\frac{\partial}{\partial\hat{r}}\left(\hat{r}^2\frac{\partial\hat{c}}{\partial\hat{r}}\right) \quad \text{in} \quad \hat{r} > \hat{R}(\hat{t}), \tag{2.24}$$

where D_l is the diffusivity of moisture in the liquid.

2.3.2 Liquid boundary conditions

The kinematic boundary conditions for the liquid are given by

$$\hat{u} = \frac{\mathrm{d}\hat{R}}{\mathrm{d}\hat{t}} \quad \text{at} \quad \hat{r} = \hat{R}, \quad \text{and} \quad \hat{u} \to 0 \quad \text{as} \quad r \to \infty. \tag{2.25a,b}$$

The normal stress balance at the gas–liquid interface is given by

$$\hat{p}_{\mathrm{B}} + \hat{\sigma}_{\hat{r}\hat{r}} = \frac{2\gamma_l}{\hat{R}} \quad \text{at} \quad \hat{r} = \hat{R}, \tag{2.26}$$

where γ_l is the surface tension and $\hat{\sigma}_{\hat{r}\hat{r}}$ is the radial component of the stress in the liquid, given by

$$\hat{\sigma}_{\hat{r}\hat{r}} = -\hat{p} + 2\mu_l\frac{\partial\hat{u}}{\partial\hat{r}}. \tag{2.27}$$

Far from the bubble, the normal stress balance is given by

$$p + \hat{\sigma}_{\hat{r}\hat{r}} \to 0 \qquad \text{as} \qquad \hat{r} \to \infty, \tag{2.28}$$

where p is the macroscale pressure. At the liquid–bubble interface, heat is consumed by the vaporisation of the moisture according to the energy balance given by

$$k_l \frac{\partial \hat{T}}{\partial \hat{r}} = \frac{D_l \mathcal{L} \rho_l}{M} \frac{\partial \hat{c}}{\partial \hat{r}} \quad \text{at} \quad \hat{r} = \hat{R}, \tag{2.29}$$

where $\mathcal{L}$ is the latent heat of vapourising water from the liquid, and M is the molecular mass of water.

We assume that the gas in the bubble is ideal, and that the temperature, pressure, and density are uniform throughout the bubble. The ideal gas law (see, *e.g.* [8]) states that the bubble pressure is given by

$$\hat{p}_{\mathrm{B}} = \frac{\hat{N}_{\mathrm{B}} R_{\mathrm{G}} \hat{T}_{\mathrm{B}}}{\hat{V}_{\mathrm{B}}}, \tag{2.30}$$

where $\hat{N}_{\mathrm{B}}(\hat{t})$ is the number of moles of gas in the bubble, R_{G} is the ideal gas constant, $\hat{T}_{\mathrm{B}}(\hat{t})$ is the temperature of the bubble and the volume, $\hat{V}_{\mathrm{B}}(\hat{t})$, of the bubble is given by

$$\hat{V}_{\mathrm{B}} = \frac{4\pi \hat{R}^3}{3}. \tag{2.31}$$

We assume that the bubble and the liquid maintain thermal equilibrium at the interface between the two fluids, so that their temperatures are equal, *i.e.*

$$\hat{T}_{\mathrm{B}}(\hat{t}) = \hat{T}(\hat{R}, \hat{t}). \tag{2.32}$$

We denote the concentration of moisture at the interface by $\hat{c}_{\mathrm{B}}(t)$, where

$$\hat{c}_{\mathrm{B}}(\hat{t}) = \hat{c}(\hat{R}, \hat{t}). \tag{2.33}$$

The number of moles of gas in the bubble, $\hat{N}_{\mathrm{B}}$, depends on the cumulative flux of water out of the liquid mixture, *i.e.*

$$\frac{\mathrm{d}\hat{N}_{\mathrm{B}}}{\mathrm{d}\hat{t}} = \frac{4\pi \hat{R}^2 D_l \rho_l}{M} \frac{\partial \hat{c}}{\partial \hat{r}} \quad \text{at} \quad \hat{r} = \hat{R}. \tag{2.34}$$

We assume that the vapour pressure of the moisture, which is equal to the pressure in the bubble, only depends on the moisture concentration and the temperature of the liquid at the liquid–bubble interface. We encompass this relationship between the pressure in the bubble and the state of the liquid in a general form,

$$\hat{p}_{\mathrm{B}} = \mathcal{P}_{\mathrm{B}}(\hat{c}_{\mathrm{B}}(\hat{t}), \hat{T}_{\mathrm{B}}(\hat{t})) \quad \text{at} \quad \hat{r} = \hat{R}, \tag{2.35}$$

where $\mathcal{P}_{\mathrm{B}}(\hat{c}_{\mathrm{B}}, \hat{T}_{\mathrm{B}})$ is a prescribed function of $\hat{c}_{\mathrm{B}}(\hat{t})$ and $\hat{T}_{\mathrm{B}}(\hat{t})$, and will depend on the chemistry and thermodynamics of the system. For a complex mixture with a dissolved volatile species, the vapour pressure of the volatile component is related to its concentration and the temperature of the mixture by a *sorption isotherm*. The sorption isotherm is typically assumed to take the form (see, *e.g.* [9])

$$\mathcal{P}_{\mathrm{B}}(\hat{c}_{\mathrm{B}}, \hat{T}_{\mathrm{B}}) = a_w(\hat{c}_{\mathrm{B}}) P_V(\hat{T}_{\mathrm{B}}), \tag{2.36}$$

where $a_w(\hat{c}_{\mathrm{B}})$ is the activity of the moisture in the mixture and $P_V(\hat{T}_{\mathrm{B}})$ is the vapour pressure of the pure form of the moisture.

The activity is a constitutive law modifying the vapour pressure by accounting for the fact that the moisture is not in its pure form, and that the moisture will interact with the other components of the mixture. The vapour pressure of pure water is given by the Claussius–Clapeyron equation [8], which is given by

$$P_V(\hat{T}_{\mathrm{B}}) = p_{\mathrm{ref}} \exp\left(-\frac{\mathcal{L}_w}{R_{\mathrm{G}}}\left(\frac{1}{T_{\mathrm{ref}}} - \frac{1}{\hat{T}_{\mathrm{B}}}\right)\right), \tag{2.37}$$

where $\mathcal{L}_w$ is the latent heat of vaporisation of water, and p_{ref} is the vapour pressure of the pure form of the moisture at temperature T_{ref} (*e.g.* 1 atm at 373K). The general form of the vapour pressure of the moisture in the mixture that we shall adopt is therefore given by

$$\mathcal{P}_{\mathrm{B}}(\hat{c}_{\mathrm{B}}, \hat{T}_{\mathrm{B}}) = a_w(\hat{c}_{\mathrm{B}}) p_{\mathrm{ref}} \exp\left(-\frac{\mathcal{L}_w}{R_{\mathrm{G}}}\left(\frac{1}{T_{\mathrm{ref}}} - \frac{1}{\hat{T}_{\mathrm{B}}}\right)\right). \tag{2.38}$$

The exact nature of the activity, $a_w(\hat{c}_{\mathrm{B}})$, for a cereal mixture must be determined experimentally. The constitutive law for the activity of water in a cereal mixture we

use throughout this work, also used by Lach [42] in their extrusion model, was found experimentally by [18] for a flour-based dough to be given by

$$a_w(\hat{c}) = \frac{a_1 \hat{c}}{1 + a_2 \hat{c}}, \tag{2.39}$$

where $a_1 = 15.3\, kg_{(\text{liquid})}/kg_{(H_2O)}$ and $a_2 = 14.3\, kg_{(\text{liquid})}/kg_{(H_2O)}$. If we use the initial temperature, T_0, as the reference temperature, the reference pressure is given by

$$p_{\text{ref}} = \frac{\hat{p}_0}{a_w(c_0)}, \tag{2.40}$$

where $\hat{p}_0$ is the initial bubble pressure, and $\hat{c}_0$ is the initial moisture concentration at the bubble interface. The general form of the constitutive law relating the bubble pressure and the state of the surrounding liquid, incorporating (2.40) into (2.38), is then given by

$$\mathcal{P}_{\text{B}}(\hat{c}_{\text{B}}, \hat{T}_{\text{B}}) = \hat{p}_0 \frac{a_w(\hat{c}_{\text{B}})}{a_w(\hat{c}_0)} \exp\left(\frac{\mathcal{L}_w}{R_{\text{G}}}\left(\frac{1}{T_0} - \frac{1}{\hat{T}_{\text{B}}}\right)\right). \tag{2.41}$$

Far from the bubble the temperature and moisture concentration remain undisturbed; the far field behaviour of $\hat{T}$ and $\hat{c}$ is given by

$$\hat{T} \to T_0 \qquad \text{and} \qquad \hat{c} \to c_0 \qquad \text{as} \quad \hat{r} \to \infty. \tag{2.42}$$

If this far-field behaviour is observed in the initial data, it will persist in the solution for $\hat{T}$ and $\hat{c}$.

2.3.3 Rayleigh–Plesset equation

The equation for conservation of mass (2.20) can be integrated subject to the kinematic condition (2.25a) to give

$$\hat{u}(\hat{r}, \hat{t}) = \frac{\hat{R}^2}{\hat{r}^2} \frac{\mathrm{d}\hat{R}}{\mathrm{d}\hat{t}} \qquad \text{in} \qquad \hat{r} > \hat{R}(\hat{t}). \tag{2.43}$$

Integrating the equation for conservation of momentum, (2.21), over $\hat{r}$, subject to boundary conditions (2.25a) and (2.25b), gives

$$\rho_l \left(\frac{\mathrm{d}\hat{R}}{\mathrm{d}\hat{t}}\right)^2 + \rho_l \hat{R} \frac{\mathrm{d}^2 \hat{R}}{\mathrm{d}\hat{t}^2} = p - \hat{p}(\hat{R}, \hat{t}). \tag{2.44}$$

Applying the dynamic conditions (2.26)–(2.28) yields the equation for the rate of bubble growth, the Rayleigh–Plesset equation [15], given by

$$\rho_l \left(\frac{\mathrm{d}\hat{R}}{\mathrm{d}\hat{t}} \right)^2 + \rho_l \hat{R} \frac{\mathrm{d}^2 \hat{R}}{\mathrm{d}\hat{t}^2} = \hat{p}_\mathrm{B} - p - \frac{2\gamma_l}{\hat{R}} - \frac{4\mu_l}{\hat{R}} \frac{\mathrm{d}\hat{R}}{\mathrm{d}\hat{t}}. \tag{2.45}$$

This equation is a second-order, nonlinear ordinary differential equation (ODE) for $\hat{R}(\hat{t})$ given $\hat{p}_\mathrm{B}(\hat{t}) - p(\hat{t})$. When coupled to a macroscale model, by mapping from the Lagrangian frame of the bubbles to the Eulerian frame of the macroscale model, derivatives with respect to $\hat{t}$ transform to the material derivative defined in (2.4).

2.3.4 Initial conditions

The initial conditions imposed in the Lagrangian reference frame of the bubble correspond to boundary conditions imposed at $z = -\ell$ in the Eulerian frame of the macroscale model. The initial microscale temperature, and moisture concentration are assumed to be equal to their respective macroscale counterparts at $z = -\ell$. Of the remaining variables, we must prescribe some, and determine the rest through the thermodynamics of the system. There is some freedom in which conditions are imposed, and which are determined. We present a self-consistent set of initial conditions based on those prescribed by [42]; however, this is not the only way of formulating the initial conditions.

The initial microscale temperature and moisture concentration are given by

$$\hat{T}(\hat{r}, 0) = T_0 \quad \text{and} \quad \hat{c}(\hat{r}, 0) = c_0 \quad \text{for} \quad \hat{r} > \hat{R}_0, \tag{2.46}$$

where T_0 and c_0 are the macroscopic temperature and moisture concentration at $z = -\ell$, and $\hat{R}_0$ is the initial bubble radius. The initial temperature and moisture concentration at the bubble interface are given respectively by

$$\hat{T}_\mathrm{B}(0) = T_0 \quad \text{and} \quad \hat{c}_\mathrm{B}(0) = c_0 \quad \text{at} \quad \hat{t} = 0. \tag{2.47}$$

We impose the initial bubble radius, $\hat{R}_0$, and the initial growth rate of the bubble, which we denote $\hat{u}_0$, such that

$$\frac{\mathrm{d}\hat{R}}{\mathrm{d}\hat{t}} = \hat{u}_0 \qquad \text{at} \qquad \hat{t} = 0. \tag{2.48}$$

As we have prescribed $\hat{T}_\mathrm{B}(0)$ and $\hat{c}_\mathrm{B}(0)$, the initial bubble pressure, $\hat{p}_0$, is given by (2.38), where we now let $T_\mathrm{ref} = 273.15\,K$ and $p_\mathrm{ref} = 100\,kPa$, which are the temperature and vapour pressure respectively of water under standard temperature and

pressure (STP) conditions [8]. Having prescribed $T_{\mathrm{B}}(0)$ and $\hat{R}_0$, and determined $\hat{p}_0$, the initial number of moles of gas can be determined from the ideal gas law, (2.30).

There is some freedom in the choice of initial conditions because we have not incorporated a model of nucleation. Instead of imposing $\hat{R}_0$, we may impose $\hat{N}_0$, and determine $\hat{R}_0$ from (2.30). We choose to impose $\hat{R}_0$ rather than $\hat{N}_0$ because the initial bubble radius is a particularly important length scale. We will see in Chapter 3 that different initial bubble radii can push the microscale model into different asymptotic regimes.

In the small-Reynolds-number limit, where the inertial terms in (2.45) can be neglected, we cannot enforce all of the initial conditions prescribed here. When we consider this limit in subsequent work, we do not prescribe the initial growth rate condition given by (2.48).

2.3.5 Summary of microscale model

The equations governing the microscale dynamics include the Rayleigh–Plesset equation (2.45), and two advection–diffusion equations, one for heat (2.22) and one for moisture (2.24). The boundary conditions imposed at the liquid–bubble interface, which account for thermodynamic interactions between phases, include a thermodynamic equilibrium condition (2.41) and a conservation of heat/mass flux condition (2.29). The condition for thermodynamic equilibrium, (2.41), is given by a constitutive law commonly used in the literature that decomposes the vapour pressure of a component in a mixture into the product of the activity of that component and the vapour pressure of a pure form of that component. The activity of the moisture is given by (2.39). Far from the bubble we impose that the conditions remain unchanged from the macroscale (2.42). The state of the bubble is given by the ideal gas law (2.30), where: the gas temperature is assumed to be equal to the liquid temperature at the interface (2.32); the number of moles of gas in the bubble is found by integrating the flux of gas out of the mixture (2.34); and the volume of the bubble is a function of its radius, as predicted by the Rayleigh–Plesset equation (2.45).

2.3.6 The cell model

In order to account for the presence of other bubbles, some authors use a microscale model in which the liquid surrounding the bubble is finite in extent [5, 60]. This so-

called cell model is identical to the disperse model, except for the boundary conditions imposed away from the liquid–bubble interface. In the cell model, instead of imposing pressure, temperature, and moisture concentration boundary conditions as $\hat{r} \to \infty$, boundary conditions are imposed at $\hat{r} = \hat{R}_{\text{cell}}$, where $\hat{R}_{\text{cell}}$ is the radius of the finite shell of liquid surrounding the bubble. In the cell model the stress balance, given by (2.28) in the disperse model, is given by

$$\hat{\sigma}_{\hat{r}\hat{r}} = -p \quad \text{at} \quad \hat{r} = \hat{R}_{\text{cell}}. \tag{2.49}$$

The kinematic boundary condition, (2.25b), is modified to

$$\hat{u} = \frac{\mathrm{d}\hat{R}_{\text{cell}}}{\mathrm{d}\hat{t}} \quad \text{at} \quad \hat{r} = \hat{R}_{\text{cell}}. \tag{2.50}$$

As the liquid is taken to be incompressible on the microscale, the rate at which the outer boundary of the cell moves can be related to the rate at which the liquid–bubble interface moves. The total volume of liquid is constant, say $\hat{V}_T$, thus

$$\hat{V}_T = \frac{4\pi\hat{R}_{\text{cell}}^3}{3} - \frac{4\pi\hat{R}^3}{3}. \tag{2.51}$$

By differentiating (2.51) with respect to time, we observe that

$$\frac{\mathrm{d}\hat{R}_{\text{cell}}}{\mathrm{d}\hat{t}} = \frac{\hat{R}^2}{\hat{R}_{\text{cell}}^2}\frac{\mathrm{d}\hat{R}}{\mathrm{d}\hat{t}}. \tag{2.52}$$

We suppose that initially, the cell has radius $R_{\text{cell}} = \mathcal{R}_0$. Imposing boundary conditions (2.49)–(2.52), instead of (2.25)–(2.28), results in a modified form of the Rayleigh–Plesset equation (2.45), namely

$$\left(1 - 2\left(\frac{\hat{R}}{\hat{R}_{\text{cell}}}\right) + \left(\frac{\hat{R}}{\hat{R}_{\text{cell}}}\right)^4\right)\left(\frac{\mathrm{d}\hat{R}}{\mathrm{d}\hat{t}}\right)^2 + \left(1 - \left(\frac{\hat{R}}{\hat{R}_{\text{cell}}}\right)\right)\hat{R}\frac{\mathrm{d}^2\hat{R}}{\mathrm{d}\hat{t}^2}$$
$$= (\hat{p}_{\text{B}} - p) - \frac{\Gamma}{\hat{R}} - \frac{4}{\hat{R}}\left(1 - \left(\frac{\hat{R}}{\hat{R}_{\text{cell}}}\right)^3\right)\frac{\mathrm{d}\hat{R}}{\mathrm{d}\hat{t}}. \tag{2.53}$$

For a finite cell, no-flux conditions are enforced on the heat and moisture at the outer liquid boundary, *i.e.*

$$\frac{\partial\hat{T}}{\partial\hat{r}} = \frac{\partial\hat{c}}{\partial\hat{r}} = 0 \quad \text{at} \quad \hat{r} = \hat{R}_{\text{cell}}, \tag{2.54}$$

which replace (2.42). The no-flux boundary conditions imposed in the cell model are included to represent the effect of neighbouring bubbles on the growth of a bubble.

When the fluid surrounding the bubble is infinite in extent, there is unlimited heat and moisture available to fuel the bubbles growth. By considering a finite shell of fluid, Amon and Denson [5] assume that each bubble only has access to a finite amount of heat and moisture; surrounding bubbles are also consuming these quantities. The size of the fluid shell, and therefore the amount of heat and moisture available to each bubble, is determined by the number of bubbles per unit volume of liquid.

The cell model is a common choice of microscale model for extrusion [3, 42, 44, 78] as it offers a conceptually simple way of accounting for some bubble dynamics, such as competition for resources like heat and moisture. There are, however, a number of issues with the cell model that lead us to use the disperse model, which considers an infinite body of liquid, instead. Specifically, imposing the fluid pressure at some fixed distance from the liquid–bubble interface is somewhat arbitrary; there is no consistent relationship between the macroscopic pressure and the pressure imposed in the cell model. In this work, we are generally only concerned with the disperse limit, so we only consider the disperse model. Moreover, we will show in Section 2.6.1 that the cell model approaches the disperse model as $\hat{R}_{\text{cell}} \to \infty$, and that both models predict similar results for early times when the finite-extent effects of the cell model do not play a role. We therefore do not expect predictions made by either model to differ significantly for the cases we consider. We find that, in the parameter regimes we are interested in for extrusion, it is easier to reduce the complexity of the disperse model than it is the cell model. So, given that both models are similar when the bubbles are small and far apart, and that it is mathematically easier to work with the disperse model, we will use the disperse model throughout this work unless otherwise stated.

2.4 Estimated parameter values

The values of the parameters that feature in the model can be found in table 2.1. Where available, we have taken parameter values given in Lach [42], as these values are industrially relevant to cereal manufacture. The values given are typical values; we will see in Chapters 3 and 4 how varying some of these parameters, particularly the initial values, changes the dynamics of the system.

Parameters			
Parameter	Diffusion	Value	Units
D_l	Diffusion coefficient of moisture (in liquid)	10^{-10}	m^2/s
a	Die diameter	10^{-3}	m
k_l	Diffusion coefficient of heat (in liquid)	$0.3 - 0.6$	$W/m/K$
$(c_v)_l$	Specific heat capacity (of liquid)	2900	J/kg/K
κ_l	Diffusivity of heat (in liquid)	$0.7 - 1.4 \times 10^{-7}$	m^2/s
μ_l	Viscosity of liquid	3×10^3	$Pa \cdot s$
$\hat{R}_0$	Initial bubble radius	10^{-5}	m
$\mathcal{R}_0$	Initial cell size	10^{-4}	m
ρ_l	Density of liquid	1400	kg/m^3
T_0	Initial temperature	403	K
T_{atm}	Atmospheric temperature	298.15 [43]	K
c_0	Initial moisture concentration	0.25	$kg_{H_2O}/kg_{(\text{liquid})}$
γ_l	Surface tension coefficient	0.04	N/m
M	Molecular mass of water	0.018 [8]	kg/mol
$\hat{N}_0$	Initial number of moles of gas in bubble	3.9×10^{-11}	mol
$\mathcal{L}$	Latent heat of vaporisation of moisture from cereal	2.1×10^5	J/mol
$\mathcal{L}_w$	Latent heat of vaporisation of water	40.65×10^3 [8]	J/mol
R_{G}	Ideal gas constant	8.314	$J/mol/K$
W	Typical flow speed of mixture	0.23	m/s
η	Bubble number density	5×10^{11}	$\text{bubbles}/m^3_{\text{liquid}}$

Table 2.1: *Typical values of the parameters that feature in the microscale–macroscale model. Unless otherwise stated, the values were taken from Lach [42].*

2.5 Dimensionless macroscale model

In this section we non-dimensionalise the model presented in Section 2.2. We suppose that there is a characteristic velocity scale, W, and a characteristic length scale, l_e. The velocity scale depends on the feed rate of the extruder, which is controlled by the extruder operator. In practice there may be two different lengthscales: the lengthscale for variation along the axis, which we denote l_e, and the typical length scale of the cross section, which we denote l_d. In this chapter we take l_e and l_d to be equal to the diameter of the die, a. In Chapter 3 we discuss how the appropriate length scale for variation along the z-axis can be found from the microscale model, and there are situations when l_e may be greater than the diameter of the die; we exploit this discrepancy in Chapter 4. We non-dimensionalise the variables by scaling

$$\begin{aligned} \boldsymbol{x} &= l_e \boldsymbol{x}', & \boldsymbol{u} &= W\boldsymbol{u}', & t &= \frac{l_e}{W}t', \\ \rho &= \rho_l \rho', & \boldsymbol{\sigma} &= \frac{\mu_l W}{l_e}\boldsymbol{\sigma}', & p &= p_{\text{atm}} + \frac{\mu_l W}{l_e}p', \\ \varkappa &= \frac{1}{l_e}\varkappa', & \mu &= \mu_l \mu', & \lambda &= \mu_l \lambda', \end{aligned} \tag{2.55}$$

where $\boldsymbol{x} = (x, y, z)$, and a prime denotes a dimensionless variable. We assume that the mixture is mostly composed of liquid; thus, we have taken the typical viscosity and density of the mixture to be the liquid viscosity, μ_l, and liquid density, ρ_l, respectively. Here, the viscous pressure scaling $\mu_l W/l_e$ has been used and p_{atm} is the pressure of the atmosphere outside the extruder; however, we will only consider the scaled value of the atmospheric pressure, p'_{atm}, defined according to

$$p_{\text{atm}} = \frac{\mu_l W p'_{\text{atm}}}{l_e}. \tag{2.56}$$

The surface of the die is defined by $G_1(x, y, z) = 0$ for $-\mathcal{Z}_n < z' < 0$, where $\mathcal{Z}_n = \ell/l_e$ is the dimensionless nucleation point, and the free surface is defined by $G_2(x, y, z, t) = 0$ for $0 < z < 1$.

This choice of scaling gives the dimensionless system (dropping primes)

$$\frac{\partial \rho}{\partial t} + \nabla \cdot (\rho \boldsymbol{u}) = 0, \tag{2.57}$$

$$Re\, \rho \frac{\mathrm{D}\boldsymbol{u}}{\mathrm{D}t} = \nabla \cdot \boldsymbol{\sigma} + St \rho \boldsymbol{e}_y, \tag{2.58}$$

in the volume bounded by $G_1(x,y,z)=0$ for $-\mathcal{Z}_n < z < 0$ and $G_2(x,y,z,t)=0$ for $0<z<1$, where $\boldsymbol{e}_y=(0,1,0)$ is the unit vector in the y direction, the dimensionless stress tensor is given by

$$\boldsymbol{\sigma} = (-p + \lambda \nabla \cdot \boldsymbol{u})\mathbb{I} + \mu\left(\nabla \boldsymbol{u} + (\nabla \boldsymbol{u})^T\right), \tag{2.59}$$

and

$$Re = \frac{\rho_l W l_e}{\mu_l}, \qquad St = \frac{\rho_l g l_e^2}{\mu_l W}, \tag{2.60}$$

are the Reynolds number and Stokes number respectively. The dimensionless boundary conditions inside the die are given by

$$\boldsymbol{u} = \boldsymbol{0} \quad \text{on} \quad G_1(x,y,z)=0, \tag{2.61}$$

for $-\mathcal{Z}_n < z < 0$. The respective dimensionless kinematic and dynamic boundary conditions on the fluid surface outside the die are given by

$$\frac{\partial G_2}{\partial t} + \boldsymbol{u}\cdot\nabla G_2 = 0, \qquad \boldsymbol{\sigma}\cdot\nabla G_2 = -\gamma^* \varkappa \nabla G_2 \quad \text{on} \quad G_2(x,y,z,t)=0, \tag{2.62}$$

for $0<z<1$, where the inverse capillary number, γ^*, is given by

$$\gamma^* = \frac{\gamma_l}{\mu_l W}. \tag{2.63}$$

2.5.1 Conservation of energy and moisture

In addition to the scalings (2.55) in Section 2.5, we non-dimensionalise the equations for conservation of energy and moisture by employing the scalings given by

$$T = T_0 + \mathcal{T}T', \qquad c = c_0 + c_0 c' \qquad c_v = (c_v)_l c_v', \qquad k = k_l k', \qquad D = D_l D',$$

where the temperature scale, $\mathcal{T} = T_0 - T_{\text{atm}}$, is the difference between the temperature at which bubbles nucleate, T_0, and the atmospheric temperature, T_{atm}, and we have taken the typical scales for the heat capacity, thermal conductivity, and diffusivity of moisture to be equal to the corresponding values for the liquid. The dimensionless governing equations, dropping the primes for convenience, for heat and moisture transport are given respectively by

$$\begin{aligned}\rho\frac{\mathrm{D}}{\mathrm{D}t}(c_v T) =& \frac{1}{Pe_T}\nabla\cdot(k\nabla T) \\ &+ \mathcal{V}\left(\mu\left(\nabla\boldsymbol{u} + (\nabla\boldsymbol{u})^T\right) : \nabla\boldsymbol{u} + \lambda(\nabla\cdot\boldsymbol{u})^2 - (p_{\text{atm}}+p)\nabla\cdot\boldsymbol{u}\right), \end{aligned} \tag{2.64}$$

$$\frac{\partial c}{\partial t} + \nabla\cdot(c\boldsymbol{u}) = \frac{1}{Pe_c}\nabla\cdot(D\nabla c), \tag{2.65}$$

in the volume bounded by $G_1(x,y,z)=0$ for $-\mathcal{Z}_n < z < 0$ and $G_2(x,y,z,t)=0$ for $0<z<1$, where

$$Pe_T = \frac{Wl_e}{\kappa_l}, \qquad Pe_c = \frac{Wl_e}{D_l}, \tag{2.66a,b}$$

are the Péclet numbers for heat and moisture transport respectively, and

$$\mathcal{V} = \frac{\mu_l W}{l_e \rho_l (c_v)_l \mathcal{T}}, \tag{2.67}$$

captures the relative importance of energy generated by viscous dissipation on the change in energy density of the fluid. The dimensionless equivalents of conditions (2.16) inside the die are given by

$$T = \frac{T_{\text{die}} - T_0}{\mathcal{T}}, \qquad \boldsymbol{n}\cdot\nabla c = 0 \quad \text{on} \quad G_1(x,y,z)=0, \tag{2.68a,b}$$

for $-\mathcal{Z}_n < z < 0$. Outside of the die the dimensionless equivalents of (2.17a–b) are given by

$$\boldsymbol{n}\cdot\nabla T = \mathcal{H}\,(T+1)\,, \quad \mathcal{P}(c,T) = p_{\text{atm}} \quad \text{on} \quad G_2(x,y,z,t)=0, \tag{2.69a,b}$$

for $0<z<1$, where $\mathcal{H} = hl_e$ is the dimensionless rate of heat transport away from the product. At the point of nucleation the dimensionless temperature and moisture concentrations are given by

$$T = 0, \qquad c = 0 \quad \text{at} \quad z = -\mathcal{Z}_n. \tag{2.70a,b}$$

The dimensionless equivalents of (2.19) are given by

$$\frac{\partial T}{\partial z} = 0, \qquad \frac{\partial c}{\partial z} = 0 \quad \text{at} \quad z = 1. \tag{2.71a,b}$$

A complete list of the macroscale dimensionless parameters, and their typical sizes, can be found in table 2.2.

2.6 Dimensionless microscale bubble model

In this section we non-dimensionalise the microscale model summarised in Section 2.3.5. For a bubble in a liquid, the relevant length scale is the initial bubble radius, $\hat{R}_0$. We use the same pressure and timescale as that of the macroscale model. Thus, we non-dimensionalise the variables according to the scalings

$$\begin{aligned}
&\hat{r} = \hat{R}_0 \hat{r}', && \hat{t} = \frac{l_e}{W}\hat{t}', && \hat{R} = \hat{R}_0 \hat{R}', \\
&\hat{u} = \frac{\hat{R}_0 W}{l_e}\hat{u}', && \hat{p} = p_{\text{atm}} + \frac{\mu_l W}{l_e}\hat{p}', && \hat{p}_{\text{B}} = \frac{\mu_l W}{l_e}\hat{p}'_{\text{B}}, \\
&\hat{N}_{\text{B}} = \hat{N}_0 + \frac{4\pi \hat{R}_0 D_l l_e \rho_l c_0}{MW}\hat{N}'_{\text{B}}, && \hat{T} = T_0 + \frac{\mathcal{L} D_l \rho_l c_0}{Mk}\hat{T}', && \hat{c} = c_0 + c_0 \hat{c}'.
\end{aligned} \tag{2.72}$$

Macroscale dimensionless parameters		
Parameter	Definition	Value
Re	$\dfrac{\rho W l_e}{\mu_l}$	3.3×10^{-4}
Pe_T	$\dfrac{W l_e}{\kappa_l}$	3.4×10^{3}
Pe_c	$\dfrac{W l_e}{D_l}$	7×10^{6}
γ^*	$\dfrac{\gamma_l}{\mu_l W}$	5×10^{-5}
$\mathcal{H}$	$l_e h$	–
St	$\dfrac{\rho_l g l_e^2}{\mu_l W}$	1.8×10^{-4}
$\mathcal{V}$	$\dfrac{\mu_l W}{l_e \rho_l (c_v)_l \mathcal{T}}$	5.8×10^{-4}

Table 2.2: *The typical sizes of the macroscale dimensionless parameters, calculated using the values listed in table 2.1. To calculate the values listed here, we have taken the typical lengthscale, l_e, to be equal to the die diameter, a.*

The velocity scale, $\hat{R}_0 W/l_e$, is the natural scale scale based on the bubble growth rate. The temperature scale, $\mathcal{L}D_l\rho_l c_0/kM$, is chosen such that both sides of the equation for heat flux at the interface, (2.29), balance. The scale for the number of moles of gas, $4\pi\hat{R}_0 D_l l_e \rho_l c_0/MW$, is chosen so that both sides of the equation for moisture flux at the interface, (2.34), balance. As stated in Section 2.3.4, the value of $\hat{N}_0$ is solved for based on the prescription of the initial states of the other variables.

With the choices of scale given in (2.72), the moisture and temperature transport within the liquid are described by the dimensionless equations, dropping primes,

$$\frac{\partial \hat{T}}{\partial t} + \frac{\hat{R}^2}{\hat{r}^2}\frac{\mathrm{d}\hat{R}}{\mathrm{d}t}\frac{\partial \hat{T}}{\partial \hat{r}} = \frac{1}{\widehat{Pe}_T \hat{r}^2}\frac{\partial}{\partial \hat{r}}\left(\hat{r}^2 \frac{\partial \hat{T}}{\partial \hat{r}}\right), \tag{2.73}$$

$$\frac{\partial \hat{c}}{\partial t} + \frac{\hat{R}^2}{\hat{r}^2}\frac{\mathrm{d}\hat{R}}{\mathrm{d}t}\frac{\partial \hat{c}}{\partial \hat{r}} = \frac{1}{\widehat{Pe}_c \hat{r}^2}\frac{\partial}{\partial \hat{r}}\left(\hat{r}^2 \frac{\partial \hat{c}}{\partial \hat{r}}\right), \tag{2.74}$$

in $\hat{r} > \hat{R}(\hat{t}\,)$. The parameters $\widehat{Pe}_T$ and $\widehat{Pe}_c$ are the effective microscale Péclet numbers associated with heat and mass transport respectively, defined to be

$$\widehat{Pe}_T = \frac{\hat{R}_0^2 W}{\kappa_l l_e}, \qquad \widehat{Pe}_c = \frac{\hat{R}_0^2 W}{D_l l_e}. \tag{2.75}$$

The dimensionless bubble radius evolves *via* the dimensionless equivalent of the Rayleigh–Plesset equation, (2.45), given by

$$\widehat{Re}\left(\frac{\mathrm{d}\hat{R}}{\mathrm{d}\hat{t}}\right)^2 + \widehat{Re}\hat{R}\frac{\mathrm{d}^2\hat{R}}{\mathrm{d}\hat{t}^2} = \hat{p}_{\mathrm{B}} - \hat{p} - p_{\mathrm{atm}} - \frac{\Gamma}{\hat{R}} - \frac{4}{\hat{R}}\frac{\mathrm{d}\hat{R}}{\mathrm{d}\hat{t}}, \tag{2.76}$$

where $\hat{Re}$ is the reduced microscale Reynolds number,

$$\widehat{Re} = \frac{\rho_l W \hat{R}_0^2}{\mu_l l_e}, \tag{2.77}$$

and

$$\Gamma = \frac{2\gamma_l l_e}{\mu_l \hat{R}_0 W}, \tag{2.78}$$

captures the influence of surface tension on bubble growth. The dimensionless bubble pressure (see (2.30) for dimensional form) is then given by

$$\hat{p}_{\mathrm{B}} = \bar{P}\frac{(\Sigma^{-1} + \hat{N}_{\mathrm{B}})(1 + \Theta\hat{T}_{\mathrm{B}})}{\hat{R}^3}, \tag{2.79}$$

where

$$\Sigma = \frac{4\pi\hat{R}_0 D_l \rho_l c_0 l_e}{MW\hat{N}_0}, \qquad \Theta = \frac{\mathcal{L} D_l \rho_l c_0}{MkT_0}, \qquad \bar{P} = \frac{3R_{\mathrm{G}}T_0 D_l \rho_l c_0 l_e^2}{\hat{R}_0^2 M \mu_l W^2}. \tag{2.80}$$

The number of moles of gas in the bubble evolves according to the dimensionless form of (2.34), given by

$$\frac{\mathrm{d}\hat{N}_{\mathrm{B}}}{\mathrm{d}\hat{t}} = \hat{R}^2\frac{\partial\hat{c}}{\partial\hat{r}} \quad \text{at} \quad \hat{r} = \hat{R}. \tag{2.81}$$

The dimensionless boundary conditions for equations (2.73) and (2.74), denoting $\hat{c}(\hat{R},\hat{t})$ and $\hat{T}(\hat{R},\hat{t})$ by $\hat{c}_{\mathrm{B}}(t)$ and $\hat{T}_{\mathrm{B}}(t)$ respectively, are given by

$$\hat{p}_{\mathrm{B}} = \mathcal{P}_{\mathrm{B}}(\hat{c}_{\mathrm{B}}, \hat{T}_{\mathrm{B}}), \qquad \frac{\partial\hat{c}}{\partial\hat{r}} = \frac{\partial\hat{T}}{\partial\hat{r}} \qquad \text{at} \quad \hat{r} = \hat{R}, \tag{2.82a,b}$$

and

$$\hat{T} \to 0, \qquad \hat{c} \to 0 \qquad \text{as} \qquad \hat{r} \to \infty. \tag{2.83a,b}$$

The dimensionless vapour pressure of the mixture (*i.e.* the bubble pressure) is the dimensionless form of (2.41), given by

$$\mathcal{P}_{\mathrm{B}}(\hat{c}_{\mathrm{B}}, \hat{T}_{\mathrm{B}}) = \hat{p}_0 \frac{a_w(\hat{c}_{\mathrm{B}})}{a_w(0)} \exp\left(\Lambda\left(1 - \frac{1}{1+\Theta\hat{T}_{\mathrm{B}}}\right)\right), \tag{2.84}$$

where

$$\Lambda = \frac{\mathcal{L}}{R_{\mathrm{G}} T_0}, \tag{2.85}$$

is the ratio of molar enthalpy of vaporisation to the thermal energy per mole of gas. The dimensionless microscale parameters, and estimates for their typical values are contained in table 2.3. We defer discussion of the implications of the magnitudes of the dimensionless parameters until Chapters 3 and 4. We note that the macroscale and microscale dimensionless parameters are related. For example, the microscale Reynolds number, $\widehat{Re}$, and Péclet numbers, $\widehat{Pe}_T$ and $\widehat{Pe}_c$, are smaller than their macroscale counterparts by a factor of $(\hat{R}_0/l_e)^2$. The microscale dimensionless surface tension term Γ, however, is greater than its macroscale counterpart γ^* by a factor of $2l_e/\hat{R}_0$.

The dimensionless initial conditions for our system are given by

$$\begin{aligned} \hat{c}(\hat{r},0) = 0, \qquad & \hat{T}(\hat{r},0) = 0, \qquad & \hat{R}(0) = 1, \qquad & \hat{p}_0 = \frac{\bar{P}}{\Sigma}, \\ \hat{u}_0 = 0, \qquad & \hat{T}_{\mathrm{B}}(0) = 0, \qquad & \hat{N}_{\mathrm{B}}(0) = 0. & \end{aligned} \tag{2.86}$$

The dimensionless system of equations includes two PDEs, (2.73) and (2.74), with their associated boundary conditions, (2.82) and (2.83), two ODEs, (2.76) and (2.81), an algebraic condition, (2.79), and the initial conditions, (2.86).

2.6.1 Dimensionless cell model

To non-dimensionalise the cell model we rescale the cell radius, $\hat{R}_{\mathrm{cell}} = \mathcal{R}_0 \hat{R}'_{\mathrm{cell}}$, where $\mathcal{R}_0$ is the initial radius of the liquid-cell, so that the dimensionless modified Rayleigh–Plesset equation is given by (dropping primes)

$$\begin{aligned} \widehat{Re}\left(1 - 2\delta\left(\frac{\hat{R}}{\hat{R}_{\mathrm{cell}}}\right) + \delta^4\left(\frac{\hat{R}}{\hat{R}_{\mathrm{cell}}}\right)^4\right)\left(\frac{\mathrm{d}\hat{R}}{\mathrm{d}\hat{t}}\right)^2 + \widehat{Re}\left(1 - \delta\left(\frac{\hat{R}}{S}\right)\right)\hat{R}\frac{\mathrm{d}^2\hat{R}}{\mathrm{d}\hat{t}^2} \\ = \hat{p}_{\mathrm{B}} - p - p_{\mathrm{atm}} - \frac{\Gamma}{\hat{R}} - \frac{4}{\hat{R}}\left(1 - \delta^3\left(\frac{\hat{R}}{\hat{R}_{\mathrm{cell}}}\right)^3\right)\frac{\mathrm{d}\hat{R}}{\mathrm{d}\hat{t}}, \end{aligned} \tag{2.87}$$

Microscale dimensionless parameters		
Parameter	Definition	Value
Γ	$\dfrac{2\gamma_l l_e}{\mu_l \hat{R}_0 W}$	3.2×10^{-2}
$\bar{P}$	$\dfrac{3R_{\mathrm{G}}T_0 D_l \rho_l c_0 l_e^2}{\hat{R}_0^2 M \mu_l W^2}$	10.5
Θ	$\dfrac{\mathcal{L} D_l \rho_l X_0}{M k T_0}$	3.2×10^{-4}
Σ	$\dfrac{4\pi \hat{R}_0 D_l \rho_l c_0 l_e}{MW \hat{N}_0}$	7.8×10^{-2}
δ	$\dfrac{\hat{R}_0}{\mathcal{R}_0}$	10^{-1}
$\widehat{Re}$	$\dfrac{\rho W \hat{R}_0^2}{\mu_l l_e}$	3.6×10^{-9}
$\widehat{Pe}_T$	$\dfrac{\hat{R}_0^2 W}{\kappa_l l_e}$	3.7×10^{-2}
$\widehat{Pe}_c$	$\dfrac{\hat{R}_0^2 W}{D_l l_e}$	78
Λ	$\dfrac{\mathcal{L}_w}{R_{\mathrm{G}} T_0}$	12.5

Table 2.3: *The typical sizes of the microscale dimensionless parameters, calculated using the values listed in table 2.1. To calculate the values listed here, we have taken the typical lengthscale, l_e, to be equal to the die diameter, a.*

where $\delta = \hat{R}_0/\mathcal{R}_0$. We can see that in the disperse limit, as $\delta \to 0$, the modified Rayleigh–Plesset equation (2.87) tends to the Rayleigh–Plesset equation (2.76). The dimensionless no-flux boundary conditions, (2.54), are given by

$$\frac{\partial \hat{T}}{\partial \hat{r}} = 0, \qquad \frac{\partial \hat{c}}{\partial \hat{r}} = 0 \qquad \text{at} \qquad \hat{r} = \hat{R}_{\mathrm{cell}}. \tag{2.88a,b}$$

2.7 Concluding remarks

In this chapter we presented a mathematical model for the extrusion of a viscous, bubbly mixture. In Section 2.1 we outlined the various stages of processing that a mixture undergoes during extrusion, and then restricted our attention to the stage

of interest in this thesis: the flash. During this stage, the mixture is composed of a viscous-liquid phase, and a gas phase contained in bubbles within the liquid. The model we presented describes the dynamics of the mixture from the point inside the extruder where bubbles nucleate, until bubble growth is arrested outside the die. Rather than model the evolution of the two phases individually, we treated the mixture as a single-phase, viscous, compressible fluid. The resultant model comprises a macroscale model for the flow of a viscous, compressible fluid, coupled to a microscale model for the evolution of bubbles within the mixture. We considered the dispersed limit for the bubbles within the mixture, where they are small and far apart, so that they do not interact within the microscale model.

In Section 2.2 we described the macroscale model. In this case, the equations governing the conservation of mass and momentum of the effective fluid are given by the compressible Navier–Stokes equations. The domain we considered is partially bounded by the immobile, impermeable die of the extruder, and for the remaining portion of the domain, the fluid is free to expand. This system is closed by relating the density of the effective fluid to the size of bubbles in the mixture, which evolve according to the microscale model. In this section, we also presented the equations for the conservation of energy and moisture in the product; however, we did not present a mechanism by which these quantities can impact the mass and momentum flow rates for the product.

In Section 2.3 we presented the microscale model, which comprises two fluids: gas, contained in bubbles; and a viscous liquid of infinite extent surrounding the bubble. At the interface between these two fluids, we imposed conditions enforcing conservation of mass, momentum, and energy, as well as a condition enforcing thermodynamic equilibrium. The pressure far from the bubble is assumed to be that of the macroscale model, thereby coupling the microscale dynamics to the macroscale. The microscale model relates the macroscale pressure to the evolution of the bubble size, and therefore to the density of the effective fluid.

In Section 2.5 we presented the dimensionless macroscale model. Analysis of this model can be found in Chapters 4 and 5. In Section 2.6 we presented the dimensionless microscale model. This model is analysed in Chapter 3, and used in Chapters 4 and 5 to close the macroscale model. Alongside the microscale model that we employed, we presented the cell model, which is commonly employed in literature. We

find, particularly for the analysis in Chapter 3, the cell model to be more difficult to work with than disperse model that we consider, so we use the disperse model throughout this work, unless otherwise stated.

Chapter 3

Analysis of the microscale model

In Section 2.6 of Chapter 2, we presented a dimensionless microscale model with parameters that can take a range of values due to uncertainty in some of the dimensional quantities. In this chapter we analyse how the dynamics of the microscale model differs depending on the parameter regime. We will make frequent reference to the model described in Section 2.6 throughout this chapter, as all of the analysis performed in this chapter is designed to solve, or approximate the solution to, this model. The conclusions drawn in this chapter are a result of asymptotic arguments. As a general principle, we choose scales associated with the richest distinguished limit. In accordance with this principle, in Section 3.1 we derive an estimate for the macroscale length over which bubble growth occurs. From this estimate we find that it is plausible for the axial length scale to be much greater than the cross-sectional length scale, which motivates a slender-limit approximation that we consider in Chapter 4. We also show in Section 3.1 that, depending on the bubble size, there are three different parameter regimes for which the dominant terms in the microscale model are different. We refer to each of these parameter regimes as a different *case*.

In Section 3.2 we describe a numerical scheme that uses the method of lines to find solutions to the microscale model. In the regimes for which the parameters are not of order unity, this numerical method becomes more computationally expensive; these regimes are the three cases presented in Section 3.1. In Section 3.3 we exploit the asymptotic structure of the model to derive reduced systems of equations for each case that are much easier to solve numerically. For one of these cases, by supposing that the macroscopic pressure is fixed, we can derive an explicit solution to the reduced model. In Section 3.3.3.2 this solution is discussed in comparison to predictions made by Rayleigh [57] for the same macroscopic forcing (*i.e.* a constant imposed pressure).

In Section 3.4 we compare the solutions obtained using the numerical method of Section 3.2 to the solutions obtained using the reduced models of Section 3.3.

3.1 A microscale-based length scale estimate

The parameters that control bubble growth depend on the physics of bubble nucleation, as well as the extruder settings (*e.g.* the flow speed W). Typical values for these parameters are contained in table 2.1; however, some of these parameters may vary significantly. In particular, the initial bubble size, $\hat{R}_0$, may vary depending on the state of the mixture when the bubbles nucleate. This leads to a range of possible dimensionless parameter values, and a number of regimes in which some physical processes become more or less prominent. We expect fundamentally different behaviour depending on which physical processes feature in the dominant balance within the model. Exploiting the asymptotic behaviour of the system can lead to systems of equations that require less effort to solve, and for which physical insight is thereby more readily obtained. In this section we consider the possible sizes of the dimensionless parameters and the consequences of retaining or discarding terms based on these parameters. By retaining terms, we introduce conditions on the dimensionless parameters, which can be used to estimate unknown parameters. We use this idea to derive an estimate of the macroscopic length scale over which bubbles grow. At the end of this section, we outline three possible cases which are allowed by the uncertainty about the exact dynamics of nucleation.

We expect the microscale Reynolds number to be small over the entire range of expected dimensionless parameter values. We therefore neglect inertial terms in the Rayleigh–Plesset equation (2.76) throughout this work. The reduced Rayleigh–Plesset equation that we consider is then given by

$$\frac{\mathrm{d}\hat{R}}{\mathrm{d}\hat{t}} = \frac{\hat{R}}{4}\left(\hat{p}_{\mathrm{B}} - p - p_{\mathrm{atm}} - \frac{\Gamma}{\hat{R}}\right). \tag{3.1}$$

By discarding second-order derivatives, we cannot enforce all of the initial conditions described in (2.86). We impose the initial bubble radius, $\hat{R}_0$, and neglect the prescription of the initial bubble growth rate, $\hat{u}_0$. Neglecting inertial terms in the cell model reduces the modified Rayleigh–Plesset equation, (2.87), to

$$\left(1 - \delta^3\left(\frac{\hat{R}}{\hat{R}_{\mathrm{cell}}}\right)^3\right)\frac{\mathrm{d}\hat{R}}{\mathrm{d}\hat{t}} = \frac{\hat{R}}{4}\left(\hat{p}_{\mathrm{B}} - p - p_{\mathrm{atm}} - \frac{\Gamma}{\hat{R}}\right). \tag{3.2}$$

Neglecting the inertial terms can have a significant effect on the behaviour of a bubble in certain situations, such as bubble collapse; this is discussed further in Section 3.3.3.2.

Two parameters that we expect to vary substantially, and have a significant effect on the dimensionless parameters, are the initial bubble radius, $\hat{R}_0$, and the flow speed, W. The initial bubble radius will depend on the physics of nucleation, which we do not have a good model for; in place of a good model, we will categorize the behaviour observed for a range of $\hat{R}_0$. The flow speed, W, can be controlled by tuning the extruder differently. Within the range of expected values for $\hat{R}_0$ and W, there will be significant changes in three fundamental quantities: the length scale over which bubble growth occurs, which we denote by L, and associated with the length scale for evolution along the z-axis or *the axial length scale*; the Péclet number for microscale heat transport, $\widehat{Pe}_T$; and the Péclet number for microscale moisture transport, $\widehat{Pe}_c$.

The axial length scale will depend on the timescale for growth of the advected bubbles, which can be deduced by considering the dominant balance in the Rayleigh–Plesset equation (3.1). In particular, we will select the parameters that ensure that $\hat{p}_{\mathrm{B}}$ is of order unity. The dimensionless parameter $\bar{P}$—defined in table 2.3 and appearing in the dimensionless bubble pressure equation (2.79)—is the ratio of the force on the liquid due to the pressure of the bubble and the viscous force resisting the growth of the bubble, which is growth rate dependent. Ensuring these forces balance, which is equivalent to ensuring $\bar{P} = \mathcal{O}(1)$, results in a *consistency condition* relating the parameters that may vary, $\hat{R}_0$ and W, to L, given by

$$\left(\frac{\hat{R}_0 W}{L}\right)^2 \approx \frac{3R_G T_0 D_l \rho_l c_0}{M\mu_l}. \tag{3.3}$$

The condition $\bar{P} = \mathcal{O}(1)$ can be interpreted as a condition between the product of the timescale of bubble growth and the initial bubble pressure; increasing the latter decreases the former. If the bubbles nucleate with higher initial pressure, the subsequent bubble growth will be more rapid, corresponding to a smaller timescale.

The timescale of bubble growth and flow speed W will determine the axial length scale, L. The diameter of the die, which we will denote d, is the *cross-sectional length scale* corresponding to the x and y axes. In Chapter 2 we assumed a single length scale corresponding to the diameter of the die, a, and took $l_e = l_d = a$. From hereon

we distinguish between the length scale for evolution along the axis of flow and the typical die diameter, and take $l_e = L$ and $l_d = a$. We can define the aspect ratio, ϵ, to be given by

$$\epsilon = \frac{a}{L}. \tag{3.4}$$

Using the consistency condition (3.3), we can express ϵ in terms of the system parameters to be given by

$$\epsilon \approx \left(\frac{3 R_G T_0 D_l \rho_{\mathrm{B}} c_0 d^2}{\hat{R}_0^2 M \mu_l W^2} \right)^{1/2}. \tag{3.5}$$

When the parameters are such that $\epsilon \ll 1$, we can make significant progress by considering the slender-limit, as in Chapter 4. Supposing the remaining parameters that comprise ϵ do not vary significantly, there are regions in $\hat{R}_0$–W space for which $\epsilon \ll 1$, so the slender-limit approximation is valid; these regions are illustrated in figure 3.1. With the parameter choices used in Lach [42], the predicted value of epsilon is $\epsilon \approx 3$, which is illustrated by the red dot on figure 3.1. Using (3.5) as a guide, a practitioner may wish to tune the extruder settings so that $\epsilon \ll 1$ and reduced models can be used.

The microscale Péclet numbers for heat and moisture transport, $\widehat{Pe}_c$ and $\widehat{Pe}_T$ respectively, vary significantly over the range of possible $\hat{R}_0$ values. The sizes of these parameters, indicating the relative importance of diffusion on the timescale of bubble growth, have a strong impact on the microscale dynamics. Fundamentally different behaviour will be observed depending on whether the Péclet number corresponding to a particular quantity is big, small, or of order unity. Because moisture diffusion is much slower than the diffusion of heat, $\widehat{Pe}_c$ is always much larger than $\widehat{Pe}_T$. There are three cases of interest, each corresponding to a parameter regime in which different processes appear in the dominant balance:

$$\text{Case I} \quad — \widehat{Pe}_T \ll \widehat{Pe}_c \ll 1, \tag{3.6}$$

$$\text{Case II} \quad — \widehat{Pe}_T \ll 1 \ll \widehat{Pe}_c, \tag{3.7}$$

$$\text{Case III} — \quad 1 \ll \widehat{Pe}_T \ll \widehat{Pe}_c. \tag{3.8}$$

By exploiting the asymptotic structure of the model in the various limits described by cases I–III, we can derive reduced models that are good approximations to the full model to leading order. This process is described in Section 3.3.

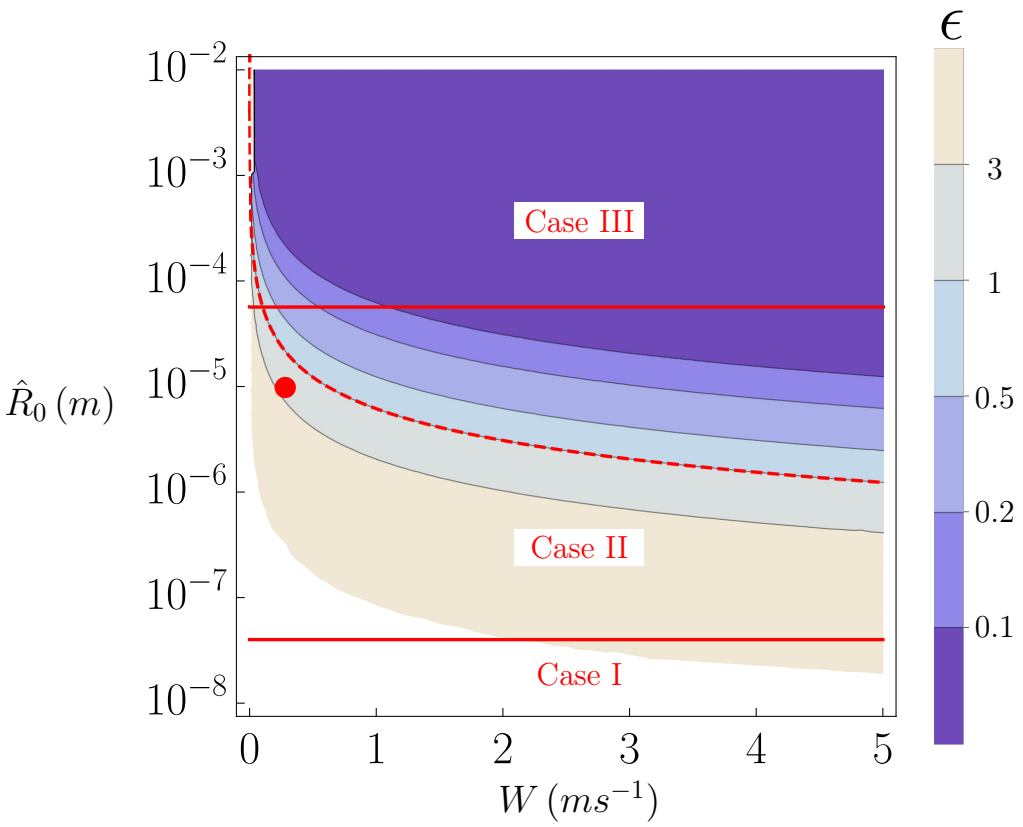

Figure 3.1: *The contours indicate the predicted aspect ratio $\epsilon = a/L$ of the extruded product for different initial bubble radius $\hat{R}_0\,(m)$ and typical velocity $W\,(ms^{-1})$. The red lines distinguish regions of qualitatively different behaviour. The dashed, red line indicates where $\epsilon = 1$; below this line $\epsilon > 1$ and above $\epsilon < 1$. The red dot indicates the parameters used by Lach [42] The solid, red lines separate the cases described by (3.6)–(3.8).*

3.2 Numerical solution of the microscale model

Using a finite-difference scheme, we can find solutions to the full microscale model presented in Section 2.6, with the Rayleigh–Plesset equation (2.76) replaced by the inertialess Rayleigh–Plesset equation (3.1). The governing equations include two partial differential equations, or *PDEs*, (2.73)–(2.74), with boundary conditions given by (2.82) and (2.83); two ordinary differential equations, or *ODEs*, (2.81) and (3.1); and algebraic equations (2.79) and (2.84). The initial conditions for this system are given by (2.86). Rather than solve the equations on a moving domain, we first make a spatial coordinate transformation that fixes the liquid domain. We then use a method-of-lines approach, discretising the spatial derivatives of the PDEs to construct a system comprising only ODEs in time, and algebraic equations. After discretising the spatial derivatives, the system of ODEs and algebraic equations (*i.e.* a Differential–Algebraic equation, or DAE, system) can be solved using MATLAB's *ode15s* function, or by using the DAE capability of a number of open source solvers like *SUNDIALS* or Julia's *DifferentialEquations* package.

3.2.1 Mapping the moving, liquid domain to a fixed domain

We first consider the spatial domain, $\hat{R}(\hat{t}\,) < \hat{r} < \infty$, as well as the PDEs for $\hat{c}(\hat{r},\hat{t}\,)$ and $\hat{T}(\hat{r},\hat{t}\,)$ on this domain. Consider the transformation from $\hat{r}$ to $\hat{s}$ given by

$$\hat{r}^3 - \hat{s}^3 = \hat{R}(\hat{t}\,)^3 - \hat{R}(0)^3, \tag{3.9}$$

where $\hat{R}(0) = 1$ is the initial bubble radius. This transforms the liquid domain from $\hat{r} \in [\hat{R}(t), \infty)$ to $\hat{s} \in [1, \infty)$. Suppose we transform from $(\hat{r},\hat{t}\,)$ to $(\hat{s},\hat{t}\,)$ and define $\widetilde{T}(\hat{s},\hat{t}\,) = \hat{T}(\hat{r},\hat{t}\,)$ and $\widetilde{c}(\hat{s},\hat{t}\,) = \hat{c}(\hat{r},\hat{t}\,)$. The PDEs for heat and water transport, (2.73) and (2.74), are transformed to

$$\frac{\partial \widetilde{T}}{\partial \hat{t}} = \frac{1}{\widehat{Pe}_T \hat{s}^2} \frac{\partial}{\partial \hat{s}} \left(B(\hat{s},\hat{R}) \frac{\partial \widetilde{T}}{\partial \hat{s}} \right) \qquad \text{for} \qquad 1 < \hat{s} < \infty, \tag{3.10}$$

and

$$\frac{\partial \widetilde{c}}{\partial \hat{t}} = \frac{1}{\widehat{Pe}_c \hat{s}^2} \frac{\partial}{\partial \hat{s}} \left(B(\hat{s},\hat{R}) \frac{\partial \widetilde{c}}{\partial \hat{s}} \right) \qquad \text{for} \qquad 1 < \hat{s} < \infty, \tag{3.11}$$

where

$$B(\hat{s},\hat{R}) = \frac{(\hat{s}^3 + \hat{R}(\hat{t}\,)^3 - 1)^{4/3}}{\hat{s}^2}. \tag{3.12}$$

We denote the values of $\widetilde{c}$ and $\widetilde{T}$ at the boundary by $\widetilde{c}_{\rm B}$ and $\widetilde{T}_{\rm B}$ respectively. The boundary conditions (2.82) and (2.83) become

$$\hat{p}_{\rm B} = \mathcal{P}_{\rm B}(\widetilde{c}_{\rm B}, \widetilde{T}_{\rm B}), \quad \frac{\partial \widetilde{c}}{\partial \hat{s}} = \frac{\partial \widetilde{T}}{\partial \hat{s}} \quad \text{at} \quad \hat{s} = 1, \tag{3.13a,b}$$

and

$$\widetilde{T} \to 0, \qquad \widetilde{c} \to 0 \qquad \text{as} \qquad \hat{s} \to \infty. \tag{3.14a,b}$$

The initial conditions remain unchanged, *i.e.*

$$\widetilde{T} = 0 \qquad \text{and} \qquad \widetilde{c} = 0 \qquad \text{at} \qquad \hat{t} = 0. \tag{3.15}$$

If instead we considered a finite body of liquid, the only required modification to this formulation is to replace the far-field boundary conditions, (3.14), by

$$\frac{\partial \widetilde{T}}{\partial \hat{s}} = 0, \qquad \frac{\partial \widetilde{c}}{\partial \hat{s}} = 0 \qquad \text{at} \qquad \hat{s} = \frac{1}{\delta}, \tag{3.16}$$

where we recall that $\delta = \hat{R}_0/\mathcal{R}_0$ is the ratio of the initial bubble radius to the initial radius of the cell. Of the remaining equations: (2.79) and (3.1) remain unchanged under the transformation, and (2.81) is transformed to

$$\frac{{\rm d}\hat{N}_{\rm B}}{{\rm d}\hat{t}} = \hat{R}^4 \frac{\partial \tilde{c}(\hat{R}, t)}{\partial \hat{s}}. \tag{3.17}$$

3.2.2 Numerical Scheme

We truncate the domain at $\hat{s} = \mathcal{S}$, where $\mathcal{S}$ is large, and discretise the interval $\hat{s} \in [1, \mathcal{S}]$ into n uniformly distributed points by setting $\hat{s}_k = 1 + \Delta\hat{s}\ (k-1)$, for $k = 1, 2, ..., n$, where $\Delta\hat{s} = (\mathcal{S}-1)/(n-1)$. A basic schematic of this discretisation is illustrated in figure 3.2. We only describe the discretisation for equation (3.11), as that for equation (3.10) is similar. We denote the value of quantity $\widetilde{c}$ at grid-point k by $\tilde{c}_k$. We discretise each derivative with respect to $\hat{s}$ using a centred-difference scheme. The diffusion equation for transport of water on the discretised spatial domain is replaced by a set of coupled ODEs for $\tilde{c}_k$, *viz.*

$$\frac{{\rm d}c_k}{{\rm d}\hat{t}} = \frac{1}{\widehat{Pe}_c \hat{s}_k^2} \left(\frac{B_{k+1/2}(\tilde{c}_{k+1} - \tilde{c}_k) - B_{k-1/2}(\tilde{c}_k - \tilde{c}_{k-1})}{\Delta\hat{s}^2} \right) \quad \text{for } k = 2, ..., n-1, \tag{3.18}$$

where $B_{k\pm\frac{1}{2}} = B(\hat{s}_k \pm \Delta\hat{s}/2, \hat{R})$. The boundary conditions, (3.13) and (3.14), become algebraic equations,

$$\hat{p}_{\rm B} = \mathcal{P}_{\rm B}(\tilde{c}_1, \tilde{T}_1), \qquad \sum_{i=1}^{j} w_i \tilde{c}_i = \sum_{i=1}^{j} w_i \tilde{T}_i, \tag{3.19a,b}$$

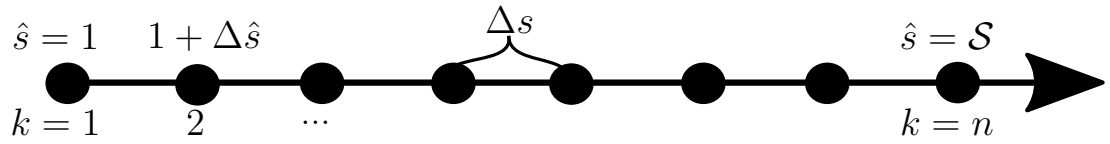

Figure 3.2: *Schematic of the discretised, infinite fluid domain. Above the grid, the $\hat{s}$ coordinates are listed (each point is $\Delta\hat{s}$ further than the last), and below, the k labels listed. We truncate the infinite domain at $\hat{s}=\mathcal{S}$.*

and

$$\tilde{T}_n = 0, \qquad \tilde{c}_n = 0, \tag{3.20a,b}$$

where w_i are the weights corresponding to the approximation of a derivative using $j-1$ points to the right of the grid point at which the derivative is being approximated. An efficient methodology for deriving these weights is described by Fornberg [26]. Using this formulation to approximate the spatial derivatives at the boundary, with $j=4$ instead of $j=2$, increases the numerical accuracy of this approximation from $\mathcal{O}(\Delta\hat{s})$ to $\mathcal{O}(\Delta\hat{s}^3)$. For $j=4$, the vector of values corresponding to the weights w_i is

$$\boldsymbol{w} = (-11/6, 3, -3/2, 1/3). \tag{3.21}$$

The resulting set of $2n+3$ DAEs includes (3.18), the discretised form of (2.73)

$$\frac{\mathrm{d}\tilde{T}_k}{\mathrm{d}\hat{t}} = \frac{1}{\widehat{Pe}_T \hat{s}_k^2}\left(\frac{B_{k+1/2}(\tilde{T}_{k+1}-\tilde{T}_k) - B_{k-1/2}(\tilde{T}_k - \tilde{T}_{k-1})}{\Delta\hat{s}^2}\right) \quad \text{for } k = 2, ..., n-1, \tag{3.22}$$

the boundary conditions, (3.19) and (3.20),

$$\hat{p}_\mathrm{B} = \mathcal{P}_\mathrm{B}(\tilde{c}_1, \tilde{T}_1), \tag{3.23}$$

$$\sum_{i=1}^{j} w_i \tilde{c}_i = \sum_{i=1}^{j} w_i \tilde{T}_i, \tag{3.24}$$

$$\tilde{T}_n = 0, \tag{3.25}$$

$$\tilde{c}_n = 0, \tag{3.26}$$

the ideal gas law (2.79),

$$\hat{p}_\mathrm{B} = \bar{P}\frac{(\Sigma^{-1} + \hat{N}_\mathrm{B})(1+\Theta\tilde{T}_1)}{\hat{R}^3}, \tag{3.27}$$

the Rayleigh–Plesset equation (3.1)

$$\frac{\mathrm{d}\hat{R}}{\mathrm{d}\hat{t}} = \frac{\hat{R}}{4}\left(\hat{p}_\mathrm{B} - p - p_\mathrm{atm} - \frac{\Gamma}{\hat{R}}\right), \tag{3.28}$$

and the approximation to the ODE for the evolution of the number of moles of gas (3.17),

$$\frac{\mathrm{d}\hat{N}_{\mathrm{B}}}{\mathrm{d}\hat{t}} = \frac{\hat{R}^4}{\Delta\hat{s}} \sum_{i=1}^{j} w_i \widetilde{c}_i. \tag{3.29}$$

To ensure accurate solutions we choose $j = 4$, the number of points, n, and domain size, $\mathcal{S}$, such that an increase in either $\mathcal{S}$ or n results in a negligible (relative to the error threshold set in the numerical solver) change in the solution.

To modify this scheme for a finite body of liquid, the far-field boundary conditions, (3.25) and (3.26), are replaced by the discretised form of (2.83) given by

$$\sum_{i=n-j}^{n} \tilde{w}_{i-n+j+1} \tilde{T}_i = 0, \qquad \sum_{i=n-j}^{n} \tilde{w}_{i-n+j+1} \tilde{c}_i = 0, \tag{3.30a,b}$$

where $\tilde{w}_i$ are the weights corresponding to a derivative using $j-1$ points to the left of the grid point at which the derivative is being approximated. For $j = 4$, the same number of points used to approximate derivatives from the right for boundary condition (3.19b), the corresponding vector of weight values is given by

$$\tilde{\boldsymbol{w}} = -\boldsymbol{w} = (11/5, -3, 3/2, -1/3). \tag{3.31}$$

Instead of imposing these boundary conditions at some truncation length $\mathcal{S}$ taken to be large enough to represent an infinite domain, we instead impose (3.30) at $\hat{s} = 1/\delta$.

The truncation length, $\mathcal{S}$, must be large enough so that neither quantity has time to diffuse as far as $\mathcal{S}$ before the simulation is terminated. This means that for smaller Péclet numbers, and therefore more significant diffusion on the relevant time scale, $\mathcal{S}$ must be larger. For a simulation over a time-span of $\hat{t}_{max}$, where the smallest Péclet number is, say, $\widehat{Pe}$, and (3.25) and (3.26) are the imposed boundary conditions, $\mathcal{S}$ must be such that

$$\mathcal{S} \gtrsim \sqrt{\frac{\hat{t}_{max}}{\widehat{Pe}}}. \tag{3.32}$$

For diffusion-dominated problems, which will require larger domains, we exploit the far-field behaviour of the solution in the small Péclet number limit to modify (3.25) and (3.26) to give more accurate approximations to the infinite fluid domain. This will allow smaller domains to be used for the same accuracy. We discuss the heat-transfer problem, however the same will be true for moisture transfer. The solution to

the diffusion-dominated heat-transport problem in $(\hat{r}, \hat{t}\,)$ coordinates, prior to transformation (3.9), will look asymptotically like

$$\hat{T}(\hat{r}, \hat{t}\,) \sim \frac{A(\hat{t}\,)}{\hat{r}}, \tag{3.33}$$

for large $\hat{r}$, where $A(\hat{t}\,)$ is a degree of freedom. If $\hat{T}$ behaves like (3.33) far from the bubble interface, then

$$\frac{\partial \hat{T}}{\partial \hat{r}} \sim -\frac{A(\hat{t}\,)}{r^2}; \tag{3.34}$$

from which we can eliminate $A(\hat{t}\,)$ from (3.33). Supposing we truncate the domain at $\hat{r} = \mathcal{R}$, we can use the far-field behaviour of $\hat{T}$ to impose a Robin boundary condition, given by

$$\hat{T} + \mathcal{R}\frac{\partial \hat{T}}{\partial \hat{r}} = 0 \qquad \text{at} \qquad \hat{r} = \mathcal{R}, \tag{3.35}$$

which exploits the far-field behaviour of the solution to give a more accurate boundary condition at our truncation length $\mathcal{R}$. After coordinate transformation from $\hat{r}$ to $\hat{s}$ by (3.9), the approximation to the far-field boundary condition (3.35) is given by

$$\hat{T} + \mathcal{S}\frac{\partial \hat{T}}{\partial \hat{s}} = 0 \qquad \text{at} \qquad \hat{s} = \mathcal{S}. \tag{3.36}$$

The discrete equivalent of this boundary condition is given by

$$\tilde{T}_n + \frac{\mathcal{S}}{\Delta \hat{s}} \sum_{i=n-j}^{n} \tilde{w}_{i-n+j+1} \tilde{T}_i = 0, \tag{3.37}$$

where the weights, $\tilde{w}_i$, are given by (3.31).

3.3 Asymptotics of the microscale model

Finding numerical solutions to the microscale model becomes more expensive when the dimensionless parameters are too extreme; particularly for larger Péclet numbers, $\widehat{Pe}_T$ and $\widehat{Pe}_c$. When $\widehat{Pe}_T$ and $\widehat{Pe}_c$ are not of of order unity, we can exploit the asymptotic behaviour of the system to derive accurate, leading-order approximations to the solutions. These asymptotic solutions are no harder to determine, and get more accurate, as the parameters become more extreme. It is often advantageous to use these solutions rather than the method described in Section 3.2 when the dimensionless parameters are not of order unity. In this section we present asymptotic approximations

to the microscale model described in Section 2.6 for the cases described in Section 3.1 by (3.6)–(3.8).

If the Péclet numbers, $\widehat{Pe}_T$ and $\widehat{Pe}_c$, are large, the microscale scaling choices made in Section 2.6 do not result in the richest distinguished limit of the dimensionless microscale model. When the Péclet number corresponding to a particular quantity is large, the total variation in that quantity, as well as the length scale over which this variation occurs, depends on the size of the Péclet number. To account for this, we rescale the microscale moisture concentration and temperature by α and β respectively, such that

$$\hat{c} = \alpha \hat{c}' \qquad \text{and} \qquad \hat{T} = \beta \hat{T}', \tag{3.38a,b}$$

where $\hat{c}'$ and $\hat{T}'$ are of order unity, and α and β are constants chosen based on the Péclet numbers. For each of the three cases we consider, (3.6)–(3.8), α and β must be chosen so that the richest distinguished limit is considered. For the remainder of this section we will only consider the rescaled quantities $\hat{c}'$ and $\hat{T}'$, and we drop the primes for convenience.

Consider the dimensionless equations (2.73) and (2.74) with boundary conditions (2.82) and (2.83), which govern the transport of heat and moisture within the liquid. The values of $\hat{T}$ and $\hat{c}$ at the liquid–bubble boundary are particularly important, so we define $\hat{T}_{\mathrm{B}}$ and $\hat{c}_{\mathrm{B}}$, given by

$$\hat{T}_{\mathrm{B}}(\hat{t}\,) = \hat{T}(\hat{R}, \hat{t}\,), \qquad \text{and} \qquad \hat{c}_{\mathrm{B}}(\hat{t}\,) = \hat{c}(\hat{R}, \hat{t}\,), \tag{3.39a,b}$$

for notational convenience, where $\hat{T}_{\mathrm{B}}$ is equal to the bubble temperature. Using the rescalings introduced in (3.38), the governing equations are given by

$$\frac{D\hat{c}}{D\hat{t}} = \frac{1}{\widehat{Pe}_c}\nabla^2\hat{c} \qquad \text{and} \qquad \frac{D\hat{T}}{D\hat{t}} = \frac{1}{\widehat{Pe}_T}\nabla^2\hat{T} \qquad \text{in} \qquad \hat{R} \leq \hat{r} < \infty, \tag{3.40a,b}$$

with boundary conditions given by

$$\frac{\partial \hat{T}}{\partial \hat{r}} = \frac{\alpha}{\beta}\frac{\partial \hat{c}}{\partial \hat{r}} \qquad \text{and} \qquad \mathcal{P}_{\mathrm{B}}(\alpha\hat{c}, \beta\hat{t}\,) = \hat{p}_{\mathrm{B}}, \qquad \text{at} \qquad \hat{r} = \hat{R}. \tag{3.41a,b}$$

and

$$\hat{T} \to 0 \qquad \text{and} \qquad \hat{c} \to 0 \qquad \text{as} \qquad \hat{r} \to \infty. \tag{3.42a,b}$$

By rescaling the moisture concentration *via* (3.39a), we introduce an α into equation (2.81), which determines the rate at which the number of moles of gas in the bubble changes and is now given by

$$\frac{\mathrm{d}\hat{N}_{\mathrm{B}}}{\mathrm{d}\hat{t}} = \alpha \hat{R}^2 \frac{\partial \hat{c}(\hat{R}, \hat{t}\,)}{\partial \hat{r}}. \tag{3.43}$$

By rescaling the temperature *via* (3.39b), we introduce a β into equation (2.79), so that after rescaling the bubble pressure is given by

$$\hat{p}_{\mathrm{B}} = \bar{P} \frac{(\Sigma^{-1} + \hat{N}_{\mathrm{B}})(1 + \Theta\beta\hat{T}_{\mathrm{B}})}{\hat{R}^3}. \tag{3.44}$$

To ensure a dominant balance in equation (3.43), we require that

$$\alpha \frac{\partial \hat{c}}{\partial \hat{r}} = \mathcal{O}(1), \tag{3.45}$$

which becomes a condition that can be used to determine α depending on the Péclet number parameter regime. By imposing condition (3.45), from (3.41 a) we obtain another consistency condition:

$$\beta \frac{\partial \hat{T}}{\partial \hat{r}} = \mathcal{O}(1), \tag{3.46}$$

which can be used to determine β depending on the Péclet number parameter regime. In Section 3.1 we deduced the macroscale axial length scale by constructing a condition that ensured a sensible dominant balance in (3.1). Conditions (3.45) and (3.46) have the same function; they ensure that we consider the richest distinguished limit.

In each of the three cases, given by (3.6)–(3.8), we can derive much simpler reduced models by refining the question we wish to consider. Not all of the microscale quantities must be known explicitly to inform the macroscale. For example, we are generally only interested in $\hat{R}$, which depends on the other microscale quantities through $\hat{p}_{\mathrm{B}}$. To determine $\hat{p}_{\mathrm{B}}$, we only need to determine the behaviour of $\hat{c}$ and $\hat{T}$ near the liquid–bubble interface. We can derive reduced models by considering the Dirichlet-to-Neumann and Neumann-to-Dirichlet maps for $\hat{c}$ and $\hat{T}$, which relate the Dirichlet and Neumann boundary data for a particular quantity. For example, the Neumann-to-Dirichlet map for $\hat{c}$ gives the value of $\hat{c}$ at the boundary as a function of Neumann boundary data. In each of the cases we consider in this section, a reduced model can be derived using the same methodology: determine the appropriate leading-order PDE system in the limit of interest; construct the Dirichlet-to-Neumann

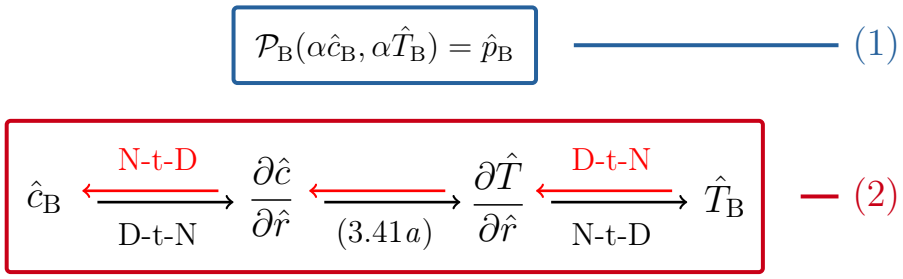

Figure 3.3: *A schematic illustrating the closure of a sub-model within the full microscale model. Two conditions relating $\hat{c}_B$ and $\hat{T}_B$ are constructed using (1) the thermodynamic equilibrium condition (3.41b) and (2) maps from Dirichlet-to-Neumann (D-t-N) and Neumann-to-Dirichlet (N-t-D) boundary data for each quantity, and the flux balance boundary condition (3.41a).*

and Neumann-to-Dirichlet maps for $\hat{c}$ and $\hat{T}$; and then use these maps to relate $\hat{c}_{\mathrm{B}}$ to $\hat{T}_{\mathrm{B}}$ so that, in conjunction with (3.41b), these quantities can be determined without solving the full PDEs. By using prior knowledge about the solution to the PDE system to construct the Dirichlet-to-Neumann and Neumann-to-Dirichlet mappings, we can reduce the complexity of the system that must be solved on the microscale. The formation of this relationship between $\hat{c}_{\mathrm{B}}$ and $\hat{T}_{\mathrm{B}}$ is illustrated schematically in figure 3.3. The evolution of the quantities of interest, $\hat{p}_{\mathrm{B}}$ and therefore $\hat{R}$, is obtained by solving a system of ODEs, algebraic equations, and integral equations; the reduced system can still be difficult to solve, but is often simpler than solving the full system. The reduction in computational cost is greater when the dimensionless parameters take more extreme values.

3.3.1 Case I: $\widehat{Pe}_T \ll \widehat{Pe}_c \ll 1$

When both $\widehat{Pe}_T$ and $\widehat{Pe}_c$ are small, the transport of heat and moisture are diffusion dominated. This regime of bubble growth corresponds to smaller bubbles, so that the natural diffusive length scale is much larger than the size of bubbles. Relative to the timescale of bubble growth, disturbances in both temperature and moisture propagate very quickly over length scales comparable to the bubble size. In this limit, the governing equations for heat and moisture transport, (3.40), are given at leading order by

$$\frac{1}{\hat{r}^2}\left(\hat{r}^2\frac{\partial \hat{T}}{\partial \hat{r}}\right) = 0 \qquad \text{and} \qquad \frac{1}{\hat{r}^2}\left(\hat{r}^2\frac{\partial \hat{c}}{\partial \hat{r}}\right) = 0 \qquad \text{in} \qquad \hat{r} \geq \hat{R}(\hat{t}\,), \qquad (3.47a,b)$$

respectively. The general solutions to (3.47a,b) in terms of $\hat{c}_{\mathrm{B}}$ and $\hat{T}_{\mathrm{B}}$, after imposing the far-field conditions (3.42), are given by

$$\hat{c}(\hat{r},\hat{t}\,) = \frac{\hat{c}_{\mathrm{B}}(\hat{t}\,)\hat{R}(\hat{t}\,)}{\hat{r}} \qquad \text{and} \qquad \hat{T}(\hat{r},\hat{t}\,) = \frac{\hat{T}_{\mathrm{B}}(\hat{t}\,)\hat{R}(\hat{t}\,)}{\hat{r}}. \tag{3.48a,b}$$

With $\alpha = \beta = 1$ in this case, the consistency conditions (3.45) and (3.46) are satisfied. In this case, the relationship between $\hat{c}_{\mathrm{B}}$ and $\hat{T}_{\mathrm{B}}$, and the respective gradients at $\hat{r} = \hat{R}$ are given by

$$\frac{\partial \hat{c}}{\partial \hat{r}} = -\frac{\hat{c}_{\mathrm{B}}}{\hat{R}}, \qquad \frac{\partial \hat{T}}{\partial \hat{r}} = -\frac{\hat{T}_{\mathrm{B}}}{\hat{R}}. \tag{3.49a,b}$$

The distinction between the Dirichlet-to-Neumann and Neumann-to-Dirichlet map in this case is not pertinent because it is easy to express (3.49) as either. Boundary condition (3.41a), as well as (3.42a,b) give

$$\hat{c}_{\mathrm{B}}(\hat{t}\,) = \hat{T}_{\mathrm{B}}(\hat{t}\,), \tag{3.50}$$

which means that the remaining boundary condition (3.41b) can be expressed as

$$\mathcal{P}_{\mathrm{B}}\left(\hat{T}_{\mathrm{B}}(\hat{t}\,), \hat{T}_{\mathrm{B}}(\hat{t}\,)\right) = \hat{p}_{\mathrm{B}}. \tag{3.51}$$

3.3.1.1 Reduced model for Case I

The resulting system comprises three equations that must be solved simultaneously for, $\hat{R}$, $\hat{N}_{\mathrm{B}}$, and $\hat{T}_{\mathrm{B}}$, given by

$$\frac{\mathrm{d}\hat{R}}{\mathrm{d}\hat{t}} = \frac{\hat{R}}{4}\left(\frac{\bar{P}(\Sigma^{-1} + \hat{N}_{\mathrm{B}})(1+\Theta\hat{T}_{\mathrm{B}})}{\hat{R}^3} - p - p_{\mathrm{atm}} - \frac{\Gamma}{\hat{R}}\right), \tag{3.52}$$

$$\frac{\mathrm{d}\hat{N}_{\mathrm{B}}}{\mathrm{d}\hat{t}} = -\hat{R}\hat{T}_{\mathrm{B}}, \tag{3.53}$$

$$\frac{(\Sigma^{-1} + \hat{N}_{\mathrm{B}})(1+\Theta\hat{T}_{\mathrm{B}})}{\hat{R}^3} = \frac{a_w(\hat{T}_{\mathrm{B}})}{\Sigma a_w(0)} \exp\left(\Lambda\left(1 - \frac{1}{1+\Theta\hat{T}_{\mathrm{B}}}\right)\right). \tag{3.54}$$

After the solutions for $\hat{R}$, $\hat{N}_{\mathrm{B}}$, and $\hat{T}_{\mathrm{B}}$ are known, the remaining bubble variables, $\hat{p}_{\mathrm{B}}$ and $\hat{c}_{\mathrm{B}}$ are given by

$$\hat{p}_{\mathrm{B}} = \frac{\bar{P}(\Sigma^{-1} + \hat{N}_{\mathrm{B}})(1+\Theta\hat{T}_{\mathrm{B}})}{\hat{R}^3}, \tag{3.55}$$

$$\hat{c}_{\mathrm{B}} = \hat{T}_{\mathrm{B}}. \tag{3.56}$$

The initial conditions for (3.52) and (3.53) are given by

$$\hat{R} = 1 \qquad \text{and} \qquad \hat{N}_{\mathrm{B}} = 0 \qquad \text{at} \qquad \hat{t} = 0, \tag{3.57a,b}$$

and $\hat{T}_{\mathrm{B}} = 0$ at $\hat{t} = 0$ by necessity due to (3.54) and the initial conditions (3.57).

3.3.2 Case II: $\widehat{Pe}_T \ll 1 \ll \widehat{Pe}_c$

The diffusion of heat is much faster than the diffusion of moisture, which means that $\widehat{Pe}_c$ can be large while $\widehat{Pe}_T$ is small. In this case, the transport of heat is diffusion dominated, and the transport of moisture is advection dominated. Based on the parameters used by Lach [42], we expect this case to be most relevant to cereal extrusion, as illustrated by the red dot on figure 3.1. In this case, in order to satisfy all of the boundary conditions, we expect a moisture boundary layer in the liquid near the bubble. Resolving this boundary layer numerically can be challenging, so we instead derive an approximation to the solution valid for large $\widehat{Pe}_c$ and small $\widehat{Pe}_T$.

In the small $\widehat{Pe}_T$ limit, the advection–diffusion equation (2.73) for microscale heat transfer reduces to

$$\frac{1}{\hat{r}^2}\left(\hat{r}^2\frac{\partial \hat{T}}{\partial \hat{r}}\right) = 0 \qquad \text{for} \qquad \hat{r} \geq \hat{R}(\hat{t}\,), \tag{3.58}$$

which can be integrated subject to the boundary condition (3.42a) to give the temperature profile

$$\hat{T}(\hat{r},\hat{t}\,) = \frac{\hat{T}_{\mathrm{B}}(\hat{t}\,)\hat{R}(\hat{t}\,)}{\hat{r}}, \tag{3.59}$$

in terms of the bubble temperature $\hat{T}_{\mathrm{B}}$. The Dirichlet-to-Neumann map for $\hat{T}$ in this case is given by

$$\frac{\partial \hat{T}}{\partial \hat{r}} = -\frac{\hat{T}_{\mathrm{B}}(\hat{t}\,)}{\hat{R}(\hat{t}\,)}, \tag{3.60}$$

which can be used to relate $\partial\hat{c}/\partial\hat{r}$ to $\hat{T}_{\mathrm{B}}$ through (3.42a), to give

$$\frac{\partial \hat{c}}{\partial \hat{r}} = -\frac{\beta\hat{T}_{\mathrm{B}}(\hat{t}\,)}{\alpha\hat{R}(\hat{t}\,)}, \tag{3.61}$$

at $\hat{r} = \hat{R}(\hat{t}\,)$. From (3.60), the consistency condition (3.45) implies that

$$\beta = 1, \tag{3.62}$$

which is consistent with the temperature scaling deduced in Section (3.3.2) when $\widehat{Pe}_T$ is small. With (3.61) and the appropriate Neumann-to-Dirichlet map, which we have yet to derive, we can construct a relationship between $\hat{T}_{\mathrm{B}}$ and $\hat{c}_{\mathrm{B}}$, akin to (3.50) for Case I, that obviates the need to solve PDEs to understand the bubble dynamics.

The large Péclet number for moisture, $\widehat{Pe}_c$, indicates the presence of a boundary

layer of lower water concentration around the surface of the bubble. By performing a local analysis of the moisture concentration near the bubble interface, we can derive the appropriate Neumann-to-Dirichlet map for the moisture concentration. We first move to a coordinate system local to the surface of the bubble by defining a local variable, $\bar{\zeta}$, that is related to $\hat{r}$ by

$$\hat{r} = \hat{R}(\hat{t}\,) + \epsilon_c \bar{\zeta}, \tag{3.63}$$

where

$$\epsilon_c = \frac{1}{\sqrt{\widehat{Pe}_c}} \ll 1, \tag{3.64}$$

and define $\bar{c}(\bar{\zeta}, \hat{t}\,) = \hat{c}(\hat{r}, \hat{t}\,)$. Under this transformation, to leading order in ϵ_c, (3.40a) is given by

$$\frac{\partial \bar{c}}{\partial \hat{t}} - \frac{2\bar{\zeta}}{\hat{R}} \frac{\mathrm{d}\hat{R}}{\mathrm{d}\hat{t}} \frac{\partial \bar{c}}{\partial \bar{\zeta}} = \frac{\partial^2 \bar{c}}{\partial \bar{\zeta}^2} \qquad \text{for} \qquad \bar{\zeta} > 0. \tag{3.65}$$

Introducing the new coordinates $(\,\zeta, \tau\,)$ *via* the transformations

$$\tau = \int_0^{\hat{t}} \hat{R}(s)^4 \mathrm{d}s, \qquad \zeta = \bar{\zeta} \hat{R}(\hat{t}\,)^2, \tag{3.66}$$

and defining $c^*(\,\zeta, \tau\,) = \bar{c}(\bar{\zeta}, \hat{t}\,)$, we find that $c^*(\,\zeta, \tau\,)$ satisfies the one-dimensional (1D) heat equation on a semi-infinite domain given by

$$\frac{\partial c^*}{\partial \tau} = \frac{\partial^2 c^*}{\partial \zeta^2} \qquad \text{for} \qquad \zeta > 0, \tag{3.67}$$

subject to the boundary conditions

$$\frac{\partial c^*(\,\zeta, \tau)}{\partial \zeta} = -\frac{\epsilon_c \hat{T}^*_{\mathrm{B}}(\tau)}{\alpha \hat{R}^*(\tau)^3} \qquad \text{at} \qquad \zeta = 0, \tag{3.68}$$

$$c^*(\,\zeta, \tau) = 0 \qquad \text{as} \qquad \zeta \to \infty, \tag{3.69}$$

where a star indicates a function of reduced time, τ, so that $\hat{T}^*_{\mathrm{B}}(\tau) = \hat{T}_{\mathrm{B}}(\hat{t})$, $\hat{c}^*_{\mathrm{B}}(\tau) = \hat{c}_{\mathrm{B}}(\hat{t})$, and $\hat{R}^*(\tau) = \hat{R}(\hat{t})$. Initially c^* is given by

$$c^*(\,\zeta, \tau) = 0 \qquad \text{at} \qquad \tau = 0. \tag{3.70}$$

From (3.68) we see that the appropriate value for α, for which both sides of this equation balance, is

$$\alpha = \epsilon_c, \tag{3.71}$$

so that (3.68) is given by

$$\frac{\partial c^*(\zeta,\tau)}{\partial \zeta} = -\frac{\hat{T}_{\mathrm{B}}^*(\tau)}{\hat{R}^*(\tau)^3} \qquad \text{at} \qquad \zeta = 0. \tag{3.72}$$

The system (3.67), (3.69), (3.70), and (3.72), comprises a classical one-dimensional diffusion equation on a semi-infinite domain whose solution (see [50] for more details) may be expressed as

$$c^*(\zeta,\tau) = -\int_0^\tau \left(\frac{e^{-\frac{\zeta^2}{4(\tau-s)}}}{\sqrt{\pi(\tau-s)}}\right) \frac{\partial c^*(0,s)}{\partial \zeta}\mathrm{d}s. \tag{3.73}$$

To determine the other quantities in the microscale system, we only require $\hat{c}_{\mathrm{B}}(t)$; therefore, we are only interested in the value of $c^*(0,\tau)$, given by

$$c^*(0,\tau) = -\int_0^\tau \left(\frac{1}{\sqrt{\pi(\tau-s)}}\right) \frac{\partial c^*(0,s)}{\partial \zeta}\mathrm{d}s, \tag{3.74}$$

which is the Neumann-to-Dirichlet map for the 1D heat equation on a semi-infinite domain. The interfacial moisture concentration, $\hat{c}_{\mathrm{B}}$, is therefore related to $\hat{T}_{\mathrm{B}}$ through (3.72) and (3.74) by

$$\hat{c}_{\mathrm{B}}^*(\tau) = \int_0^\tau \frac{\hat{T}_{\mathrm{B}}^*(s)}{\hat{R}^*(s)^3\sqrt{\pi(\tau-s)}}\mathrm{d}s. \tag{3.75}$$

An important consequence of the rescaling (3.71), is that the leading order change in moisture concentration is of order ϵ_c. This means that the activity of moisture does not play an important role in the thermodynamic equilibrium condition (3.41*b*), which, at leading order in ϵ_c is given by

$$\mathcal{P}_{\mathrm{B}}(0,\hat{T}_{\mathrm{B}}) = \hat{p}_{\mathrm{B}}; \tag{3.76}$$

that is, in this limit, the vapour pressure of moisture depends only on the temperature.

3.3.2.1 Reduced model for Case II

In this case, the system comprises three equations that must be solved simultaneously for $\hat{R}$, $\hat{N}_{\mathrm{B}}$, and $\hat{T}_{\mathrm{B}}$, which are given by

$$\frac{\mathrm{d}\hat{R}}{\mathrm{d}\hat{t}} = \frac{\hat{R}}{4}\left(\frac{\bar{P}}{\Sigma}\mathrm{e}^{\Lambda\left(1-\frac{1}{1+\Theta\hat{T}_{\mathrm{B}}}\right)} - p - p_{\mathrm{atm}} - \frac{\Gamma}{\hat{R}}\right), \tag{3.77}$$

$$\frac{\mathrm{d}\hat{N}_{\mathrm{B}}}{\mathrm{d}\hat{t}} = -\hat{T}_{\mathrm{B}}\hat{R}, \tag{3.78}$$

$$\mathrm{e}^{\Lambda\left(1-\frac{1}{1+\Theta\hat{T}_{\mathrm{B}}}\right)} = \frac{(1+\Sigma\hat{N}_{\mathrm{B}})(1+\Theta\hat{T}_{\mathrm{B}})}{\hat{R}^3}, \tag{3.79}$$

after which, $\hat{p}_{\mathrm{B}}$ and τ are given by

$$\hat{p}_{\mathrm{B}} = \frac{(\Sigma^{-1} + \hat{N}_{\mathrm{B}})(1 + \Theta\hat{T}_{\mathrm{B}})}{\hat{R}^3}, \tag{3.80}$$

$$\tau = \int_0^{\hat{t}} \hat{R}^4 \, \mathrm{d}s, \tag{3.81}$$

and then $\hat{c}_{\mathrm{B}}$ is given by

$$\hat{c}^*_{\mathrm{B}}(\tau) = \int_0^{\tau} \frac{\hat{T}^*_{\mathrm{B}}(s)}{\hat{R}^*(s)^3\sqrt{\pi(\tau - s)}} \, \mathrm{d}s. \tag{3.82}$$

The initial conditions for the ODEs (3.77) and (3.78) are given by

$$\hat{R} = 1 \qquad \text{and} \qquad \hat{N}_{\mathrm{B}} = 0 \qquad \text{at} \qquad \hat{t} = 0, \tag{3.83a,b}$$

and $\hat{T}_{\mathrm{B}} = 0$ at $\hat{t} = 0$ from (3.79). As with Case I, the complexity of the system has been reduced to solving a coupled system of two ODEs and an algebraic equation driven by a macroscale pressure, p. In fact, the system (3.77)–(3.79) can be expressed as just two coupled ODEs, and a third ODE which can be solved after the first two. Deriving this system involves differentiating equation (3.79), and then replacing derivatives of $\hat{R}$ and $\hat{N}_{\mathrm{B}}$ by (3.77) and (3.78) respectively. The result is an ODE for $\hat{T}_{\mathrm{B}}$, given by

$$\begin{aligned}\frac{\mathrm{d}\hat{T}_{\mathrm{B}}}{\mathrm{d}\hat{t}} = &-\frac{\left(1 + \Theta\hat{T}_{\mathrm{B}}\right)^3}{\Theta(\Lambda - 1 - \Theta\hat{T}_{\mathrm{B}})} \mathrm{e}^{\Lambda\left(1 - \frac{1}{1+\Theta\hat{T}_{\mathrm{B}}}\right)} \left(\frac{\Sigma\hat{T}_{\mathrm{B}}}{\hat{R}^3} \right. \\ &\left. + \frac{3}{4(1 + \Theta\hat{T}_{\mathrm{B}})} \mathrm{e}^{\Lambda\left(1 - \frac{1}{1+\Theta\hat{T}_{\mathrm{B}}}\right)} \left(\frac{\bar{P}}{\Sigma} \mathrm{e}^{\Lambda\left(1 - \frac{1}{1+\Theta\hat{T}_{\mathrm{B}}}\right)} - p - p_{\mathrm{atm}} - \frac{\Gamma}{\hat{R}} \right) \right),\end{aligned} \tag{3.84}$$

an ODE for $\hat{R}$ (3.77), and an ODE for $\hat{N}_{\mathrm{B}}$ (3.78), all of which depend only on $\hat{R}$ and $\hat{T}_{\mathrm{B}}$. Expressing the coupled part of the reduced system in this form does not reduce the complexity of the system, but may be advantageous if the system needs to be solved using a software that cannot handle DAE systems; the range of solvers that can handle systems of ODEs is far greater than those that can solve DAE systems.

3.3.3 Case III: $1 \ll \widehat{Pe}_T \ll \widehat{Pe}_c$

In this case, the microscale transport of both heat and moisture are advection dominated; however, we expect diffusive boundary layers for both quantities in the liquid near the bubble. Because $\widehat{Pe}_c$ is always much larger than $\widehat{Pe}_T$, the length scale of

the moisture boundary layer will be much smaller than that of the thermal boundary layer. The methodology employed to analyse the boundary layers will be much the same as we used in Case II. For each boundary layer, we consider the local behaviour near the liquid bubble interface. Define ϵ_T, the length scale of the thermal boundary layer, by

$$\epsilon_T = \frac{1}{\sqrt{\widehat{Pe}_T}}, \tag{3.85}$$

where $\epsilon_c \ll \epsilon_T \ll 1$ and ϵ_c is defined by (3.64). We first introduce a spatial coordinate, $\bar{\zeta}$, to describe the moisture boundary layer, which is defined according to

$$\hat{r} = \hat{R} + \epsilon_c \bar{\zeta}, \tag{3.86}$$

and define $\bar{c}(\bar{\zeta}, \hat{t}\,) = \hat{c}(\hat{r}, \hat{t}\,)$. Under this transformation, to leading order in ϵ_c, (2.74) becomes

$$\frac{\partial \bar{c}}{\partial \hat{t}} - \frac{2\bar{\zeta}}{\hat{R}} \frac{\mathrm{d}\hat{R}}{\mathrm{d}\hat{t}} \frac{\partial \bar{c}}{\partial \bar{\zeta}} = \frac{\partial^2 \bar{c}}{\partial \bar{\zeta}^2} \qquad \text{for} \qquad \bar{\zeta} > 0. \tag{3.87}$$

Introducing the new coordinates $(\,\zeta, \tau\,)$ *via* the transformations

$$\tau = \int_0^{\hat{t}} \hat{R}(s)^4 \mathrm{d}s \qquad \text{and} \qquad \zeta = \hat{R}^2 \bar{\zeta}, \tag{3.88a,b}$$

and defining $c^*(\,\zeta, \tau\,) = \bar{c}(\bar{\zeta}, \hat{t}\,)$, we find that $c^*(\,\zeta, \tau\,)$ satisfies the heat equation

$$\frac{\partial c^*}{\partial \tau} = \frac{\partial^2 c^*}{\partial \zeta^2} \qquad \text{for} \qquad \zeta > 0, \tag{3.89}$$

where initially $c^*(\,\zeta, \tau\,)$ is given by

$$c^*(\,\zeta, \tau) = 0 \qquad\qquad \text{at} \qquad \tau = 0. \tag{3.90}$$

If we suppose that we have Dirichlet data for $c^*(\zeta, \tau)$ at $\zeta = 0$, the general solution is given by

$$c^*(\zeta, \tau) = \int_0^{\tau} \frac{c^*(0, s)\zeta}{2\sqrt{\pi}(\tau - s)^{3/2}} \mathrm{e}^{-\frac{\zeta^2}{4(\tau - s)}} \mathrm{d}s, \tag{3.91}$$

from which we can derive the Dirichlet-to-Neumann map for $c^*(\,\zeta, \tau\,)$. Differentiating (3.91) with respect to ζ gives

$$\frac{\partial c^*(\zeta, \tau)}{\partial \zeta} = \int_0^{\tau} \frac{c^*(0, s)}{2\sqrt{\pi}(\tau - s)^{3/2}} \left(1 - \frac{\zeta^2}{2(\tau - s)}\right) \mathrm{e}^{-\frac{\zeta^2}{4(\tau - s)}} \mathrm{d}s; \tag{3.92}$$

however, the limit $\zeta \to 0$ must be taken with care because of the singular behaviour of the integrand as $s \to \tau$. To address this, we express (3.92) in a form which makes taking the limit $\zeta \to 0$ much simpler [36]

$$\frac{\partial c^*(\zeta,\tau)}{\partial \zeta} = \int_0^\tau \frac{c^*(0,s) - c^*(0,\tau)}{2\sqrt{\pi}(\tau-s)^{3/2}} \left(1 - \frac{\zeta^2}{2(\tau-s)}\right) \mathrm{e}^{-\frac{\zeta^2}{4(\tau-s)}} \mathrm{d}s - \frac{c^*(0,\tau)}{\sqrt{\pi\tau}}. \tag{3.93}$$

Then, taking the limit $\zeta \to 0$ gives the Dirichlet-to-Neumann map for $c^*(\,\zeta,\tau\,)$,

$$\frac{\partial c^*(\zeta,\tau)}{\partial \zeta} = \int_0^\tau \frac{c^*(0,s) - c^*(0,\tau)}{2\sqrt{\pi}(\tau-s)^{3/2}} \mathrm{d}s - \frac{c^*(0,\tau)}{\sqrt{\pi\tau}}, \tag{3.94}$$

which, after transforming back into $(\hat{r},\hat{t}\,)$ coordinates, gives the Dirichlet-to-Neumann map for $\hat{c}$:

$$\frac{\partial \hat{c}}{\partial \hat{r}} = \epsilon_c^{-1} \hat{R}^2 \left(\int_0^\tau \frac{\hat{c}_{\mathrm{B}}^*(s) - \hat{c}_{\mathrm{B}}^*(\tau)}{2\sqrt{\pi}(\tau-s)^{3/2}} \mathrm{d}s - \frac{\hat{c}_{\mathrm{B}}^*(\tau)}{\sqrt{\pi\tau}} \right), \tag{3.95}$$

where τ is a function of $\hat{t}$ given by (3.88a). From the consistency condition (3.45) and (3.95), we can deduce the appropriate moisture scaling factor α is given by

$$\alpha = \epsilon_c = \frac{1}{\sqrt{\widehat{Pe}_c}}, \tag{3.96}$$

which is the same as in Case II. We now consider the thermal boundary layer, and introduce a spatial coordinate, $\bar{\eta}$, defined by

$$\hat{r} = \hat{R} + \epsilon_T \bar{\eta}, \tag{3.97}$$

and define $\bar{T}(\bar{\eta},\hat{t}\,) = \hat{T}(\hat{r},\hat{t}\,)$. To leading order in ϵ_T, (3.40b) becomes

$$\frac{\partial \bar{T}}{\partial \hat{t}} - \frac{2\bar{\eta}}{\hat{R}} \frac{\mathrm{d}\hat{R}}{\mathrm{d}\hat{t}} \frac{\partial \bar{T}}{\partial \bar{\eta}} = \frac{\partial^2 \bar{T}}{\partial \bar{\eta}^2} \qquad \text{for} \qquad \bar{\eta} > 0. \tag{3.98}$$

To eliminate the advective term in this equation, we introduce (η,τ) coordinates defined by

$$\tau = \int_0^{\hat{t}} \hat{R}(s)^4 \mathrm{d}s \qquad \text{and} \qquad \eta = \hat{R}^2 \bar{\eta}. \tag{3.99}$$

Defining $T^*(\eta,\tau) = \bar{T}(\bar{\eta},\hat{t}\,)$, we find that after the coordinate transform (3.99), equation (3.98) reduces to a 1D heat equation for $T^*(\eta,\tau)$ given by

$$\frac{\partial T^*}{\partial \tau} = \frac{\partial^2 T^*}{\partial \eta^2} \qquad \text{for} \qquad \eta > 0, \tag{3.100}$$

where initially $T^*(\eta,\tau)$ is given by

$$T^*(\,\eta,\tau) = 0 \qquad \text{at} \qquad \tau = 0. \tag{3.101}$$

The Neumann-to-Dirchlet map for $T^*(\eta,\tau)$ is therefore given by

$$T^*(\eta,\tau) = -\int_0^\tau \frac{1}{\sqrt{\pi(\tau-s)}}\frac{\partial T^*}{\partial \eta}(0,s)\mathrm{d}s, \tag{3.102}$$

Note that $\partial T^*/\partial\eta$ and $\partial\hat{T}/\partial\hat{r}$ are related by

$$\frac{\partial \hat{T}}{\partial \hat{r}} = \frac{(\hat{R}^*)^2}{\epsilon_T}\frac{\partial T^*}{\partial \eta}. \tag{3.103}$$

This indicates that $\partial\hat{T}/\partial\hat{r} = \mathcal{O}(\epsilon_T^{-1})$, which in conjunction with the consistency condition (3.46) suggests that the appropriate temperature rescaling factor, β, in this case is given by

$$\beta = \epsilon_T = \frac{1}{\sqrt{\widehat{Pe}_T}}. \tag{3.104}$$

This is analogous to the rescaling of the moisture concentration by the width of the moisture boundary layer.

Boundary condition (3.41a) relates the heat and moisture flux at the boundary; so, using (3.95), we can express the Neumann boundary data for $\hat{T}$ in terms of $\hat{c}_\mathrm{B}$ as

$$\frac{\partial T^*}{\partial \eta}(0,\tau) = \int_0^\tau \frac{\hat{c}^*_\mathrm{B}(s)-\hat{c}^*_\mathrm{B}(\tau)}{2\sqrt{\pi}(\tau-s)^{3/2}}\,\mathrm{d}s - \frac{\hat{c}^*_\mathrm{B}(\tau)}{\sqrt{\pi\tau}}. \tag{3.105}$$

This, when incorporated into (3.102), gives

$$\hat{T}^*_\mathrm{B}(\tau) = -\int_0^\tau \frac{1}{\sqrt{\pi(\tau-s)}}\left(\int_0^s \frac{\hat{c}^*_\mathrm{B}(\sigma)-\hat{c}^*_\mathrm{B}(s)}{2\sqrt{\pi}(s-\sigma)^{3/2}}\,\mathrm{d}\sigma - \frac{\hat{c}^*_\mathrm{B}(s)}{\sqrt{\pi s}}\right)\mathrm{d}s, \tag{3.106}$$

which relates $\hat{T}_\mathrm{B}$ to $\hat{c}_\mathrm{B}$. This relationship closes a reduced, sub-system of the full system; the thermodynamics are determined by $\hat{T}_\mathrm{B}$ and $\hat{c}_\mathrm{B}$, which are related to $\hat{R}$ and $\hat{p}_\mathrm{B}$ through (3.41b) and (3.106). Note that, through the use of boundary condition (3.41a), we can replace the Neumann data for $\hat{T}$ in (3.102) by Neumann data for $\hat{c}$, giving

$$\hat{T}^*_\mathrm{B}(\tau) = -\int_0^\tau \frac{1}{\sqrt{\pi(\tau-s)}}\frac{\partial c^*}{\partial \hat{\eta}}(0,s)\mathrm{d}s, \tag{3.107}$$

	$\widehat{Pe}_c \lesssim 1$	$\widehat{Pe}_c \gg 1$
$\widehat{Pe}_T \lesssim 1$	$\alpha = \beta = 1$	$\alpha = \dfrac{1}{\sqrt{\widehat{Pe}_c}},\ \beta = 1$
$\widehat{Pe}_T \gg 1$	$\times$	$\alpha = \dfrac{1}{\sqrt{\widehat{Pe}_c}},\ \beta = \dfrac{1}{\sqrt{\widehat{Pe}_T}}$

Table 3.1: *The required moisture concentration rescaling, α, and temperature, β, depending on the Péclet number regime. The cross for $\widehat{Pe}_T \gg 1$ and $\widehat{Pe}_c \lesssim 1$ indicates that this parameter regime is not of physical interest.*

where the right hand side is the Neumann-to-Dirichlet map for $\hat{c}^*_{\mathrm{B}}$. Therefore, we have rescaled $\hat{c}$ and $\hat{T}$ in such a way that they are equal at the boundary, that is

$$\hat{c}_{\mathrm{B}} = \hat{T}_{\mathrm{B}}. \tag{3.108}$$

This was also the found in Case I, when diffusion was dominant for both quantities (*i.e.* equation (3.50)).

The appropriate values of α and β have been determined for all three cases, as summarised in table 3.1. It is the presence of a boundary layer in a particular quantity that necessitates the rescaling of that quantity. This is a consequence of enforcing that, over the timescale of bubble growth, the dimensionless fluxes of both heat and moisture are of order unity. As we approach the extreme limit, $\widehat{Pe}_c, \widehat{Pe}_c \gg \infty$, the total changes in both $\hat{c}$ and $\hat{T}$ vanish. As a consequence, the thermodynamics of the system are massively simplified; for constant moisture concentration and temperature, the bubble pressure is constant. The effect of the moisture vapourising is still observed in the system through the change in the number of moles of gas in the bubble.

3.3.3.1 Reduced model for Case III

In this case, the system comprises six equations that can be solved sequentially for $\hat{R}$, $\hat{N}_{\mathrm{B}}$, $\hat{p}_{\mathrm{B}}$, $\hat{T}_{\mathrm{B}}$, $\hat{c}_{\mathrm{B}}$, and τ. First, (3.41b) gives a constant bubble pressure,

$$\hat{p}_{\mathrm{B}} = \frac{\bar{P}}{\Sigma}, \tag{3.109}$$

to leading order in ϵ_T. This means that the bubble growth predicted by the Rayleigh–Plesset equation (3.1) is only coupled to the macroscopic pressure, p, and can be solved independently of the evolution of the other variables; that is, the bubble growth can be found by solving the ODE

$$\frac{\mathrm{d}\hat{R}}{\mathrm{d}\hat{t}} = \frac{\hat{R}}{4}\left(\frac{\bar{P}}{\Sigma} - p - p_{\mathrm{atm}} - \frac{\Gamma}{\hat{R}}\right). \tag{3.110}$$

With constant bubble pressure (3.109) and in the limit $\beta\hat{T}_{\mathrm{B}} \to 0$, rearranging the expression for the bubble pressure (3.44) gives $\hat{N}_{\mathrm{B}}$ to be

$$\hat{N}_{\mathrm{B}} = \frac{\hat{R}^3 - 1}{\Sigma}. \tag{3.111}$$

The reduced time variable, τ, is given by evaluating

$$\tau = \int_0^{\hat{t}} \hat{R}^4 \,\mathrm{d}s. \tag{3.112}$$

By differentiating (3.111), the rate of change of $\hat{N}_{\mathrm{B}}$ is given by

$$\frac{\mathrm{d}\hat{N}_{\mathrm{B}}}{\mathrm{d}\hat{t}} = \frac{3\hat{R}^2}{\Sigma}\frac{\mathrm{d}\hat{R}}{\mathrm{d}\hat{t}}, \tag{3.113}$$

which, in conjunction with (3.43), gives the moisture concentration gradient at the bubble interface to be

$$\alpha\frac{\partial\hat{c}}{\partial\hat{r}} = \frac{3\hat{R}}{4\Sigma}\left(\frac{\bar{P}}{\Sigma} - p - p_{\mathrm{atm}} - \frac{\Gamma}{\hat{R}}\right), \tag{3.114}$$

where $\alpha = \epsilon_c$. With the moisture gradient given by (3.114), we can bypass the Dirichlet-to-Neumann map for the moisture concentration given by (3.95). The moisture gradient is related to the temperature gradient at the boundary through the flux balance boundary condition (3.41a), giving

$$\beta\frac{\partial\hat{T}}{\partial\hat{r}} = \frac{3\hat{R}}{4\Sigma}\left(\frac{\bar{P}}{\Sigma} - p - p_{\mathrm{atm}} - \frac{\Gamma}{\hat{R}}\right), \tag{3.115}$$

where $\beta = \epsilon_T$. Substituting this expression for the temperature gradient into (3.102), using (3.103), gives $\hat{T}^*_{\mathrm{B}}$ to be

$$\hat{T}^*_{\mathrm{B}}(\tau) = -\frac{3}{4\Sigma}\int_0^{\tau} \frac{1}{R^*(s)\sqrt{\pi(\tau - s)}}\left(\frac{\bar{P}}{\Sigma} - p^*(s) - p_{\mathrm{atm}} - \frac{\Gamma}{\hat{R}^*(s)}\right)\mathrm{d}s, \tag{3.116}$$

where $p^*(\tau) = p(\hat{t}\,)$. Finally, $\hat{c}_{\mathrm{B}}$ is given by (3.108) to be

$$\hat{c}_{\mathrm{B}} = \hat{T}_{\mathrm{B}}. \tag{3.117}$$

Initially we have that

$$\hat{R} = 1 \qquad \text{at} \qquad \hat{t} = 1, \tag{3.118}$$

which is the only necessary initial condition in this case.

3.3.3.2 Case III with constant p: the Rayleigh problem

In this section we suppose that the macroscale pressure, p, is constant, and obtain explicit time-dependent solutions to the reduced model of case III for $\hat{R}$, $\hat{N}_{\mathrm{B}}$, τ, $\hat{T}_{\mathrm{B}}$, and $\hat{c}_{\mathrm{B}}$. We then discuss the qualitatively different behaviour that is observed, depending on the relationship between two parameters—one describing the effect of surface tension, Γ, and another describing the pressure difference between the bubble and the macroscopic pressure. Finally, we compare our predictions to those of Rayleigh [57], who considered a similar problem in the inertial regime.

Rayleigh studied the collapse of a spherical cavity of constant pressure in a liquid of infinite extent [57]. Rayleigh's solution, in the absence of viscosity and surface tension, predicts a finite time of collapse where, near the time of collapse, the velocity of the bubble interface blows up. Rayleigh suggests that this singular behaviour is prevented in reality by the pressure increase in the gas as it is condensed; using Boyle's law instead of a constant pressure results in solutions in which the bubble pressure counters unbounded velocity increase. In the absence of viscosity, the bubble will rebound and then oscillate between contraction and rebound. Bubble dynamics in this regime have been studied in connection with structural damage due to cavitation [13], as a result of pressure waves and jet formation as the bubble collapses, and sonoluminescence [28], when the temperature increase due to compression of the gas is so great that light is emitted. The similarity between the reduced model of case III, in which the bubble pressure is constant, and the problem first considered by Rayleigh motivates the comparison in this section.

When the macroscale pressure is constant, the reduced model for Case III, namely the equation for bubble growth (3.110), is similar to the problem first considered by Rayleigh: the collapse (or growth) of a spherical cavity of constant pressure. A key difference is that we are interested in the low-Reynolds-number limit. In addition,

we have a reduced model for the thermodynamics (3.111)–(3.117) which is valid until $\hat{R} \approx \epsilon_T$ when (3.98) is no longer accurate.

If the macroscopic pressure $p = C$, where C is a constant, and we define $\mathcal{P}$ to be the difference in pressure between the bubble and the macroscale,

$$\mathcal{P} = \frac{\bar{P}}{\Sigma} - C - p_{\text{atm}}, \tag{3.119}$$

we can integrate (3.110) subject to (3.118) to give the explicit solution for $\hat{R}$:

$$\hat{R} = \frac{\Gamma}{\mathcal{P}} + \left(1 - \frac{\Gamma}{\mathcal{P}}\right) \mathrm{e}^{\mathcal{P}\hat{t}/4}. \tag{3.120}$$

From this expression, we can categorise three eventual behaviours: finite-time bubble collapse, a steady-state bubble radius, or exponential bubble growth. Which of these three behaviours a bubble exhibits depends on the sign of $\mathcal{P}$, and the magnitude of Γ (note that $\Gamma > 0$). The long-time behaviour of a bubble in $\mathcal{P}$–Γ phase space is illustrated in figure 3.4. Bubbles will collapse if $\mathcal{P} < \Gamma$, which corresponds to regions I and II, coloured blue in figure 3.4. Region I, $\mathcal{P} < 0$, corresponds to the case when the bubble pressure is lower than the pressure of the liquid; both surface tension and pressure effects will shrink the bubble. In region II, $0 < \mathcal{P} < \Gamma$, the bubble pressure is larger than the imposed liquid pressure; however, surface tension dominates and bubbles in this region will collapse. When $\mathcal{P} = 0$, so that the bubble pressure and liquid pressure are equal, $\hat{R}$ is not given by (3.120)—having assumed that $\mathcal{P} \neq 0$ to derive this form—and we must instead consider (3.110) for $\mathcal{P} = 0$ given by

$$\frac{\mathrm{d}\hat{R}}{\mathrm{d}\hat{t}} = -\frac{\Gamma}{4}, \tag{3.121}$$

which can be integrated subject to (3.118) to give

$$\hat{R} = 1 - \frac{\Gamma\hat{t}}{4}. \tag{3.122}$$

For each of these cases, we can determine the time of bubble collapse, which we denote $\hat{t}_c$, given by

$$\hat{t}_c = \begin{cases} \dfrac{4}{\mathcal{P}} \ln\left(\dfrac{\Gamma}{\Gamma - \mathcal{P}}\right) & \text{if} \quad \mathcal{P} < \Gamma, \ \mathcal{P} \neq 0, \\ \dfrac{4}{\Gamma} & \text{if} \quad \mathcal{P} = 0. \end{cases} \tag{3.123}$$

The collapse time when $\mathcal{P} = 0$, $\hat{t}_c = 4/\Gamma$, can either be determined by solving (3.122) for $\hat{t}$ when $\hat{R} = 0$, or by taking the limit $\mathcal{P} \to 0$ of $\hat{t}_c$ when $\mathcal{P} < \Gamma$ and $\mathcal{P} \neq 0$.

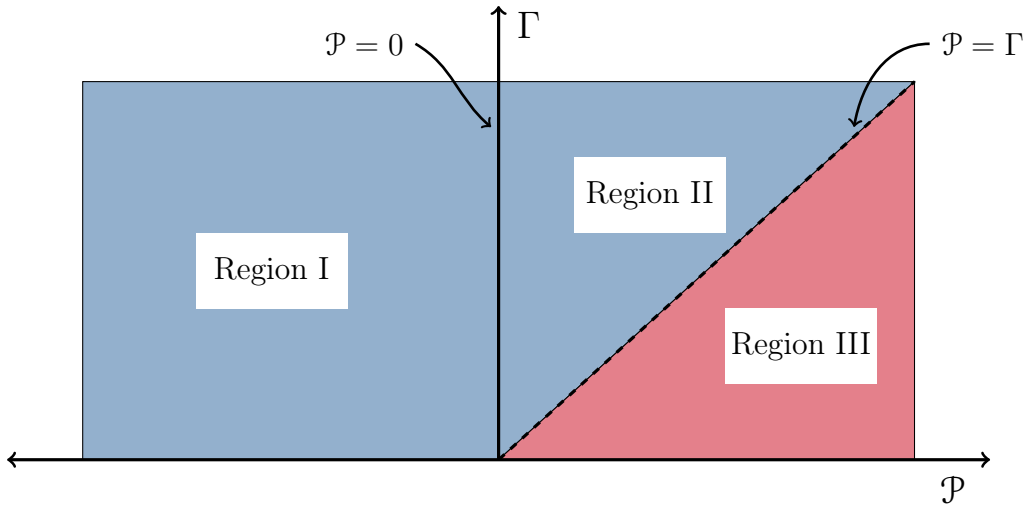

Figure 3.4: *Regions of bubble collapse (blue) or growth (red) for Case III; that is, when* $1 \ll \widehat{Pe}_T \ll \widehat{Pe}_c$. *Region I,* $\mathcal{P} < 0$, *corresponds to bubble collapse and temperature increase due to the liquid pressure being greater than the bubble pressure. Region II,* $0 < \mathcal{P} < \Gamma$,*corresponds to bubble collapse and temperature increase when the bubble pressure is greater than the liquid pressure, but surface tension still drives collapse. Region III,* $\mathcal{P} > \Gamma$, *corresponds to bubble growth and temperature decrease when the bubble pressure overcomes both the surrounding liquid pressure and surface tension.*

When $\mathcal{P} = \Gamma$, the bubble radius is fixed; in this case the right hand side of (3.110) vanishes for $\hat{R}(0) = 1$. This corresponds to the case when the pressure forces and surface tension are perfectly balanced. We can see that this equilibrium is unstable by considering the bubble-growth equation (3.110), now expressed in terms of $\mathcal{P} = \Gamma$, given by

$$\frac{\mathrm{d}\hat{R}}{\mathrm{d}\hat{t}} = \frac{\mathcal{P}}{4}\left(\hat{R} - 1\right). \tag{3.124}$$

Any perturbation of $\hat{R}$ to, say, to $\hat{R}+\delta$ will result in growth, for $\delta > 0$, or contraction, for $\delta < 0$; in either case tending away from $\hat{R} = 1$. When $\mathcal{P} > \Gamma$, illustrated by Case III on figure 3.4, the bubble grows exponentially.

With an explicit solution for $\hat{R}(\hat{t}\,)$, given by (3.120), we can derive explicit expressions for $\hat{N}_\mathrm{B}$, τ, $\hat{T}_\mathrm{B}$, and $\hat{c}_\mathrm{B}$. The number of moles of gas in the bubble is given by direct substitution of (3.120) into (3.111), so that

$$\hat{N}_\mathrm{B} = \frac{\left(\dfrac{\Gamma}{\mathcal{P}} + \left(1 - \dfrac{\Gamma}{\mathcal{P}}\right)\mathrm{e}^{\mathcal{P}\hat{t}/4}\right)^3 + 1}{\Sigma}. \tag{3.125}$$

The reduced time variable, τ, can be found explicitly by substituting (3.120) into (3.112), and evaluating the integral; elementary calculus gives

$$\tau = \sum_{k=1}^{4} \binom{4}{k} \frac{4}{k\mathcal{P}} \left(\frac{\Gamma}{\mathcal{P}}\right)^{4-k} \left(1 - \frac{\Gamma}{\mathcal{P}}\right)^{k} \left(\mathrm{e}^{\frac{k\mathcal{P}}{4}\hat{t}} - 1\right) + \left(\frac{\Gamma}{\mathcal{P}}\right)^{4} \hat{t}. \tag{3.126}$$

The bubble temperature, given by (3.116), can be given explicitly in terms of $\hat{t}$. We first note that (3.116) is given by

$$\hat{T}_{\mathrm{B}}^{*}(\tau) = -\frac{3\mathcal{P}}{4\Sigma} \int_{0}^{\tau} \frac{1}{\hat{R}^{*}(s)\sqrt{\pi\,(\tau - s)}} \left(1 - \frac{\Gamma}{\mathcal{P}\hat{R}^{*}(s)}\right) \mathrm{d}s. \tag{3.127}$$

By change of integration variable, noting that

$$\mathrm{d}\tau = \hat{R}^{4}\mathrm{d}\hat{t}, \tag{3.128}$$

(3.127) can be expressed as an integral over $\hat{t}$:

$$\hat{T}_{\mathrm{B}}(\hat{t}) = -\frac{3\mathcal{P}}{4\Sigma} \int_{0}^{\hat{t}} \frac{\hat{R}(s)^{3} - \dfrac{\Gamma}{\mathcal{P}}\hat{R}(s)^{2}}{\sqrt{\pi \int_{s}^{\hat{t}} \hat{R}(\sigma)^{4}\mathrm{d}\sigma}} \mathrm{d}s, \tag{3.129}$$

where $\hat{R}$ is given by (3.120).

Whether the temperature increases or decreases depends on whether the bubble is collapsing or growing. In the case where $\mathcal{P} > \Gamma$ and the bubble is growing, region III in figure 3.4, $\hat{T}_{\mathrm{B}}$ will decrease. Physically, this temperature drop is a consequence of heat being used to vaporise gas at the interface as well as the gas in the bubble expanding. As the bubble grows, gas must be added to the bubble at a greater rate in order to maintain constant bubble pressure. After some time, the assumptions made in order to derive the reduced model for Case III will break down in this parameter regime, namely the assumption that $\beta|\hat{T}_{\mathrm{B}}| \ll 1$, and the solution derived in this section will no longer be valid.

When $\mathcal{P} < \Gamma$, corresponding to regions I and II in figure 3.4, the temperature increases to a maximum value, and then cools slightly before the bubble collapses. The temperature during bubble collapse for a range of $\mathcal{P}$ values is shown in figure 3.5a. The temperature spike occurs earlier and is more pronounced for faster bubble collapse, which occurs for more negative $\mathcal{P}$ values. After this peak, the temperature cools slightly, but remains higher than its initial value. For a collapsing bubble, the

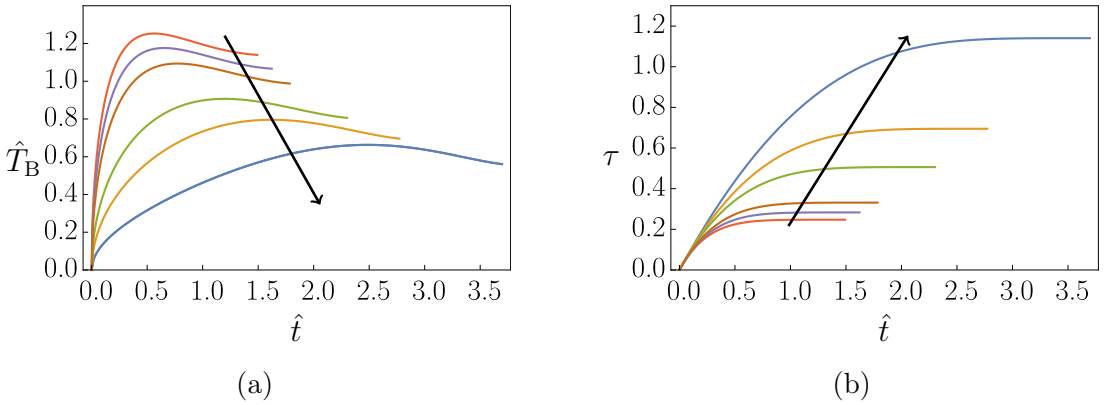

Figure 3.5: *Example solutions of* (a) *the bubble temperature,* $\hat{T}_B$*, and* (b) τ *for* $\Sigma = 1$*,* $\Gamma = 2$ *and* $\mathcal{P}$ *values in* $\{-1.5, -1, -0.5, 0.5, 1, 1.5\}$*. The arrow indicates the direction of increasing* $\mathcal{P}$*.*

reduced time τ, given by (3.126), which tends to a constant value, which is illustrated for the same range of $\mathcal{P}$ values in figure 3.5b.

For bubble collapse in the inertial regime, the regime of interest for Rayleigh in 1917 [57], the bubble growth rate and liquid pressure are singular near the point of collapse. Rayleigh suggested that the pressure in a cavity filled with gas will not remain constant, but the thermodynamics of the gas will counteract the singular behaviour of the collapse. A consequence of this is very high temperatures in the gas until the bubble rebounds and grows. In the regime we consider, which is dominated by viscosity and accounts for some thermal diffusion away from the bubble as well as gas dissolution, the temperature does not blow up. The maximum temperature is obtained before total collapse. The temperature at the instant the bubble vanishes can be determined by substituting the collapse time, $\hat{t}_c$ from (3.123), into the temperature, (3.129). The final temperature of a collapsing bubble, depending on $\mathcal{P}$ and Γ for a fixed Σ, is shown in figure 3.6a. For larger surface tension, and larger liquid pressure compared to bubble pressure (corresponding to a more negative $\mathcal{P}$) we observe larger final bubble temperatures. These larger temperatures are due to the greater rate of bubble collapse in this region of parameter space. As the rate of bubble contraction slows down, which occurs for more positive $\mathcal{P}$ and smaller surface tension, Γ, the final temperature is lower. In the limit $\mathcal{P} \nearrow \Gamma$, which indicates that $\mathcal{P}$ approaches Γ from below, there is no temperature change. For $\mathcal{P} > \Gamma$, the temperature decreases until the model breaks down; there is no final temperature in this regime as the bubble never collapses.

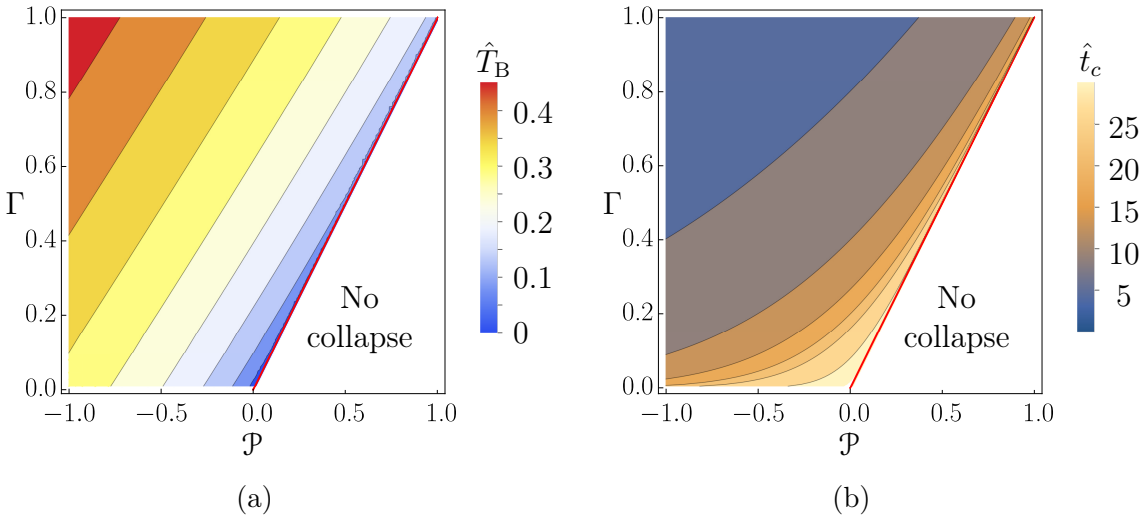

Figure 3.6: (a) *The bubble temperature, $\hat{T}_B$ at the time the bubble completely collapses for $\Sigma = 1$. The figure illustrates the increase in final temperature for more negative values of $\mathcal{P}$ and higher Γ. In* (b) *the time taken to collapse, $\hat{t}_c$ is shown in $\mathcal{P}$–Γ phase space; $\hat{t}_c$ grows without limit as $\Gamma \to 0$ for $\mathcal{P} < 0$ and as $\mathcal{P} \nearrow \Gamma$.*

For $\mathcal{P} \nearrow \Gamma$, the rate of heat flux into the liquid is slow and the total time to collapse long enough that the change in temperature tends to zero. The temperature at the moment of collapse depends on to the inverse of the collapse time, illustrated in figure 3.6b; in general, a shorter collapse time corresponds to a higher final temperature. For longer collapse times, this correlation breaks down. For $\Gamma = \mathcal{P}$, the bubble neither grows nor contracts, so the change in temperature tending to zero as we approach this limit is not surprising.

The reduced model we are considering for Case III can break down for a number of reasons. For a growing bubble, the temperature will continue to decrease until the assumption that $\beta\hat{T}_{\mathrm{B}} \ll 1$ breaks down. For a collapsing bubble, the bubble radius approaches the thermal boundary layer thickness so equation (3.98), from which we reduced the spherically symmetric heat equation to the 1D heat equation, is no longer accurate. The model may also break down as assumptions we have made about the physics become invalid. For late times during bubble collapse, breaking of spherical symmetry is observed experimentally [15]. For small enough bubble radius $\hat{R}$, and a small number of moles of gas $\hat{N}_{\mathrm{B}}$, there will not be enough gas in the bubble for there to be a well defined pressure and the thermodynamic law we built into our model are no longer valid.

For the collapse of a cavity of constant pressure, our predictions are notably different from those of Rayleigh [57]. In the inertial regime considered by Rayleigh, the speed of collapse grows without bound, as does the pressure in the surrounding liquid. In the viscous regime we consider, the collapse speed is finite, and the pressure in the surrounding liquid (which is equal to the macroscale pressure in the viscous limit) is constant. A thermodynamic argument, that the pressure in the bubble increases as the bubble collapses, is used to regularise the singular behaviour of Rayleigh's original model. In our model, as long as $\mathcal{P} < \Gamma$, no quantity increases without bound during collapse; however, the reduced model we consider breaks down as $\hat{R} \to 0$ when the bubble size becomes comparable to the thermal boundary layer width.

3.4 Comparison between asymptotic and numerical solutions

Each of the cases we have considered in sections (3.3.1)–(3.3.3) capture the dynamics of a bubble in different asymptotic limits. In this section we test the quality of the asymptotic predictions by comparing them to the solution of the full microscale model using the numerical method described in Section 3.2. For this comparison we will assume that the Péclet numbers, $\widehat{Pe}_c$ and $\widehat{Pe}_T$, can be varied without changing any of the other dimensionless parameters in the system. In reality, it is impossible to independently vary the Péclet numbers without varying some of the other dimensionless parameters. The comparison we make in this section is therefore more of a mathematical one than a physical one. The results are intended to indicate how accurate the solutions to the reduced models are, away from the limits for which they derived, compared with numerical solutions to the full model.

In both cases I and II, $\widehat{Pe}_T$ is assumed to be small; however, $\widehat{Pe}_c$ is small in Case I, but large in Case II. We can compare the bubble dynamics between these regimes by supposing $\widehat{Pe}_T$ to be small, and varying $\widehat{Pe}_c$ from a small value to a large value (*i.e.* a transition from Case I to Case II). The variations in predictions for $\hat{R}$, $\hat{N}_{\mathrm{B}}$, $\hat{p}_{\mathrm{B}}$, $\hat{T}_{\mathrm{B}}$, and $\hat{c}_{\mathrm{B}}$ between cases I and II are illustrated in figure 3.7. To generate these solutions, we have supposed that for $\hat{t} > 0$ the macroscopic pressure is constant and below the vapour pressure of the mixture so that bubbles will grow. A physical analogue to this type of imposed external pressure would be a sudden depressurisation of the mixture. We can see that the asymptotic solutions bound the numerical solutions, and

the numerical solution agrees with the asymptotic solutions in the relevant limits. The bubble growth predicted for Case II is greater than that of Case I (shown in figure 3.7a), which can be attributed to the higher bubble pressure (figure 3.7c). The number of moles of gas in the bubble increases faster in Case II than in Case I; this is despite the transition from a regime in which diffusion dominates, to a regime in which a moisture boundary layer is present. The values of $\hat{T}_{\mathrm{B}}$ and $\hat{c}_{\mathrm{B}}$ shown in figures 3.8d and 3.8e are the values prior to the re-scaling introduced in (3.38). For Case II, $\alpha \to 0$, so the moisture concentration around the bubble does not change appreciably, which is illustrated by the blue-dashed line in figure 3.7e. This suggests that, even though the relative distance over which diffusion acts is smaller in Case II compared to Case I, and that the total change in $\hat{c}_{\mathrm{B}}$ tends to zero as we approach Case II by increasing $\widehat{Pe}_c$, the diffusive flux of moisture into the bubble is greater. A greater concentration of moisture around the bubble, as well as more gas in the bubble, indicates why the predicted bubble pressure is greater in Case II than Case I despite the lower bubble temperature (the predicted temperature is illustrated in figure 3.7d).

By comparing the value of each variable at a particular time, say $\hat{t} = 1$, between the asymptotic solutions and the numerical solutions, we can better understand how accurate the solutions to the reduced system will be. The values of $\hat{R}$, $\hat{N}_{\mathrm{B}}$, $\hat{p}_{\mathrm{B}}$, $\hat{T}_{\mathrm{B}}$, and $\hat{c}_{\mathrm{B}}$ for small $\widehat{Pe}_T$, at $\hat{t} = 1$, for a range of $\widehat{Pe}_c$ values, are shown in figure 3.8. Each of the sub-figures in figure 3.8 indicate the change in some aspect of the physics as $\widehat{Pe}_c$ is independently varied. In this comparison, we note that the reduced model for Case I agrees with the numerical solution to the full model for $\widehat{Pe}_c$ almost as large as 1. For the reduced model of Case II to be accurate, $\widehat{Pe}_c$ should be at least as big as 10^2.

We can perform a similar test for the transition between Case II and Case III: Numerical solutions are calculated for a large value of $\widehat{Pe}_c$, and a range of $\widehat{Pe}_T$ values from small to large; some results are illustrated in figure 3.9. The outcome is qualitatively similar to the transition between cases I and II: a fan of the numerical solutions at intermediate $\widehat{Pe}_T$ values between the solutions in the small and large $\widehat{Pe}_T$ limits. The values of $\hat{R}$, $\hat{N}_{\mathrm{B}}$, $\hat{p}_{\mathrm{B}}$, and $\hat{T}_{\mathrm{B}}$ at $\hat{t} = 1$, shown in figure 3.10, also show a similar trend when compared to the transition between cases I and II. Namely, to approximate the small $\widehat{Pe}_T$ limit, the value of $\widehat{Pe}_T$ does not need to be particularly small, however, for the reduced model of Case II to be accurate, $\widehat{Pe}_T$ must be reasonably large.

The agreement between the predictions of the reduced model in either case, and

the numerical solution to the full model in the corresponding limit is valuable for two reasons: it indicates that each model is being solved with sufficient accuracy, and it indicates the type of error we are likely to make using a particular reduced model. For the latter point, consider a particular example, say, the value of $\hat{R}$ at $\hat{t} = 1$, as shown in figure 3.10. If we are considering a system with a large $\widehat{Pe}_c$ and a large $\widehat{Pe}_T$, and choose to use the reduced model of Case III, the predicted value of $\hat{R}$ at $\hat{t} = 1$ will be a slight overestimate. Under the same conditions we are likely to overestimate $\hat{N}_{\mathrm{B}}$ and $\hat{p}_{\mathrm{B}}$, and underestimate the change in $\hat{c}_{\mathrm{B}}$. Whether we underestimate or overestimate the change in $\hat{T}_{\mathrm{B}}$ will depend on the parameter values.

In figure 3.11 we show the numerical predictions for the values of $\hat{R}$, $\hat{N}_{\mathrm{B}}$, $\hat{p}_{\mathrm{B}}$, $\hat{T}_{\mathrm{B}}$, and $\hat{c}_{\mathrm{B}}$ respectively at $\hat{t} = 1$ for a range of $\widehat{Pe}_T$ and $\widehat{Pe}_c$ values. From these figures, we can see the error we would expect if we were to use the reduced model rather than the numerical solution for particular values of $\widehat{Pe}_T$ and $\widehat{Pe}_c$. The bottom left corner of these figures corresponds to the region for which the reduced model of Case I is valid. We define the error between the numerical solution, say f_{n}, and the asymptotic solution, say f_{a}, at $\hat{t} = 1$ to be given by

$$E := \left| \frac{f_{\mathrm{n}} - f_{\mathrm{a}}}{f_{\mathrm{a}}} \right|. \tag{3.130}$$

If the $\widehat{Pe}_T$ and $\widehat{Pe}_c$ values are within the red-dashed lines on figures (3.11a,b) then the error, E, from using the reduced model of Case I is less than 0.1%. The bottom right, and top right regions of figures (3.11a–e) correspond to regions where the reduced models of Case II and Case III respectively are valid. When $\widehat{Pe}_T$ and $\widehat{Pe}_c$ are contained within the green-dashed lines and the nearest corner of figure 3.11a, the error between the numerical solution and the corresponding reduced model is less than 1%. Similarly, the black lines of figure 3.11*b* outline the region of parameter space for which the error associated with using the corresponding reduced model is less than 5%. These error estimates correspond to particular choices of the remaining parameters. Different parameter values are likely to change the exact positions of these error curves; however, the curves still indicate that it is possible to obtain accurate approximations to the solutions using the reduced models. From these estimates we can conclude that the reduced models derived in Sections 3.3.1–3.3.3 are accurate for a large range of parameter values; for $\widehat{Pe}_T$ and $\widehat{Pe}_c$ values of order unity, the reduced models are less accurate and the numerical solution should be used.

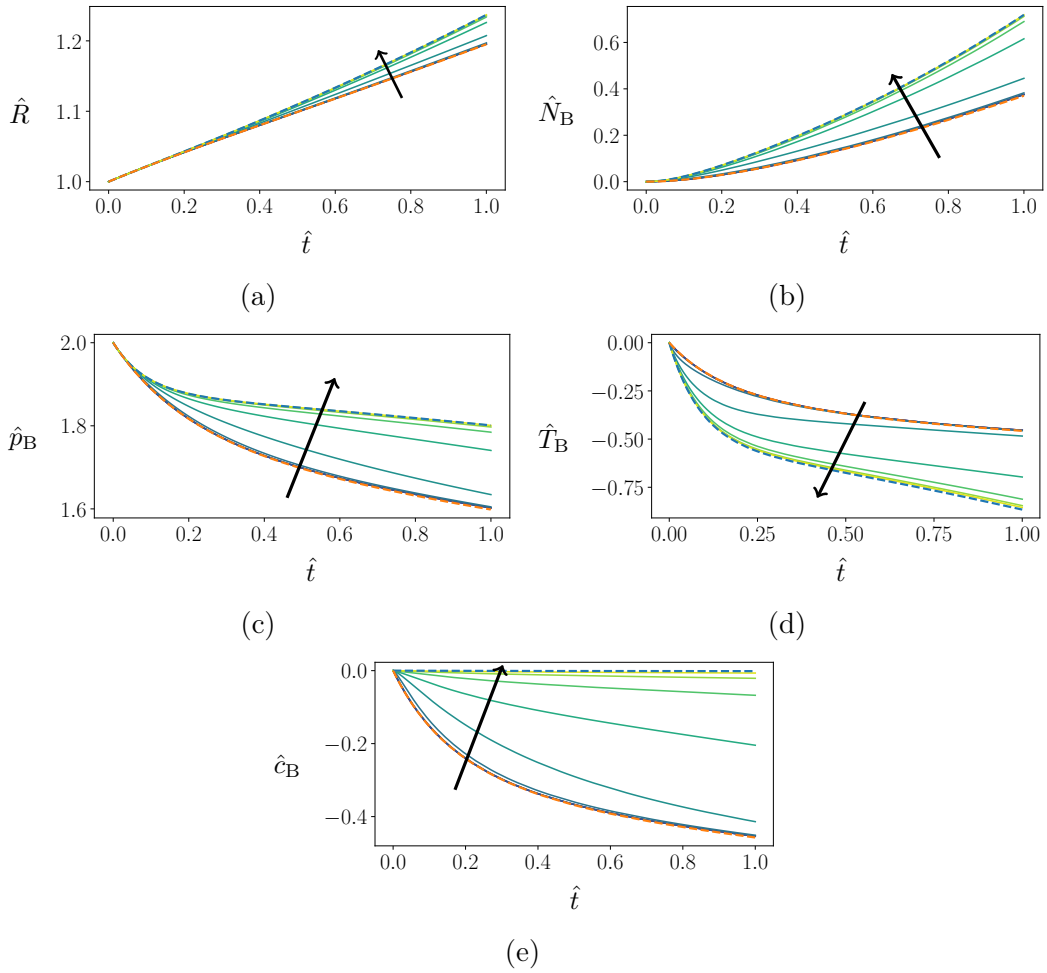

Figure 3.7: *Bubble dynamics for a constant macroscopic pressure, $p = 0$, for small $\widehat{Pe}_T$, in the limit relevant to Case I (orange dashed), Case II (blue dashed) and numerical solutions for $\widehat{Pe}_c = 10^i$ for $i \in \{-4, -3, -2, -1, 0, 1, 2, 3, 4\}$ (solid green lines). For these simulations the remaining dimensionless parameters have been kept the same: $\bar{P} = 2$, $\Sigma = 1$, $\Theta = 0.01$, $\Lambda = 12$, and $p_{atm} = 0.1$. The arrows indicate the direction of increasing $\widehat{Pe}_c$.*

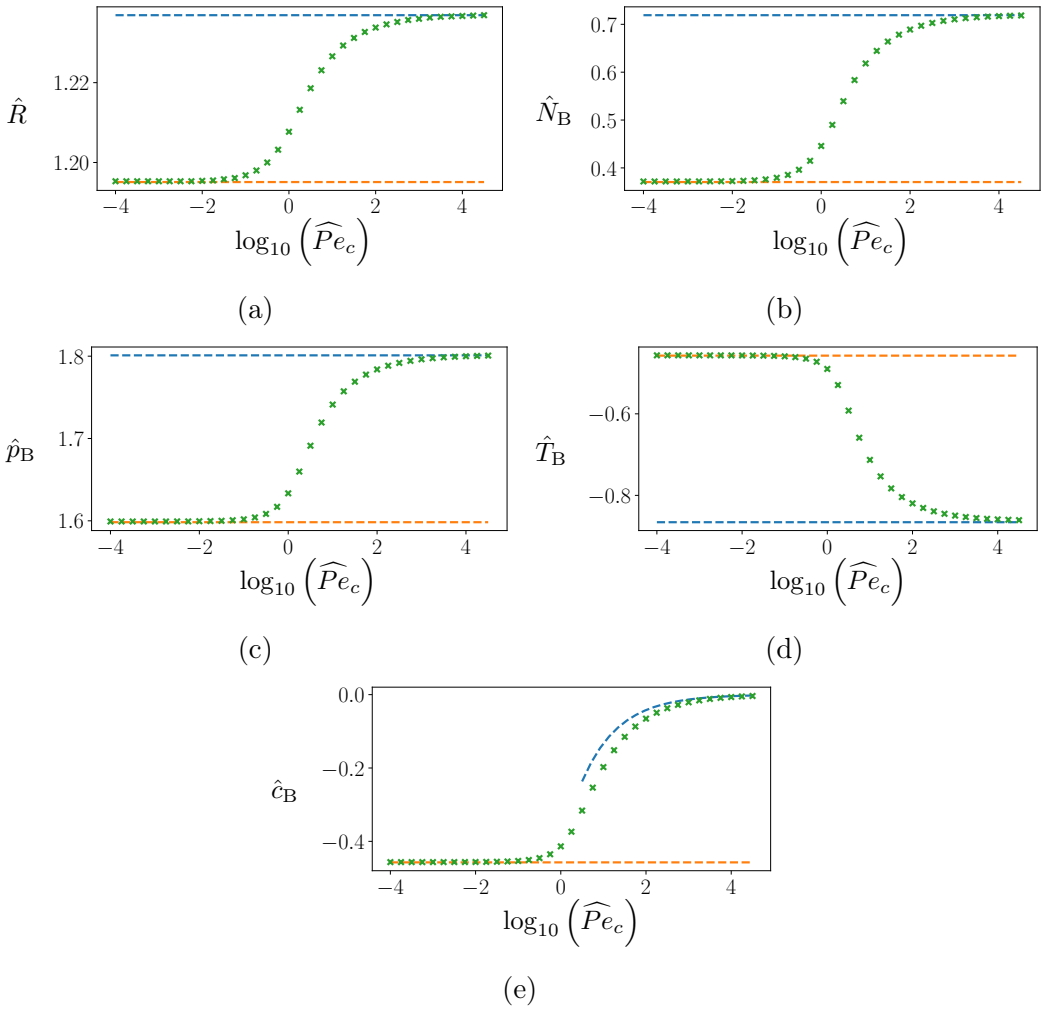

Figure 3.8: *Predicted values of* (a) $\hat{R}$, (b) $\hat{N}_{\mathrm{B}}$, (c) $\hat{p}_{\mathrm{B}}$, (d) $\hat{T}_{\mathrm{B}}$, *and* (e) $\hat{c}_{\mathrm{B}}$ *at* $\hat{t} = 1$, *for* $\widehat{Pe}_c$ *large. The solution in the small* $\widehat{Pe}_c$ *limit, according to the reduced model for Case I, is shown by the orange dashed line, and in the large* $\widehat{Pe}_c$ *limit, according to the reduced model of Case II, is shown by the blue dashed line. Green crosses indicate the prediction of the numerical solution to the full model. For these simulations, the external pressure is constant* $p = 0$, *and the remaining dimensionless parameters have been kept the same:* $\bar{P} = 2$, $\Sigma = 1$, $\Theta = 0.01$, $\Lambda = 12$, *and* $p_{atm} = 0.1$.

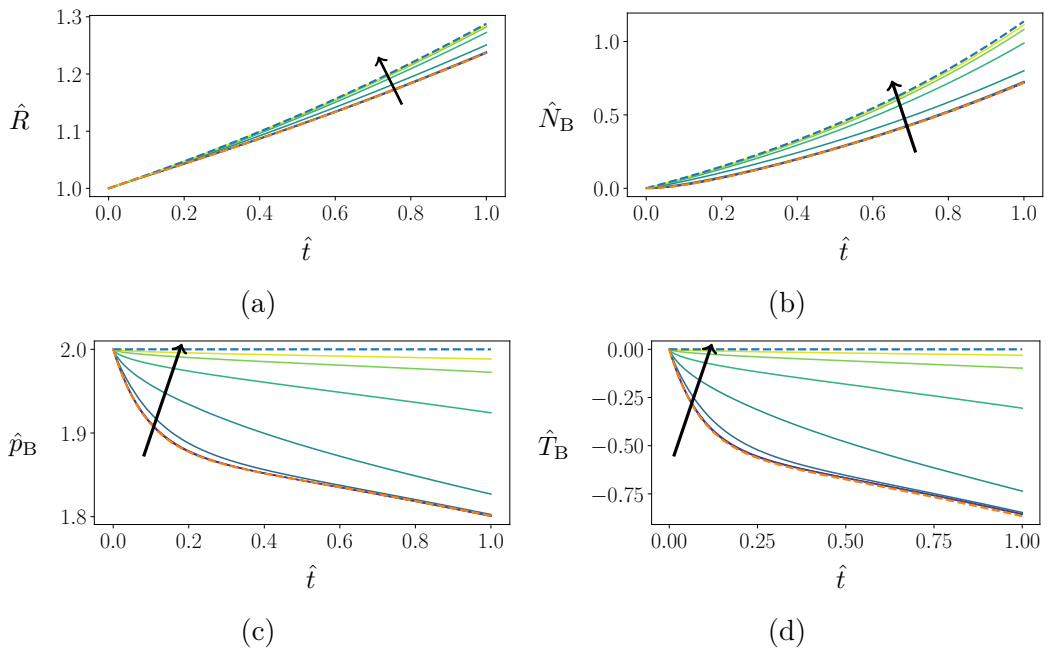

Figure 3.9: *Bubble dynamics for a constant macroscopic pressure, $p = 0$, for large $\widehat{Pe}_c$, in the limit relevant to Case II (orange dashed), Case III (blue dashed) and numerical solutions for $\widehat{Pe}_T = 10^i$ for $i \in \{-4, -3, -2, -1, 0, 1, 2, 3, 4\}$ (solid green lines). For these simulations, the external pressure is constant $p = 0$, and the remaining dimensionless parameters have been kept the same: $\bar{P} = 2$, $\Sigma = 1$, $\Theta = 0.01$, $\Lambda = 12$, and $p_{atm} = 0.1$. The arrows indicate the direction of increasing $\widehat{Pe}_T$.*

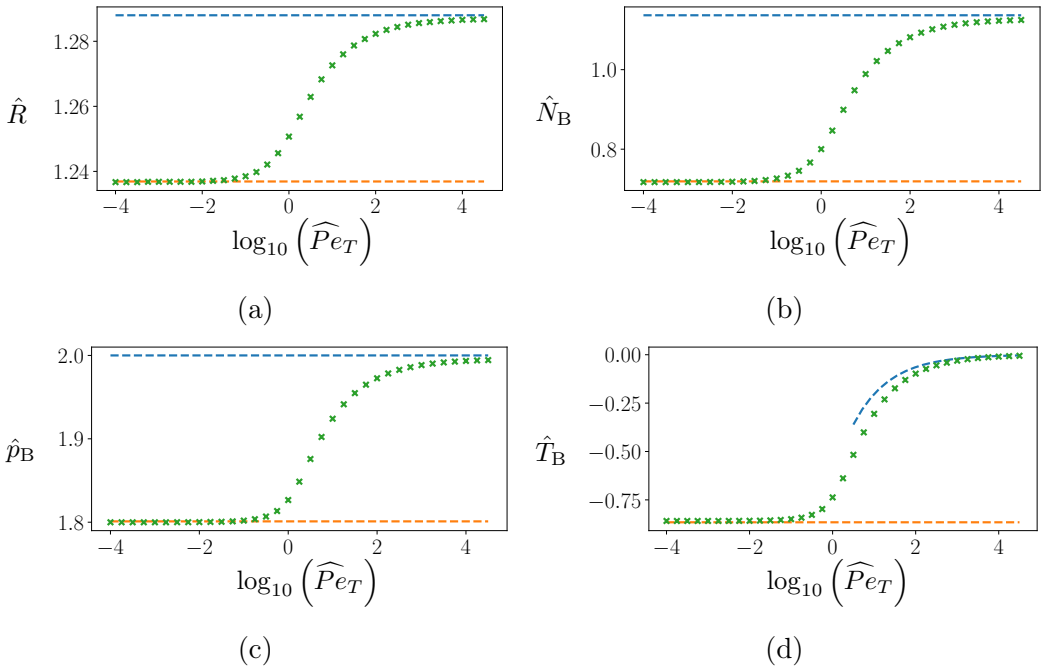

Figure 3.10: *Predicted values of* (a) $\hat{R}$, (b) $\hat{N}_{\mathrm{B}}$, (c) $\hat{p}_{\mathrm{B}}$, (d) $\hat{T}_{\mathrm{B}}$, *and* (e) $\hat{c}_{\mathrm{B}}$ *at* $\hat{t} = 1$ *for* $\widehat{Pe}_c$ *large. The solution in the small* $\widehat{Pe}_T$ *limit, according to the reduced model for Case II, is shown by the orange dashed line, and in the large* $\widehat{Pe}_T$ *limit, according to the reduced model of Case III, is shown by the blue dashed line. Green crosses indicate the prediction of the numerical solution to the full model. For these simulations the remaining dimensionless parameters have been kept the same:* $\bar{P} = 2$, $\Sigma = 1$, $\Theta = 0.01$, $\Lambda = 12$, *and* $p_{atm} = 0.1$.

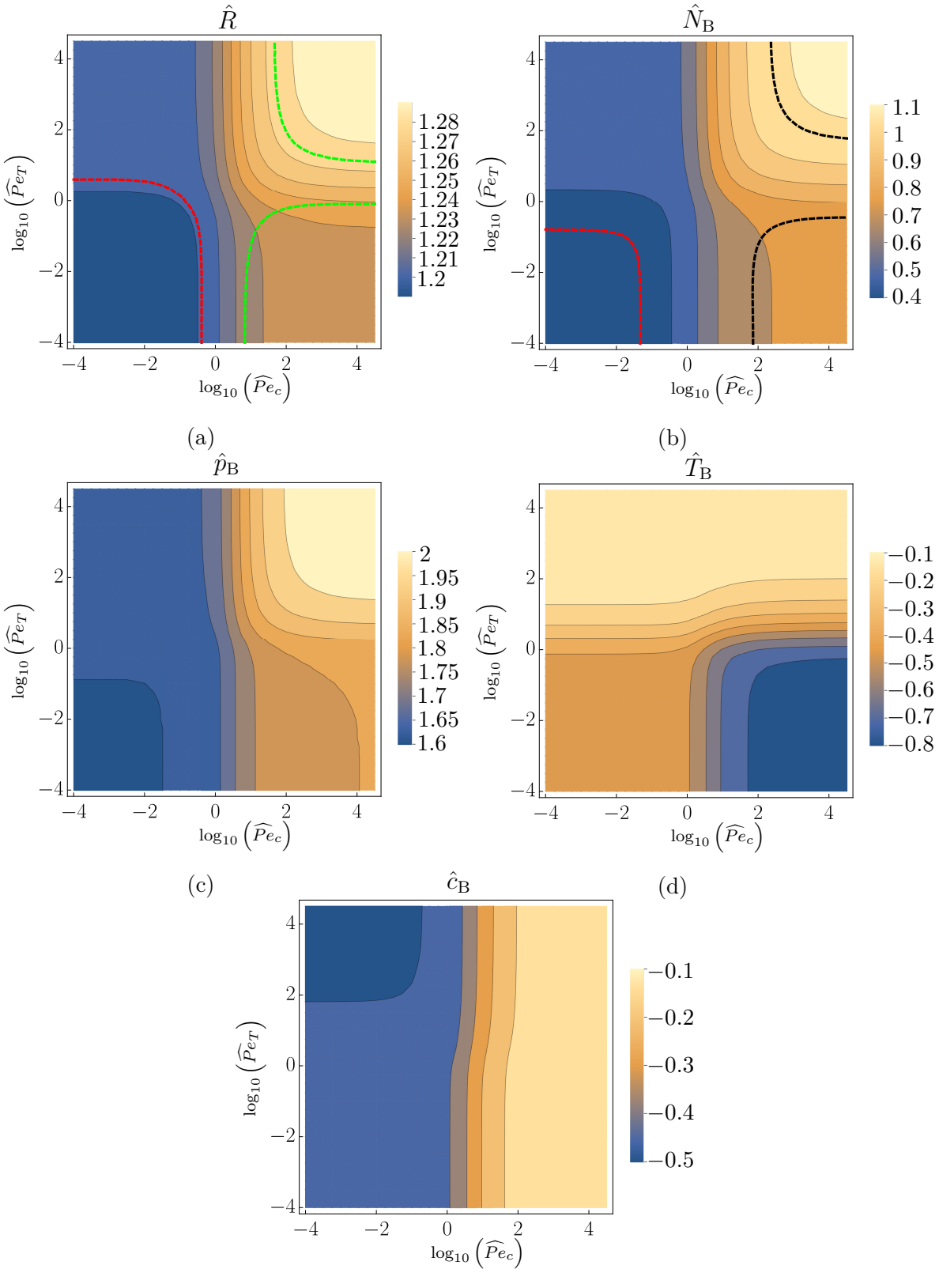

Figure 3.11: *The value of each variable at* $\hat{t} = 1$ *for a constant macroscopic pressure,* $p = 0$*, for a range of* $\widehat{Pe}_T$ *and* $\widehat{Pe}_c$ *values. For these simulations the remaining dimensionless parameters have been kept the same:* $\bar{P} = 2$*,* $\Sigma = 1$*,* $\Theta = 0.01$*,* $\Lambda = 12$*, and* $p_{atm} = 0.1$*. Using the reduced models in the regions bounded by the dashed lines give error (compared to the numerical solution) of* 0.1% *(red),* 1% *(green) and* 5% *(black).*

3.5 Discussion

This chapter contains an analysis of the microscale model presented in Section 2.6 of Chapter 2, using both numerical techniques and asymptotic analysis. In Section 3.1 we discussed the dimensionless parameters in the system of equations governing the microscale model. Because the Reynolds number is small, we neglected inertial terms on the microscale, which simplified the Rayleigh–Plesset equation. From the simplified Rayleigh–Plesset equation we constructed a consistency condition, given by (3.3), and from this deduced the macroscopic length scale over which the bubbles evolve. This suggests that the appropriate length scale for the axis along which the product flows may differ from the length scale for the cross-flow. We also described three cases, each corresponding to different values of the Péclet numbers, $\widehat{Pe}_T$ and $\widehat{Pe}_c$, for which we have derived reduced models by exploiting the asymptotic behaviour of the system.

In Section 3.2, we described a numerical scheme for finding solutions to the microscale model. This method makes no assumptions about the sizes of the dimensionless parameters; however, it becomes more expensive if the dimensionless parameters, namely $\widehat{Pe}_T$ and $\widehat{Pe}_c$, are very small, or very large. In Section 3.3, we presented reduced models that approximate the microscale model for each of the cases described in Section 3.1. These models do make assumptions about the sizes of $\widehat{Pe}_T$ and $\widehat{Pe}_c$; however, they are much easier to solve than the full model, and are no more difficult to solve as the Péclet numbers become more extreme in size.

The general procedure used to derive reduced models corresponding to each case in Section 3.3 is the same. Namely, we related the interfacial temperature and moisture concentration using the Dirichlet-to-Neumann, and Neumann-to-Dirichlet map for each quantity. We thereby eliminated the need to solve the PDEs corresponding to each quantity in order to understand the bubble dynamics. The reduced models for Cases I, II, and III were presented in Sections 3.3.1.1, 3.3.2.1, and 3.3.3.1 respectively. The most complicated of these reduced models, corresponding to Case I, requires solving a coupled system of two ODEs and an algebraic equation, which is considerably simpler than solving the full system. The simplest, corresponding to Case III, only requires solving a single ODE. If only one of the Péclet numbers is of order unity, then it is still possible to derive a reduced model by exploiting the size of the remaining Péclet number; however, the reduction in the complexity of the system is not as significant, and the reduced system of equations will still contain a PDE.

In Section 3.3.3.2, we assumed that the far-field pressure is constant, so that the reduced model corresponding to Case III described the evolution of a bubble of constant pressure under a constant imposed pressure. This problem is similar to a problem studied by Rayleigh [57], who considered the inertial collapse of a bubble. For the reduced model, which corresponds to the viscosity dominated collapse of this bubble, we determined an analytic solution for the size of the bubble as a function of time. We observed that, unlike the inertial driven collapse of a bubble, the collapse speed is finite during the collapse of the bubble. We were also able to determine analytic expressions for a number of other key variables that describe the thermodynamics of this system. We found that, for a collapsing bubble, the temperature of the bubble reaches some maximum value, and then cools slightly. If the bubble is growing instead, the temperature drops rapidly.

The utility of the reduced models for each case extends beyond the fact that they are simpler to solve numerically. We demonstrated the existence of an explicit analytic solution in Case III for a constant macroscale pressure. While this is not necessarily possible in the other Cases, the simplicity of the resulting reduced models makes them tenable to analysis using techniques such as a phase plane analysis. In addition, the reduced models, unlike the full model, can be solved backwards in time. The full model contains the heat equation, which is ill-posed when solving backwards in time. If we are only interested in $\hat{R}$, the relevant parts of the reduced models that determine $\hat{R}$ only contain ODEs and algebraic equations. Being able to solve the microscale model backwards in time leads to the possibility of solving the inverse problem for extrusion, where the final state is prescribed and the initial state determined, as long as the appropriate macroscale model is also well-posed backwards in time.

In Section 3.4, we compared the solutions found using the numerical method described in Section 3.2, to the reduced models described in Section 3.3. We found that, as long as the Péclet numbers are in the appropriate parameter regime, the reduced models agree with the numerical solution, which suggests that these reduced models can be reliably used in these cases. How close the Péclet numbers must be to the limits corresponding to each Case depends on the Case. In general, the Péclet numbers do not need to be particularly small, say $\widehat{Pe} \approx 10^{-1}$, in order to use a reduced model valid in the limit $\widehat{Pe} \to 0$. In order to use a model valid for large Péclet numbers, we require the Péclet number to be reasonably large, say $\widehat{Pe} \approx 10^{2}$.

Chapter 4

Extensional flow of a compressible fluid

In this chapter we derive a reduced model for the evolution of a compressible fluid being extruded through a die when the ratio of length to width, ϵ, is small. We only consider flow outside of the die. In Section 4.1 we consider the two-dimensional (2D) case of a thin sheet of fluid. This geometry is suitable for approximating extrusion through a slit. Following this, in Section 4.2, we present the equivalent reduced formulation in a three-dimensional (3D) geometry. In both 2D and 3D, the full set of equations governing the behaviour of a compressible fluid are predominately reduced using the methodology described in [38], as well as in subsequent work by [17], for deriving the Trouton model for an incompressible fluid. For a compressible fluid, we make the additional assumption that the viscosity and density of the fluid are uniform across each cross-section at leading order as $\epsilon \to 0$. This imposes a consistency condition that the pressure across the cross-section must be uniform at leading order as $\epsilon \to 0$.

In Section 4.1.2 we assume the existence of a steady state, and subsequently find two conserved quantities related to the mass and momentum flow rate. Under these conditions, the macroscale system is governed by a single ordinary differential equation (ODE) relating the pressure to the rate of change of the density. In Section 4.1.3 we note that if we incorporate a simple microscale model relating the density to the pressure, the resulting ODE depends only on the density, allowing us to present an implicit analytic solution to the system. In Section 4.1.4 we compare this simple model to one with a more complete description of the thermodynamics presented in Chapter 3. We observe significant differences between the two models, illustrating the importance of accounting for all of the relevant processes when modelling extrusion.

In later sections, 4.3 and 4.4, we consider extensions of the reduced model that are possible when the governing equations are modified. In Section 4.3, we consider a modified form of the relationship between the pressure and the density. The new relationship we employ no longer requires that the consistency condition of uniform pressure in the cross-section must hold. We do this in order to study the change in shape of the fluid cross-section as the product evolves, which we are unable to do when we enforce a uniform pressure in the cross-section. In Section 4.3.2 we describe the scheme used to find solutions to the problem derived in Section 4.3. A solution is then presented and discussed in Section 4.3.3.

In Section 4.4 we consider the conservation of energy of the fluid, and the effect that the temperature might have on the dynamics of the system. We introduce a temperature-dependent viscosity, and a modified coupling between the temperature on the microscale and the macroscale. We use the reduced models derived in this chapter to investigate the consequences of the introduced thermodynamics. In Section 4.5 we summarise the findings of this chapter and make some concluding remarks.

4.1 The two-dimensional case

4.1.1 A long thin sheet

We consider the flow of a viscous, compressible sheet of fluid. We will modify the model for compressible flow described in Section 2.5 for a 2D geometry in the z–y plane, where we maintain the convention of defining the z-axis to be the axis along which the fluid flows. All variables in the following equations have been scaled according to the scalings given by (2.55), where we take l_e to be equal to the lengthscale over which bubbles grow, L. We assume that the centre-line is straight and aligned with the z-axis. We neglect the effect of gravity on the sheet, as any unbalanced force along the y-axis would deflect the centre-line of the sheet. The fluid flows between the free surfaces $y = \pm h(z,t)$, as illustrated in figure 4.1. The flow speed, $\boldsymbol{u} = (w, v)$, pressure, p, and density, ρ, of the fluid are functions of z, y, and time, t. We define the material derivative by

$$\frac{\mathrm{D}}{\mathrm{D}t} \coloneqq \frac{\partial}{\partial t} + w\frac{\partial}{\partial z} + v\frac{\partial}{\partial y}. \tag{4.1}$$

The equations relating $\boldsymbol{u}$, p, and ρ are given by

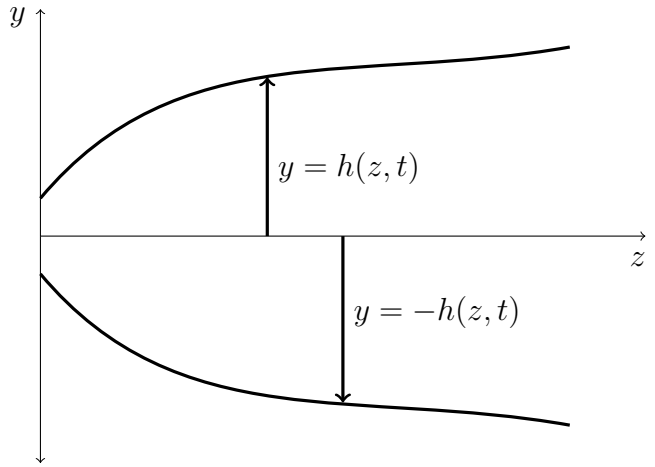

Figure 4.1: *Schematic of the 2D flow of a compressible fluid between the free surfaces* $y = \pm h(z,t)$.

$$\frac{\partial \rho}{\partial t} + \frac{\partial}{\partial z}(\rho w) + \frac{\partial}{\partial y}(\rho v) = 0, \tag{4.2}$$

$$Re\rho \frac{\mathrm{D}w}{\mathrm{D}t} = \frac{\partial}{\partial z}(\sigma_{11}) + \frac{\partial}{\partial y}(\sigma_{12}), \tag{4.3}$$

$$Re\rho \frac{\mathrm{D}v}{\mathrm{D}t} = \frac{\partial}{\partial z}(\sigma_{21}) + \frac{\partial}{\partial y}(\sigma_{22}), \tag{4.4}$$

in $z > 0$ and $-h(z,t) \leq y \leq h(z,t)$, where

$$\sigma_{11} = -p + \lambda\left(\frac{\partial w}{\partial z} + \frac{\partial v}{\partial y}\right) + 2\mu\frac{\partial w}{\partial z}, \tag{4.5}$$

$$\sigma_{12} = \sigma_{21} = \mu\left(\frac{\partial w}{\partial y} + \frac{\partial v}{\partial z}\right), \tag{4.6}$$

$$\sigma_{22} = -p + \lambda\left(\frac{\partial w}{\partial z} + \frac{\partial v}{\partial y}\right) + 2\mu\frac{\partial v}{\partial y}, \tag{4.7}$$

are the stress components. The conservation-of-mass and conservation-of-momentum equations for a general compressible fluid must be closed by an additional relationship between the state variables. In Chapter 2 we presented a model for bubbly flow where this closure relationship was encapsulated in a microscale model; however, much of the analysis we perform in this chapter applies in a more general setting. We begin this chapter by introducing a general closure relationship of the form

$$\mathcal{F}(\rho, p, \boldsymbol{u}, \nabla\rho) = 0; \tag{4.8}$$

we will specify the form of $\mathcal{F}$ when necessary. Equation (4.8) describes a closure relationship that depends only on the macroscopic state variables; however, we will

also consider closures that depend on a microscale evolution.

The system presented is symmetric around the centre-line, so we only consider the fluid in the domain $0 \leq y \leq h(z,t)$ and impose symmetry boundary conditions on $y = 0$. On the free surface at $y = h(z,t)$, the kinematic and dynamic boundary conditions in component form are given by

$$\frac{\partial h}{\partial t} + w\frac{\partial h}{\partial z} - v = 0, \tag{4.9}$$

$$-\sigma_{11}\frac{\partial h}{\partial z} + \sigma_{12} = \gamma^* \varkappa \frac{\partial h}{\partial z}, \tag{4.10}$$

$$-\sigma_{21}\frac{\partial h}{\partial z} + \sigma_{22} = -\gamma^* \varkappa, \tag{4.11}$$

where $\varkappa$ is the curvature of the free surface and γ^* is the dimensionless surface-tension coefficient. For the free surface $y = h(z,t)$, the curvature is given by

$$\varkappa = -\left(1 + \left(\frac{\partial h}{\partial z}\right)^2\right)^{-3/2} \frac{\partial^2 h}{\partial z^2}. \tag{4.12}$$

On the centre-line, $y = 0$, we impose symmetry boundary conditions given by

$$\frac{\partial w}{\partial y} = 0, \qquad v = 0. \tag{4.13}$$

In Section 2.5 we assumed that the axial and cross-sectional length scale were comparable, and equal to the die diameter, a. In Section 3.1 we discussed how the microscale dynamics influence the axial length scale on the macroscale. Consequentially, the aspect ratio, the ratio between the cross-sectional and axial length scale, may be small. For a sheet with characteristic length L in the z-direction, and thickness a in the y-direction, we define $\epsilon = a/L$ to be the aspect ratio of the sheet and assume it to be small. We consider the long–thin limit in which ϵ is small, and begin by rescaling

$$y = \epsilon y', \qquad v = \epsilon v', \tag{4.14}$$

for a dominant balance between all three terms in (4.2), where we will drop the primes from hereon for convenience. The rescaled dimensionless system is given by

$$\frac{\partial \rho}{\partial t} + \frac{\partial}{\partial z}(\rho w) + \frac{\partial}{\partial y}(\rho v) = 0, \tag{4.15}$$

$$\epsilon^2 Re\rho \frac{\mathrm{D}w}{\mathrm{D}t} = \epsilon^2 \frac{\partial}{\partial z}(\sigma_{11}) + \frac{\partial}{\partial y}(\sigma_{12}), \tag{4.16}$$

$$\epsilon^2 Re\rho \frac{\mathrm{D}v}{\mathrm{D}t} = \frac{\partial}{\partial z}(\sigma_{21}) + \frac{\partial}{\partial y}(\sigma_{22}), \tag{4.17}$$

$$\mathcal{F}(\rho, p, \boldsymbol{u}, \nabla\rho) = 0, \tag{4.18}$$

in $z > 0$ and $0 \leq y \leq h(z,t)$, where

$$\sigma_{11} = -p + \lambda\left(\frac{\partial w}{\partial z} + \frac{\partial v}{\partial y}\right) + 2\mu\frac{\partial w}{\partial z}, \tag{4.19}$$

$$\sigma_{12} = \sigma_{21} = \mu\left(\frac{\partial w}{\partial y} + \epsilon^2\frac{\partial v}{\partial z}\right), \tag{4.20}$$

$$\sigma_{22} = -p + \lambda\left(\frac{\partial w}{\partial z} + \frac{\partial v}{\partial y}\right) + 2\mu\frac{\partial v}{\partial y}. \tag{4.21}$$

The dimensionless boundary conditions on $y = h(z,t)$ are

$$\frac{\partial h}{\partial t} + w\frac{\partial h}{\partial z} - v = 0, \tag{4.22}$$

$$-\epsilon^2\sigma_{11}\frac{\partial h}{\partial z} + \sigma_{12} = \Gamma^*\epsilon^2\varkappa\frac{\partial h}{\partial z}, \tag{4.23}$$

$$-\sigma_{21}\frac{\partial h}{\partial z} + \sigma_{22} = -\Gamma^*\varkappa, \tag{4.24}$$

where, in the long–thin limit, the curvature, $\varkappa$, is given by

$$\varkappa \approx -\frac{\partial^2 h}{\partial z^2}, \tag{4.25}$$

and the parameter Γ^* is given by

$$\Gamma^* = \frac{\gamma^*}{\epsilon}, \tag{4.26}$$

where the inverse capillary number, γ^*, is given by (2.63). The symmetry boundary conditions on $y = 0$ are given by

$$\frac{\partial w}{\partial y} = 0, \qquad v = 0. \tag{4.27}$$

For now we consider the richest distinguished limit in which Re and Γ^* are both of order unity, and later show that in the small-Reynolds-number limit the governing equations simplify further. We expand each variable in powers of ϵ^2 and denote leading-order quantities with a superscript (0), and first-order quantities with a superscript (1). For example, we expand the density to give

$$\rho = \rho^{(0)} + \epsilon^2\rho^{(1)} + \mathcal{O}(\epsilon^4), \tag{4.28}$$

as $\epsilon \to 0$, where $\rho^{(0)}$ is the leading-order density, and $\rho^{(1)}$ is the first-order density (all other variables are denoted similarly). In doing so we obtain the leading-order

system from (4.15)–(4.17) given by

$$\frac{\partial \rho^{(0)}}{\partial t} + \frac{\partial}{\partial z}\left(\rho^{(0)} w^{(0)}\right) + \frac{\partial}{\partial y}\left(\rho^{(0)} v^{(0)}\right) = 0, \tag{4.29}$$

$$\frac{\partial}{\partial y}\left(\mu^{(0)} \frac{\partial w^{(0)}}{\partial y}\right) = 0, \tag{4.30}$$

$$\frac{\partial}{\partial z}\left(\mu^{(0)} \frac{\partial w^{(0)}}{\partial y}\right) + \frac{\partial}{\partial y}\left(-p^{(0)} + \lambda^{(0)}\left(\frac{\partial w^{(0)}}{\partial z} + \frac{\partial v^{(0)}}{\partial y}\right) + 2\mu^{(0)} \frac{\partial v^{(0)}}{\partial y}\right) = 0, \tag{4.31}$$

between $y = 0$ and $y = h^{(0)}(z,t)$. The leading-order boundary conditions on $y = h^{(0)}(z,t)$ are given by

$$\frac{\partial h^{(0)}}{\partial t} + w^{(0)} \frac{\partial h^{(0)}}{\partial z} - v^{(0)} = 0, \tag{4.32}$$

$$\mu^{(0)} \frac{\partial w^{(0)}}{\partial y} = 0, \tag{4.33}$$

$$-\mu^{(0)} \frac{\partial w^{(0)}}{\partial y} \frac{\partial h^{(0)}}{\partial z} - p^{(0)} + \lambda^{(0)}\left(\frac{\partial w^{(0)}}{\partial z} + \frac{\partial v^{(0)}}{\partial y}\right) + 2\mu^{(0)} \frac{\partial v^{(0)}}{\partial y} = \Gamma^* \frac{\partial^2 h^{(0)}}{\partial z^2}, \tag{4.34}$$

while on $y = 0$ the boundary conditions are given by

$$\frac{\partial w^{(0)}}{\partial y} = 0, \qquad v^{(0)} = 0. \tag{4.35}$$

Equation (4.30) and boundary condition (4.33) imply that the leading-order axial velocity, $w^{(0)}$, is only a function of z and t.

In the methodology outlined in Howell [38], a reduced model for the evolution of a thin, viscous, incompressible sheet of fluid is derived by integrating the governing equations over the cross-section of the sheet (*i.e.* integrating between $y = 0$ and $y = h^{(0)}(z,t)$). Applying the same methodology to the governing equations when the sheet is compressible, (4.29)–(4.31), does not yield such a spectacular reduction in the complexity of the model. In particular, the resulting system contains many integrals that do not readily simplify, and no reduction in the dimensionality of the system is obtained. We proceed instead by assuming that $\rho^{(0)}$ and $\mu^{(0)}$ are independent of y. While these assumptions restrict the applicability of the resulting system, they allow for substantial analytic progress. After assuming that the density is uniform in y, the conservation-of-mass equation (4.29) can be expressed as

$$\frac{\partial w^{(0)}}{\partial z} + \frac{\partial v^{(0)}}{\partial y} = -\frac{1}{\rho^{(0)}}\left(\frac{\partial \rho^{(0)}}{\partial t} + w^{(0)} \frac{\partial \rho^{(0)}}{\partial z}\right), \tag{4.36}$$

implying that the term on the left-hand side is independent of y. Following the methodology of Howell [38], we integrate the leading-order conservation-of-mass equation (4.29) between the centre-line and the free surface $y = h^{(0)}(z,t)$, and apply the kinematic boundary condition (4.32). The resulting reduced conservation-of-mass equation is given by

$$\frac{\partial}{\partial t}\left(\rho^{(0)}h^{(0)}\right) + \frac{\partial}{\partial z}\left(\rho^{(0)}w^{(0)}h^{(0)}\right) = 0. \tag{4.37}$$

The first-order conservation-of-z-momentum equation is given by

$$\begin{aligned} Re\rho^{(0)}\frac{\mathrm{D}w^{(0)}}{\mathrm{D}t} =& \frac{\partial}{\partial z}\left(-p^{(0)} + \lambda^{(0)}\left(\frac{\partial w^{(0)}}{\partial z} + \frac{\partial v^{(0)}}{\partial y}\right) + 2\mu^{(0)}\frac{\partial w^{(0)}}{\partial z}\right) \\ &+ \frac{\partial}{\partial y}\left(\mu^{(0)}\left(\frac{\partial w^{(1)}}{\partial y} + \frac{\partial v^{(0)}}{\partial z}\right)\right), \end{aligned} \tag{4.38}$$

with boundary condition given by

$$\begin{aligned} -\left(-p^{(0)} + \lambda^{(0)}\left(\frac{\partial w^{(0)}}{\partial z} + \frac{\partial v^{(0)}}{\partial y}\right) + 2\mu^{(0)}\frac{\partial w^{(0)}}{\partial z}\right)\frac{\partial h^{(0)}}{\partial z} + \mu^{(0)}\left(\frac{\partial w^{(1)}}{\partial y} + \frac{\partial v^{(0)}}{\partial z}\right) \\ = -\Gamma^*\frac{\partial^2 h^{(0)}}{\partial z^2}\frac{\partial h^{(0)}}{\partial z}, \end{aligned} \tag{4.39}$$

on $y = h^{(0)}(z,t)$. Integrating (4.38) between $y = 0$ and $y = h^{(0)}(z,t)$ subject to boundary condition (4.39) on $y = h^{(0)}(z,t)$ gives

$$\begin{aligned} Re\rho^{(0)}h^{(0)}\frac{\mathrm{D}w^{(0)}}{\mathrm{D}t} =& -\Gamma^*\frac{\partial^2 h^{(0)}}{\partial z^2}\frac{\partial h^{(0)}}{\partial z} \\ &+ \frac{\partial}{\partial z}\left(\int_0^{h^{(0)}(z,t)}\left(-p^{(0)} + \lambda^{(0)}\left(\frac{\partial w^{(0)}}{\partial z} + \frac{\partial v^{(0)}}{\partial y}\right) + 2\mu^{(0)}\frac{\partial w^{(0)}}{\partial z}\right)\mathrm{d}y\right). \end{aligned} \tag{4.40}$$

The leading-order y-momentum equation (4.31) is given by

$$\frac{\partial}{\partial y}\left(-p^{(0)} + \lambda^{(0)}\left(\frac{\partial w^{(0)}}{\partial z} + \frac{\partial v^{(0)}}{\partial y}\right) + 2\mu^{(0)}\frac{\partial v^{(0)}}{\partial y}\right) = 0, \tag{4.41}$$

which, given boundary condition (4.34), implies that

$$-p^{(0)} + \lambda^{(0)}\left(\frac{\partial w^{(0)}}{\partial z} + \frac{\partial v^{(0)}}{\partial y}\right) + 2\mu^{(0)}\frac{\partial v^{(0)}}{\partial y} = \Gamma^*\frac{\partial^2 h^{(0)}}{\partial z^2}. \tag{4.42}$$

Using (4.36) to eliminate $\partial v^{(0)}/\partial y$, we obtain

$$-p^{(0)} + \lambda^{(0)}\left(\frac{\partial w^{(0)}}{\partial z} + \frac{\partial v^{(0)}}{\partial y}\right) + 2\mu^{(0)}\frac{\partial w^{(0)}}{\partial z} = \Gamma^*\frac{\partial^2 h^{(0)}}{\partial z^2} + 4\mu^{(0)}\frac{\partial w^{(0)}}{\partial z} + \frac{2\mu^{(0)}}{\rho^{(0)}}\frac{\mathrm{D}\rho^{(0)}}{\mathrm{D}t}. \tag{4.43}$$

Having assumed that $\rho^{(0)}$ is independent of y, we can see from (4.43) that $p^{(0)}$ is also independent of y. This allows us to construct a self-consistent model when we incorporate a closure relation of the form $\mathcal{F}(\rho^{(0)}, p^{(0)}, \boldsymbol{u}^{(0)}, \partial\rho^{(0)}/\partial z)=0$. This is an important feature of the 2D model, and we will show in Section 4.2 that in 3D the assumption of uniform density in a cross-section does not necessarily imply uniform pressure in a cross-section. Substitution of (4.43) into (4.40) yields the conservation-of-momentum equation given by

$$Re\rho^{(0)}h^{(0)}\frac{\mathrm{D}w^{(0)}}{\mathrm{D}t} = \Gamma^*\frac{\partial^3 h^{(0)}}{\partial z^3}h^{(0)} + \frac{\partial}{\partial z}\left(4\mu^{(0)}\frac{\partial w^{(0)}}{\partial z}h^{(0)} + \frac{2\mu^{(0)}h^{(0)}}{\rho^{(0)}}\frac{\mathrm{D}\rho^{(0)}}{\mathrm{D}t}\right). \tag{4.44}$$

Equations (4.37) and (4.44) form the basis of a reduced model for the evolution of a thin, compressible sheet of fluid. These two equations describe the mass and stress balance in the sheet respectively. By integrating over the thin dimension of the sheet, we have reduced the dimensionality of the problem, making any subsequent analysis of the system much easier. With the appropriate closure, (4.37) and (4.44) describe the evolution of the sheet thickness, fluid velocity, and density in both time, and along the length of the sheet (*i.e.* the z-direction). If we were to close the system by assuming the density to be constant (*i.e.* that the fluid is incompressible), (4.37) and (4.44) would reduce to the equations for the extensional flow of an incompressible sheet given by Howell [37]. We have not yet prescribed a closure relating the pressure in the sheet to the evolution of the density. In the following sections, 4.1.2–4.1.4, we illustrate how this model might be employed when considering bubbly mixtures that behave as single-phase compressible fluids. Henceforth we will drop superscripts and all variables will correspond to leading-order quantities.

4.1.2 Steady Stokes flow with zero surface tension

For steady flow in the absence of surface tension ($\Gamma^* = 0$) and inertia ($Re = 0$), equations (4.37) and (4.44) reduce to

$$\rho w h = \mathcal{Q}, \tag{4.45}$$

$$\frac{2\mu}{\rho^2 w^2}\frac{\mathrm{d}}{\mathrm{d}z}\left(\rho w^2\right) = \frac{\mathcal{T}}{\mathcal{Q}}, \tag{4.46}$$

where the mass flux $\mathcal{Q}$ and the tension in the sheet $\mathcal{T}$ are constants. For the case in which there is no tension in the sheet, we have two conserved quantities given by

$$\rho w h = \mathcal{Q}, \tag{4.47}$$

$$\rho w^2 = \mathcal{M}, \tag{4.48}$$

for $\mathcal{M}$ constant. In the absence of surface-tension and inertia, we can obtain an expression for the pressure by combining (4.36), (4.42), and (4.48) to give

$$p = -\frac{(\lambda+\mu)w}{\rho}\frac{\mathrm{d}\rho}{\mathrm{d}z}. \tag{4.49}$$

We can therefore present a closed, steady system governing the dynamics of a 2D compressible sheet given by

$$\rho w h = \mathcal{Q}, \tag{4.50}$$

$$\rho w^2 = \mathcal{M}, \tag{4.51}$$

$$p = -\frac{(\lambda+\mu)w}{\rho}\frac{\mathrm{d}\rho}{\mathrm{d}z}, \tag{4.52}$$

$$\mathcal{F}\left(\rho, p, w, \frac{\mathrm{d}\rho}{\mathrm{d}z}\right) = 0. \tag{4.53}$$

At $z = 0$ we impose that $w = h = 1$ and $\rho = 1/(1+\tilde{\eta})$. For subsequent calculations using these boundary conditions we have $\mathcal{Q} = \mathcal{M} = 1/(1+\tilde{\eta})$. In practice it may be that the flow rate $\mathcal{Q}$ is prescribed instead of the velocity, so that $w = (1+\tilde{\eta})\mathcal{Q}$ at $z = 0$ and $\mathcal{M} = (1+\tilde{\eta})\mathcal{Q}^2$.

4.1.3 Example with a simple microscale coupling

In this section we consider a simple closure relation $\mathcal{F}$ relevant to a bubbly mixture. Through this example we will gain insight into the system's response to varying some if its parameters; insights that are much more obscure in the full model. The simple microscale coupling we use in this section is that of a bubbly mixture, where the bubble pressure is related to its volume through Boyle's law [8].

The dimensionless density can be related to the dimensionless bubble radius through (2.8), giving

$$\rho = \frac{1}{1+\tilde{\eta}\hat{R}^3}, \tag{4.54}$$

where

$$\tilde{\eta} = \frac{4\pi\hat{R}(0)^3\eta}{3}. \tag{4.55}$$

The evolution of the bubble radius in time is given by (3.1). In the macroscale frame,

the bubbles are advected, so the time derivatives in (3.1) are material derivatives in the macroscale frame. Moreover, we have assumed that the density is uniform over the cross-section, so $\hat{R}$ must also be uniform. If we seek a steady state solution for $\hat{R}$, then

$$w\frac{\mathrm{d}\hat{R}}{\mathrm{d}z} = \frac{\hat{R}}{4}\left(\hat{p}_{\mathrm{B}} - p - p_{\mathrm{atm}} - \frac{\Gamma}{\hat{R}}\right). \tag{4.56}$$

Using the relationship between the bubble size and mixture density, (4.54), the bubble evolution equation can be written in terms of the evolution of the density to give the closure relation

$$\mathcal{F}\left(\rho, p, w, \frac{\mathrm{d}\rho}{\mathrm{d}z}\right) = w\frac{\mathrm{d}\rho}{\mathrm{d}z} + \frac{3(1-\rho)\rho}{4}\left(\hat{p}_{\mathrm{B}} - p - p_{\mathrm{atm}} - \frac{\Gamma\tilde{\eta}^{1/3}\rho^{1/3}}{(1-\rho)^{1/3}}\right). \tag{4.57}$$

Using (4.51), (4.52), and (4.57) we can eliminate p and the result is an ODE for the density given by

$$\frac{\mathrm{d}\rho}{\mathrm{d}z} = -\frac{3(1-\rho)\rho^{3/2}\left(\hat{p}_{\mathrm{B}} - p_{\mathrm{atm}} - \dfrac{\Gamma\tilde{\eta}^{1/3}\rho^{1/3}}{(1-\rho)^{1/3}}\right)}{4\mathcal{M}^{1/2}(1+3(1-\rho)(\lambda+\mu)/4)}, \tag{4.58}$$

where $\rho_0 = 1/(1+\tilde{\eta})$ is the density at $z = 0$, and we suppose that the product is cut at $z = 1$.

The thermodynamics on the microscale govern $\hat{p}_{\mathrm{B}}$, and the full microscale model presented in Section 2.6 contains all of the pertinent physics. To illustrate the microscale–macroscale coupling in practice, we will consider a thermodynamic model on the microscale that is much simpler than the model of Section 2.6. We will assume that the temperature and quantity of gas in the bubble is fixed, and that the gas obeys Boyle's law, so that the pressure in the gas, $\hat{p}_{\mathrm{B}}$, is inversely proportional to the bubble volume; that is,

$$\hat{p}_{\mathrm{B}} = \frac{C\tilde{\eta}\rho}{1-\rho}, \tag{4.59}$$

where the parameter C is given by

$$C = \frac{3\hat{N}_0 R_{\mathrm{G}} T_0}{4\pi\hat{R}(0)^3}. \tag{4.60}$$

Under these conditions, the evolution of the density along the fibre is given by

$$\frac{\mathrm{d}\rho}{\mathrm{d}z} = -\frac{3(1-\rho)\rho^{3/2}}{4\mathcal{M}^{1/2}(1+3(1-\rho)(\lambda+\mu)/4)}\left(\frac{C\tilde{\eta}\rho}{1-\rho} - p_{\mathrm{atm}} - \frac{\Gamma\tilde{\eta}^{1/3}\rho^{1/3}}{(1-\rho)^{1/3}}\right). \tag{4.61}$$

This autonomous ODE admits the implicit analytic solution

$$\int_{\rho_0}^{\rho} -\frac{\mathcal{M}^{1/2}(4+3(1-\rho')(\lambda+\mu))}{3(1-\rho')\left(\rho'\right)^{3/2}\left(\frac{C\tilde{\eta}\rho'}{1-\rho'} - p_{\mathrm{atm}} - \frac{\Gamma\tilde{\eta}^{1/3}\rho^{1/3}}{(1-\rho)^{1/3}}\right)}\,\mathrm{d}\rho' = z. \tag{4.62}$$

The microscale model we have described includes two dimensionless parameters: C, and $\tilde{\eta}$, which depend on the nature of bubble nucleation in the mixture. We typically expect that the bubble pressure, $\hat{p}_{\mathrm{B}}$, would be higher than the atmospheric pressure, p_{atm}, so that, by (4.61), the density of the mixture will decrease as it evolves; some illustrative examples are shown in figure 4.2a. In this case, a decrease in density corresponds to an increase in the sheet half-thickness, h, and velocity, w, as illustrated in figures 4.2b and 4.2c respectively. The decrease in density of the mixture is a direct consequence of the bubbles in our mixture growing, as illustrated in figure 4.2d. The bubbles will grow if the pressure inside the bubble is greater than the fluid pressure far from the bubble, which we can observe from the Rayleigh–Plesset equation (4.56). If $\hat{p}_{\mathrm{B}}$ is lower than atmospheric pressure, p_{atm}, the bubbles will contract and the trends we observed in the density, sheet half-thickness, and velocity would reverse.

As we increase $\tilde{\eta}$, more significant changes occur in the macroscale variables ρ, h, and w, despite the fact that the bubble growth is reduced (see figure 4.2). If we define the final half-thickness to be the value of h at $z = 1$, we see that the total change in sheet thickness has a non-monotonic dependence on the volume fraction ratio, $\tilde{\eta}$, as illustrated in 4.3a. It is worth remembering at this point that we have made a number of assumptions in deriving our macroscale model, including the assumption that the gas component is dispersed in the liquid component. We might expect that our model becomes less accurate for larger values of $\tilde{\eta}$, as the gas phase becomes the dominant component of the mixture.

In general, increasing C will produce greater overall bubble growth, and hence greater expansion in the product, as illustrated in figure 4.3b. This is because, in our formulation, C only determines the initial bubble pressure and is independent of $\tilde{\eta}$. The dependence of the sheet's evolution on $\tilde{\eta}$ is more complex because $\tilde{\eta}$ influences both

the bubble pressure, and the initial density. So, even though C and $\tilde{\eta}$ can both be tuned to vary the pressure in the bubbles—changing the evolution of the product—$\tilde{\eta}$ also changes the initial density of the product leading to the non-monotonic behaviour we observe in figure 4.3a. We also note that changing C alters the value of $\tilde{\eta}$ that produces the maximum growth in the sheet thickness, say $\tilde{\eta}_{opt}$, as shown in figure 4.3c.

In order to produce sheets with particular properties, understanding how the parameters that obtain this maximum depend on each other will be important. This kind of insight is far easier to access using the reduced model described in this section when compared to the original system: (4.2)–(4.4), and (4.8).

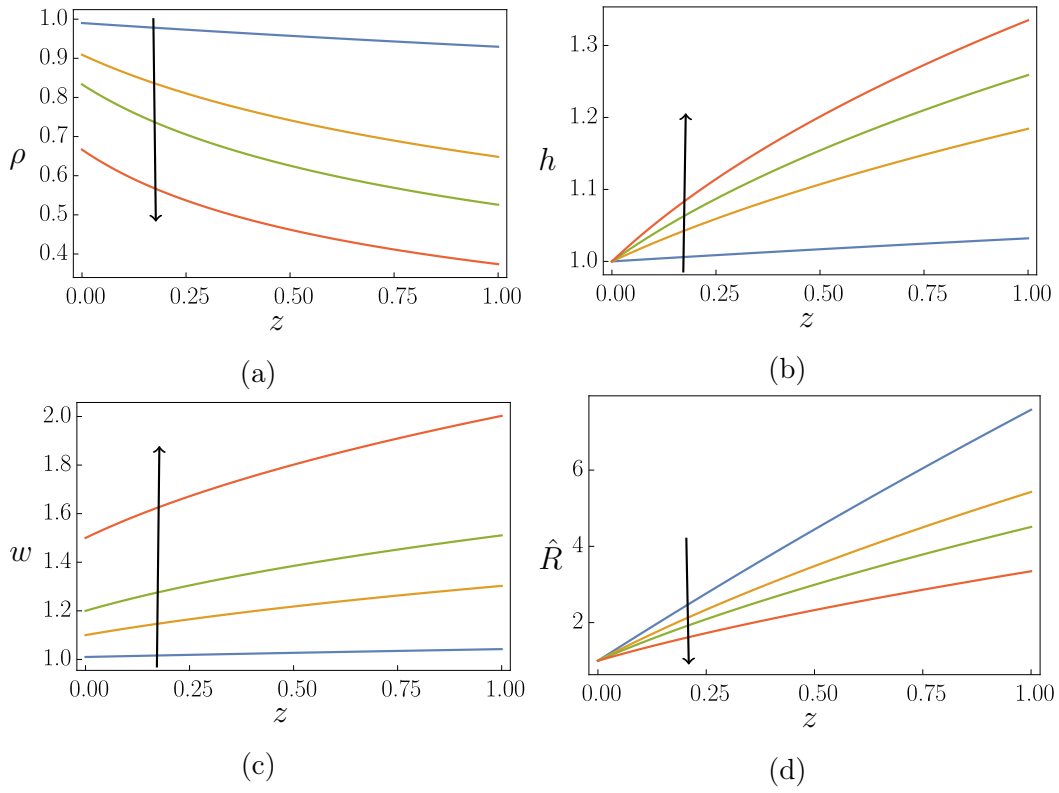

Figure 4.2: *Predictions for* (a) *the density,* ρ, (b) *sheet half-thickness,* h, (c) *velocity,* w, *and* (d) *bubble radius,* $\hat{R}$, *for initial volume fraction* $\tilde{\eta} = 0.01, 0.1, 0.2, 0.5$ *where the arrow indicates the direction of increasing* $\tilde{\eta}$. *These figures were produced using equation (4.59) as a constitutive law for the bubble pressure with* $C = 10$, $p_{atm} = 0.1$, $\mathcal{Q} = \mathcal{M} = 1/(1+\tilde{\eta})$, *and* $(\lambda + \mu) = 1$. *These figures were produced by solving (4.61) for* ρ, *and then returning* w, h, *and* $\hat{R}$ *from (4.51), (4.50), and (4.54) respectively.*

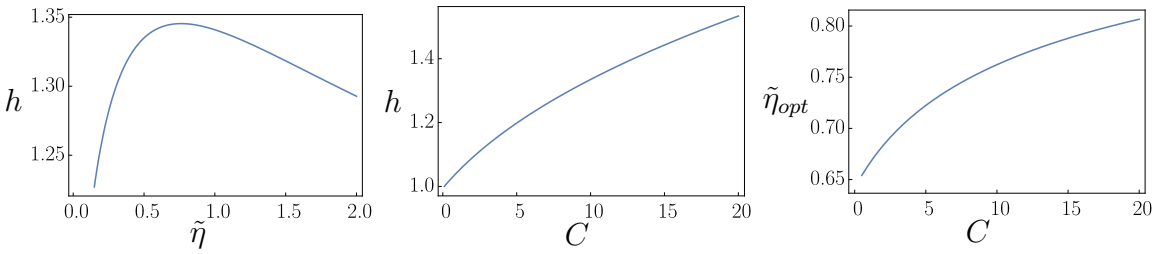

(a) (b) (c)

Figure 4.3: *Predictions for:* (a) *the sheet half-thickness,* h*, at* $z = 1$ *as the initial volume fraction,* $\tilde{\eta}$ *is varied,* (b) h *at* $z = 1$ *as* C *is varied, and* (c) *the value of* $\tilde{\eta}$ *that results in the largest growth as* C *is varied. These predictions were made using (4.62) with* $p_{atm} = 0.1$*,* $\mathcal{Q} = \mathcal{M} = 1/(1+\tilde{\eta})$*,* $(\lambda + \mu) = 1$*, and* $\Gamma = 3.2 \times 10^{-2}$*.*

4.1.4 Example with a more thermodynamically complete coupling

The constitutive law for the bubble pressure (4.59) is a simplification of the full microscale model presented in Chapter 3. To be precise, we have assumed that the amount of gas inside the bubbles and the temperature of the bubbles do not change. In reality, we expect these quantities to change. By accounting for the additional thermodynamics, we are allowing C to change as the product evolves because the temperature, $\hat{T}_{\mathrm{B}}$, and number of moles of gas, $\hat{N}_{\mathrm{B}}$, in the bubbles will vary.

To compare the impact of neglecting aspects of the microscale thermodynamics, through the use of Boyle's law for the bubble pressure, we consider the reduced microscale model for Case II in Section 3.3.2, given by equations (3.77)–(3.82) with initial conditions given by (3.83). The time since bubble nucleation in the microscale frame is related to axial distance in the macroscale frame by

$$\hat{t} = \int_0^z \frac{1}{w(\sigma)} \mathrm{d}\sigma. \tag{4.63}$$

In the macroscale frame, the microscale time derivatives are transformed to the time-steady, macroscale material derivatives given by

$$\frac{\mathrm{d}}{\mathrm{d}\hat{t}} = w \frac{\mathrm{d}}{\mathrm{d}z}. \tag{4.64}$$

The microscale initial conditions at $\hat{t} = 0$ serve as the boundary conditions on $z = 0$ in the macroscale frame. We use the parameters given in tables 2.2 and 2.3 unless otherwise stated.

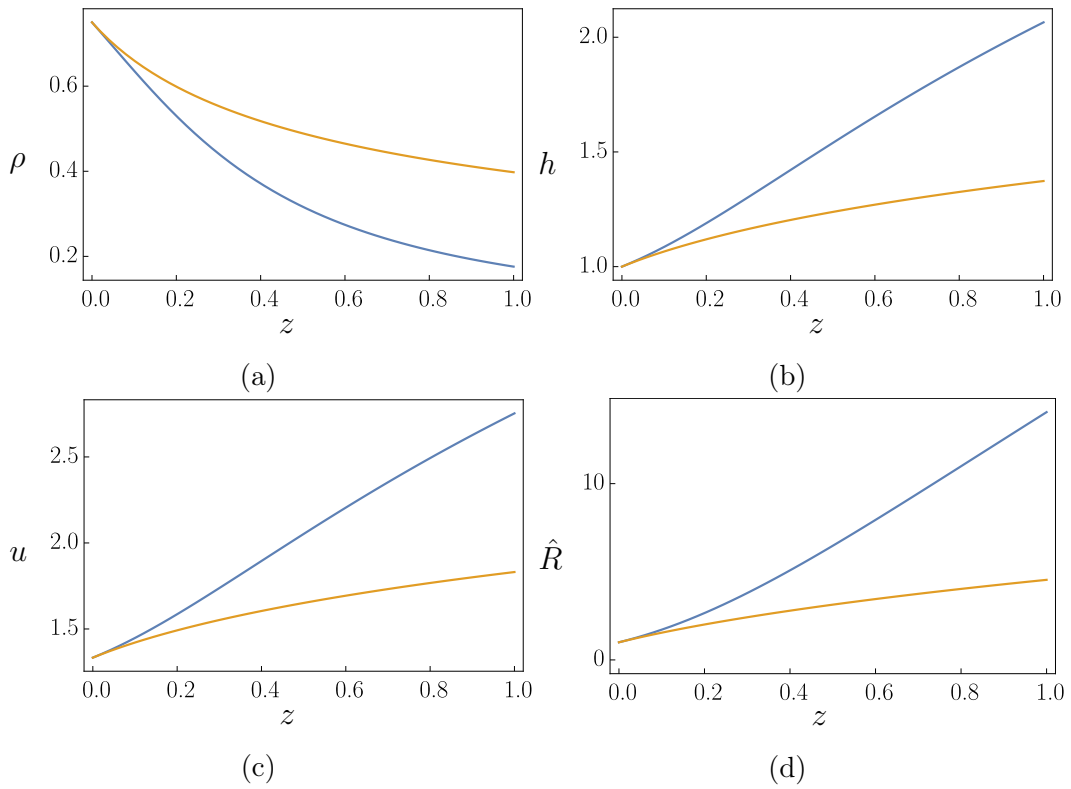

Figure 4.4: *Comparison between* (a) *the density,* ρ, (b) *sheet half-thickness,* h, (c) *velocity,* w, *and* (d) *bubble radius,* $\hat{R}$ *for two different bubble-pressure constitutive laws. More significant change occurs in all variables when the more complete model of the microscale thermodynamics described in Chapter 3 (blue) is used to determine the bubble pressure when compared to equation (4.59) (orange). Both sets of results start with* $C = 10$*, and the remaining parameters given in tables 2.2 and 2.3; however, in the more complete microscale model* C *is allowed to vary as the temperature and amount of gas in the bubble changes.*

The simulations shown in figure 4.4 start with the same value of C for the sake of comparison. We observe greater bubble growth when the more complicated thermodynamics are included, as shown in figure 4.4d. This corresponds to a greater drop in the density, and greater increases in the half-thickness and the velocity of the sheet, as illustrated in figures 4.4a, 4.4b, and 4.4c respectively. Comparison between the two different constitutive laws for the bubble pressure illustrates the importance in accounting for all of the ongoing physical processes as the resulting evolution of the product is significantly different depending on the model used.

4.2 A three-dimensional compressible flow model

We now consider the fully three-dimensional model describing the extrusion of a fibre of fluid in the slender limit with a non-axisymmetric cross-section. We describe the free-surface by $G(x, y, z, t) = 0$, as illustrated in figure 4.5. The region corresponding to a cross-section of the extruded product at some point along the axis of flow (*i.e.* the z-axis) is denoted by Ω.

We do not consider the deflection of the centre-line, or rotation of the fibre. Dewynne *et al.* [19] demonstrate that the centreline of an incompressible fluid fibre can deflect if inertial and gravitational effects are significant. Moreover, Cummings and Howell [17] demonstrate that surface tension can induce lateral momentum on non-symmetric cross sections. In practice, the effects of inertia are negligible, based on the Reynolds number in table 2.2; however, we retain inertial terms for much of this analysis. For consistency we restrict our attention to fluid fibres with cross-sections that are symmetric with respect to both the x and y axes and, as in the 2D case, we neglect the effects of gravity.

The governing equations are the same as those given in Section 2.5; however, in this chapter we neglect the gravitational term, whose influence is governed by the Stokes number St, in equation (2.58). The dimensionless equations governing conservation of mass and momentum are given by

$$\frac{\partial \rho}{\partial t} + \nabla \cdot (\rho \boldsymbol{u}) = 0, \tag{4.65}$$

$$Re\rho \frac{\mathrm{D}\boldsymbol{u}}{\mathrm{D}t} = \nabla \cdot \boldsymbol{\sigma}, \tag{4.66}$$

where the liquid velocity $\boldsymbol{u} = (u, v, w)$ in Cartesian coordinates and the stress tensor is given by

$$\boldsymbol{\sigma} = (-p + \lambda \nabla \cdot \boldsymbol{u})\mathbb{I} + \mu \left(\nabla \boldsymbol{u} + (\nabla \boldsymbol{u})^T \right), \tag{4.67}$$

where $\mathbb{I}$ is the identity tensor. The respective kinematic and dynamic boundary conditions on the surface at $G(x, y, z, t) = 0$ are given by

$$\frac{\partial G}{\partial t} + \boldsymbol{u} \cdot \nabla G = 0, \qquad \text{and} \qquad \boldsymbol{\sigma} \cdot \nabla G = -\gamma^* \varkappa \nabla G, \tag{4.68}$$

where $\varkappa = \nabla \cdot \boldsymbol{n}$ is the curvature of the surface, and $\boldsymbol{n}$ is the outward pointing unit normal to the boundary. Much of this discussion is independent of the form of the

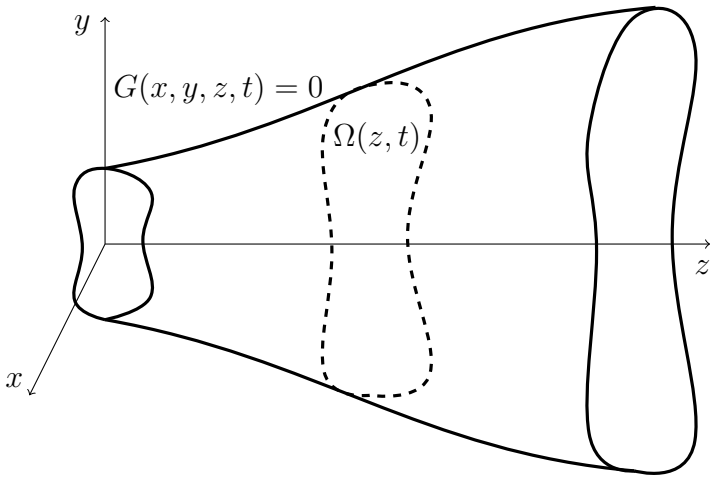

Figure 4.5: *Schematic of the three-dimensional flow of a compressible fluid bounded by the surface given by* $G(x, y, z, t) = 0$. *The domain* $\Omega(z, t)$ *refers to a cross-section of the extruded product.*

system used to close these equations. We discuss the closure of these equations when we present a reduced system at the end of this section.

Just as in 2D, we now consider the case where the axial and cross-sectional length scales are different. For a fluid fibre with characteristic axial length L, and thickness of $\mathcal{O}(\epsilon L)$, we rescale the appropriate variables

$$x = \epsilon x', \qquad y = \epsilon y', \qquad u = \epsilon u', \qquad v = \epsilon v', \qquad \varkappa = \frac{1}{\epsilon}\varkappa', \tag{4.69}$$

which gives the modified dimensionless system in component form (dropping primes)

$$\frac{\partial \rho}{\partial t} + \frac{\partial}{\partial x}(\rho u) + \frac{\partial}{\partial y}(\rho v) + \frac{\partial}{\partial z}(\rho w) = 0, \tag{4.70}$$

$$\begin{aligned}\epsilon^2 Re\rho \frac{\mathrm{D}u}{\mathrm{D}t} =& \frac{\partial}{\partial x}\left(-p + \lambda\left(\frac{\partial u}{\partial x} + \frac{\partial v}{\partial y} + \frac{\partial w}{\partial z}\right) + 2\mu\frac{\partial u}{\partial x}\right) + \frac{\partial}{\partial y}\left(\mu\left(\frac{\partial u}{\partial y} + \frac{\partial v}{\partial x}\right)\right) \\ &+ \frac{\partial}{\partial z}\left(\mu\left(\epsilon^2\frac{\partial u}{\partial z} + \frac{\partial w}{\partial x}\right)\right),\end{aligned} \tag{4.71}$$

$$\begin{aligned}\epsilon^2 Re\rho \frac{\mathrm{D}v}{\mathrm{D}t} =& \frac{\partial}{\partial x}\left(\mu\left(\frac{\partial u}{\partial y} + \frac{\partial v}{\partial x}\right)\right) + \frac{\partial}{\partial y}\left(-p + \lambda\left(\frac{\partial u}{\partial x} + \frac{\partial v}{\partial y} + \frac{\partial w}{\partial z}\right) + 2\mu\frac{\partial v}{\partial y}\right) \\ &+ \frac{\partial}{\partial z}\left(\mu\left(\epsilon^2\frac{\partial v}{\partial z} + \frac{\partial w}{\partial y}\right)\right),\end{aligned} \tag{4.72}$$

$$\begin{aligned}\epsilon^2 Re\rho \frac{\mathrm{D}w}{\mathrm{D}t} =& \frac{\partial}{\partial x}\left(\mu\left(\epsilon^2\frac{\partial u}{\partial z} + \frac{\partial w}{\partial x}\right)\right) + \frac{\partial}{\partial y}\left(\mu\left(\epsilon^2\frac{\partial v}{\partial z} + \frac{\partial w}{\partial y}\right)\right) \\ &+ \epsilon^2\frac{\partial}{\partial z}\left(-p + \lambda\left(\frac{\partial u}{\partial x} + \frac{\partial v}{\partial y} + \frac{\partial w}{\partial z}\right) + 2\mu\frac{\partial w}{\partial z}\right),\end{aligned} \tag{4.73}$$

in the region bounded by $G(x, y, z, t) = 0$.

The modified boundary conditions on $G(x, y, z, t) = 0$ are given by

$$\frac{\partial G}{\partial t} + u\frac{\partial G}{\partial x} + v\frac{\partial G}{\partial y} + w\frac{\partial G}{\partial z} = 0, \tag{4.74}$$

$$\left(-p + \lambda\left(\frac{\partial u}{\partial x} + \frac{\partial v}{\partial y} + \frac{\partial w}{\partial z}\right) + 2\mu\frac{\partial u}{\partial x}\right)\frac{\partial G}{\partial x} + \mu\left(\frac{\partial u}{\partial y} + \frac{\partial v}{\partial x}\right)\frac{\partial G}{\partial y} + \mu\left(\epsilon^2\frac{\partial u}{\partial z} + \frac{\partial w}{\partial x}\right)\frac{\partial G}{\partial z} = -\Gamma^*\varkappa\frac{\partial G}{\partial x}, \tag{4.75}$$

$$\mu\left(\frac{\partial u}{\partial y} + \frac{\partial v}{\partial x}\right)\frac{\partial G}{\partial x} + \left(-p + \lambda\left(\frac{\partial u}{\partial x} + \frac{\partial v}{\partial y} + \frac{\partial w}{\partial z}\right) + 2\mu\frac{\partial v}{\partial y}\right)\frac{\partial G}{\partial y} + \mu\left(\epsilon^2\frac{\partial v}{\partial z} + \frac{\partial w}{\partial y}\right)\frac{\partial G}{\partial z} = -\Gamma^*\varkappa\frac{\partial G}{\partial y}, \tag{4.76}$$

$$\mu\left(\epsilon^2\frac{\partial u}{\partial z} + \frac{\partial w}{\partial x}\right)\frac{\partial G}{\partial x} + \mu\left(\epsilon^2\frac{\partial v}{\partial z} + \frac{\partial w}{\partial y}\right)\frac{\partial G}{\partial y} + \epsilon^2\left(-p + \lambda\left(\frac{\partial u}{\partial x} + \frac{\partial v}{\partial y} + \frac{\partial w}{\partial z}\right) + 2\mu\frac{\partial w}{\partial z}\right)\frac{\partial G}{\partial z} = -\epsilon^2\Gamma^*\varkappa\frac{\partial G}{\partial z}, \tag{4.77}$$

where Γ^* is defined by (4.26). As in the 2D case, we expand each variable in powers of ϵ^2 to obtain the leading-order system

$$\frac{\partial \rho^{(0)}}{\partial t} + \frac{\partial}{\partial x}\left(\rho^{(0)}u^{(0)}\right) + \frac{\partial}{\partial y}\left(\rho^{(0)}v^{(0)}\right) + \frac{\partial}{\partial z}\left(\rho^{(0)}w^{(0)}\right) = 0, \tag{4.78}$$

$$\frac{\partial}{\partial x}\left(-p^{(0)} + \lambda^{(0)}\left(\frac{\partial u^{(0)}}{\partial x} + \frac{\partial v^{(0)}}{\partial y} + \frac{\partial w^{(0)}}{\partial z}\right) + 2\mu^{(0)}\frac{\partial u^{(0)}}{\partial x}\right) + \frac{\partial}{\partial y}\left(\mu^{(0)}\left(\frac{\partial u^{(0)}}{\partial y} + \frac{\partial v^{(0)}}{\partial x}\right)\right) + \frac{\partial}{\partial z}\left(\mu^{(0)}\frac{\partial w^{(0)}}{\partial x}\right) = 0, \tag{4.79}$$

$$\frac{\partial}{\partial x}\left(\mu^{(0)}\left(\frac{\partial u^{(0)}}{\partial y} + \frac{\partial v^{(0)}}{\partial x}\right)\right) + \frac{\partial}{\partial y}\left(-p^{(0)} + \lambda^{(0)}\left(\frac{\partial u^{(0)}}{\partial x} + \frac{\partial v^{(0)}}{\partial y}\frac{\partial w^{(0)}}{\partial z}\right) + 2\mu^{(0)}\frac{\partial v^{(0)}}{\partial y}\right) + \frac{\partial}{\partial z}\left(\mu^{(0)}\frac{\partial w^{(0)}}{\partial y}\right) = 0, \tag{4.80}$$

$$\frac{\partial}{\partial x}\left(\mu^{(0)}\frac{\partial w^{(0)}}{\partial x}\right) + \frac{\partial}{\partial y}\left(\mu^{(0)}\frac{\partial w^{(0)}}{\partial y}\right) = 0, \tag{4.81}$$

in the region bounded by $G^{(0)}(x,y,z,t)=0$. The leading-order boundary conditions on $G^{(0)}(x,y,z,t)=0$ are

$$\frac{\partial G^{(0)}}{\partial t}+u^{(0)}\frac{\partial G^{(0)}}{\partial x}+v^{(0)}\frac{\partial G^{(0)}}{\partial y}+w^{(0)}\frac{\partial G^{(0)}}{\partial z}=0, \tag{4.82}$$

$$\left(-p^{(0)}+\lambda^{(0)}\left(\frac{\partial u^{(0)}}{\partial x}+\frac{\partial v^{(0)}}{\partial y}+\frac{\partial w^{(0)}}{\partial z}\right)+2\mu^{(0)}\frac{\partial u^{(0)}}{\partial x}\right)\frac{\partial G^{(0)}}{\partial x} + \mu^{(0)}\left(\frac{\partial u^{(0)}}{\partial y}+\frac{\partial v^{(0)}}{\partial x}\right)\frac{\partial G^{(0)}}{\partial y}+\mu^{(0)}\frac{\partial w^{(0)}}{\partial x}\frac{\partial G^{(0)}}{\partial z}=-\Gamma^{*}\varkappa^{(0)}\frac{\partial G^{(0)}}{\partial x}, \tag{4.83}$$

$$\mu^{(0)}\left(\frac{\partial u^{(0)}}{\partial y}+\frac{\partial v^{(0)}}{\partial x}\right)\frac{\partial G^{(0)}}{\partial x}+\left(-p^{(0)}+\lambda^{(0)}\left(\frac{\partial u^{(0)}}{\partial x}+\frac{\partial v^{(0)}}{\partial y}+\frac{\partial w^{(0)}}{\partial z}\right)+2\mu^{(0)}\frac{\partial v^{(0)}}{\partial y}\right)\frac{\partial G^{(0)}}{\partial y} + \mu^{(0)}\frac{\partial w^{(0)}}{\partial y}\frac{\partial G^{(0)}}{\partial z}=-\Gamma^{*}\varkappa^{(0)}\frac{\partial G^{(0)}}{\partial y}, \tag{4.84}$$

$$\mu^{(0)}\frac{\partial w^{(0)}}{\partial x}\frac{\partial G^{(0)}}{\partial x}+\mu^{(0)}\frac{\partial w^{(0)}}{\partial y}\frac{\partial G^{(0)}}{\partial y}=0, \tag{4.85}$$

and the relevant first-order equation is

$$Re\rho^{(0)}\frac{\mathrm{D}w^{(0)}}{\mathrm{D}t}=\mu^{(0)}\left(\frac{\partial^2 w^{(1)}}{\partial x^2}+\frac{\partial^2 w^{(1)}}{\partial y^2}\right)+\mu^{(0)}\frac{\partial}{\partial z}\left(\frac{\partial u^{(0)}}{\partial x}+\frac{\partial v^{(0)}}{\partial y})\right) + \frac{\partial}{\partial z}\left(-p^{(0)}+\lambda^{(0)}\left(\frac{\partial u^{(0)}}{\partial x}+\frac{\partial v^{(0)}}{\partial y}+\frac{\partial w^{(0)}}{\partial z}\right)+2\mu^{(0)}\frac{\partial w^{(0)}}{\partial z}\right), \tag{4.86}$$

in the region bounded by $G^{(0)}(x,y,z,t)=0$, and the boundary condition on $G^{(0)}(x,y,z,t)=0$ is

$$\mu^{(0)}\left(\frac{\partial w^{(1)}}{\partial x}+\frac{\partial u^{(0)}}{\partial z}\right)\frac{\partial G^{(0)}}{\partial x}+\mu^{(0)}\left(\frac{\partial w^{(1)}}{\partial y}+\frac{\partial v^{(0)}}{\partial z}\right)\frac{\partial G^{(0)}}{\partial y} + \left(-p^{(0)}+\lambda^{(0)}\left(\frac{\partial u^{(0)}}{\partial x}+\frac{\partial v^{(0)}}{\partial y}+\frac{\partial w^{(0)}}{\partial z}\right)+2\mu^{(0)}\frac{\partial w^{(0)}}{\partial z}\right)\frac{\partial G^{(0)}}{\partial z}=-\Gamma^{*}\varkappa_0\frac{\partial G^{(0)}}{\partial z}. \tag{4.87}$$

Motivated by [38], we reduce the dimensionality of the model by integrating the conservation equations (4.78) and (4.86) over the cross-section of the fluid. By (4.81) and (4.85), $w^{(0)}$ is independent of x and y. As in the 2D case, we are unable to make significant progress unless we assume that the density is independent of the cross-sectional coordinates x and y. We also make the assumption that $\mu^{(0)}$ is independent of x and y.

The method of reducing the system of equations described in Howell [38] is as follows: integrate the appropriate conservation equations over the cross-section, impose the required Reynolds transport theorems (as stated in Dewynne *et al.* [20]) to re-order integration and differentiation operations, and then use the boundary conditions to

eliminate the surface integral terms that arise. We follow this approach by first integrating the leading-order conservation-of-mass equation (4.78) over the cross-section $\Omega^{(0)}$, and imposing (4.82), which gives the reduced conservation-of-mass equation

$$\frac{\partial}{\partial t}\left(\rho^{(0)}A^{(0)}\right)+\frac{\partial}{\partial z}\left(\rho^{(0)}w^{(0)}A^{(0)}\right)=0, \tag{4.88}$$

where

$$A^{(0)}(z,t)=\iint_{\Omega^{(0)}}\mathrm{d}x\mathrm{d}y \tag{4.89}$$

is the cross-sectional area of the fibre at a stationary z and time t. Integrating the first-order conservation-of-momentum equation (4.86) over the cross-section $\Omega^{(0)}$ and imposing (4.87) gives

$$\begin{aligned}Re\rho^{(0)}A^{(0)}\frac{\mathrm{D}w^{(0)}}{\mathrm{D}t}=&\frac{\partial}{\partial z}\left(\iint_{\Omega^{(0)}}-p^{(0)}+\lambda^{(0)}\left(\frac{\partial u^{(0)}}{\partial x}+\frac{\partial v^{(0)}}{\partial y}+\frac{\partial w^{(0)}}{\partial z}\right)+2\mu^{(0)}\frac{\partial w^{(0)}}{\partial z}\,\mathrm{d}x\mathrm{d}y\right)\\&-\Gamma^{*}(S^{(0)})_{z},\end{aligned} \tag{4.90}$$

where

$$S^{(0)}(z,t)=\int_{\partial\Omega^{(0)}}\mathrm{d}s \tag{4.91}$$

is the arc-length perimeter of the fibre at a stationary z and time t. In order to evaluate the integral in (4.90) we follow the approach taken by Howell [38] and introduce an Airy stress function, $\mathcal{A}(x,y,t;z)$, which is in our case defined in a given cross-section, $\Omega^{(0)}$, by

$$\frac{\partial^2\mathcal{A}}{\partial y^2}=-p^{(0)}+\lambda^{(0)}\left(\frac{\partial u^{(0)}}{\partial x}+\frac{\partial v^{(0)}}{\partial y}+\frac{\partial w^{(0)}}{\partial z}\right)+2\mu^{(0)}\frac{\partial u^{(0)}}{\partial x}, \tag{4.92}$$

$$-\frac{\partial^2\mathcal{A}}{\partial y\partial x}=\mu^{(0)}\left(\frac{\partial u^{(0)}}{\partial y}+\frac{\partial v^{(0)}}{\partial x}\right), \tag{4.93}$$

$$\frac{\partial^2\mathcal{A}}{\partial x^2}=-p^{(0)}+\lambda^{(0)}\left(\frac{\partial u^{(0)}}{\partial x}+\frac{\partial v^{(0)}}{\partial y}+\frac{\partial w^{(0)}}{\partial z}\right)+2\mu^{(0)}\frac{\partial v^{(0)}}{\partial y}. \tag{4.94}$$

If we denote the 2D gradient operator by ∇_2, by summing (4.92) and (4.94) we can see that

$$\nabla_2^2\mathcal{A}=-2\left(p^{(0)}+\lambda^{(0)}\left(\frac{\partial u^{(0)}}{\partial x}+\frac{\partial v^{(0)}}{\partial y}+\frac{\partial w^{(0)}}{\partial z}\right)+\mu^{(0)}\left(\frac{\partial u^{(0)}}{\partial x}+\frac{\partial v^{(0)}}{\partial y}\right)\right). \tag{4.95}$$

The assumption of uniform density and viscosity in the cross-section, along with (4.78), implies that

$$\frac{\partial u^{(0)}}{\partial x} + \frac{\partial v^{(0)}}{\partial y} = -\frac{1}{\rho^{(0)}} \left(\frac{\partial \rho^{(0)}}{\partial t} + w^{(0)} \frac{\partial \rho^{(0)}}{\partial z} \right); \tag{4.96}$$

the key point being that the quantity on the left-hand side of this equation is independent of the cross-section coordinates x and y. We shall define a quantity $\mathcal{P}$ for shorthand, given by

$$\mathcal{P} = p^{(0)} - \lambda^{(0)} \left(\frac{\partial u^{(0)}}{\partial x} + \frac{\partial v^{(0)}}{\partial y} + \frac{\partial w^{(0)}}{\partial z} \right). \tag{4.97}$$

Neglecting x and y derivatives of $w^{(0)}$, the first derivatives of $\mathcal{P}$ are defined in (4.79) and (4.80) to be given by

$$\frac{\partial \mathcal{P}}{\partial x} = \frac{\partial}{\partial x} \left(2\mu^{(0)} \frac{\partial u^{(0)}}{\partial x} \right) + \frac{\partial}{\partial y} \left(\mu^{(0)} \left(\frac{\partial u^{(0)}}{\partial y} + \frac{\partial v^{(0)}}{\partial x} \right) \right), \tag{4.98}$$

$$\frac{\partial \mathcal{P}}{\partial y} = \frac{\partial}{\partial x} \left(\mu^{(0)} \left(\frac{\partial u^{(0)}}{\partial y} + \frac{\partial v^{(0)}}{\partial x} \right) \right) + \frac{\partial}{\partial y} \left(2\mu^{(0)} \frac{\partial v^{(0)}}{\partial y} \right). \tag{4.99}$$

By differentiating (4.98) and (4.99) by x and y respectively, we can show that

$$\nabla_2^2 \mathcal{P} = 0. \tag{4.100}$$

The combination of (4.95), (4.96), and (4.100) imply that the Airy stress function satisfies

$$\nabla_2^4 \mathcal{A} = 0 \qquad \text{in} \qquad \Omega^{(0)}, \tag{4.101}$$

with

$$\mathcal{A} = 0, \qquad \text{and} \qquad \frac{\partial \mathcal{A}}{\partial n} = -\Gamma^* \qquad \text{on} \qquad \partial\Omega^{(0)}. \tag{4.102a,b}$$

We can re-arrange (4.95) to give

$$\frac{1}{2} \left(\frac{\partial^2 \mathcal{A}}{\partial x^2} + \frac{\partial^2 \mathcal{A}}{\partial y^2} \right) + 2\mu^{(0)} \frac{\partial w^{(0)}}{\partial z} - \mu^{(0)} \left(\frac{\partial u^{(0)}}{\partial x} + \frac{\partial v^{(0)}}{\partial y} \right)$$
$$= -p^{(0)} + \lambda^{(0)} \left(\frac{\partial u^{(0)}}{\partial x} + \frac{\partial v^{(0)}}{\partial y} + \frac{\partial w^{(0)}}{\partial z} \right) + 2\mu^{(0)} \frac{\partial w^{(0)}}{\partial z}. \tag{4.103}$$

The left-hand side of (4.103) can be substituted into the integral of (4.90). This substitution makes the integral easier to evaluate, and, in conjunction with the boundary condition for the Airy stress function (4.102b), we subsequently find

$$\iint_{\Omega^{(0)}} \frac{1}{2} \left(\frac{\partial^2 \mathcal{A}}{\partial x^2} + \frac{\partial^2 \mathcal{A}}{\partial y^2} \right) + 2\mu^{(0)} \frac{\partial w^{(0)}}{\partial z} - \mu^{(0)} \left(\frac{\partial u^{(0)}}{\partial x} + \frac{\partial v^{(0)}}{\partial y} \right) \mathrm{d}x\mathrm{d}y$$
$$= -\frac{\Gamma^* S^{(0)}}{2} + A^{(0)} \left(3\mu^{(0)} \frac{\partial w^{(0)}}{\partial z} + \frac{\mu^{(0)}}{\rho^{(0)}} \frac{\mathrm{D}\rho^{(0)}}{\mathrm{D}t} \right). \tag{4.104}$$

The result of combining (4.90) and (4.104) is an averaged conservation-of-momentum equation given by

$$Re\rho^{(0)}A^{(0)}\frac{\mathrm{D}w^{(0)}}{\mathrm{D}t} = \frac{\partial}{\partial z}\left(3A^{(0)}\mu^{(0)}\frac{\partial w^{(0)}}{\partial z} + \frac{\mu^{(0)}A^{(0)}}{\rho^{(0)}}\frac{\mathrm{D}\rho^{(0)}}{\mathrm{D}t}\right) + \frac{\Gamma^*}{2}\frac{\partial S^{(0)}}{\partial z}. \tag{4.105}$$

By summing equations (4.92) and (4.94), the pressure can be expressed as

$$p^{(0)} = -\frac{1}{2}\left(\frac{\partial^2\mathcal{A}}{\partial x^2} + \frac{\partial^2\mathcal{A}}{\partial y^2}\right) + (\lambda^{(0)} + \mu^{(0)})\left(\frac{\partial u^{(0)}}{\partial x} + \frac{\partial v^{(0)}}{\partial y}\right) + \lambda^{(0)}\frac{\partial w^{(0)}}{\partial z}. \tag{4.106}$$

With the possible exception of the Airy-stress-function terms, the other terms comprising the pressure are uniform throughout the cross-section. In order for this system to be self-consistent with the assumption that the density is uniform throughout the cross-section, the Airy stress function must satisfy the 2D Poisson equation (with constant forcing). This places an additional constraint on the solution to equation (4.101) subject to the boundary conditions (4.102). In fact, we must now solve

$$\nabla_2^2\mathcal{A} = \mathcal{C}, \tag{4.107}$$

for some $\mathcal{C}(z,t)$, subject to the boundary conditions (4.102), which is an overdetermined system. By integrating (4.107) over $\Omega^{(0)}$, subject to (4.102b), we find that $\mathcal{C} = -\Gamma^* S^{(0)}/A^{(0)}$.

For general domains, $\Omega^{(0)}$, and non-negligible surface tension, we cannot find a solution for $\mathcal{A}$ that is consistent with the assumption of uniform density (and hence pressure). In these cases, it is not possible to construct a self-consistent model with the incorporation of a closure relation, say

$$\mathcal{F}\left(\rho, p, \boldsymbol{u}, \nabla\rho\right) = 0; \tag{4.108}$$

however, for circular cross-sections of radius $\sqrt{A^{(0)}/\pi}$, there is a solution, which is given by

$$\mathcal{A}(x,y) = \frac{\Gamma^*}{2}\sqrt{\frac{\pi}{A^{(0)}}}\left(\frac{A^{(0)}}{\pi} - \sqrt{x^2+y^2}\right). \tag{4.109}$$

Additionally, at leading order, for general domains $\Omega^{(0)}$ and negligible surface tension ($\Gamma^* = 0$), $\mathcal{A} = 0$ in $\Omega^{(0)}$ satisfies all of the constraints. So, for either a circular cross-section with non-zero surface tension, or an arbitrary-shaped cross-section with negligible surface tension, the pressure is given by

$$p^{(0)} = \frac{\Gamma^*}{2}\sqrt{\frac{\pi}{A^{(0)}}} - \frac{(\lambda^{(0)} + \mu^{(0)})}{\rho^{(0)}}\left(\frac{\partial\rho^{(0)}}{\partial t} + \frac{\partial}{\partial z}\left(\rho^{(0)}w^{(0)}\right)\right) + \lambda^{(0)}\frac{\partial w^{(0)}}{\partial z}. \tag{4.110}$$

To summarise, the reduced system of equations governing the behaviour of a thin compressible fibre in three-dimensions is given by (dropping superscripts from hereon)

$$\frac{\partial}{\partial t}\left(\rho A\right)+\frac{\partial}{\partial z}\left(\rho A w\right)=0, \tag{4.111}$$

$$Re\left(\frac{\partial}{\partial t}\left(\rho w A\right)+\frac{\partial}{\partial z}\left(\rho A w^{2}\right)\right)=\frac{\partial}{\partial z}\left(3A\mu\frac{\partial w}{\partial z}+\frac{\mu A}{\rho}\frac{\mathrm{D}\rho}{\mathrm{D}t}\right)+\frac{\Gamma^{*}}{2}\frac{\partial S}{\partial z}, \tag{4.112}$$

$$p=\frac{\Gamma^{*}}{2}\sqrt{\frac{\pi}{A}}-\frac{(\lambda+\mu)}{\rho}\left(\frac{\partial\rho}{\partial t}+\frac{\partial}{\partial z}\left(\rho w\right)\right)+\lambda\frac{\partial w}{\partial z}, \tag{4.113}$$

$$\mathcal{F}\left(\rho,p,w,\frac{\partial\rho}{\partial z}\right)=0, \tag{4.114}$$

where

$$A=\iint_{\Omega}\mathrm{d}x\mathrm{d}y, \qquad\qquad S=\oint_{\partial\Omega}\mathrm{d}s. \tag{4.115}$$

4.2.1 Steady flow

In this section we consider the time steady behaviour of equations (4.111)–(4.115). We retain the Reynolds number and surface tension terms for the initial analysis. In the latter part of this section we neglect the inertial and surface tension terms, which can be justified for extrusion based on the size of Re and Γ^{*} contained in table 2.2, in order to derive a simpler reduced model. Consider the steady momentum equation (4.112), which can be expressed as

$$\frac{\mathrm{d}}{\mathrm{d}z}\left(Re\rho A w^{2}-3A\mu\frac{\partial w}{\partial z}-\frac{\mu w A}{\rho}\frac{\partial\rho}{\partial z}-\frac{\Gamma^{*}S}{2}\right)=0, \tag{4.116}$$

meaning the quantity inside the brackets is constant, say M, along the fibre. From the conservation-of-mass equation (4.111) we have

$$\frac{\mathrm{d}w}{\mathrm{d}z}=-\frac{w}{\rho A}\frac{\mathrm{d}}{\mathrm{d}z}\left(\rho A\right). \tag{4.117}$$

Substituting this expression into the conservation-of-momentum equation (4.116) gives

$$Re\rho A w^{2}+\frac{3w\mu}{\rho}\frac{\mathrm{d}}{\mathrm{d}z}\left(\rho A\right)-\frac{\mu w A}{\rho}\frac{\mathrm{d}}{\mathrm{d}z}-\frac{\Gamma^{*}S}{2}=M. \tag{4.118}$$

By noting that

$$3\frac{\mathrm{d}}{\mathrm{d}z}\left(\rho A\right)-A\frac{\mathrm{d}\rho}{\mathrm{d}z}=\frac{1}{\rho A^{2}}\frac{\mathrm{d}}{\mathrm{d}z}\left(\rho^{2}A^{3}\right), \tag{4.119}$$

equation (4.119) can be expressed in terms of a single derivative given by

$$\frac{\mu w}{\rho^2 A^2}\frac{\mathrm{d}}{\mathrm{d}z}\left(\rho^2 A^3\right) = M - Re\rho A w^2 + \frac{\Gamma^* S}{2}. \tag{4.120}$$

If we suppose that $S \to S_\infty$, $A \to A_\infty$, and $\rho \to \rho_\infty$ as $z \to \infty$, then the reduced steady-state system is given by

$$\rho w A = \mathcal{Q}, \tag{4.121}$$

$$w\frac{\mathrm{d}}{\mathrm{d}z}\left(\rho^2 A^3\right) = \Gamma^*\frac{\rho^2 A^2}{2\mu}\left(S - S_\infty\right) + Re\frac{\mathcal{Q}^2}{\mu}\left(\rho A - \rho_\infty A_\infty\right), \tag{4.122}$$

$$p = -\frac{\Gamma^*}{2}\sqrt{\frac{\pi}{A}} - \left(\frac{\lambda+\mu}{\rho}\right)\frac{\mathrm{d}}{\mathrm{d}z}(\rho w) + \lambda\frac{\mathrm{d}w}{\mathrm{d}z}, \tag{4.123}$$

$$\mathcal{F}\left(p, \rho, w, \frac{\mathrm{d}\rho}{\mathrm{d}z}\right) = 0, \tag{4.124}$$

where $\mathcal{Q}$ is the mass flow rate. We note that, for consistency, the values of S_∞, A_∞, ρ_∞, and w_∞ (the value of w as $z \to \infty$) are related by the conditions

$$Q = \rho_\infty w_\infty A_\infty, \qquad\qquad M = Re\rho_\infty A_\infty w_\infty^2 - \frac{\Gamma^* S_\infty}{2}.$$

We can understand the implications of the steady equations by interpreting them physically. The axial tension per unit length along the fluid is given by

$$\mathcal{T} = 3A\mu\frac{\mathrm{d}w}{\mathrm{d}z} + \frac{\mu A w}{\rho}\frac{\mathrm{d}\rho}{\mathrm{d}z}. \tag{4.125}$$

The classical "Trouton ratio" [76] in this case is 3 and can be seen in the coefficient of the derivative of the axial velocity. Using the relation

$$3\rho\frac{\mathrm{d}w}{\mathrm{d}z} + w\frac{\mathrm{d}\rho}{\mathrm{d}z} = \frac{1}{w^2}\frac{\mathrm{d}}{\mathrm{d}z}\left(w^3\rho\right), \tag{4.126}$$

we can express the tension as

$$\mathcal{T} = \frac{A\mu}{\rho w^2}\frac{\mathrm{d}}{\mathrm{d}z}\left(w^3\rho\right). \tag{4.127}$$

By eliminating w using equation (4.121) we arrive at an expression for the tension given by

$$\mathcal{T} = -\frac{\mathcal{Q}\mu}{\rho^3 A^3}\frac{\mathrm{d}}{\mathrm{d}z}\left(\rho^2 A^3\right). \tag{4.128}$$

The imposition of a steady solution for large distances, z, to arrive at equation (4.122) requires that there is no tension on the fibre. In this case, and for $Re \ll 1$ and $\Gamma^* \ll 1$, the conservation-of-momentum equation (4.122) can be integrated to give

$$\rho^2 A^3 = \mathcal{M}. \tag{4.129}$$

The resulting system in this parameter regime consists of two algebraic equations, (4.121) and (4.129) corresponding to conserved quantities; the pressure, given by

$$p = -\left(\frac{\lambda+\mu}{\rho}\right)\frac{\mathrm{d}}{\mathrm{d}z}(\rho w) + \lambda\frac{\mathrm{d}w}{\mathrm{d}z}; \tag{4.130}$$

and the, as yet unspecified, closure condition (4.124). Excluding the closure condition, the remaining equations can be reduced to a single ODE given by

$$\frac{\mathrm{d}\rho}{\mathrm{d}z} = -\frac{\mathcal{M}^{1/3}\rho^{4/3}p}{\mathcal{Q}(\lambda+2\mu/3)}. \tag{4.131}$$

The resulting reduced model for the density, pressure, velocity, and cross-sectional area consists of (4.121), (4.124), (4.129), and (4.131). We incorporate the pertinent microscale dynamics though (4.124). For example, as illustrated for the two-dimensional case in Section 4.1.3, the Rayleigh–Plesset equation (4.56) can be used to relate the pressure to the evolution of the density. In this case we must prescribe an appropriate constitutive law for the bubble pressure, for example (4.59) or one of the reduced models detailed in Chapter 3.

4.3 Cross-flow problem

The reduced model for the 3D flow of a compressible fluid in Section 4.2 was derived by supposing that the density is uniform in each cross-section of the fluid. Given the relationship between density and pressure (4.108), this reduced model is only valid in cases for which the pressure would also be uniform across the cross-section: when surface tension is negligible, or for an axisymmetric cross-section. Neither of these cases gives any insight into how the cross-sectional shape of the fluid will change, other than changes in the cross-sectional area. In this section we modify the pressure–density relationship to one in which density may remain uniform in each cross-section, even if the pressure is not. With this modification we can consider cases with non-negligible surface tension and non-axisymmetric cross-sectional shapes.

Rather than using (4.108), which assumes that the evolution of the density at some

point depends on the pressure at that point, we will instead assume that the evolution of the density depends on the cross-sectionally averaged pressure. Defining the cross-sectionally averaged pressure, $\bar{p}$, by

$$\bar{p} = \frac{1}{A} \iint_{\Omega} p \, \mathrm{d}x\mathrm{d}y, \tag{4.132}$$

we replace (4.108) by

$$\mathcal{F}(\rho, \bar{p}, \boldsymbol{u}, \nabla\rho) = 0. \tag{4.133}$$

With a closure of this form for a bubbly mixture, we are assuming that all of the bubbles throughout the cross-section evolve uniformly, despite the fact that the local pressure may vary.

To leading order in ϵ^2 we found p to be given by (4.106), which we used to impose a consistency condition on the Airy stress function, $\mathcal{A}$, given by (4.107). By instead integrating (4.106) over the cross-section, we can derive an expression for the averaged leading-order pressure, $\bar{p}$. Integrating (4.106), subject to boundary conditions (4.102b) for $\mathcal{A}$, and dividing both sides by A gives

$$\bar{p} = \frac{\Gamma^* S}{2A} - \frac{(\lambda + \mu)}{\rho} \left(\frac{\partial \rho}{\partial t} + \frac{\partial}{\partial z} (\rho w) \right) + \lambda \frac{\partial w}{\partial z}. \tag{4.134}$$

A key difference between this expression and (4.106) is that S must be known to calculate the pressure. In this case, the axial evolution of the fluid depends on the cross-sectional evolution. We will show, by using a methodology inspired by Cummings and Howell [17], that the cross-sectional shape evolution can be expressed independently of the axial evolution.

We found in (4.96), when ρ and w are independent of x and y, that we could express the conservation-of-mass equation as

$$\frac{\partial u}{\partial x} + \frac{\partial v}{\partial y} = J(z, t), \tag{4.135}$$

where, for notational convenience we have defined

$$J(z, t) := -\frac{1}{\rho} \left(\frac{\partial \rho}{\partial t} + \frac{\partial}{\partial z} (\rho w) \right). \tag{4.136}$$

If $J(z, t) = 0$, (4.135) describes conservation of mass for an incompressible fluid in 2D. This motivates introducing a transformation of u and v that eliminates the right-hand side of (4.135).

We define modified velocities $\bar{u}$ and $\bar{v}$ given by

$$\bar{u} = \Gamma^* u + \frac{x}{2} J(z,t), \qquad \text{and} \qquad \bar{v} = \Gamma^* v + \frac{y}{2} J(z,t), \tag{4.137a,b}$$

reducing the conservation-of-mass equation (4.135) to

$$\nabla_2 \cdot \bar{\boldsymbol{u}} = 0, \tag{4.138}$$

where $\bar{\boldsymbol{u}} = (\bar{u}, \bar{v})$, and the 2D gradient operator is defined by

$$\nabla_2 := \left(\frac{\partial}{\partial x}, \frac{\partial}{\partial y} \right). \tag{4.139}$$

Note that while $\bar{p}$ denotes the cross-sectionally averaged pressure, none of the other barred variables in this section refer to averaged quantities.

For an incompressible fluid $J(z,t) = \partial w^{(0)}/\partial z$, and the transformation given by (4.137) is the same as that of Cummings and Howell [17]. Substitution of the modified velocities into the conservation-of-momentum equations in the x and y direction, (4.79) and (4.80) respectively, yields

$$\Gamma^* \nabla_2^2 \bar{\boldsymbol{u}} = \nabla_2 \left(p - (\lambda + \mu) J(z,t) + \lambda \frac{\partial w}{\partial z} \right). \tag{4.140}$$

If we define an *effective pressure*, $\breve{p}$, by

$$\breve{p} = \frac{1}{\Gamma^*} \left(p - \lambda \nabla \cdot \boldsymbol{u} - \mu J(z,t) \right), \tag{4.141}$$

we can recast (4.140) into the form

$$\nabla_2^2 \bar{\boldsymbol{u}} = \nabla_2 \breve{p}, \tag{4.142}$$

which is equivalent to the conservation-of-momentum equations for an incompressible fluid.

The boundary conditions on $G(x,y,z,t) = 0$, previously given by (4.82)–(4.84), after applying transformation (4.137), are given by

$$\frac{\partial G}{\partial t} + \Gamma^* \bar{u} \frac{\partial G}{\partial x} + \Gamma^* \bar{v} \frac{\partial G}{\partial y} + w \frac{\partial G}{\partial z} = -\frac{1}{2} \left(x \frac{\partial G}{\partial x} + y \frac{\partial G}{\partial y} \right) J(z,t), \tag{4.143}$$

$$\left(-\breve{p} + 2\mu \frac{\partial \bar{u}}{\partial x} \right) \frac{\partial G}{\partial x} + \mu \left(\frac{\partial \bar{u}}{\partial y} + \frac{\partial \bar{v}}{\partial x} \right) \frac{\partial G}{\partial y} = -\varkappa \frac{\partial G}{\partial x}, \tag{4.144}$$

$$\mu \left(\frac{\partial \bar{u}}{\partial y} + \frac{\partial \bar{v}}{\partial x} \right) \frac{\partial G}{\partial x} + \left(-\breve{p} + 2\mu \frac{\partial \bar{v}}{\partial x} \right) \frac{\partial G}{\partial y} = -\varkappa \frac{\partial G}{\partial y}, \tag{4.145}$$

where $\partial G/\partial x$ and $\partial G/\partial y$ are the components of the unit normal vector in the x and y directions respectively.

Consider the Lagrangian coordinate transformation given by

$$t = \bar{t}, \qquad x = \sqrt{A}\bar{x}, \qquad y = \sqrt{A}\bar{y}, \qquad z = Z(\bar{z}, \bar{t}). \tag{4.146a,b,c,d}$$

where

$$\frac{\partial Z}{\partial \bar{t}} = w \qquad \text{and} \qquad Z(\bar{z}, 0) = \bar{z}. \tag{4.147a,b}$$

We also consider rescaling $\breve{p}$ to $\tilde{p}$ given by

$$\tilde{p} = \sqrt{A}\breve{p}. \tag{4.148}$$

The conservation-of-mass and conservation-of-momentum equations, (4.138) and (4.142) respectively, are transformed to

$$\overline{\nabla} \cdot \bar{\boldsymbol{u}} = 0, \qquad \text{and} \qquad \overline{\nabla}_2^2 \bar{\boldsymbol{u}} = \overline{\nabla}_2 \tilde{p}, \tag{4.149a,b}$$

where $\overline{\nabla}_2$ is the 2D gradient operator with respect to $(\bar{x}, \bar{y})$ coordinates, defined by

$$\overline{\nabla}_2 := \left(\frac{\partial}{\partial \bar{x}}, \frac{\partial}{\partial \bar{y}} \right), \tag{4.150}$$

and the dynamic boundary conditions (4.144) and (4.145) are given by

$$\left(-\tilde{p} + 2\mu \frac{\partial \bar{u}}{\partial \bar{x}} \right) \frac{\partial G}{\partial \bar{x}} + \mu \left(\frac{\partial \bar{u}}{\partial \bar{y}} + \frac{\partial \bar{v}}{\partial \bar{x}} \right) \frac{\partial G}{\partial \bar{y}} = -\varkappa \frac{\partial G}{\partial \bar{x}}, \tag{4.151}$$

$$\mu \left(\frac{\partial \bar{u}}{\partial \bar{y}} + \frac{\partial \bar{v}}{\partial \bar{x}} \right) \frac{\partial G}{\partial \bar{x}} + \left(-\tilde{p} + 2\mu \frac{\partial \bar{v}}{\partial \bar{x}} \right) \frac{\partial G}{\partial \bar{y}} = -\varkappa \frac{\partial G}{\partial \bar{y}}. \tag{4.152}$$

When the transformation given by (4.137) is applied to the kinematic boundary condition (4.143), we find

$$0 = \frac{\partial G}{\partial \bar{t}} + \left(\frac{\Gamma^* \bar{u}}{\sqrt{A}} + \frac{\bar{x}}{2A} \left(AJ - \frac{\partial A}{\partial \bar{t}} \right) \right) \frac{\partial G}{\partial \bar{x}} + \left(\frac{\Gamma^* \bar{v}}{\sqrt{A}} + \frac{\bar{y}}{2A} \left(AJ - \frac{\partial A}{\partial \bar{t}} \right) \right) \frac{\partial G}{\partial \bar{y}}. \tag{4.153}$$

After coordinate transformation (4.146), the conservation-of-mass equation (4.111) is given by

$$\frac{\partial}{\partial \bar{t}} (\rho A) - \frac{\bar{x}}{2} \frac{\partial A}{\partial \bar{t}} \frac{\partial \rho}{\partial \bar{x}} - \frac{\bar{y}}{2} \frac{\partial A}{\partial \bar{t}} \frac{\partial \rho}{\partial \bar{y}} + \rho A \frac{\partial w}{\partial z} = 0, \tag{4.154}$$

and $\bar{J}(\bar{z},\bar{t}) = J(z,t)$ is given by

$$\bar{J}(\bar{z},\bar{t}) = -\frac{1}{\rho}\left(\frac{\partial\rho}{\partial\bar{t}} - \frac{\bar{x}}{2A}\frac{\partial A}{\partial\bar{t}}\frac{\partial\rho}{\partial\bar{x}} - \frac{\bar{y}}{2A}\frac{\partial A}{\partial\bar{t}}\frac{\partial\rho}{\partial\bar{y}} + \rho\frac{\partial w}{\partial\bar{z}}\right). \tag{4.155}$$

We can show using (4.154) and (4.155) that

$$A\bar{J} - \frac{\partial A}{\partial\bar{t}} = 0; \tag{4.156}$$

thus, the kinematic boundary condition, (4.153), reduces to

$$\frac{\sqrt{A}}{\Gamma^*}\frac{\partial G}{\partial\bar{t}} + \bar{u}\frac{\partial G}{\partial\bar{x}} + \bar{v}\frac{\partial G}{\partial\bar{y}} = 0. \tag{4.157}$$

We are effectively left with Stokes equations (4.149*a*,*b*) with dynamic boundary conditions (4.151) and (4.152), and kinematic boundary condition (4.157); the latter containing the only time derivative in the system. By introducing a *reduced time*, τ, given by

$$\tau = \int_0^{\bar{t}} \frac{\Gamma^*}{\sqrt{A}}\,\mathrm{d}s, \tag{4.158}$$

we arrive at a system that is independent of the axial evolution. The resulting system for the flow in the cross-section can be solved independently of the axial-flow problem; however, the axial-flow problem depends on the solution to the cross-flow problem.

In the modified domain $\bar{\Omega}$, whose boundary is defined by $\bar{G}(\bar{x},\bar{y},\tau) = 0$, the equations governing the cross-flow problem are given by

$$\overline{\nabla}_2 \cdot \bar{\boldsymbol{u}} = 0, \tag{4.159}$$

$$\overline{\nabla}_2^2\bar{\boldsymbol{u}} = \overline{\nabla}_2\tilde{p}, \tag{4.160}$$

with boundary conditions on $\bar{G}(\bar{x},\bar{y},\tau) = 0$ given by

$$\frac{\partial\bar{G}}{\partial\tau} + \bar{u}\frac{\partial\bar{G}}{\partial\bar{x}} + \bar{v}\frac{\partial\bar{G}}{\partial\bar{y}} = 0, \tag{4.161}$$

$$\left(-\tilde{p} + 2\mu\frac{\partial\bar{u}}{\partial\bar{x}}\right)\frac{\partial\bar{G}}{\partial\bar{x}} + \mu\left(\frac{\partial\bar{u}}{\partial\bar{y}} + \frac{\partial\bar{v}}{\partial\bar{x}}\right)\frac{\partial\bar{G}}{\partial\bar{y}} = -\varkappa\frac{\partial\bar{G}}{\partial\bar{x}}, \tag{4.162}$$

$$\mu\left(\frac{\partial\bar{u}}{\partial\bar{y}} + \frac{\partial\bar{v}}{\partial\bar{x}}\right)\frac{\partial\bar{G}}{\partial\bar{x}} + \left(-\tilde{p} + 2\mu\frac{\partial\bar{v}}{\partial\bar{y}}\right)\frac{\partial\bar{G}}{\partial\bar{y}} = -\varkappa\frac{\partial\bar{G}}{\partial\bar{y}}. \tag{4.163}$$

The necessary initial condition for this system is the initial die shape, which is given by $\bar{G}(\bar{x}, \bar{y}, 0) = 0$. This system is equivalent to the equations of Stokes flow in 2D describing the dynamics of a 2D blob of fluid under the action of unit surface tension. This cross-flow problem is the same as that obtained for an incompressible fluid by Cummings and Howell [17]. This system has two useful features: it is parameter independent and can be solved independently of the macroscale model. This means that this 2D problem can be solved once, for a given initial boundary profile, and the same results are valid for all parameters and initial conditions for the axial-flow model.

4.3.1 The coupled cross-flow/axial system

In this section we describe the coupling between the 2D cross-flow problem, given by equations (4.159)–(4.163), and the axial-flow problem. The axial-flow model, with the modified constitutive law introduced by (4.133), comprises the conservation-of-mass equation given by (4.111), conservation-of-momentum given by (4.112), and the averaged pressure given by (4.134). In addition, to solve the axial-flow problem we must determine the map between τ and $\bar{t}$ given by (4.158) in order to determine $S(\tau(z, \bar{t}))$. By solving both the 2D cross-flow problem and the 1D axial-flow problem, we can generate the 3D surface for an extruded compressible flow.

To solve this coupled system efficiently, consider the flow of information between models, which we illustrate in figure 4.6. In addition, consider the time-steady behaviour of the axial model, just as we did in Section 4.2.1. Instead of solving for the map between τ and $\bar{t}$, (4.158) can be cast as a map between τ and z using $(4.146d)$ and $(4.147a)$ giving

$$\tau = \int_0^z \frac{\Gamma^*}{w\sqrt{A}}\,\mathrm{d}s. \tag{4.164}$$

Solving the 2D cross-flow problem only requires the die shape. The output of this model is the shape of the boundary and its perimeter in $(\bar{x}, \bar{y}, \tau)$ coordinates. This problem need only be solved once for a given die shape. The arc-length perimeter influences the dynamics of the axial-flow problem; so this, and also the necessary

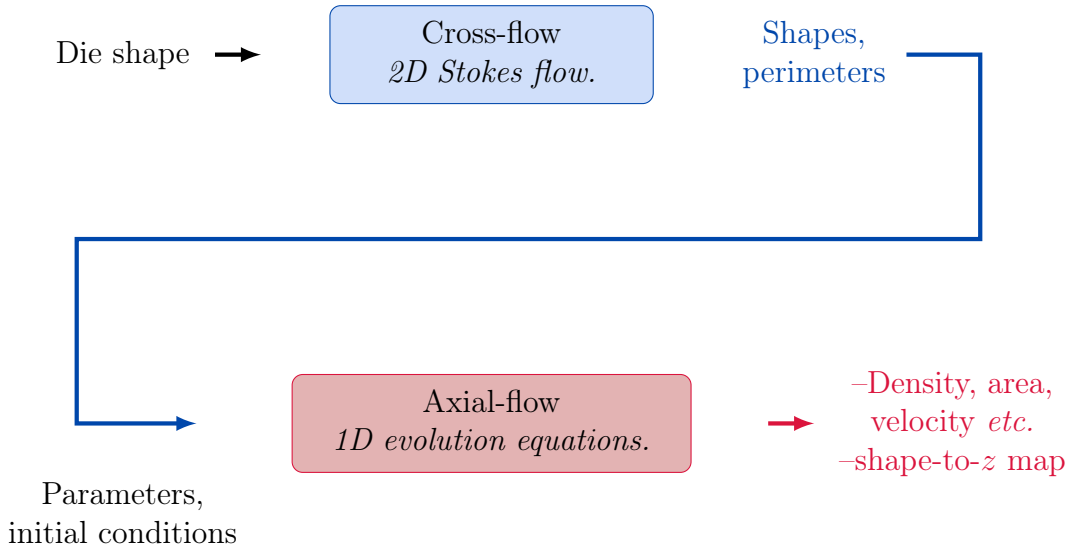

Figure 4.6: *A schematic of the flow of information when solving the 2D cross-flow problem and the 1D axial-flow problem.*

parameters and initial conditions, must be incorporated into the axial-flow model. Solving the axial-flow problem returns the density, cross-sectional area, and velocity along the axis of flow, as well as the map between τ and z. The τ–z map can be used to map the cross-section at time τ from the cross-flow model, to the axial position z, and hence to build a 3D profile of the extruded fluid.

4.3.2 Finding solutions

In this section we describe a procedure for finding solutions to the coupled 2D cross-flow problem and 1D axial-flow problem described in Section 4.3.1. The cross-flow problem (4.159)–(4.163) is a free-boundary problem; the boundary evolves in τ according to the kinematic boundary condition (4.161). We discretise the time derivative in (4.161) using a first-order forward-difference approximation. Suppose that the boundary at time $\tau^i = i\Delta\tau$, where i is a positive integer and $\Delta\tau$ is the time-step, is given by $\bar{G}^i(\bar{x}, \bar{y}) = 0$. The time-discretised kinematic boundary condition gives

$$\bar{G}^{i+1} = \bar{G}^i + \Delta\tau \left(\bar{u}^i \left(\frac{\partial \bar{G}}{\partial x} \right)^i + \bar{v}^i \left(\frac{\partial \bar{G}}{\partial y} \right)^i \right), \tag{4.165}$$

where $\bar{u}^i$ and $\bar{v}^i$ are the $\bar{x}$ and $\bar{y}$ velocity components at time τ^i respectively, and $\bar{G}^0$ is the initial cross-section shape. Using (4.165), we can construct an iterative method

for solving the reduced-time-dependent cross-flow problem. At each time-step, we solve the equations of Stokes flow for a prescribed $\bar{G}^i$, without the kinematic boundary condition (4.161); that is, we solve equations (4.159) and (4.160) on the domain bounded by $\bar{G}^i = 0$, with boundary conditions (4.162) and (4.163). The equation parametrising the boundary is then updated using (4.165).

We use a mixed finite element approach—guided by Süli [69], and Brenner and Scott [15]—to solve the Stokes-flow problem given by (4.159) and (4.160), with boundary conditions (4.162) and (4.163). Taking the dot product of (4.159) with a sufficiently smooth, two-component vector function $\boldsymbol{g}$, integrating the result over $\bar{\Omega}$, and then integrating by parts subject to (4.162) and (4.163), yields

$$\iint_{\bar{\Omega}} -\mu \nabla \boldsymbol{g} : \nabla \bar{\boldsymbol{u}} + \tilde{p} \nabla \cdot \boldsymbol{g} \, \mathrm{d}\bar{x} \mathrm{d}\bar{y} = \oint_{\partial \bar{\Omega}} \varkappa \boldsymbol{g} \cdot \bar{\boldsymbol{n}} \, \mathrm{d}\bar{s}, \tag{4.166}$$

where $\bar{\boldsymbol{n}}$ is the outward pointing unit normal to the boundary $\partial\bar{\Omega}$. Multiplying (4.159) by a sufficiently smooth function q, and integrating over $\bar{\Omega}$ yields

$$\iint_{\bar{\Omega}} q \nabla \cdot \bar{\boldsymbol{u}} \, \mathrm{d}\bar{x} \mathrm{d}\bar{y} = 0. \tag{4.167}$$

Let $H^1(\bar{\Omega})$ denote the space of square-integrable functions with square-integrable derivatives. We define the function space $\boldsymbol{V} := H^1(\bar{\Omega}) \times H^1(\bar{\Omega})$, and Q to be the space of square-integrable functions on $\bar{\Omega}$. The weak formulation of this system involves finding $(\bar{\boldsymbol{u}}, p) \in \boldsymbol{V} \times Q$ such that

$$\iint_{\bar{\Omega}} -\mu \nabla \boldsymbol{g} : \nabla \bar{\boldsymbol{u}} + \tilde{p} \nabla \cdot \boldsymbol{g} + q \nabla \cdot \bar{\boldsymbol{u}} \, \mathrm{d}\bar{x} \mathrm{d}\bar{y} = \oint_{\partial \bar{\Omega}} \varkappa \boldsymbol{g} \cdot \bar{\boldsymbol{n}} \, \mathrm{d}\bar{s}, \tag{4.168}$$

for all $\boldsymbol{g} \in \boldsymbol{V}$ and $q \in Q$. By supposing that $\boldsymbol{V}_h \subset \boldsymbol{V}$ and $Q_h \subset Q$, a discrete approximation to (4.168) is finding $\bar{\boldsymbol{u}}_h \in \boldsymbol{V}_h$ and $\tilde{p}_h \in Q_h$ such that

$$\iint_{\bar{\Omega}} -\mu \nabla \boldsymbol{g}_h : \nabla \bar{\boldsymbol{u}}_h + \tilde{p}_h \nabla \cdot \boldsymbol{g}_h + q_h \nabla \cdot \bar{\boldsymbol{u}}_h \, \mathrm{d}\bar{x} \mathrm{d}\bar{y} = \oint_{\partial \bar{\Omega}} \varkappa \boldsymbol{g}_h \cdot \bar{\boldsymbol{n}}_h \, \mathrm{d}\bar{s}, \tag{4.169}$$

for all $\boldsymbol{g}_h \in \boldsymbol{V}_h$ and $q_h \in Q_h$, where $\bar{\boldsymbol{n}}_h$ is the discrete approximation to $\bar{\boldsymbol{n}}$. We use the Taylor–Hood element, where $\boldsymbol{V}_h$ is a vector function space of piecewise continuous quadratics and Q_h is a function space of continuous piecewise linear functions.

We only consider discrete representations of $\bar{G}$; so, we must construct good approximations to the curvature $\varkappa$ and surface normals. A discrete representation of $\bar{G}^i$ is given by the set of n points $\bar{\boldsymbol{x}}^i_j = (\bar{x}^i_j, \bar{y}^i_j)$, where $j = 1, 2, ..., n$. These points may, for

example, constitute the boundary nodes of a mesh. To approximate the curvature of the boundary, for each node we find the circle of best fit for the node itself and its neighbouring points. The radius of this circle is an approximation to the local radius of curvature of the surface. The displacement between the node and the centre of this circle can be normalised to give an approximation for $\bar{\boldsymbol{n}}$.

The Stokes-flow problem given by (4.159) and (4.160), with boundary conditions (4.162) and (4.163), does not have a unique solution. Given a solution with velocity $\bar{\boldsymbol{u}}$, we can add an arbitrary constant vector to the velocity, and the result will also be a solution. By symmetry, we are interested in the solution with zero net velocity; that is

$$\int_{\bar{\Omega}} \bar{\boldsymbol{u}} \, \mathrm{d}\bar{x}\mathrm{d}\bar{y} = \boldsymbol{0}. \tag{4.170}$$

We enforce this constraint weakly using Lagrange multipliers. We must also impose the constraint of no rotation; however, in our simulations we only consider initial data that is symmetric in the y-axis so this constraint is automatically satisfied. We modify the weak formulation so that we also find $\boldsymbol{\lambda} \in \mathbb{R}^2$ such that

$$\iint_{\bar{\Omega}} -\mu \nabla \boldsymbol{g}_h : \nabla \bar{\boldsymbol{u}}_h + \tilde{p}_h \nabla \cdot \boldsymbol{g}_h + q_h \nabla \cdot \bar{\boldsymbol{u}}_h + \boldsymbol{\lambda} \cdot \boldsymbol{g}_h + \hat{\boldsymbol{\lambda}} \cdot \bar{\boldsymbol{u}}_h \, \mathrm{d}\bar{x}\mathrm{d}\bar{y} = \oint_{\partial\bar{\Omega}} \varkappa \boldsymbol{g}_h \cdot \bar{\boldsymbol{n}}_h \, \mathrm{d}s, \tag{4.171}$$

for all $\hat{\boldsymbol{\lambda}} \in \mathbb{R}^2$.

For each $\bar{G}^i$ we can determine the corresponding perimeter in $(\bar{x}, \bar{y})$ coordinates, given by

$$\bar{S}^i = \oint \mathrm{d}\bar{s} = \oint \left(\mathrm{d}\bar{x}^2 + \mathrm{d}\bar{y}^2\right)^{1/2} \approx \sum_{j=1}^{n} \left(\left(\Delta \bar{x}_j^i\right)^2 + \left(\Delta \bar{y}_j^i\right)^2 \right)^{1/2}, \tag{4.172}$$

where $\Delta \bar{x}_j^i = \bar{x}_{j+1}^i - \bar{x}_j^i$ and $\Delta \bar{y}_j^i = \bar{y}_{j+1}^i - \bar{y}_j^i$ are the $\bar{x}$ and $\bar{y}$ displacements between neighbouring boundary points, and we define $\bar{\boldsymbol{x}}_{n+1}^i = \bar{\boldsymbol{x}}_1^i$.

The time-steady axial system comprises the conservation-of-mass equation (4.121), the conservation-of-axial-momentum equation (4.122), the cross-sectionally averaged pressure equation (4.134), the modified microscale closure (4.133), and the τ–z map (4.164). Given that we know the perimeter, $\bar{S}$, calculated in $(\bar{x}, \bar{y})$ coordinates, the perimeter, S^i, in (x, y) coordinates, at $\tau = i\Delta\tau$ is given by

$$S^i = \sqrt{A}\bar{S}^i. \tag{4.173}$$

We interpolate the set of perimeters, S^i, to give a continuous representation of S as a function of τ, allowing for arbitrary z steps to be used when solving the axial model. By solving the axial model, we determine, as functions of the axial position z, the density, ρ; the area, A; the axial velocity, w; the averaged pressure, $\bar{p}$; and the reduced time, τ.

4.3.3 An illustrative example

In this section we present an illustrative example using the method described in Section 4.3.2, following the flow of information depicted in figure 4.6. With the initial die shape, we can solve the 2D Stokes-flow problem independently of the rest of the system. Note that when we derived the reduced axial model, we restricted our attention to cross-sections that are symmetric with respect to both the x and y axis; however, for this illustrative example we use a more industrially relevant cross-section shape.

The boundaries corresponding to a number of values of τ are shown in figure 4.7a. In this case, the initial boundary shape is illustrated by the solid blue line, and contains some sharp features. As τ advances, the sharp features of this shape smooth out, and for long τ we are left with a circle, illustrated by the solid red line.

With the perimeter for each shape given by (4.172) and (4.173), we can solve the axial-flow model. A key output of the axial-flow model indicating how the shape evolves along the z-axis is $\tau(z)$, which is illustrated in figure 4.7b. Faster evolution of τ corresponds to more rapid shape change. In this case we can see more rapid evolution for smaller z values, followed by steady growth in τ further from the origin.

The evolution of the axial variables: A, ρ, and w, contributes to the change in τ, and therefore the amount of shape change, through (4.164). To prevent shape change, w or A must be large; this slows the evolution of τ. A simple principle by which this can be enacted is to promote as much bubble growth as possible, as early as possible; thereby decreasing the density and increasing both the flow speed and cross-sectional area. An increase in bubble radius, as illustrated in figure 4.8a, reduces the density of the mixture, illustrated in figure 4.8b, and increases the area and velocity of the mixture, illustrated in figures 4.8c and 4.8d respectively.

With a solution to both the 2D cross-flow problem, and the axial-flow problem, we

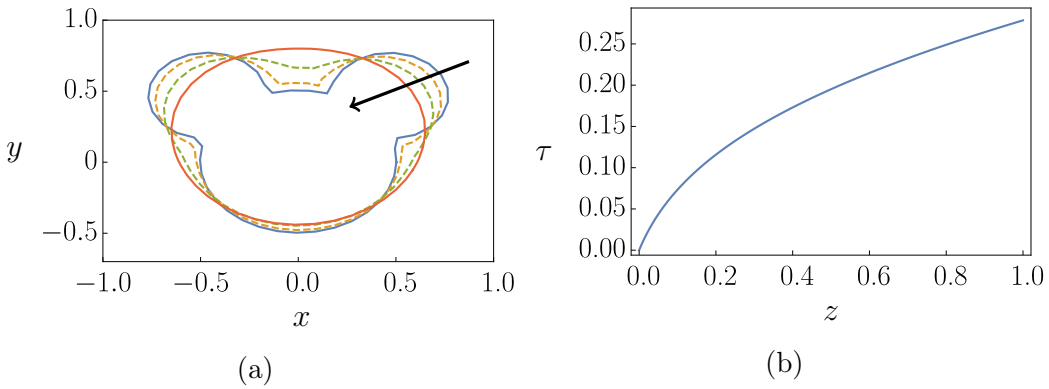

Figure 4.7: (a) *Evolution of a cross-section initially taking the shape of the solid blue line, and some time later taking the shape of the solid red line. The arrow indicates increasing* τ. (b) *The value of the reduced time* τ *along the* z *axis for* $\Gamma^* = 1.5$, $C = 150$, $\rho(0) = 0.75$, $w(0) = 1$, $A(0) = \pi$, *and* $\hat{R}(0) = 1$*; all other parameters are those contained in tables 2.2 and 2.3.*

can construct a 3D representation of the surface of the fluid. We map each cross-section, given at τ, to its corresponding position on the z axis, given by the map from z to τ described by (4.164). Additionally, we must re-scale the $\bar{x}$ and $\bar{y}$ coordinates using (4.146b) and (4.146c) to give the cross-section boundary in (x, y) coordinates. The result is illustrated in figure 4.8e. A representation such as the one depicted in figure 4.8e highlights the geometric changes undergone by the product: the change in area of the cross-section, and the smoothing out of the sharper features from the initial cross-section.

4.4 Temperature-dependent viscosity

We have until now assumed that changes in the macroscale temperature have no impact on the microscale or macroscale dynamics. We have therefore not discussed the equation of conservation of energy. If there is substantial cooling, this will change the dynamics of the system. Conservation of energy on the macroscale is described by (2.64). Based on the value of $\mathcal{V}$ in table 2.2, we expect the source term corresponding to viscous heating and work associated with expansion to be negligible. In addition, the macroscopic Péclet number for heat transport, Pe_T is large, so we expect temperature variation to be confined to boundary layers near the surface of the fluid. So, based on the model presented in Chapter 2, we do not expect the macroscale temperature to change appreciably. In this section, we consider modifying the microscale–macroscale coupling to allow for heat consumed on the microscale

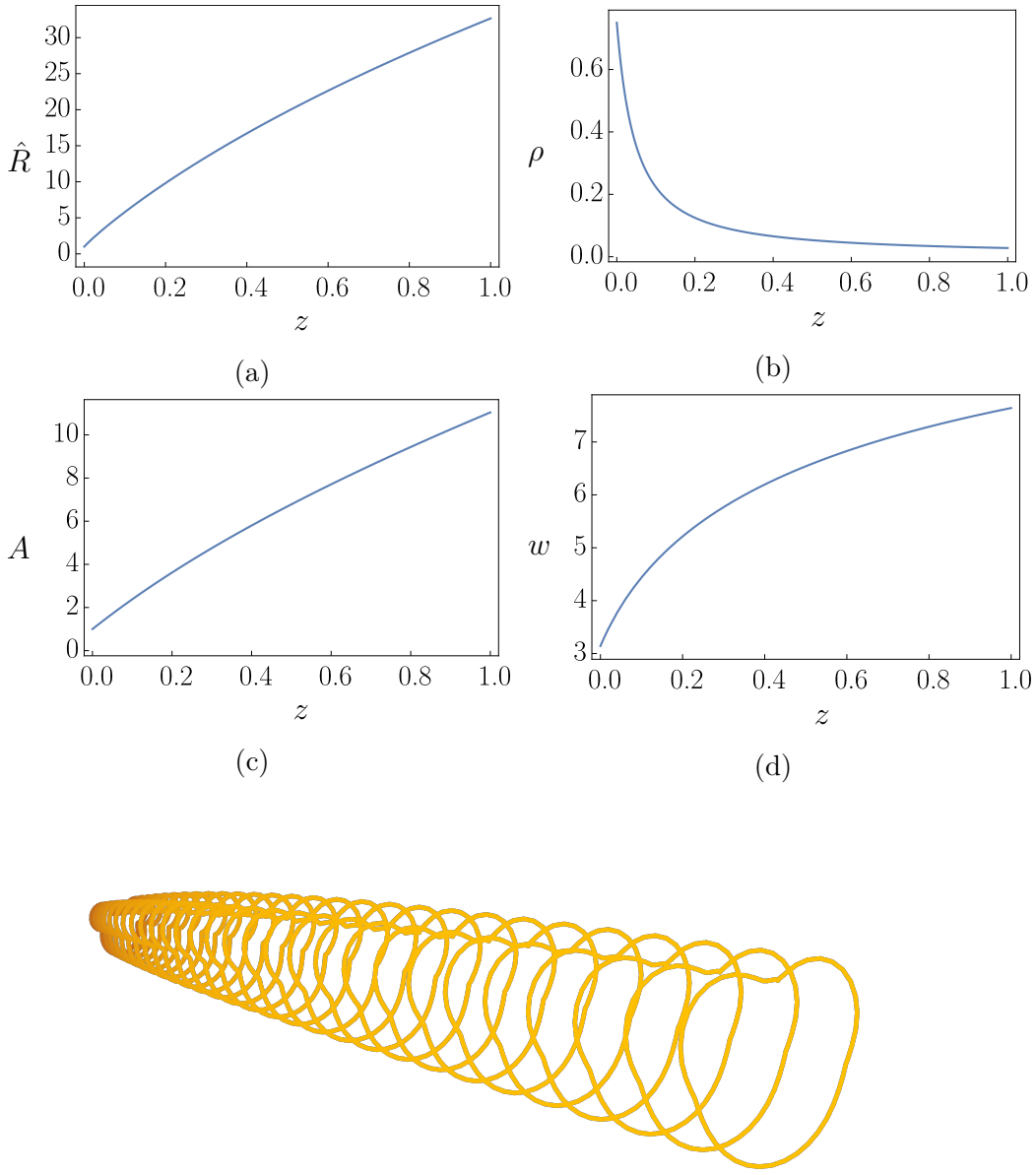

Figure 4.8: *The value of* (a) R, (b) ρ, (c) A, *and* (d) w *along the* z *axis for* $\Gamma^* = 1.5$, $C = 150$, $\rho(0) = 0.75$, $w(0) = 1$, $A(0) = \pi$, *and* $\hat{R}(0) = 1$; *all other parameters are those contained in tables 2.2 and 2.3.* (e) *A 3D reconstruction of the fluid surface combining the solution to the 2D cross-flow model and the 1D axial-flow model.*

to affect the macroscale and vice versa.

Given the nature of the microscale–macroscale coupling we consider, it is not consistent to couple a changing macroscopic temperature to the microscale through the far-field behaviour of the microscale temperature. This is because the microscale problem is time dependent, so disturbances made to the temperature far from the bubble take time to propagate to the bubble. In Chapter 3 we considered two cases in which the microscale model was diffusion dominated, and we neglect the time-derivatives in the microscale heat equation; these were Cases I and II. For either of these cases, we propose a heat sink term in the macroscale conservation-of-energy equation corresponding to total heat flux in the microscale model from the far-field (*i.e.* far from the bubble) towards the bubble. The heat flux across a sphere containing the bubble is independent of its radius when heat transfer is diffusion dominated, so we can describe the heat sink corresponding to a single bubble by the dimensionless total heat flux at the bubble interface, given by

$$q_T = 4\pi \hat{R}^2 \frac{\partial \hat{T}}{\partial \hat{r}}, \tag{4.174}$$

where $\hat{T}$ is the microscale temperature, and $\hat{r}$ is the microscale radial coordinate. Given this sink term only applies to the diffusion-dominated Cases I and II, we can use the Neumann-to-Dirichlet maps derived in Sections 3.3.1 and 3.3.2, given by (3.49*b*) and (3.59), to express the temperature gradients in terms of the bubble temperature, and hence the total heat flux corresponding to a single bubble is given by

$$q_T = -4\pi \hat{R} \hat{T}_{\mathrm{B}}. \tag{4.175}$$

Given that there are η bubbles per unit volume of liquid at any given point in our mixture, the heat-sink term corresponding to microscale heat consumption, Q_T, is given by

$$Q_T = \eta q_T. \tag{4.176}$$

Another interpretation for Q_T is that it represents an interfacial heat source term at the liquid–gas boundary. This corresponds to the energy from the liquid that goes into the latent heat required to vapourise the moisture.

Consider the heat equation given by (2.64). Neglecting the contribution of the viscous dissipation terms, and incorporating a microscale heat sink given by (4.176), gives the

dimensionless conservation-of-energy equation (in the domain bounded by the surface at $G(x,y,z,t)=0$)

$$\frac{\partial}{\partial t}\left(\rho c_v T\right)+\nabla\cdot\left(\rho c_v T\boldsymbol{u}\right)=\frac{1}{Pe_T}\nabla\cdot\left(k\nabla T\right)+Qq_T, \tag{4.177}$$

where Q a dimensionless quantity related to the temperature change induced by loss of heat from the macroscale to the microscale, and is given by

$$Q=\frac{\hat{R}_0\eta\mathcal{L}c_0D_l}{\mathcal{T}M(c_v)_l}. \tag{4.178}$$

The dimensional terms that comprise Q can be found in table 2.1. Re-scaling according to (4.69), gives

$$\begin{aligned}\frac{\partial}{\partial t}\left(\rho c_v T\right)+\frac{\partial}{\partial x}\left(\rho c_v Tu\right)+\frac{\partial}{\partial y}\left(\rho c_v Tv\right)+\frac{\partial}{\partial z}\left(\rho c_v Tw\right)&\\ =\frac{1}{Pe_T\epsilon^2}\left(\frac{\partial}{\partial x}\left(k\frac{\partial T}{\partial x}\right)+\frac{\partial}{\partial y}\left(k\frac{\partial T}{\partial y}\right)\right)+\frac{1}{Pe_T}\frac{\partial}{\partial z}\left(k\frac{\partial T}{\partial z}\right)+Qq_T.&\end{aligned} \tag{4.179}$$

The dimensionless boundary condition on $G(x,y,z,t)=0$ is given by

$$\begin{aligned}\left(\left(\frac{\partial G}{\partial x}\right)^2+\left(\frac{\partial G}{\partial y}\right)^2+\epsilon^2\left(\frac{\partial G}{\partial z}\right)^2\right)^{-1/2}\left(\frac{1}{\epsilon^2}\left(\frac{\partial G}{\partial x}\frac{\partial T}{\partial x}+\frac{\partial G}{\partial y}\frac{\partial T}{\partial y}\right)+\frac{\partial G}{\partial z}\frac{\partial T}{\partial z}\right)&\\ =\mathcal{H}^*\left(T+1\right),&\end{aligned} \tag{4.180}$$

where $\mathcal{H}^*=\mathcal{H}/\epsilon$, and we suppose that $\mathcal{H}^*$ is of order unity.

Expanding T in powers of ϵ^2 gives, at leading order,

$$\frac{\partial}{\partial x}\left(k\frac{\partial T^{(0)}}{\partial x}\right)+\frac{\partial}{\partial y}\left(k\frac{\partial T^{(0)}}{\partial y}\right)=0, \tag{4.181}$$

with boundary condition given by

$$\frac{\partial G^{(0)}}{\partial x}\frac{\partial T^{(0)}}{\partial x}+\frac{\partial G^{(0)}}{\partial y}\frac{\partial T^{(0)}}{\partial y}=0. \tag{4.182}$$

If k is positive, (4.181) and (4.182) imply that $T^{(0)}$ is also independent of x and y.

At $\mathcal{O}(\epsilon^2)$, the heat equation is given by

$$\begin{aligned}\frac{\partial}{\partial t}\left(\rho^{(0)}c_vT^{(0)}\right)+\frac{\partial}{\partial x}\left(\rho^{(0)}c_vT^{(0)}u^{(0)}\right)+\frac{\partial}{\partial y}\left(\rho^{(0)}c_vT^{(0)}v^{(0)}\right)+\frac{\partial}{\partial z}\left(\rho^{(0)}c_vT^{(0)}w^{(0)}\right)&\\ =\frac{1}{Pe_T}\left(\frac{\partial}{\partial x}\left(k\frac{\partial T^{(1)}}{\partial x}\right)+\frac{\partial}{\partial y}\left(k\frac{\partial T^{(1)}}{\partial y}\right)\right)+\frac{1}{Pe_T}\frac{\partial}{\partial z}\left(k\frac{\partial T^{(0)}}{\partial z}\right)+Qq_T,&\end{aligned} \tag{4.183}$$

with boundary condition given by

$$\frac{1}{|\nabla_2 G^{(0)}|}\left(\frac{\partial G^{(0)}}{\partial x}\frac{\partial T^{(1)}}{\partial x}+\frac{\partial G^{(0)}}{\partial y}\frac{\partial T^{(1)}}{\partial y}+\frac{\partial G^{(0)}}{\partial z}\frac{\partial T^{(0)}}{\partial z}\right)=\mathcal{H}^*\left(T^{(0)}+1\right), \qquad (4.184)$$

where $|\nabla_2 G^{(0)}| = \left((\partial G^{(0)}/\partial x)^2 + (\partial G^{(0)}/\partial y)^2\right)^{1/2}$. Given we have assumed that the density is uniform over the cross-section, and therefore that the bubble dynamics are uniform over the cross-section, we assume that Q_T is uniform across the cross-section.

Just as in Section 4.2, we integrate the governing equation (4.183) over the cross-section, subject to the kinematic boundary condition (4.82), which gives

$$\frac{\partial}{\partial t}\left(\rho^{(0)}c_v T^{(0)}A^{(0)}\right)+\frac{\partial}{\partial z}\left(\rho^{(0)}c_v T^{(0)}A^{(0)}w^{(0)}\right)=QA^{(0)}q_T + \oint_{\Omega^{(0)}}\frac{1}{Pe_T|\nabla_2 G^{(0)}|}\left(\frac{\partial T^{(1)}}{\partial x}\frac{\partial G^{(0)}}{\partial x}+\frac{\partial T^{(1)}}{\partial z}\frac{\partial G^{(0)}}{\partial y}+\frac{\partial T^{(0)}}{\partial z}\frac{\partial G^{(0)}}{\partial z}\right)\mathrm{d}s. \qquad (4.185)$$

Imposing the heat-flux boundary condition (4.184), we can evaluate the integral in (4.185), providing the contribution of heat transfer at the boundary to the change in temperature of the fluid. The reduced conservation-of-energy equation is given by

$$\frac{\partial}{\partial t}\left(\rho^{(0)}c_v T^{(0)}A^{(0)}\right)+\frac{\partial}{\partial z}\left(\rho^{(0)}c_v T^{(0)}A^{(0)}w^{(0)}\right)=\frac{S^{(0)}\mathcal{H}^*}{Pe_T}\left(T^{(0)}+1\right)+QA^{(0)}q_T. \qquad (4.186)$$

For simplicity, given that we expect Pe_T to be large (see table 2.2), we will neglect the first term on the right-hand side of (4.186) for the remainder of this section.

The reduced conservation-of-energy equation, (4.186), was derived by assuming that $\epsilon^2 Pe_T \ll 1$ and $Pe_T \gg 1$. While this is not the distinguished limit of this problem, which occurs for $\epsilon^2 Pe_T$ of order unity, this is the appropriate regime to capture the long–thin limit, in which $\epsilon \to 0$ whilePe_T remains fixed. For values of ϵ that we might expect in practice, which we discuss in Section 3.3 of Chapter 3, the product $\epsilon^2 Pe_T$ may be large as $Pe_T \gg \epsilon^{-2}$.

If the macroscale temperature varies, we must modify parts of the microscale model to account for this. When we non-dimensionalised the microscale model in Section 2.6, we supposed that

$$\hat{T} = T_0 + \frac{\mathcal{L}D_l\rho_l c_0}{Mk}\hat{T}', \qquad (4.187)$$

where T_0 is the initial temperature of the product. We now instead suppose that

$$\hat{T} = T_0 + \mathcal{T}T + \frac{\mathcal{L}D_l\rho_l c_0}{Mk}\hat{T}', \tag{4.188}$$

where T is the macroscale temperature. In effect, $\hat{T}'$ represents the temperature difference between the microscale and macroscale; far from the bubble, the temperature is that of the macroscale. If we consider the reduced microscale model corresponding to case II presented in Section 3.3.2.1—the reduced model most relevant for extrusion—the modifications required to account for this new microscale–macroscale coupling include modifying the thermodynamic equilibrium condition such that (3.118) is given by

$$\frac{\mathrm{d}\hat{R}}{\mathrm{d}\hat{t}} = \frac{\hat{R}}{4}\left(\frac{\bar{P}}{\Sigma}\exp\left(\Lambda\left(1 - \frac{1}{1 + \mathcal{T}T/T_0 + \Theta\hat{T}_\mathrm{B}}\right)\right) - p - p_\mathrm{atm} - \frac{\Gamma}{\hat{R}}\right), \tag{4.189}$$

and (3.79) is given by

$$\exp\left(\Lambda\left(1 - \frac{1}{1 + \mathcal{T}T/T_0 + \Theta\hat{T}_\mathrm{B}}\right)\right) = \frac{(1 + \Sigma\hat{N}_\mathrm{B})(1 + \mathcal{T}T/T_0 + \Theta\hat{T}_\mathrm{B})}{\hat{R}^3}; \tag{4.190}$$

and modifying the bubble pressure (3.80) to

$$\hat{p}_\mathrm{B} = \frac{(\Sigma^{-1} + \hat{N}_\mathrm{B})(1 + \mathcal{T}T/T_0 + \Theta\hat{T}_\mathrm{B})}{\hat{R}^3}. \tag{4.191}$$

By allowing for macroscale temperature changes to influence the microscale, we change the thermodynamics of the microscale. Previously, bubbles were assumed to be surrounded by a liquid with unlimited heat. In theory, a bubble could grow indefinitely as heat can be continually supplied to the bubble. In this case, when the final liquid pressure is below the initial liquid pressure, conditions far from the bubble are not in equilibrium, so there will always be a flux of both moisture and heat towards the bubble. If we account for cooling of the liquid far from the bubble, it is possible for the system to equilibrate at the lower liquid pressure by cooling to the appropriate temperature.

The viscosity of a liquid may increase with temperature; for some liquids this change can be significant. For example, the viscosity of glass depends strongly on its temperature [51]. Axial temperature gradients can arise during the drawing of glass fibres [74], having a significant effect on viscosity and dynamics of the fibre. For a starchy mixture, which is a polymer solution, a viscosity increase occurs during cooling. This

increase is thought to occur because, at lower temperatures, there is less thermal energy available to overcome the frictional interactions between neighbouring molecules [75]. We can still construct a cross-flow problem when the viscosity varies axially by following the methodology of Stokes *et al.* [66, 67]. Instead of defining modified velocities $\bar{u}$ and $\bar{v}$ by (4.137), we define

$$\bar{u} = \frac{\Gamma^*}{\mu(T)}u + \frac{x}{2}J(z,t), \qquad \text{and} \qquad \bar{v} = \frac{\Gamma^*}{\mu(T)}v + \frac{y}{2}J(z,t), \tag{4.192}$$

and instead of defining the reduced time τ by (4.158) , we define

$$\tau = \int_0^t \frac{\Gamma^*}{\mu\sqrt{A}}\mathrm{d}s. \tag{4.193}$$

The resulting cross-flow system, (4.159)–(4.162), remains unchanged.

The exact behaviour of the mixture viscosity as a function of temperature is unknown and highly dependent on the composition of the mixture. To model the effect of viscosity increase with cooling, and the presence of a glass transition at some glass-transition temperature T_G, we use an Arrhenius-type relation [75] given by

$$\mu(T) = \exp\left(a\left(\frac{1}{1 - T/\mathcal{T}} - 1\right)\right), \tag{4.194}$$

where a is a dimensionless constant representing the sensitivity of the viscosity to temperature change away from the glass transition, and

$$\mathcal{T} = \frac{T_\mathrm{G} - T_0}{\mathcal{T}}, \tag{4.195}$$

is a dimensionless constant indicating the location of the glass transition; glass transition occurs when $T = \mathcal{T}$.

A temperature-dependent viscosity (4.194), and the modified thermodynamics (4.189)–(4.191), describe two mechanisms by which the thermodynamics can arrest the growth of bubbles. As the product approaches the glass-transition temperature, its viscosity sharply increases, slowing down bubble growth. If, however, the microscale system reaches thermodynamic equilibrium before the mixture reaches the glass-transition temperature, the bubbles will stop growing, but the mixture will still evolve in other ways (such as shape change). To observe the key difference between these two mechanisms, consider the reduced time variable, τ, given by (4.193), and the equation for bubble growth, given by (4.189). Bubbles will stop growing if either

$$\hat{p}_\mathrm{B} - p - p_\mathrm{base} - \frac{\Gamma}{\hat{R}} = 0 \qquad \text{or} \qquad \mu \to \infty; \tag{4.196}$$

the former corresponds to thermodynamic equilibrium, and the latter corresponds to a glass transition. The shape of the cross-section will stop evolving if τ tends to a constant value, which can happen if $\mu \to \infty$. If μ tends to a constant, which would be the case if the microscale model reaches thermodynamic equilibrium at a temperature above the glass-transition temperature, then τ will grow linearly with z. Thus, we have two cases: either the bubbles stop growing before the glass transition, and the cross-sectional shape of the mixture tends to a circle under the action of surface tension; or, the temperature cools to the glass-transition temperature and the shape of the product is fixed.

We can understand the difference between these two cases by solving the 2D cross-flow problem coupled to the model for axial evolution for two different glass-transition temperatures: one relatively high, so that glass transition occurs before microscale thermodynamic equilibrium; and one relatively low, so that thermodynamic equilibrium is attained before the glass transition occurs. For the former, the reduced time, τ, asymptotes as $T \to T_{\mathrm{G}}$, and hence $\mu \to \infty$, as illustrated in figure 4.9a. For the latter case, when the glass transition occurs at a lower temperature, $\tau \sim z$ for $z \to \infty$. There is no discernible difference in the density predicted in each case, as shown in figure 4.9b; however, the cross-sectional area will evolve differently depending on the dominant thermodynamic mechanism, as illustrated in figure 4.9c. The value of T_{G} changes the evolution of the shape. The evolution of the cross-section for both the high and low T_{G} values is shown in figure 4.9d. With solutions to the cross-sectional model for different τ, and the solutions for A and τ, we can reconstruct an approximation to the extruded surface in 3D, as shown in figure 4.9e. In this case we have encoded the temperature of the product through the colour of the surface. The transition from red to blue indicates the cooling of the product.

The analysis completed in this section is predicated on a number of assumptions in order to derive averaged reduced models. Some of these assumptions simply restrict the cases to which these models can be applied, and others assume physics distinct from the model constructed in Chapter 2; namely, the modified constitutive law given by (4.133) and the microscale–macroscale thermal coupling given by (4.176). Despite this, the resulting reduced model gives physical insight that is not obvious from the full macroscale model. For example, we observe two fundamentally different long-time behaviours of the mixture depending on the relationship between T_{G} and the thermodynamics of the microscale. The reduced equations, namely the reduced time

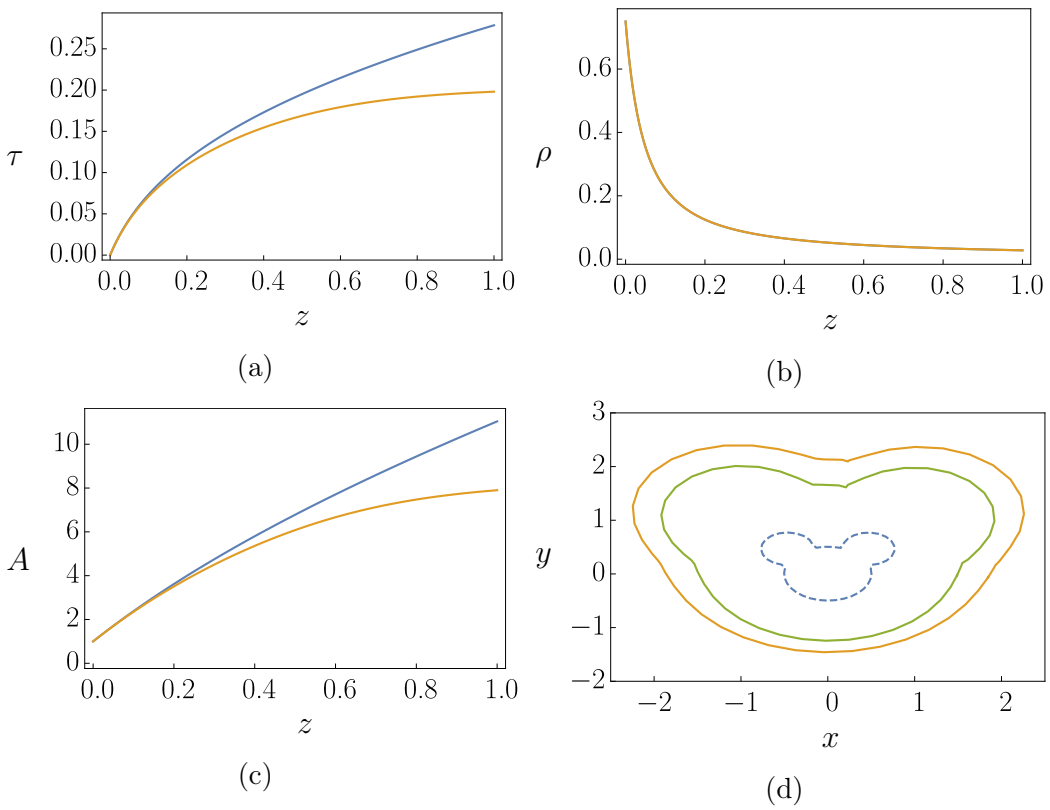

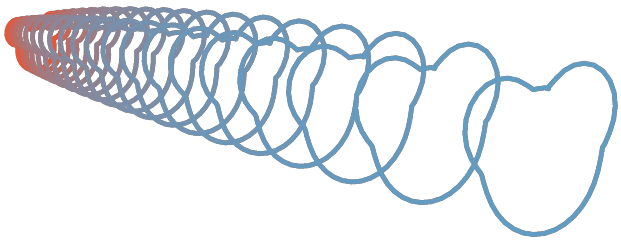

(e)

Figure 4.9: *The value of* (a) τ, (b) ρ, *and* (c) A *along the* z *axis for* $\Gamma^* = 1.5$, $C = 150$, $\rho(0) = 0.75$, $w(0) = 1$, $A(0) = \pi$, $\hat{R}(0) = 1$, *and either* $\mu = 1$ *(blue) or* $\mu(T)$ *given by (4.194), where* $\mathcal{T} = -0.13$, *and* $a = 9 \times 10^{-5}$ *(orange); all other parameters are those contained in tables 2.2 and 2.3.* (d) *the initial (blue dashed) and final cross-sections for* $\mu = 1$ *(green) and* $\mu(T)$ *given by (4.194) (orange)* (e) *the 3D reconstruction of the surface, combining the solution to the 2D cross-flow problem and the axial-flow problem when* $\mu(T)$ *is given by (4.194). The colour indicates temperature, red indicates* $T = 0$ *and blue indicates* $T = -0.13$*: in dimensional units this corresponds to cooling from 429K to 373.15K.*

in each case (4.164) and (4.193), give an insight into why the behaviour observed is different.

4.5 Concluding remarks

In this chapter we have derived models for the extensional flow of a viscous, compressible fluid in geometries that are long and thin. These models are analogous to the Trouton model in incompressible flow. We consider two distinct geometries: a long and thin sheet equivalent to a flow in 2D, and a long and thin fibre of fluid in 3D. We found in 2D that under certain conditions (*i.e.* neglecting centre-line deflection, gravity, surface-tension and inertia), the governing equations can be simplified to a form that is much easier to work with. In this reduced system we found that when there is no tension on the sheet we have two conserved quantities: the first represents conservation of mass, while the second is a consequence of conservation of momentum.

The simplicity of the reduced 2D model allowed us to probe how different microscale models of closure, $\mathcal{F}$, can modify the dynamics of the sheet. Even in the simplest case, when we neglected most of the thermodynamics (considered in Section 4.1.3), we observed non-trivial behaviour in how the evolution of the sheet depends on the microscale parameters. An example of this was the dependence of the total expansion of the sheet on the initial volume fraction parameter $\tilde{\eta}$. We observed that, with all other parameters held constant, there was an optimal $\tilde{\eta}$, denoted $\tilde{\eta}_{opt}$, that resulted in the greatest expansion of the sheet. The value $\tilde{\eta}_{opt}$ depends on the values of the other parameters, as we showed by varying the bubble pressure parameter C. Trying to understand this dependence using the full 3D model for compressible flow would be very complicated, but being able to work with a reduced model makes the task much more tractable.

In Section 4.1.4 we made a comparison between the simplest closure model and the one presented in Chapter 3 containing a more complete description of the thermodynamics of extrusion. This emphasised the importance of making sure the appropriate microscale model is used. The additional benefit of working with the reduced model is that insight into why the two models are different is more readily available. In this case, accounting for the exsolution of gas into the bubbles in the microscale model resulted in higher bubble pressures, hence greater bubble growth. This corresponded to greater expansion of the sheet.

In Section 4.2 we applied the same methodology to the 3D case of a slender fibre. We found that there were two key differences between the 2D and 3D cases. Firstly, in 2D the assumption of uniform density in a cross-section implies uniform pressure. This means that a consistent model can be constructed, even when surface tension is included. In 3D this is not the case, and we must restrict the systems that we apply the model to such that the pressure in the cross-section can be uniform (and thus consistent with the assumption of uniform density). In 3D, the model we presented can be applied for arbitrary cross-section shapes when the effects of surface tension are negligible at leading-order. Additionally, when the Airy stress function satisfies the additional constraint (4.107), such as when the cross-section is circular, the pressure will be uniform and a self-consistent model is possible. The second key difference between the 2D and 3D models is the conserved quantities that result by considering the case when there is no tension. In 2D the quantity ρh^2 is conserved, while in 3D the quantity $\rho^2 A^3$ is conserved. The reduced models presented in this chapter can be used in a number of ways to better understand extrusion processes in industry. One use for these models is making good approximations of some important physical quantities, such as: the total expansion of the product, or the final density of the product. Furthermore, the predictions made using these reduced models can be used as initial guesses when searching for numerical solutions to the full system. Good initial guesses increase the likelihood that iterative solvers converge, and reduce convergence time. In particularly difficult cases, the solutions to the reduced models will be valid in the long and thin limit, from which we can use numerical continuation to search for solutions in the parameter regime of interest.

In Section 4.3 we considered a modified constitutive law for closure that allowed us to derive a 2D cross-flow problem. This cross-flow problem was parameter independent, and independent of the axial-flow model derived in Section 4.2. This 2D model can be used to understand how the cross-sectional shape of an extruded fibre will evolve. Any initial shape evolves towards a circle, and the degree to which this occurs is governed by the evolution of the reduced time, τ given by (4.158). With a 2D cross-flow model, and a 1D axial-flow model, we reconstructed a 3D representation of the fluid surface. Even though we modified the physics in order to derive this 2D model, it can still provide valuable insights. Namely, qualitative features of shape change, and quantities such as the reduced time τ, by which the extent of shape change can be understood.

In Section 4.4, we considered the macroscale conservation-of-energy equation, and derived equation (4.186) for the evolution of the temperature along the axis of flow in the long thin limit. We also modified the thermodynamics of our system, introducing effects by which the temperature could alter the dynamics of the system. These included coupling the macroscale temperature to the microscale, which was valid for Cases I and II considered in Chapter 3. We also introduced a temperature-dependent viscosity to account for thickening behaviour of starchy mixtures as they cool. Using the methodology of Stokes *et al.* [66, 67], we introduced a modified reduced time given by (4.193), and derived a set of equations describing a 2D cross-flow problem equivalent to the constant-viscosity case. The key difference between the constant-viscosity, and temperature-dependent-viscosity cases is encapsulated in the corresponding τ definitions, given by (4.164) and(4.193) respectively. Given the complexity of the full system, especially with the modified thermodynamics introduced in Section 4.4, capturing the key physics (controlling shape change) in just a single variable, τ, makes analysis, and control, of the system much easier.

Chapter 5

Numerical solutions to the compressible-flow equations

5.1 Outline

In this chapter we describe and utilise a numerical method for finding solutions to the macroscale model described in Chapter 2 for 2D and axisymmetric flow. These geometries are practically relevant: the 2D case corresponds to extrusion through a slit, and the axisymmetric case corresponds to extrusion through a circular die. Additionally, in both cases, we can transform the (unknown) fluid domain to a rectangular domain. In Section 5.2 we describe the governing equations. A key modification to the model that we make at this stage is to introduce slip between the die and the fluid. We do this to mitigate numerical difficulties that arise where the velocity vanishes on the die, as well as to weaken the stress singularity that arises where a free boundary meets a no-slip boundary. In Section 5.3 we present a map that takes the free-boundary domain to a rectangular domain. This simplifies the system as, in the new coordinate system, the domain is known *a priori*; however, the associated cost of this transformation is an increase in the complexity of the equations governing conservation of mass and momentum. To solve this complicated system of equations, we decompose the system into two coupled subsystems: for one subsystem, we suppose that the density is known, and then solve for the corresponding pressure and velocity; for the second subsystem, we suppose that the pressure and velocity are known, and solve for the corresponding density. The combined solution is found by iterating between these two subsystems until the change in the respective solutions is below a set tolerance. The method of solving this first subsystem, and the relationship between the subsystems, is described in Section 5.4.

Given the bespoke nature of this scheme, we first verify its accuracy and convergence properties on a well-studied problem, the incompressible stick-slip problem, in Section 5.4.3. Since we introduce a slip length on the wall, the problem we solve numerically is the *partial-stick/slip* problem. We verify in this section that our solution to the partial-stick/slip problem converges to the solution for the stick-slip problem in the limit where the slip length vanishes. We then present solutions to the full 2D, compressible, free-boundary problem in Section 5.6. In Section 5.6.2 we compare solutions found using this method to the reduced model in the slender limit detailed in Chapter 4. In Section 5.7 we consider the stress singularity on the boundary at the point where the partial-slip boundary changes to a full-slip boundary. In this section we verify the behaviour expected in the incompressible case, as well as contrast and compare this behaviour to that in the compressible case. We then rationalise this comparison by considering the limit in which the fluid is weakly compressible. In Section 5.8 we present the formulation of this numerical method in the axisymmetric case.

5.2 Model equations

In this section we present the governing equations for a steady, compressible flow in 2D. A schematic of the scenario that we consider is shown in figure 5.1. The fluid domain is denoted Ω', and the governing equations for the fluid in Ω' will be the same as those used in Chapter 4. We consider a scenario in which, along some curve, Γ'_i, bubbles nucleate in the fluid. We are interested in the dynamics of the mixture after this point. Due to symmetry, we only solve the governing equations for half of the fluid, denoting the line of symmetry by Γ'_s. We denote the boundary of the die by Γ'_d, and the free boundary by Γ'_f. We denote the end of the domain by Γ'_o. We employ the same scalings used in Chapter 4, in which we introduced ϵ *via* (4.14); however, in this case we do not suppose that ϵ is small. Additionally, we neglect inertial effects on physical grounds (the Reynolds number, contained in table 2.2, is small).

The equations governing the steady flow of a compressible fluid in 2D, in Ω', are

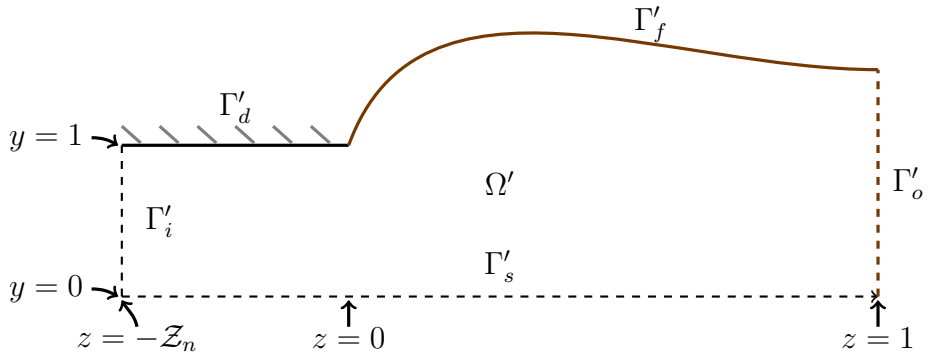

Figure 5.1: *Solution domain, Ω' in Cartesian coordinates. The boundaries are denoted by Γ'_d for the die, Γ'_i for the inlet, Γ'_s for the line of symmetry, Γ'_o for the outlet, and Γ'_f for the free boundary. The inlet, Γ'_i, is at $\mathcal{Z}_n = -\ell/L$.*

given by

$$\frac{\partial}{\partial z}(\rho w) + \frac{\partial}{\partial y}(\rho v) = 0, \tag{5.1}$$

$$\epsilon^2 \frac{\partial}{\partial z}\left(-p + \lambda\left(\frac{\partial w}{\partial z} + \frac{\partial v}{\partial y}\right) + 2\mu\frac{\partial w}{\partial z}\right) + \frac{\partial}{\partial y}\left(\mu\left(\frac{\partial w}{\partial y} + \epsilon^2\frac{\partial v}{\partial z}\right)\right) = 0, \tag{5.2}$$

$$\frac{\partial}{\partial z}\left(\mu\left(\frac{\partial w}{\partial y} + \epsilon^2\frac{\partial v}{\partial z}\right)\right) + \frac{\partial}{\partial y}\left(-p + \lambda\left(\frac{\partial w}{\partial z} + \frac{\partial v}{\partial y}\right) + 2\mu\frac{\partial v}{\partial y}\right) = 0. \tag{5.3}$$

We suppose that the centre-line of the fluid is aligned with the z axis, w and v denote the z and y components of the velocity respectively, p denotes the pressure, and ρ denotes the density. The parameters μ and λ are the dimensionless dynamic viscosity and second coefficient of viscosity respectively. The density of a bubbly mixture depends on the size of bubbles according to

$$\rho = \frac{1}{1 + \tilde{\eta}\hat{R}^3}, \tag{5.4}$$

where the bubble radius, $\hat{R}$, evolves according to the inertialess Rayleigh–Plesset equation, (3.1). The time-steady form of (3.1), in the Eulerian frame of the extruder, is given by

$$w\frac{\partial \hat{R}}{\partial z} + v\frac{\partial \hat{R}}{\partial y} = \frac{\hat{R}}{4}\left(\hat{p}_{\mathrm{B}} - p - p_{\mathrm{atm}} - \frac{\Gamma}{\hat{R}}\right), \tag{5.5}$$

in Ω'. We will consider two different types of constitutive law for $\hat{p}_{\mathrm{B}}$: the first, Boyle's law [8], where

$$\hat{p}_{\mathrm{B}} = \frac{C}{\hat{R}^3}, \tag{5.6}$$

and C is a constant; and the second, the full microscale model detailed in Chapter 2, Section 2.6.

We impose the initial bubble size, $\hat{R}_0$, and hence the initial density, ρ_0, on Γ_i'; as well as the flow profile given by

$$v = 0 \qquad \text{and} \qquad w = w(y). \tag{5.7a,b}$$

On the free boundary Γ_f', we impose the kinematic and dynamic boundary conditions, respectively given by

$$\boldsymbol{u} \cdot \boldsymbol{n} = 0 \qquad \text{and} \qquad \boldsymbol{\sigma} \cdot \boldsymbol{n} = \boldsymbol{0}, \tag{5.8a,b}$$

where $\boldsymbol{n}$ is the outward pointing unit normal to the surface, and we neglect the effect of surface tension on the macroscale. On the line of symmetry Γ_s', we impose symmetry boundary conditions given by

$$\frac{\partial w}{\partial y} = 0 \qquad \text{and} \qquad v = 0. \tag{5.9}$$

On the outlet, Γ_o', we impose that there is no stress; that is,

$$\boldsymbol{\sigma} \cdot \boldsymbol{e}_z = \boldsymbol{0}, \tag{5.10}$$

where $\boldsymbol{e}_z$ is the unit normal in the z direction. In the model described in Chapter 2, we imposed a no-slip boundary condition between the fluid and die wall, in this case along Γ_d'. In this chapter, we consider a Navier-slip law [43] on Γ_d', given by

$$-\beta \frac{\partial w}{\partial y} = w, \tag{5.11}$$

where β is the dimensionless slip length, which we take to zero to recover a no-slip boundary. We introduce β in order to perform numerical continuation; however, it is related to a physical quantity, the slip length β', by $\beta' = \epsilon L \beta$. The remaining boundary condition on Γ_d', given by

$$v = 0, \tag{5.12}$$

enforces that the die is immobile and impermeable, and that we assume no separation in advance of the corner where the die, Γ_d', meets the free boundary, Γ_f.

5.3 A partial hodograph transformation

In this section we consider a coordinate transformation that maps the unknown domain Ω', illustrated in figure 5.1, to a rectangular domain, denoted by Ω and illustrated in figure 5.2. This coordinate transformation, which we will refer to as a *partial hodograph* transformation—alluding to the *full* hodograph transformation in which the independent and dependent variables are interchanged—is a map from (z, y) coordinates to (ϕ, ψ) coordinates, where ψ is the stream function of the fluid and $\phi = z$. The boundaries in (z, y) coordinates are transformed to their analogues in (ϕ, ψ) coordinates. The curve along which bubbles nucleate, in (ϕ, ψ) coordinates, is denoted by Γ_i, the line of symmetry is denoted by Γ_s, the boundary of the die is denoted by Γ_d, the free boundary is denoted by Γ_f, and the end of the domain is denoted by Γ_o.

The stream function for compressible flow (in 2D Cartesian (z, y) coordinates) is defined by

$$\frac{\partial \psi}{\partial y} = \rho w, \quad \text{and} \quad \frac{\partial \psi}{\partial z} = -\rho v, \tag{5.13a,b}$$

with $\psi = 0$ on Γ_s' without loss of generality. For w and ρ positive, ψ increases everywhere with y, so this change in variables is permitted. Consider the transformation of the dependent variables

$$\hat{w}(\phi, \psi) = w(z, y), \quad \hat{v}(\phi, \psi) = v(z, y), \quad \hat{\rho}(\phi, \psi) = \rho(z, y), \quad \hat{p}(\phi, \psi) = p(z, y).$$

Using the chain rule, the z and y derivatives are given by

$$\frac{\partial(\cdot)}{\partial z} = \frac{\partial(\cdot)}{\partial \phi} - \rho v \frac{\partial(\cdot)}{\partial \psi}, \qquad \frac{\partial(\cdot)}{\partial y} = \rho w \frac{\partial(\cdot)}{\partial \psi}. \tag{5.14a,b}$$

Transforming the system of equations given by (5.1)–(5.3), and dropping hats from hereon, gives the conservation-of-mass equation,

$$\frac{\partial}{\partial \phi}(\rho w) - \rho v \frac{\partial}{\partial \psi}(\rho w) + \rho w \frac{\partial}{\partial \psi}(\rho v) = 0, \tag{5.15}$$

the conservation-of-z-momentum equation,

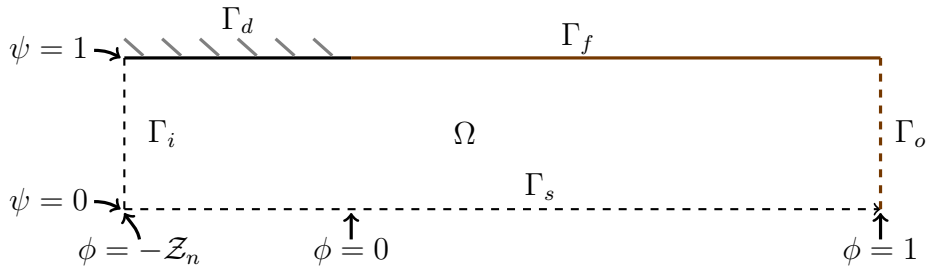

Figure 5.2: *Solution domain, Ω in the streamline coordinates. The boundaries are denoted by Γ_d for the die, Γ_i for the inlet, Γ_s for the line of symmetry, Γ_o for the outlet, and Γ_f for the free boundary (which is fixed in ϕ in the (ϕ, ψ) plane).*

$$\begin{aligned}
&\epsilon^2\frac{\partial}{\partial\phi}\left(2\mu\left(\frac{\partial w}{\partial\phi}-\rho v\frac{\partial w}{\partial\psi}\right)\right)-\epsilon^2\rho v\frac{\partial}{\partial\psi}\left(2\mu\left(\frac{\partial w}{\partial\phi}-\rho v\frac{\partial w}{\partial\psi}\right)\right)\\
&+\rho w\frac{\partial}{\partial\psi}\left(\mu\left(\rho w\frac{\partial w}{\partial\psi}+\epsilon^2\frac{\partial v}{\partial\phi}-\epsilon^2\rho v\frac{\partial v}{\partial\psi}\right)\right)=\\
&\qquad\epsilon^2\frac{\partial}{\partial\phi}\left(p-\lambda\left(\frac{\partial w}{\partial\phi}-\rho v\frac{\partial w}{\partial\psi}+\rho w\frac{\partial v}{\partial\psi}\right)\right)\\
&\qquad-\epsilon^2\rho v\frac{\partial}{\partial\psi}\left(p-\lambda\left(\frac{\partial w}{\partial\phi}-\rho v\frac{\partial w}{\partial\psi}+\rho w\frac{\partial v}{\partial\psi}\right)\right),
\end{aligned}\tag{5.16}$$

and the conservation-of-y-momentum equation,

$$\begin{aligned}
&\frac{\partial}{\partial\phi}\left(\mu\left(\rho w\frac{\partial w}{\partial\psi}+\epsilon^2\frac{\partial v}{\partial\phi}-\epsilon^2\rho v\frac{\partial v}{\partial\psi}\right)\right)-\rho v\frac{\partial}{\partial\psi}\left(\mu\left(\rho w\frac{\partial w}{\partial\psi}+\epsilon^2\frac{\partial v}{\partial\phi}-\epsilon^2\rho v\frac{\partial v}{\partial\psi}\right)\right)\\
&\qquad+\rho w\frac{\partial}{\partial\psi}\left(2\mu\rho w\frac{\partial v}{\partial\psi}\right)=\rho w\frac{\partial}{\partial\psi}\left(p-\lambda\left(\frac{\partial w}{\partial\phi}-\rho v\frac{\partial w}{\partial\psi}+\rho w\frac{\partial v}{\partial\psi}\right)\right),
\end{aligned}\tag{5.17}$$

respectively, all on the domain Ω. After applying the partial hodograph transformation to the Rayleigh–Plesset equation, (5.5), the time-steady evolution of $\hat{R}$ in Ω is given by

$$w\frac{\partial\hat{R}}{\partial\phi}=\frac{\hat{R}}{4}\left(\hat{p}_{\mathrm{B}}-p-p_{\mathrm{atm}}-\frac{\Gamma}{\hat{R}}\right).\tag{5.18}$$

If we use Boyle's law, (5.6), for $\hat{p}_{\mathrm{B}}$, then we can formulate the system entirely in terms of macroscopic quantities; that is, using relationship between the density and bubble radius given by (5.4), as well as (5.18), and (5.6), we can close the system of equations given by (5.41), (5.42), and (5.43), with

$$w\frac{\partial\rho}{\partial\phi}=-\frac{3(1-\rho)\rho}{4}\left(\frac{C\tilde{\eta}\rho}{1-\rho}-p-p_{\mathrm{atm}}-\frac{\Gamma\tilde{\eta}^{1/3}\rho^{1/3}}{(1-\rho)^{1/3}}\right).\tag{5.19}$$

We deduce that the normal vector to the free surface Γ_f, $\boldsymbol{n}$, from the kinematic boundary condition (5.8a), is given by

$$\boldsymbol{n} = \frac{1}{\sqrt{w^2+v^2}} \begin{pmatrix} -v \\ w \end{pmatrix}, \tag{5.20}$$

which, from hereon, we incorporate into the boundary conditions on Γ_f. The transformed stress boundary conditions on the free surface, Γ_f, (5.8b), are given by

$$-\left(2\mu\left(\frac{\partial w}{\partial \phi} - \rho v \frac{\partial w}{\partial \psi}\right) - \left(p - \lambda\left(\frac{\partial w}{\partial \phi} - \rho v \frac{\partial w}{\partial \psi} + \rho w \frac{\partial v}{\partial \psi}\right)\right)\right)\epsilon^2 v + \left(\mu\left(\frac{\partial v}{\partial \phi} - \rho v \frac{\partial v}{\partial \psi} + \rho w \frac{\partial w}{\partial \psi}\right)\right) w = 0, \tag{5.21}$$

$$-\left(\mu\left(\frac{\partial v}{\partial \phi} - \rho v \frac{\partial v}{\partial \psi} + \rho w \frac{\partial w}{\partial \psi}\right)\right) v + \left(2\mu\rho w \frac{\partial v}{\partial \psi} - \left(p - \lambda\left(\frac{\partial w}{\partial \phi} - \rho v \frac{\partial w}{\partial \psi} + \rho w \frac{\partial v}{\partial \psi}\right)\right)\right) w = 0. \tag{5.22}$$

The boundary conditions on the die, Γ_d, (5.11) and (5.12), are respectively given by

$$w = -\beta\rho w \frac{\partial w}{\partial \psi} \qquad \text{and} \qquad v = 0, \tag{5.23a,b}$$

and the symmetry boundary conditions on Γ_s, (5.9), are given by

$$\frac{\partial w}{\partial \psi} = 0 \qquad \text{and} \qquad v = 0. \tag{5.24a,b}$$

The no-axial-stress boundary conditions, (5.10), at the end of the domain, Γ_o are given by

$$-p + \lambda\left(\frac{\partial w}{\partial \phi} - \rho v \frac{\partial w}{\partial \psi} + \rho w \frac{\partial v}{\partial \psi}\right) + 2\mu\left(\frac{\partial w}{\partial \phi} - \rho v \frac{\partial w}{\partial \psi}\right) = 0, \tag{5.25}$$

$$\left(\frac{\partial v}{\partial \phi} - \rho v \frac{\partial v}{\partial \psi} + \rho w \frac{\partial w}{\partial \psi}\right) = 0. \tag{5.26}$$

The prescribed velocity profile on where the bubbles nucleate, Γ_i, is given by

$$v = 0 \qquad \text{and} \qquad w = w(\psi). \tag{5.27a,b}$$

We prescribe that the density is uniform, ρ_0, on Γ_i.

The transformation described in this section, the partial hodograph transformation,

is similar to the von Mises transformation in viscous boundary layer theory [72], and has been applied to problems with viscoelastic fluids [58]. In the case described in [58], this transformation was used to simplify the governing equations in a boundary layer. In our case, we do not use the partial hodograph to simplify the governing equations; however, the common aspect of viscoelastic flow and the compressible flow we consider is a constitutive law for the state of the fluid that evolves along streamlines. Given that we must also determine the location of a free boundary, the benefits of the partial hodograph transformation are two-fold: the transformed domain is fixed; and the streamlines are known *a priori*, which makes integrating a constitutive law along the streamlines much easier. The resulting scheme is a hybrid Eulerian/Lagrangian formulation of the free-boundary problem.

We prescribe a Poiseuille flow profile for a channel with slip. The velocity profile is given by

$$w(y) = \frac{1}{2}\Pi\left(y^2 - (1+2\beta)\right), \tag{5.28}$$

where Π is the pressure gradient, which we choose such that the total mass flux is 1; that is, the pressure gradient is given by

$$\Pi = -\frac{3}{\rho_0(1+3\beta)}. \tag{5.29}$$

To prescribe $w(\psi)$, we must determine the map between y and ψ on Γ_i, which can be derived from the definition of ψ in (5.13) giving

$$\psi = \int_0^y \rho_0 w(s)\mathrm{d}s. \tag{5.30}$$

Using this definition, the velocity profile given by (5.28), and the pressure gradient given by (5.29), the relationship between ψ and y is given by

$$\psi = \frac{3}{2(1+3\beta)}\left((1+2\beta)y - \frac{1}{3}y^3\right), \tag{5.31}$$

which is a cubic equation for y. Solving (5.31) for y, and selecting the appropriate solution, gives

$$y = \frac{(1-i\sqrt{3})(1+2\beta) + (1+i\sqrt{3})\left((1+3\beta)\psi + (\psi^2(1+3\beta)^2 - (1+2\beta)^3)^{1/2}\right)^{2/3}}{2\left(\psi(1+3\beta) + (\psi^2(1+3\beta)^2 - (1+2\beta)^3)^{1/2}\right)^{1/3}}, \tag{5.32}$$

which is real-valued for $0 \leq \psi \leq 1$, and can be substituted into (5.28) to give the inlet velocity as a function of ψ.

5.4 Direct numerical simulations

In this section, we describe a numerical scheme for finding solutions to the governing equations in Ω. We will consider two cases of differing complexity. The first is when the macroscale system can be expressed entirely in terms of macroscale quantities, without microscale quantities. More generally, the first case we consider concerns systems for which the evolution of the state variables depends only on their current state, and not the history of the system. The second is a situation for which the evolution of the microscale model depends on the history of the fluid; this case requires evaluating path integrals along the streamlines. We consider the first case to illustrate the efficacy of the scheme we have proposed, which exploits the partial hodograph transformation, and to study the behaviour of a compressible fluid with fewer degrees of freedom. The second case is more relevant to extrusion of a bubble mixture; additionally, systems with similar properties are found in other applications, including in the extrusion of a viscoelastic fluid [58].

5.4.1 The weak formulation of the problem

In this section we present the weak formulation of the system of PDEs presented in Section 5.3. We let $H^1(\Omega)$ be the space of square-integrable functions with square-integrable derivatives, and let $L^2(\Omega)$ be the space of square-integrable functions on Ω. We make use of the following function spaces, from which our solutions will be given:

$$W = \left\{ w \in H^1(\Omega) : w|_{\Gamma_i} = w(\psi) \right\}, \tag{5.33}$$

$$V = \left\{ v \in H^1(\Omega) : v|_{\Gamma_i \cup \Gamma_d \cup \Gamma_s} = 0 \right\}, \tag{5.34}$$

$$Q = \left\{ q \in L^2(\Omega) \right\}, \tag{5.35}$$

$$K = \left\{ k \in H^1(\Omega) : k|_{\Gamma_i} = \rho_0 \right\}, \tag{5.36}$$

where $k|_\Gamma$ denotes the value of k on the boundary Γ. In addition, we define the following function spaces, from which we will take our test functions:

$$W^T = \left\{ w \in H^1(\Omega) : w|_{\Gamma_i} = 0 \right\}, \tag{5.37}$$

$$V^T = V = \left\{ v \in H^1(\Omega) : v|_{\Gamma_i \cup \Gamma_d \cup \Gamma_s} = 0 \right\}, \tag{5.38}$$

$$Q^T = Q = \left\{ q \in L^2(\Omega) \right\}, \tag{5.39}$$

$$K^T = \left\{ k \in H^1(\Omega) : k|_{\Gamma_i} = 0 \right\}. \tag{5.40}$$

Multiplying the transformed conservation-of-mass equation, (5.15), by a test function, $q \in Q^T$, and integrating over Ω yields

$$\iint_\Omega \left(\frac{\partial(\rho w)}{\partial \phi} - \rho v \frac{\partial(\rho w)}{\partial \psi} + \rho w \frac{\partial(\rho v)}{\partial \psi} \right) q \, \mathrm{d}\phi \mathrm{d}\psi = 0. \tag{5.41}$$

Similarly, we multiply (5.16) and (5.17) by $g \in W^T$ and $h \in V^T$ respectively. Integrating the resulting equations over Ω, integrating by parts, and imposing the boundary conditions given by (5.21), (5.22), (5.23), (5.25), and (5.26) gives

$$\begin{aligned} &\iint_\Omega - \left(2\mu \left(\frac{\partial w}{\partial \phi} - \rho v \frac{\partial w}{\partial \psi} \right) - \left(p - \lambda \left(\frac{\partial w}{\partial \phi} - \rho v \frac{\partial w}{\partial \psi} + \rho w \frac{\partial v}{\partial \psi} \right) \right) \right) \epsilon^2 \frac{\partial g}{\partial \phi} \\ &+ \left(2\mu \left(\frac{\partial w}{\partial \phi} - \rho v \frac{\partial w}{\partial \psi} \right) - \left(p - \lambda \left(\frac{\partial w}{\partial \phi} - \rho v \frac{\partial w}{\partial \psi} + \rho w \frac{\partial v}{\partial \psi} \right) \right) \right) \epsilon^2 \frac{\partial}{\partial \psi} (g \rho v) \\ &\quad - \mu \left(\epsilon^2 \frac{\partial v}{\partial \phi} - \epsilon^2 \rho v \frac{\partial v}{\partial \psi} + \rho w \frac{\partial w}{\partial \psi} \right) \frac{\partial}{\partial \psi} (\rho w g) \, \mathrm{d}\phi \mathrm{d}\psi - \int_{\Gamma_d} \rho g \mu \frac{w^2}{\beta} \, \mathrm{d}\phi = 0, \end{aligned} \tag{5.42}$$

and

$$\begin{aligned} &\iint_\Omega -\mu \left(\epsilon^2 \frac{\partial v}{\partial \phi} - \epsilon^2 \rho v \frac{\partial v}{\partial \psi} + \rho w \frac{\partial w}{\partial \psi} \right) \frac{\partial h}{\partial \phi} + \mu \left(\epsilon^2 \frac{\partial v}{\partial \phi} - \epsilon^2 \rho v \frac{\partial v}{\partial \psi} + \rho w \frac{\partial w}{\partial \psi} \right) \frac{\partial}{\partial \psi} (h \rho v) \\ &\quad - \left(2\mu \rho w \frac{\partial v}{\partial \psi} - \left(p - \lambda \left(\frac{\partial w}{\partial \phi} - \rho v \frac{\partial w}{\partial \psi} + \rho w \frac{\partial v}{\partial \psi} \right) \right) \right) \frac{\partial}{\partial \psi} (\rho w h) \, \mathrm{d}\phi \mathrm{d}\psi = 0 \end{aligned} \tag{5.43}$$

respectively.

The complexity of the system of equations used to close the compressible conservation-of-mass and conservation-of-momentum equations will determine the appropriate solution method. If we suppose that the bubble pressure is given by Boyle's law, then the system of equations is closed by (5.19). In this case, the evolution of the macroscopic quantities at any point depends only on the state at that point; there is no history dependence on the evolution. Multiplying equation (5.19) with $k \in K^T$, and integrating over Ω, yields

$$\iint_\Omega k \left(w \frac{\partial \rho}{\partial \phi} + \frac{3(1-\rho)\rho}{4} \left(\frac{C \tilde{\eta} \rho}{1-\rho} - p - p_{\mathrm{atm}} - \frac{\Gamma \tilde{\eta}^{1/3} \rho^{1/3}}{(1-\rho)^{1/3}} \right) \right) \mathrm{d}z \mathrm{d}\psi = 0. \tag{5.44}$$

We can therefore express the weak formulation of this problem as follows: find $(w, v, p, \rho) \in W \times V \times Q \times K$ such that (5.41), (5.42), (5.43), and (5.44) are satisfied for all $q \in Q^T$, $g \in W^T$, $h \in V^T$, and $k \in K^T$.

With the more complete thermodynamic description in the full microscale model

in Section 2.6 of Chapter 2 (compared to simply using Boyle's law) the evolution of the mixture depends on more than just the current macroscopic state of the system. In order to understand the evolution of the product, the density, velocity, and pressure are insufficient; we must also know the state of microscale quantities such as the number of moles of gas, $\hat{N}_{\mathrm{B}}$, which depend on the history of the mixture from the point of bubble nucleation. In this case, the numerical scheme we employ must be able to evaluate integrals along fluid streamlines.

5.4.2 Iterative method

We decompose the full problem into two sub-problems: a macroscale problem, where the density is an input and the velocity and pressure are determined; and a microscale problem, where the velocity (and therefore streamlines) and pressure are inputs, and the microscale model is integrated along the streamlines to determine the density. We iterate between these two sub-problems, using the solution for each to inform the input fields for the other, until the predictions for each sub-problem do not vary significantly between iterations. A schematic of this iterative procedure is illustrated in figure 5.3.

The first sub-problem, for which ρ is prescribed, and w, v, and p must be determined, can be solved using the mixed finite element method. The weak formulation of this sub-problem is as follows: find $(w, v, p) \in W \times V \times Q$ such that (5.41), (5.42), and (5.43), are satisfied for all $q \in Q^T$, $g \in W^T$, and $h \in V^T$, where ρ is prescribed.

By supposing that $W_h \subset W$, $V_h \subset V$, $Q_h \subset Q$, $W_h^T \subset W^T$, $V_h^T \subset V^T$, and $Q_h^T \subset Q^T$, where a subscript h denotes a finite-dimensional function space, we can construct a discrete approximation to the weak formulation of this sub-problem. We replace (w, v, p) in (5.41), (5.42), and (5.43) by (w_h, v_h, p_h), respectively, where $w_h \in W_h$, $v_h \in V_h$, and $p_h \in Q_h$. Similarly, we replace (g, h, q) in (5.41), (5.42), and (5.43) by (g_h, h_h, q_h), respectively, where $g_h \in W_h^T$, $h_h \in V_h^T$, and $q_h \in Q_h^T$. The discrete approximation to the weak formulation of this sub-problem is to find (w_h, v_h, p_h) such that (5.41), (5.42), and (5.43), after replacing the original functions by their discrete approximations, are satisfied for all (g_h, h_h, q_h). Details of the solver we employed are given in Section 5.4.3.

Given the solution for (w, v, p) from the first sub-problem, the second sub-problem involves solving the microscale model along the streamlines given by (w, v). In (ϕ, ψ)

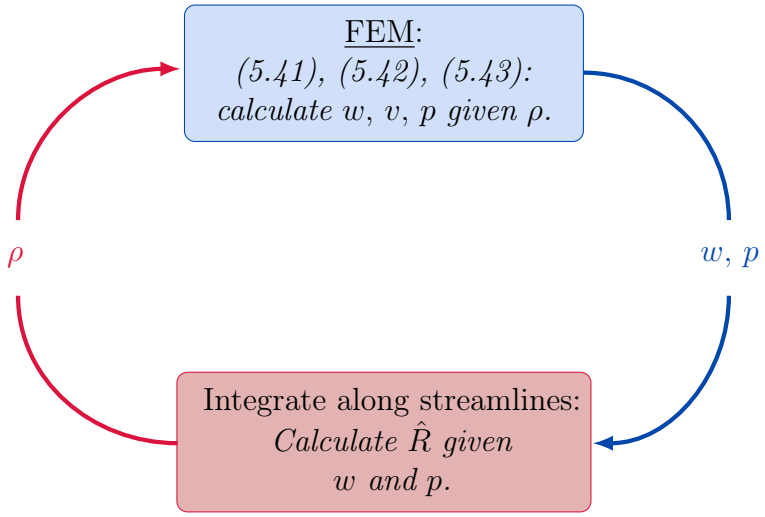

Figure 5.3: *A schematic of the iterative procedure for finding solutions. One subproblem, comprising equations (5.41), (5.42), and (5.43), is solved by inputting a particular ρ and using the finite element method (FEM). The solutions to the field variables from this problem, namely w and p, are passed to the microscale model, which is integrated along the streamlines to determine an updated ρ.*

coordinates, this involves integrating the microscale model, coupled to w and p from the macroscale, along lines of constant ψ. The microscale solution determines $\hat{R}$, and hence ρ, along each streamline. A solution for ρ in Ω can then be constructed, say, by interpolating ρ onto Ω.

5.4.3 Numerical details and challenges

Finding solutions to the finite element problem presented in Section 5.4.1 can be challenging. This problem is nonlinear, so we use an iterative method; the damped-Newton–Raphson method [70]. If a poor initial guess is used, the solver will diverge from the solution. To circumvent this issue, we can perform numerical continuation from a case where the solution can be found relatively easily, to the case we are interested in. It is easier to find a solution when the fluid is nearly incompressible, *i.e.* $\tilde{\eta}$ is small, the slip length, β, is large, and the mesh is coarse. The scheme we use is as follows: the incompressible problem, which is described further in Section 5.5, is first solved on a coarse mesh with $\beta = 1$; this provides the initial guess for the compressible problem on a coarse mesh with $\beta = 1$; the mesh is then refined; and finally the slip parameter, β, is reduced. There are likely to be more efficient schemes for refining the mesh and reducing β; however, we favour robustness over efficiency

at this stage.

There are two main challenges associated with the no-slip case: the transformation from y to ψ breaks down if $w = 0$, and the slow advection speed of bubbles near the no-slip surface can lead to issues with the macroscale–microscale coupling. The former becomes problematic due to the large field gradients induced in the solution near no-slip surfaces, and makes finding the inverse transformation much more expensive. The latter, the breakdown of the microscale–macroscale coupling, arises because, in the derivation of a microscale model, we make some assumptions about the macroscale that no longer hold if $w \to 0$. In this case, we assume a timescale related to macroscale flow speed and lengths; however, bubbles advected along the slow particle paths near a no-slip surface have much more time to grow or contract. Thus, the predicted dynamics of these bubbles are not reflective of the true dynamics. These issues were the main motivators for introducing a slip length β.

5.4.4 Inverse transformation

Once a solution is obtained in (ϕ, ψ) space, the inverse mapping to (z, y) space can be deduced. The inverse transformation is found by solving (5.13a), so

$$y = \int_0^{\psi} \frac{1}{\rho w} \mathrm{d}\psi. \tag{5.45}$$

Using the composite Simpson's rule [70], we construct an iterative procedure for calculating the map from ψ to y. For a given ϕ, and $i = 2, 3, ..., n$,

$$y_i = y_{i-1} + \frac{h}{3}\left(\frac{1}{\rho(\phi, \psi_{2i-2})w(\phi, \psi_{2i-2})} + \frac{1}{\rho(\phi, \psi_{2i-1})w(\phi, \psi_{2i-1})} + \frac{1}{\rho(\phi, \psi_{2i})w(\phi, \psi_{2i})}\right), \tag{5.46}$$

where $h = 1/(2n)$, $\psi_j = jh$, and

$$y_0 = 0, \qquad \psi_0 = 0. \tag{5.47}$$

This procedure maps ψ_{2i} to y_i.

5.5 Results for test problems

In this section we consider the incompressible stick-slip problem, which has an analytic solution, to demonstrate the efficacy of the numerical scheme proposed in Section 5.4. The incompressible stick-slip problem refers to the flow of an incompressible fluid

confined to a channel, where the channel wall changes from no-slip to infinite slip at some point. This problem is useful to study for two reasons: there is a singularity where the boundary condition changes from no-slip to infinite slip [46], which is an effect that we must capture in our extrusion simulations; and there exists an analytic solution, given by Richardson [59] and shown in Appendix A, which we can use to verify the accuracy of our numerical solution in the limit $\beta \to 0$.

To consider this problem, we modify the weak formulation detailed in Section 5.4. For an incompressible fluid, we can take $\rho = 1$, which returns the equations that would have been obtained had we started with the Stokes equations. For the incompressible stick-slip problem, we must modify the conditions imposed on the free boundary. The no-stress boundary conditions, (5.21) and (5.22), on Γ_f are replaced by

$$\frac{\partial w}{\partial \psi} = 0 \qquad \text{and} \qquad v = 0. \tag{5.48a,b}$$

In addition, we redefine the function space V, previously given by (5.34), to be given by

$$V = \left\{ v \in H^1(\Omega) : v|_{\Gamma_f \cup \Gamma_i \cup \Gamma_d \cup \Gamma_s} = 0 \right\}, \tag{5.49}$$

and we redefine the function space V^T, previously given by (5.38), to be given by

$$V^T = V = \left\{ v \in H^1(\Omega) : v|_{\Gamma_f \cup \Gamma_i \cup \Gamma_d \cup \Gamma_s} = 0 \right\}. \tag{5.50}$$

We solve this problem on $(\phi, \psi) \in [-0.5, 0.5] \times [0, 1]$, which, given that the original domain is fixed, we expect to map back to the domain $(z, y) \in [-0.5, 0.5] \times [0, 1]$. For the sake of this test, we take $\epsilon = 1$ and suppose that the die meets the free boundary at $z = 0$.

An example of the streamlines and a contour plot of the pressure are shown in figures 5.4a and 5.4b, respectively. There are a number of interesting features that can be observed by considering the streamlines: the deflection of the streamlines closer to the wall near the point at which the boundary condition changes, the horizontal velocity of the streamlines tending to the same value in the full-slip region, and the rapid change in horizontal velocity where the boundary condition changes. Comparing these results to the pressure, we observe that the streamline deflection occurs near a local region of low pressure. This low pressure region corresponds to the pressure singularity at the point where the boundary condition changes to full slip.

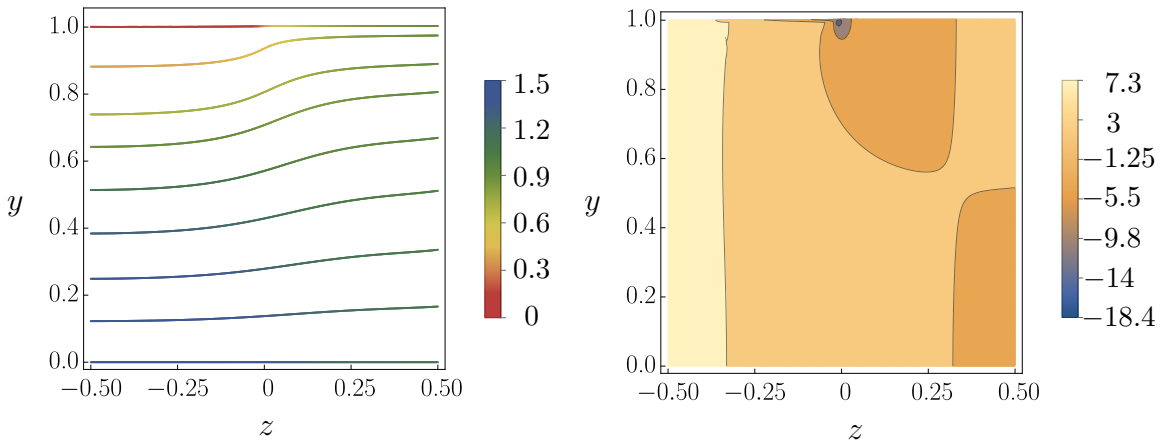

(a) (b)

Figure 5.4: (a) *A streamline plot for the incompressible stick-slip problem; the colour of the streamline indicates the z-velocity of fluid.* (b) *A contour plot of pressure for the incompressible stick-slip problem. Both figures correspond to results where* $\beta = 0.02$ *and* $\epsilon = 1$. *All other parameters are those contained in table 2.2.*

By comparing the numerical solution with slip, to the analytic solution without slip, we can verify that taking $\beta \to 0$ gives better approximations to the no-slip case. Denoting the numerical approximation to the z component of the velocity, w, for a slip length β by $w_{\mathrm{n}}(z, y; \beta)$, and the analytic prediction by $w_{\mathrm{a}}(z, y)$, we define the error, $\mathrm{E}_{\mathrm{n}}(z; \beta)$, between the two predictions by

$$\mathrm{E}_{\mathrm{n}}(z;\beta) := \left(\int_0^1 (w_{\mathrm{n}}(z, y; \beta) - w_{\mathrm{a}}(z, y))^2 \mathrm{d}y \right)^{1/2}. \tag{5.51}$$

By calculating the error for $z = 0.25$ and a number of values of β, we observe the solutions converging as β is decreased, as shown in figure 5.5. This instils confidence that we can approximate the behaviour of a system with a no-slip boundary by replacing it with a boundary that has a small slip value; despite the fact that some features of the problem, like the nature of the stress singularity, are fundamentally different.

5.6 Simulations with the full model

In this section we use the numerical method described in Sections 5.2–5.4 to find solutions to the full extrusion model presented in Chapter 2. We then use this numerical method to test the validity of the asymptotic analysis performed in Chapter 4.

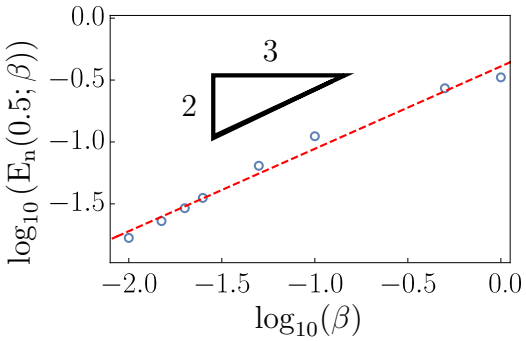

Figure 5.5: *Error between the numerical solution to the stick-slip problem with slip length β, and the analytic solution as $\beta \to 0$. The red-dashed line illustrates the line of best fit through the error values and has a slope of 0.66.*

5.6.1 Numerical results

In this section, we illustrate some solutions to the full system of equations; that is, we do not make use of any of the reduced models derived in Chapters 3 and 4. The method we use is described in Section 5.4.2, and the solution to the microscale model along each streamline is found using the method-of-lines scheme detailed in Section 3.2.2. The microscale time derivatives in the system of equations presented in Section 3.2.2 are given by

$$\frac{\mathrm{d}}{\mathrm{d}\hat{t}} = w\frac{\mathrm{d}}{\mathrm{d}\phi} \tag{5.52}$$

in (ϕ, ψ) coordinates. The microscale initial conditions at $\hat{t} = 0$, given by (2.86), are boundary conditions on Γ_i. In this case, we integrate the microscale model along 30 evenly spaced streamlines, and then interpolate the results onto Ω.

The results of a simulation, performed using the parameters in table 2.2 and 2.3 with the exception of $\gamma^* = 0$, are illustrated in figure 5.6. The streamlines, shown in figure 5.6a, remain almost parallel while bounded by the impermeable boundary, for $z < 0$, and fan out in the free-boundary region, for $z > 0$. With these full simulations, we can confirm, qualitatively, a prediction made in Chapter 4; namely, the simultaneous expansion and acceleration of a compressible fluid. This behaviour is not possible for an incompressible fluid, and is only possible in this case because the density of the compressible fluid decreases so that the mass flow rate is still conserved. The cross-sectionally averaged velocity and density are shown in figure 5.6d.

The rapid change in pressure near where the impermeable boundary and free boundary meet, which can be seen in the illustration of the pressure in figure 5.6b, indicates the presence of a pressure singularity where the boundary condition changes. A change in type of boundary condition, in this case from a slip boundary to a free boundary, gives rise to a die-swell singularity at the point between them. The form of the singularity remains to be identified. In this section we shall discuss the consequences of this pressure singularity, and in Section 5.7 we study the nature of this singularity.

The response of a compressible fluid to a pressure singularity will depend on the constitutive law used to close the system of equations. For a bubbly mixture, the bubbles will respond to the pressure *via* (5.18). A local region of low pressure, just as we would expect where the fluid detaches from the die, will result in rapid growth in the bubbles advected through this region. Therefore, we expect to observe larger bubbles on the streamlines that pass closer to the pressure singularity. Moreover, we expect these streamlines to be closer to the slip boundary Γ_d, and therefore bubbles will be advected more slowly along these streamlines compared to those in the centre of the channel. So, due to the lower pressure, as well as having more time to grow, we expect the bubbles closer to the edge to be larger than those at the centre of the channel.

The variation in density throughout the fluid is illustrated in figure 5.6c. In the region bounded by the impermeable boundary, the density is approximately uniform. This indicates that, for this choice of parameters, there is no significant cross-sectional density gradient induced by the lower flow speeds (and therefore greater time available to grow) near the wall. For $z > 0$ we see noticeable variation in the density from the centre of the fluid to the free surface. Namely, the density at the edge of the fluid is lower than the density at the centre.

The density variation, particularly across the cross-section at $z = 1$ is industrially relevant. If the product being extruded is some type of food, this density variation will result in a different texture, or *mouth-feel*, between the edge and core of the product. Understanding the factors that control the final bubble-size distribution in the cross-section will allow for greater control over the properties of the final product. If we only consider the variation in density from the centre to the edge of the fluid at $z = 1$, which is illustrated in figure 5.7a, we observe the maximum density at the

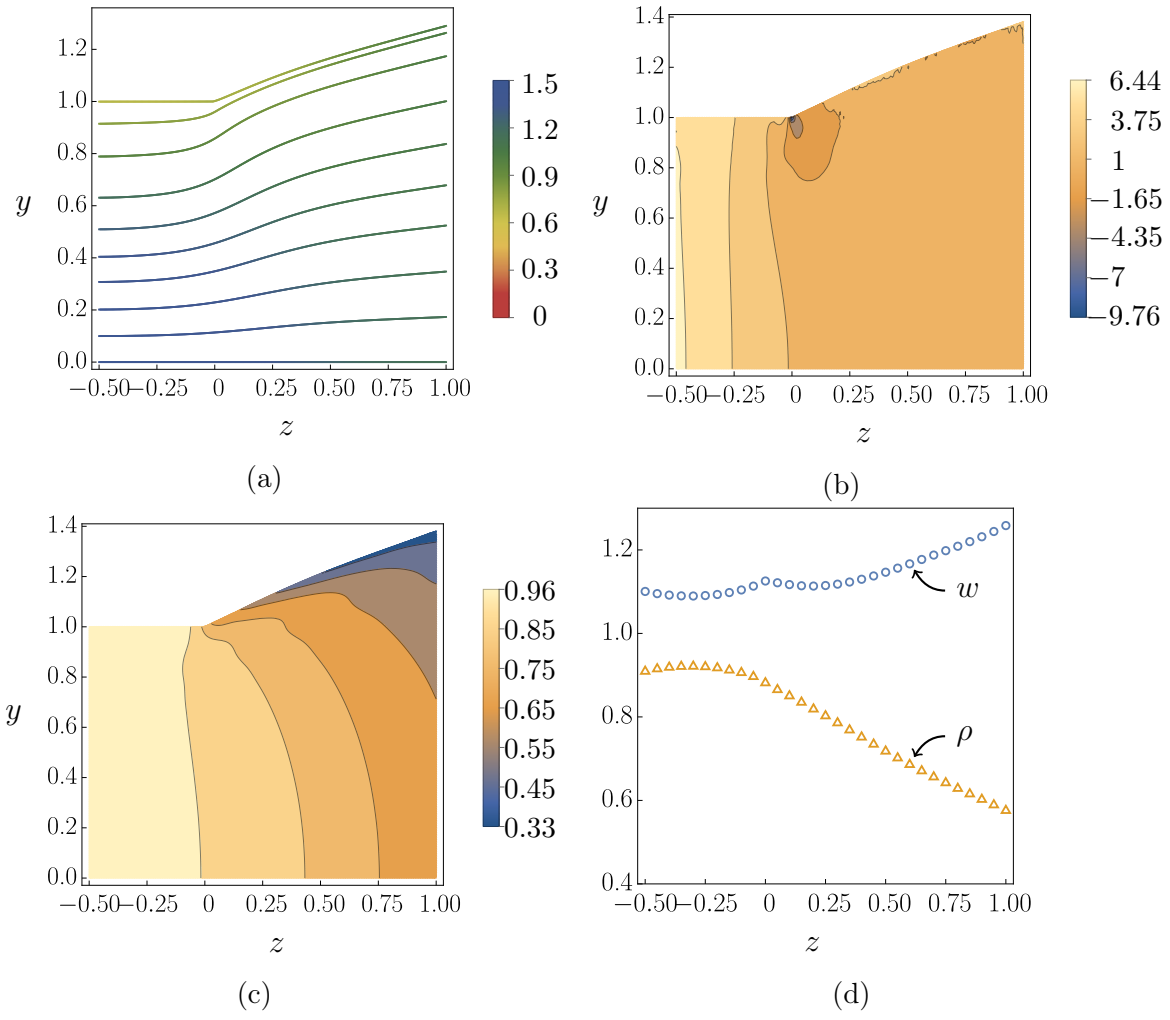

Figure 5.6: (a) *A streamline plot, where the colour of the streamline indicates the magnitude of w, for the extrusion of a compressible fluid. Contour plots of* (b) *pressure and* (c) *density for the extrusion of a compressible fluid. The parameters used in this simulation are those contained in tables 2.2 and 2.3, as well as $\epsilon = 1$ and $\beta = 0.1$.* (d) *The average velocity (blue circles) and density (yellow triangles).*

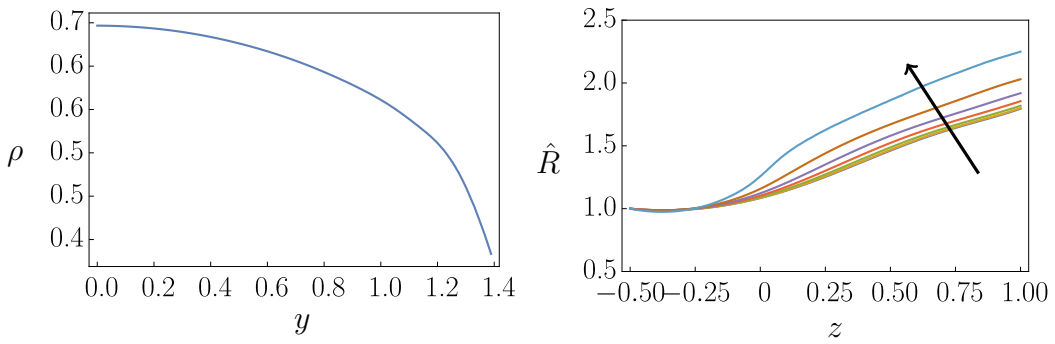

(a) (b)

Figure 5.7: (a) *The density at $z = 1$ from the centre to the edge of the fluid.* (b) *The radius of bubbles along a number of streamlines ranging from $\psi = 0$ to $\psi = 1$ in intervals of $\Delta\psi = 1/7$, the arrow indicates the direction of increasing streamline number. The parameters used in this case are the same as those used in figure 5.6.*

centre of the fluid, and a decrease towards the edge. The density gradient is greatest near the edge of the fluid, which corresponds to the region of the fluid that passed closest to the pressure singularity.

We can look to the microscale model to better understand the cross-sectional density variation at $z = 1$. The size of bubbles along a number of streamlines is illustrated in figure 5.7b. The rate of change of the size of the bubbles is roughly the same on all streamlines away from $z = 0$; however, near $z = 0$, bubbles grow more rapidly if they are closer the pressure singularity. Given that the discrepancy between bubble size from the centre of the fluid to the edge is dependent on the strength of the pressure singularity, any mechanism by which this singularity can be manipulated will result in different density variation throughout the cross-section.

Having introduced a slip length, β, and with the knowledge that, for the incompressible partial-slip/slip problem considered by Salamon *et al.* [62], the pressure singularity behaves like $p \sim \ln(r)/\beta$, we can manipulate the strength of the singularity by varying β. As the value of β is decreased, the difference between the density at the centre of the fluid, and the density at the edge of the fluid at $z = 1$ widens, as illustrated in figure 5.8. Some of the behaviour we observe in figure 5.8 is non-intuitive; namely, the density at the edge of the fluid is non-monotonic in β.

To understand the results illustrated in figure 5.8, we consider the factors that control bubble growth, and how the slip length affects these factors. Using the schematic in

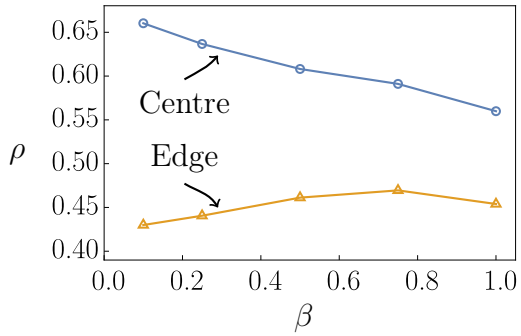

Figure 5.8: *The density at the centre (blue circles) and edge (yellow triangles) of the fluid at* $z = 1$ *for different slip lengths.*

figure 5.3 as a guide, the density variation along z depends on the pressure, p, and axial velocity, w. Lower pressure promotes bubble growth, while higher pressure resists growth, and may even result in collapse. Greater velocities allow less time for bubble growth. Decreasing the slip length has three consequences on the pressure and velocity fields:

1. there will be a stronger pressure singularity;
2. there will be a greater velocity differential between the centre of the fluid and the fluid near the boundary;
3. the axial pressure gradient for $z < 0$ will be greater.

The third of these consequences can be understood by considering the pressure gradient for Poiseuille flow as a function of slip (5.29), which increases as slip is decreased.

The density at the centre of the fluid, illustrated by blue circles in figure 5.8, increases as the slip length is decreased. For each of the three effects that slip might have on p and w, we now consider the effect this would have on bubbles in the centre of the fluid. The pressure singularity where the die, Γ_d, meets the free boundary, Γ_f, acts locally, and has very little impact as far away as the centre of the fluid. Therefore, we do not expect the strengthening of this singularity as β is decreased to have much effect on bubbles in the centre of the fluid. As β is decreased, keeping the mass flux fixed, the velocity at the centre of the fluid will increase, allowing less time for bubbles to grow by the time they reach $z = 1$. A larger pressure gradient in $z < 0$, which reaches atmospheric pressure, p_{atm}, near $z = 0$, leads to higher pressures in $z < 0$, which will prevent bubble growth. So, by considering each of the three effects that the slip might have on p and w in the centre of the fluid, we conclude

that decreasing β should only decrease the final bubble size, and hence increase the density at $z = 1$. This explains the monotonic increase in density at the centre of the fluid as β decreases illustrated in figure 5.8.

The density at the edge of the fluid is non-monotonic as β is decreased, as illustrated in figure 5.8. We again consider the effect of β on p and w, this time for bubbles near the edge of the fluid. Bubbles near the slip wall will experience the effect of a stronger singularity, and will be advected more slowly for smaller slip values. Both of these changes will promote greater bubble growth. An exception to this trend would be if the pressure in $z < 0$ is great enough to shrink the bubbles, and the flow speed slow enough to allow significant contraction. The greater pressures in $z < 0$, as a result of decreasing β, will resist bubble growth. So, unlike bubbles on the centre-line, the mechanisms by which decreasing β can affect bubble growth are in competition; some promote bubble growth, and others resist it. This competition explains the non-monotonicity observed in the final density at the edge of the fluid illustrated in figure 5.8.

5.6.2 Comparison to asymptotics

Using the numerical scheme detailed in this chapter, we can assess the accuracy of the leading-order system considered in Chapter 4. We modify the solution domain from Section 5.6.1 so that we only consider the flow outside of the die; that is, we consider the region $0 < z < 1$. In figure 5.2, this corresponds to moving the inlet to $z = 0$, eliminating Γ_d from the domain, and leaving only Γ_f on $\psi = 1$, as illustrated in figure 5.9. In this case, we prescribe a uniform inlet flow profile for w and a uniform density in order to be consistent with the assumptions made in the derivation of the leading-order system.

The system of equations that we wish to verify from Chapter 4 is composed of (4.50)–(4.53); the equations corresponding to steady inertialess flow with zero surface tension. For the sake of this comparison, we will close the system of equations using the simple microscale closure derived from Boyle's law in Section 4.1.3. This means that we replace the generic closure (4.53) with (4.57), where $\hat{p}_{\mathrm{B}}$ is given by (4.59), and that the density can be found by solving the autonomous ODE (4.61). Although finding solutions to this leading-order system is far simpler than it is for the full system, the question remains: do the solutions to the leading-order system accurately represent the solutions to the full system?

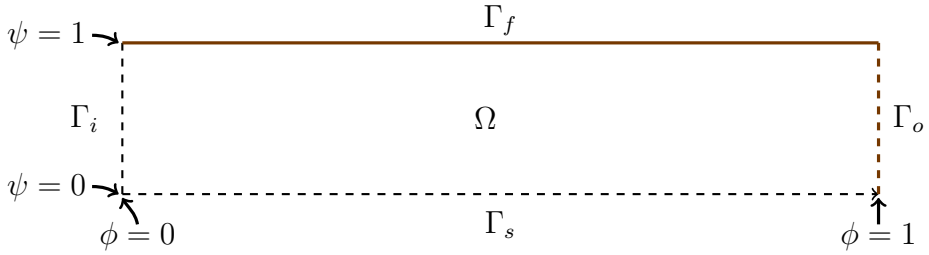

Figure 5.9: *Solution domain, Ω, in the streamline coordinates. The boundaries are denoted by Γ_d for the die, Γ_i for the inlet, Γ_s for the line of symmetry, Γ_o for the outlet, and Γ_f for the free boundary (which is fixed in ϕ in the (ϕ, ψ) plane).*

We expect the numerical solution to asymptote to the leading-order, asympotic solution in the limit as $\epsilon \to 0$. We illustrate the numerical prediction of the half-width, h, for various values of ϵ, as well as the solution of the leading-order model in figure 5.10a. Qualitatively, the leading-order solution captures the behaviour of each numerical solution illustrated; however, it is clearly far more accurate for the lower values of ϵ.

For a quantitative measure of the agreement between the solution to the full system and the leading-order system, we will define a measure of error, and then determine how this error reduces as $\epsilon \to 0$. We measure error with respect to the L_2-norm, defining the error, E, to be given by

$$E(\epsilon) := \left(\int_0^1 \left(h_{\mathrm{n}}(z;\epsilon) - h_{\mathrm{a}}(z) \right)^2 \mathrm{d}z \right)^{1/2}, \tag{5.53}$$

where $h_{\mathrm{a}}(z)$ is the leading-order height, and $h_{\mathrm{n}}(z;\epsilon)$ is the numerical solution for the height. We calculate E for the solutions illustrated in figure 5.10a, and illustrate these values in figure 5.10b. The slope of $\log_{10}(\epsilon)$ *v.s.* $\log_{10}(E)$ is approximately 1, which indicates that the solutions are converging linearly in ϵ. The reason we see linear convergence, as opposed to ϵ^2, is discussed by O'Kiely *et al.* [52], and is due to a boundary layer of size $\mathcal{O}(\epsilon)$ near $z = 0$.

5.7 Analysis of the corner singularity

In Section 5.6.1, we identified the presence of a pressure singularity at the point where the compressible fluid detaches from the die wall. We then demonstrated that this

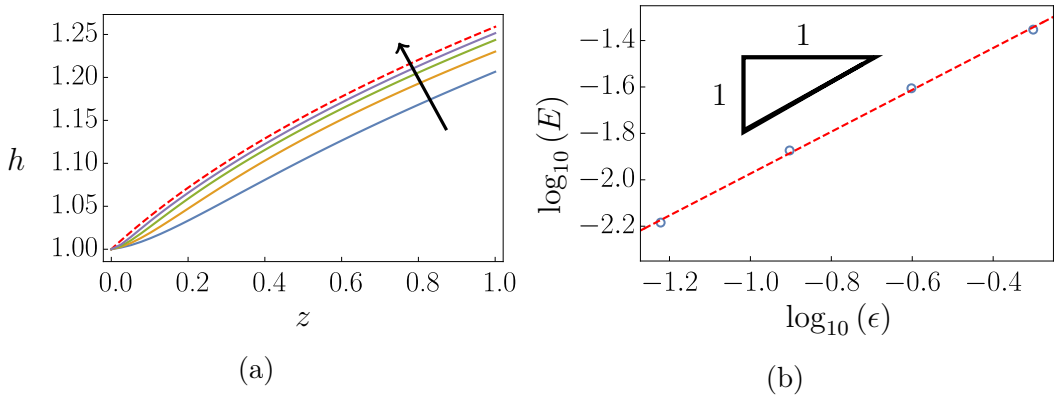

Figure 5.10: (a) *The half-width, h, as predicted by the reduced, slender-limit model of Chapter 4, Section 4.1.3 (red, dashed) and from numerical solutions with* $\epsilon = \{1, 1/2, 1/4, 1/8\}$. *The arrow indicates the direction of decreasing* ϵ. (b) $\log_{10}$ *of the error, E, between the numerical solution and the asymptotic solution in the limit* $\epsilon \to 0$ *defined by (5.53). The slope of* $\log_{10}(E)$ *vs.* $\log_{10}(\epsilon)$ *is approximately 1, indicating linear convergence as* $\epsilon \to 0$.

singularity affects the final product; namely, the fluid that passes closer to this singularity will be less dense. Furthermore, we demonstrated that manipulating this singularity (by changing the slip-length) changes the properties of the final product. This means that, from an industrial perspective, it is important to understand this pressure singularity and how to manipulate it. We have yet to identify the form of this singularity for a compressible fluid; however, Salamon *et al.* [62] demonstrate that the pressure, p, for an incompressible fluid scales with $\ln(r)/\beta$, where r is the distance to the point of detachment and we recall that β is the slip length. In this section we consider the form of the pressure singularity for a compressible fluid, and compare this to the incompressible case.

Studies of the pressure singularity near the point of detachment are usually performed by considering the local behaviour near this point. Locally, the fluid boundary comprises a wall and a free surface, as illustrated in figure 5.11; because of the local geometry, this is referred to as corner flow. In this section we first consider corner-flow problems in the literature concerning incompressible fluids. We then consider the local pressure profile for a compressible fluid, predicted using numerical simulations, and compare these predictions to those of the analogous incompressible case. Finally, we rationalise this comparison by performing asymptotic analysis for a weakly compressible fluid.

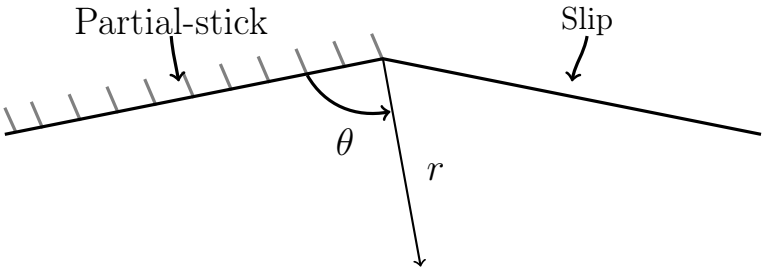

Figure 5.11: *An illustration of the corner flow for the partial-stick/slip problem.*

5.7.1 Literature review: the die-swell singularity

For a viscous, incompressible fluid separating from a rigid boundary at an angle of π, Michael [46] showed that there must be a singularity in the pressure at the point of separation. This was shown by considering a polar coordinate system with its origin at the point of separation, and then solving for the stream function by finding the local behaviour of $\psi(r, \theta)$ as $r \to 0$. In order to satisfy all of the boundary conditions, the stream function must include a term that results in a $r^{-1/2}$ singularity in the pressure; without this term, there are insufficient degrees of freedom to satisfy the boundary conditions. In fact, even stronger singular terms are mathematically allowed, but these are neglected on physical grounds. The discovery of this singular behaviour by Michael has motivated subsequent study into the behaviour of flow near the point of separation for a range of different flow scenarios. For example, Moffat [48] classified the behaviour of an incompressible fluid for a range of corner-flow problems with different boundary conditions and detachment angles.

We discussed the stick–slip problem in Section 5.5. The analytic solution presented by Richardson [59] contains the same pressure singularity predicted by Michael [46]; namely, p scales with $r^{-1/2}$ as $r \to 0$. Our numerical method replaces the no-slip boundary condition with a slip law. This fundamentally changes the nature of the pressure singularity. By performing a local analysis near the point of detachment for the *partial-slip/slip* problem, Salamon *et al.* [62] demonstrate that introducing a slip length leads to local pressure behaviour where p scales with $\ln(r)/\beta$. This singularity presents itself as the region of rapid variation in the pressure contour plot illustrated by figure 5.4b. Salamon *et al.* [63] also considered the partial-slip/slip problem for a viscoelastic fluid, and found that there is no fundamental change in the nature of the singularity at the point of detachment; that is, the local pressure still scales with $\ln(r)/\beta$. So, in this case, introducing a slip length changes the nature of the pressure

singularity, but then modifying the constitutive law for the stress in the fluid does not. In this section we compare the nature of the pressure singularity in the incompressible partial-slip/slip problem to the compressible partial-stick/slip problem.

5.7.2 Numerical results

To study the difference between the pressure singularity for compressible and incompressible fluids, we will use the simplest example of a viscous, compressible fluid considered in this thesis. We consider a bubbly mixture, where the pressure in the bubbles is given by Boyle's law. The corresponding microscale closure law is given by (5.19). The governing equations for the compressible partial-stick/slip problem are derived using the same steps described in Section 5.5, except we do not set $\rho = 1$.

We first study the pressure in the incompressible partial-slip/slip problem in more detail. From the local analysis performed by Salamon *et al.*[63], we expect to see stronger pressure drops for smaller slip lengths. Our numerical solutions reflect this behaviour. The pressure profiles for a number of slip lengths are illustrated in figure 5.12a. If we instead consider the pressure as a function of $\ln(r)$, as we illustrate in figure 5.12b, we observe a linear relationship. This suggests that we have recovered the pressure scaling behaviour predicted by Salamon *et al.* [62].

We perform a similar analysis for the compressible problem. The pressure local to the detachment point for a range of slip lengths is illustrated in figure 5.13a. We note that, qualitatively, the pressure behaves similarly: the pressure decreases as the detachment point is approached, and decreasing the slip length results in a more prominent pressure drop. For a compressible fluid, the effective compressibility can change, and will be a function of, among other things, the fraction of the mixture that is made up of gas. We use $\tilde{\eta}$—which is the volume fraction ratio of gas to liquid, given by (4.55)—as a proxy for the compressibility, and plot p as a function of $\ln(r)$ for a range of $\tilde{\eta}$ values in figure 5.13b. In this same figure we also illustrate the result for an incompressible fluid, which corresponds to $\tilde{\eta} = 0$. We observe that as $\tilde{\eta}$ is increased, the pressure in the compressible case increases; however, we still observe that p scales like $\ln(r)$. So, while the values of the predicted pressure change with compressibility, these results suggest that the logarithmic nature of the singularity does not.

We observe the convergence of the compressible solution to the incompressible so-

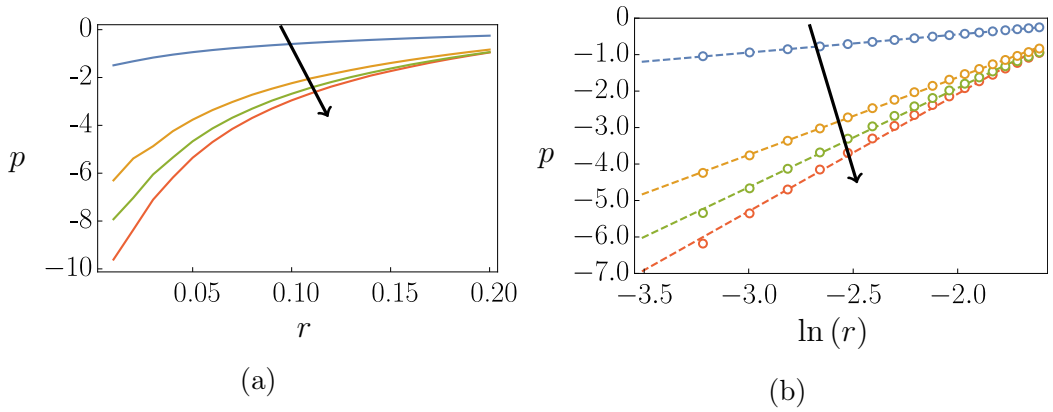

Figure 5.12: (a) *The pressure near the point where the partial-slip and full-slip boundary meet for an incompressible fluid; r denotes the distance from the meeting point, and the pressures shown are taken along a straight line perpendicular to the boundary. In this case, solutions are shown for slip lengths $\beta = \{1, 0.1, 0.05, 0.02\}$, where the arrow indicates decreasing β.* (b) *Sample points of the pressure shown in* (a)*, but, now plotted against* $\ln(r)$*. The dashed lines indicate the line of best fit through these points.*

lution by considering the slope of p *vs.* $\ln(r)$ as a function of $\tilde{\eta}$; we illustrate these values for the slope in figure 5.13c. For small $\tilde{\eta}$, the slope of p *vs.* $\ln(r)$ tends to that for the incompressible problem. While there is a quantitative discrepancy between the more compressible case and the incompressible case, this does not suggest that the nature of the singularity is different. In fact, the convergence of the compressible case to the incompressible case for small $\tilde{\eta}$ suggests that this is a regular perturbation, and does not correspond to a singular limit; however, we consider this perturbation further in the following section.

5.7.3 Corner flow of a weakly compressible fluid

We study the weakly compressible limit to better understand the connection between the nature of the pressure singularity for compressible and incompressible fluids. We first define the weakly compressible limit. The fluids we consider in this thesis are compressible because they contain vapour bubbles of negligible density that can change size. The relationship between the density of the fluid and the bubble size is given by

$$\rho = \frac{1}{1 + \tilde{\eta}\hat{R}^3}; \tag{5.54}$$

so, if $\tilde{\eta} = 0$ there are no bubbles, $\rho = 1$, and the fluid is incompressible. We define the weakly compressible limit to be the limit $\tilde{\eta} \to 0$.

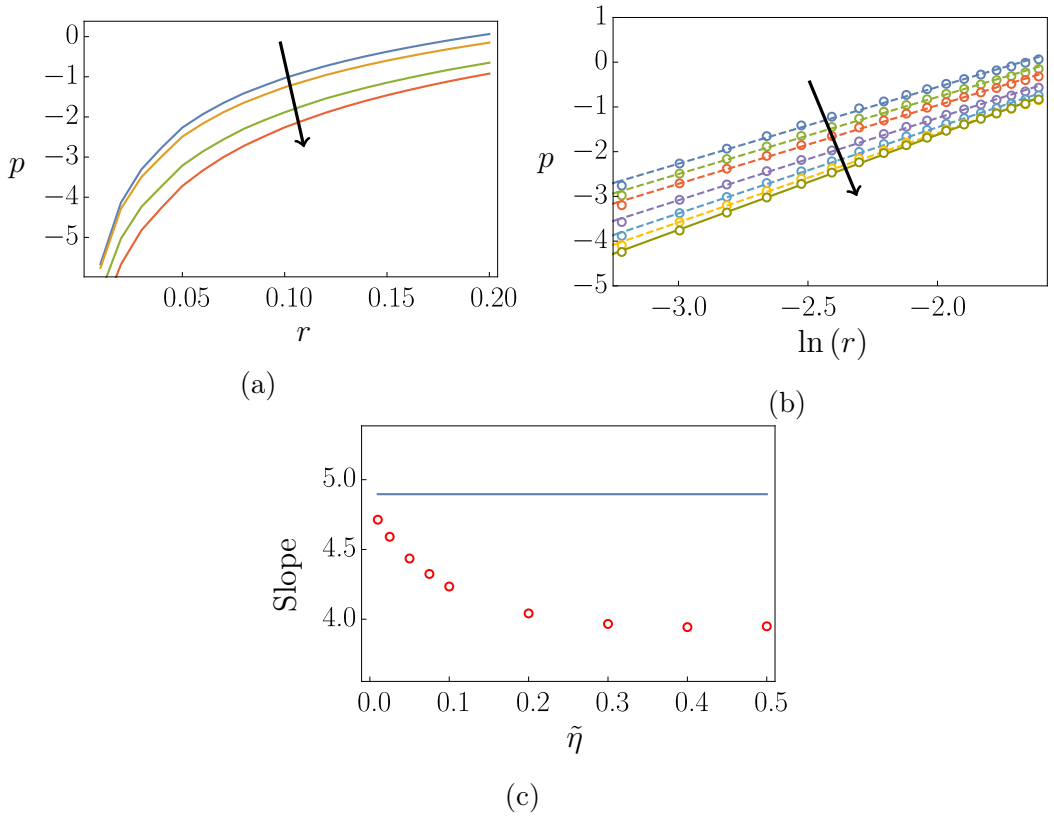

Figure 5.13: (a) *The pressure near the point where the partial-slip and full-slip boundary meet for an incompressible fluid; r denotes the distance from the point where Γ_d and Γ_f meet, and the pressures shown are taken along a straight line perpendicular to the no-slip boundary. In this case, solutions are shown for slip lengths $\beta = \{1, 0.1, 0.05, 0.02\}$ and $\tilde{\eta} = 0.1$. The arrow indicates the direction of decreasing β.* (b) *The pressure, p, as a function of* $\ln(r)$ *for $\beta = 0.1$ and $\tilde{\eta} = \{0.05, 0.1, 0.2, 0.3, 0.5\}$, as well as for the incompressible case (shown by the dashed green line). The arrow indicates the direction of decreasing $\tilde{\eta}$.* (c) *The slope of p vs* $\ln(r)$ *for the same $\tilde{\eta}$ as in* (b); *the blue line indicates the slope for an incompressible fluid.*

We study the local behaviour of the fluid near the point where Γ_d and Γ_f meet. The local problem can be represented as a corner-flow problem, for which two different types of boundaries meet at a given angle, as illustrated in figure 5.11. This is the same geometry considered in much of the literature concerned with singularities at changes in boundary condition (*e.g.* see [46, 48, 62]), and for which analytic solutions exist for incompressible flows. We use a polar coordinate system with its origin where the two different boundaries meet; (r, θ) denote local cylindrical polar coordinates, as illustrated in figure 5.11. For comparison to our numerical simulations, we are interested in the case where Γ_d is a partial slip boundary with a slip length β, and Γ_f is a full-slip boundary.

Consider the governing equations for the steady flow of a compressible fluid given by

$$\nabla \cdot (\rho \boldsymbol{u}) = 0, \tag{5.55}$$

$$\nabla \cdot \boldsymbol{\sigma} = 0, \tag{5.56}$$

$$\boldsymbol{u} \cdot \nabla \rho = -\frac{3(1-\rho)\rho}{4} \left(\frac{C\tilde{\eta}\rho}{1-\rho} - p - p_{\text{atm}} - \frac{\Gamma \tilde{\eta}^{1/3} \rho^{1/3}}{(1-\rho)^{1/3}} \right), \tag{5.57}$$

where

$$\boldsymbol{\sigma} = \left(-p + \lambda \nabla \cdot \boldsymbol{u}\right) \mathbb{I} + \mu \left(\nabla \boldsymbol{u} + \nabla \boldsymbol{u}^T \right), \tag{5.58}$$

and (5.57) is derived in a similar manner to the closure used in Chapter 4 given by (4.57). The parameters that control the rate of density change are C, which is constant, the dimensionless atmospheric pressure, p_{atm}, and the dimensionless surface tension, Γ. We suppose that $\tilde{\eta} \ll 1$, and expand the dependent variables in powers of $\tilde{\eta}$, so that

$$\rho = 1 + \tilde{\eta}\rho^{(1)} + \mathcal{O}(\tilde{\eta}^2), \tag{5.59}$$

$$\boldsymbol{u} = \boldsymbol{u}^{(0)} + \tilde{\eta}\boldsymbol{u}^{(1)} + \mathcal{O}(\tilde{\eta}^2), \tag{5.60}$$

$$p = p^{(0)} + \tilde{\eta}p^{(1)} + \mathcal{O}(\tilde{\eta}^2). \tag{5.61}$$

The leading-order system of equations is given by

$$\nabla \cdot \boldsymbol{u}^{(0)} = 0, \tag{5.62}$$

$$\nabla^2 \boldsymbol{u}^{(0)} = \nabla p^{(0)}, \tag{5.63}$$

which is equivalent to the equations of Stokes flow for an incompressible fluid. At first order we have an equation for $\rho^{(1)}$ given by

$$\boldsymbol{u}^{(0)} \cdot \nabla \rho^{(1)} = -\frac{3C}{4} - \frac{3\rho^{(1)}(p^{(1)} + p_{\text{atm}})}{4} + \frac{3\Gamma}{4}. \tag{5.64}$$

So, the leading-order system, comprising equations (5.62) and (5.63), is independent of the density, and the solutions for $\boldsymbol{u}_0$ and p_0 then inform equation (5.64) for the first-order density ρ_1. A key consequence of this decoupling is that the leading-order conservation-of-mass and conservation-of-momentum equations, (5.62) and (5.63), are those of an incompressible fluid, for which solutions in a range of scenarios can be found in literature for different corner-flow problems (see in particular the work of Moffatt [48]). The solution to the incompressible partial-slip/slip problem [62] has a logarithmic pressure singularity at $r = 0$. Therefore, we expect that, for small $\tilde{\eta}$ values, the nature of the singularity is unchanged, which is supported by the numerical solutions illustrated in figure 5.13.

The key finding of the analysis of a weakly compressible fluid, for a bubbly fluid with density given by (5.54), is that, to leading order in $\tilde{\eta}$, the density decouples from the conservation-of-mass and conservation-of-momentum equations. The dynamics of the fluid will be those of an incompressible fluid, with an order $\tilde{\eta}$ density correction. It is therefore not surprising that we do not observe a change in the nature of the singularity for the partial-stick/slip problem. Given the singular nature of p_0, and the dependence of ρ_1 on p_0, there may be cases for which $\tilde{\eta}\rho_1$ becomes order 1, and the leading-order equations given by (5.62) and (5.63) are no longer valid; however, the numerical solutions illustrated in figure 5.13b indicate that, for the cases we consider, the leading-order equations are not modified significantly enough to change the nature of the pressure singularity.

5.8 Axisymmetric equations

The same method of finding solutions to the 2D system, considered in Sections 5.3 and 5.4, can be applied to the 3D system in an axisymmetric geometry. The definition of the stream function in 3D is different to that for the 2D case, (5.13); however, the key steps in deriving a system of equations, which are solved on a rectangular domain, are the same. Namely, we perform a partial hodograph transformation, and then find the weak formulation of the resulting system of equations in order to construct a numerical scheme using finite elements.

5.8.1 Governing equations and weak form

In this section, we summarise the equations governing axisymmetric flow, and the key differences between the 2D case and the axisymmetric case. The details of the algebra required to construct a weak formulation of the axisymmetric problem are contained in Appendix B.

We use a cylindrical coordinate system, where r now denotes the radial distance from the centre of the fluid (we assume the centre-line of the fluid is fixed), and, as in the 2D case, z is the axial coordinate. The radial coordinate is non-dimensionalised in the same manner as x and y; that is, the dimensionless radius, r', is given by

$$r = \epsilon L r'. \tag{5.65}$$

All other variables are non-dimensionalised using the same scalings that lead to the 3D equations, (4.70)–(4.73), in Cartesian coordinates described in Chapter 4. We only consider dimensionless quantities and drop primes from hereon. The velocity is given by $\boldsymbol{u} = (w, u)$, where w and u are the axial and radial components of velocity respectively. The fluid domain in (z, r) coordinates looks similar to the fluid domain illustrated in figure 5.1, but with y replaced by r. We describe the axisymmetric case using similar notation to the 2D case. Namely, Γ'_i, Γ'_s, Γ'_o, Γ'_f, and Γ'_d denote the inlet, line of symmetry (*i.e.* the centre-line in this case), the outlet, the free boundary, and the die respectively. We denote the domain in (r, z) coordinates by Ω'.

The equation governing conservation of mass in Ω', for the steady, axisymmetric flow of a compressible fluid, is given by

$$\frac{1}{r}\frac{\partial}{\partial r}\left(r\rho u\right) + \frac{\partial}{\partial z}\left(\rho w\right) = 0, \tag{5.66}$$

and the conservation-of-r-momentum and conservation-of-z-momentum equations in Ω' are respectively given by

$$\frac{1}{r}\frac{\partial}{\partial r}\left(r\left(-p + \lambda\left(\frac{1}{r}\frac{\partial}{\partial r}\left(ru\right) + \frac{\partial w}{\partial z}\right) + 2\mu\frac{\partial u}{\partial r}\right)\right) + \frac{\partial}{\partial z}\left(\mu\left(\epsilon^2\frac{\partial u}{\partial z} + \frac{\partial w}{\partial r}\right)\right) = 0, \tag{5.67}$$

$$\frac{1}{r}\frac{\partial}{\partial r}\left(r\mu\left(\epsilon^2\frac{\partial u}{\partial z} + \frac{\partial w}{\partial r}\right)\right) + \epsilon^2\frac{\partial}{\partial z}\left(-p + \lambda\left(\frac{1}{r}\frac{\partial}{\partial r}\left(ru\right) + \frac{\partial w}{\partial z}\right) + 2\mu\frac{\partial w}{\partial z}\right) = 0. \tag{5.68}$$

This system is closed in the same way as the 2D system; that is, by coupling it to a microscale model for bubble growth, assuming that the bubbles are advected by the

fluid. On Γ_i' we prescribe the initial density, ρ_0, as well as the inlet flow profile given by

$$u = 0 \qquad \text{and} \qquad w = w(r). \tag{5.69a,b}$$

On the free boundary, Γ_f', we impose the kinematic and dynamic boundary conditions, neglecting surface tension, respectively given by

$$\boldsymbol{u} \cdot \boldsymbol{n} = 0 \qquad \text{and} \qquad \boldsymbol{\sigma} \cdot \boldsymbol{n} = 0. \tag{5.70a,b}$$

On the line of symmetry Γ_s', we impose symmetry boundary conditions given by

$$\frac{\partial w}{\partial r} = 0 \qquad \text{and} \qquad u = 0. \tag{5.71a,b}$$

On Γ_o' we impose that there is no stress; that is,

$$\boldsymbol{\sigma} \cdot \boldsymbol{e}_z = \boldsymbol{0}. \tag{5.72}$$

We impose a Navier-slip law [43] on Γ_d', just as we did for the 2D case, given by

$$-\beta \frac{\partial w}{\partial r} = w, \tag{5.73}$$

where β is the slip length, which we take to zero to recover a no-slip boundary. The remaining boundary condition on Γ_d' is given by

$$u = 0, \tag{5.74}$$

which enforces that the die is immobile.

By defining a stream function according to

$$\rho u = -\frac{1}{r}\frac{\partial \psi}{\partial z}, \qquad \rho w = \frac{1}{r}\frac{\partial \psi}{\partial r}, \tag{5.75a,b}$$

and defining $\phi = z$, we can perform a partial hodograph transform in a similar manner to the 2D case described in Section 5.3. We can then construct the weak-formulation of the axisymmetric problem on a rectangular domain. The details of this process are contained in Appendix B. The key difference between the 2D and axisymmetric cases is that, after the partial hodograph transformation, the (previously) independent variable r, features in the transformed governing equations. This means that the inverse mapping, from (ψ, ϕ) to (r, z) coordinates, must be determined as part of the solution. One way of achieving this is to build the inverse mapping into the weak formulation of the problem.

The inverse mapping is given by solving the differential equation given by

$$1 - r\rho w \frac{\partial r}{\partial \psi} = 0, \tag{5.76}$$

which is a re-expression of (5.75b). In the 2D case, we evaluate the analogous inverse mapping, given by (5.45), after solving the equations in (ψ, ϕ) coordinates.

Finding solutions to the axisymmetric equations is made more challenging by the coordinate singularity near $r = 0$. This manifests through the solution to the pressure; preliminary results suggest erroneous pressures values near the ϕ axis. These errors can be more tightly confined to a region near the ϕ axis by improving the resolution of the mesh in this region. For incompressible flow, as long as the mesh is sufficiently fine so that the erroneous pressure values are tightly bound to the ϕ axis, this does not significantly impact the solution to the velocity field. For compressible problems, the pressure has a much stronger effect on the solution. If the pressure along the ϕ axis is not accurately resolved, the corresponding effect on the density field will be significant. Over predicting the pressure can lead to unphysical bubble collapse, giving unreliable predictions for the properties of the final product. This issue as $r \to 0$ must be suitably managed for this method to be used in the simulation of extrusion.

5.9 Summary of chapter

In this chapter we discussed a methodology for finding solutions to the steady-state extrusion model presented in Chapter 2. This new methodology was introduced in order to deal with two complicating aspects of the model: the free boundary, and a constitutive law that must be integrated along the particle paths. The methodology we detailed was designed to exploit the streamline structure. Because of this, the method is restricted to 2D and axisymmetric geometries; however, both of these cases are industrially relevant.

In Section 5.2, we described the macroscale model in 2D (z, y) Cartesian coordinates. We modified the original macroscale model from Chapter 2 by introducing a slip length on the die wall. In Section 5.3 we introduced a partial hodograph transformation that maps the fluid domain in (z, y) coordinates to a fixed domain in (ϕ, ψ) coordinates, where ψ is the stream function and $\phi = z$. The advantages of

this transformation are two-fold: the free boundary is mapped to a fixed boundary and no longer needs to be determined as part of the solution; and the streamlines, along which the constitutive law that must be integrated, are all parallel to the ϕ axis.

We detailed the numerical method used to solve these equations in Section 5.4. The appropriate method depends on whether or not the microscale constitutive law can be represented entirely in terms of macroscale quantities. When this is the case, such as when the bubble pressure is given by Boyle's law, the microscale closure can be incorporated into the macroscale equations, and a mixed finite element method can be used to find solutions. The weak formulation in this case was presented in Section 5.4. When this is not the case, and integrals must be evaluated along the streamlines, we decompose the full problem into two sub-problems. This was the scenario we consider in Section 5.4.2. The first sub-problem determines w, v, and p by assuming a solution for ρ. The second sub-problem determines ρ from the microscale model by assuming a solution for w and p along the streamlines. These two sub-problems are solved iteratively, using the output of one as the input for the other, until the respective fields no longer change. The resulting procedure can determine solutions to the full system of equations described in Chapter 2.

In Section 5.4.3 we described some of the numerical difficulties that this problem poses. The complexity of the governing equations (particularly in the transformed, (ϕ, ψ) coordinate system), demands a good initial guess for the solution. We find these initial guesses using numerical continuation; starting from a problem that is relatively easy to solve, and then varying the appropriate parameters towards the case of interested. The introduction of a slip length, β, reflects this ethos of using continuation. We encounter numerical difficulties near regions of slow flow. This is particularly problematic near the no-slip boundary. Introducing a large slip length makes the problem much easier to solve, and then decreasing the slip length allows us to approach the no-slip case. An additional benefit of introducing a slip length is the relaxation of the inverse-square-root pressure singularity to a logarithmic singularity at the end of the die.

In the remainder of the chapter we evaluated the efficacy of the numerical method by considering a number of different cases. In Section 5.5 we considered the incompressible, stick-slip problem, which admits an analytic solution. We verified that, as $\beta \to 0$, the numerical solution converges to the analytic solution. In Section 5.6, we solved

the full system of equations presented in Chapter 2, using the iterative procedure described in Section 5.4.2. The compressibility of the fluid we considered introduces a range of behaviours that are not observed for incompressible fluids. Some of these we observed in Chapter 4, and confirmed in this chapter, including the simultaneous acceleration and expansion of the fluid. Others can only be observed by solving the full system of equations. The most important observation from an industrial perspective is the development of non-uniform cross-sectional densities, as this phenomenon will affect the properties of the final product. We discussed the presence of a cross-sectional density gradient, as well as how it can be manipulated by changing the slip length, β.

In Section 5.6.2, we compared the slender-limit solutions of Chapter 4 to the full numerical solutions of this chapter. The slender-limit solutions only consider the fluid outside the die, so we modified our domain to consider the appropriate geometry. The slender-limit solution captured the important features of the numerical solution for ϵ as large as 1; however, the quantitative agreement between the solutions is much better for smaller ϵ. The error between the slender-limit solution and the numerical solution was found to decrease linearly in ϵ.

In Section 5.7 we considered the pressure distribution local to where a partial-slip boundary meets a full-slip boundary; namely, we considered the form of the pressure singularity that present at this point. We first considered an incompressible fluid, and verified that we observe that p scales with $\ln(r)$; as predicted by Salamon *et al.* [62]. We then considered a fluid with a simple pressure–density closure relation. In this case we supposed that the fluid contained bubbles whose pressure was given by Boyle's law. We found, numerically, that the introduction of compressibility did not appear to change the nature of the pressure singularity. We then analysed the weakly compressible limit in order to get a better understanding of why this might be the case. In this limit, the change in density decouples from the conservation-of-mass and conservation-of-momentum equations for the fluid. Consequentially, the stress field in the flow, and hence the pressure, will be the same as if the fluid was incompressible. Based on the weakly compressible-limit analysis, we would not expect to see the nature of the pressure singularity change for weakly compressible fluids.

In Section 5.8 we considered an axisymmetric geometry. The governing equations in this case contained some key differences to the 2D case that required modifying

the solution method slightly. One key difference was that, after performing the partial hodograph transformation, the radial coordinate r was present in the governing equations. This means that for the axisymmetric system, the inverse map from ψ to r must be determined at the same time that the remaining governing equations are solved.

Chapter 6

Concluding remarks

In this chapter we summarise the findings of this thesis, and discuss opportunities for future work. Future work includes extensions, which are lines of inquiry made possible through this work, and improvements, which are tasks that will improve the applicability of our work. We end this chapter with a discussion on the industrial relevance of this work, and how it might be used by an industrialist.

6.1 Summary

In Chapter 1 we introduced a manufacturing technique known as extrusion. While this technique is in widespread use, simulation of this process is not. This motivated the work contained in this thesis. We described methods of simulating extrusion in order to aid in the development of new products by reducing the financial cost of, and time spent, performing experiments. In Chapter 1, Section 1.3, we reviewed literature on extrusion and models for related processes.

In Chapter 2 we presented a model for extrusion based on the semi-discrete models found in the literature; namely, the model of Lach [42]. The difference between the model presented in Chapter 2 and those found in literature is that the model we presented in Chapter 2 is expressed in an entirely continuum framework. The more mathematically general framework we used to describe extrusion allowed for the analysis we performed in subsequent chapters.

Our analysis of the model presented in Chapter 2 uses a principle of modularity; breaking the full model into simpler, coupled sub-components. The first example of this principle is the separation of microscale and macroscale dynamics. In this case, the method for solving the microscale model can be developed independently of the

method used to solve the macroscale model.

In Chapter 3 we considered the microscale model in isolation. In doing so, we deduced a macroscopic length scale over which bubbles grow that depends on the microscale parameters. We also deduced, based on the microscale dimensionless parameters, three different asymptotic regimes, or *Cases*. Each of these cases describes a different Péclet number regime: in Case I, $\widehat{Pe}_c \ll \widehat{Pe}_T \ll 1$; in Case II, $\widehat{Pe}_c \ll 1 \ll \widehat{Pe}_T$; and in Case III, $1 \ll \widehat{Pe}_c \ll \widehat{Pe}_T$. For each of these cases we were able to derive reduced models that approximate the solution to the full microscale model. Following this analysis of the microscale dimensionless parameters, we considered two methods for finding solutions to the microscale model: solving the full system of equations numerically, or solving reduced systems of equations to give approximate solutions. We found an analytic solution to the reduced model for Case III when the macroscale pressure is constant.

In Chapter 4 we considered the macroscale model in the long–thin limit. We presented a leading-order model that describes the evolution of some key quantities for a viscous, compressible fluid along the axis of flow in both two-dimensions (2D) and three-dimensions (3D). The 2D model describes the flow of a sheet of fluid, and the 3D model describes the flow of a thread, or fibre of fluid. The leading-order model in each case was derived in a similar manner to the Trouton model for incompressible flow. In order to progress, we assumed that the density was uniform over the cross-section. In 2D, under this assumption, the pressure will necessarily be uniform in the cross-section as well. In 3D, when the density is uniform in the cross-section, the pressure will only be uniform if the cross-section is circular or surface tension is negligible. The inverse capillary number, γ^*, which is defined in (2.63) and describes the relative effect of surface tension acting against the viscosity of the fluid, is small for practically relevant parameters (see table 2.2). As a result, the assumption that surface tension is negligible does not restrict the applicability of the reduced model significantly. In both of the cases for which this model is valid, when surface tension is small or the cross-section is circular, we expect the cross-sectional area to change, but not the shape.

In order to consider cases with significant surface tension, we proposed a modified pressure–density closure relationship. Instead of supposing that the density at each point depends on the pressure at that point, we supposed that the density at each

point evolves according to the cross-sectionally averaged pressure. With this modified closure relation, cross-sectional pressure variation induced by the surface-tension-driven flow does not lead to cross-sectional density variation. As a result, much of the analysis required to derive the Trouton-like model can be extended to account for cases with non-negligible surface tension. One effect of surface tension is to change the shape of the cross-section. The rate at which this shape change occurs is captured by studying the evolution of a 2D blob of fluid with an artificial time variable, τ, which can be related to the axial distance, z. Dilating the map between τ and z—by increasing the cross-sectional area or axial speed, or decreasing the inverse capillary number—slows down the axial evolution of the cross-sectional shape; in this case the final shape will more closely resemble the die through which it was extruded. The reduced model for the shape change is another example of modularity, decomposing the model into easier-to-solve, sub-components. In this case, the model for the changing shape of the cross-section can be solved independently of the model for axial evolution.

The simplicity of the Trouton-like model allowed for the study of mixtures with more complicated physical properties. In Section 4.4 we incorporated a temperature dependent fluid viscosity into our extrusion model. We also incorporated a microscale heat sink term, which corresponded to heat lost from the liquid in order to vapourise the gas. In the long–thin limit, when $\epsilon^2 Pe_T \ll 1$, we derived a reduced conservation-of-energy equation given by (4.186). Using the resulting reduced model, we were able to study the interplay between the thermodynamics of gas vapourisation and the increasing viscosity of the mixture as it cooled. In particular, we found two different long-time behaviours for the product depending on which mechanism acted first to arrest bubble growth. If the increasing viscosity as the product cools is the dominant effect, then the shape of the cross-section will stop evolving. If bubble growth is arrested by thermodynamic means—for example, if the vapour pressure of the mixture decreases to the reference pressure as the product cools—before the viscosity increases significantly, then the cross-section will continue to evolve until it is circular. The reduced models derived in Chapter 4 are particularly well suited to a study of this kind compared to the full model. In addition, the reduced time variables with a constant viscosity and a temperature dependent viscosity, (4.164) and (4.193) respectively, provide simple tools by which the evolution of the cross-sectional shape can be understood without needing to solve the full model directly.

In Chapter 5 we presented a numerical scheme for solving the full model described

in Chapter 2. This scheme, which can be applied in geometries for which the stream function can be defined, incorporates a partial hodograph transformation. This transformation maps the domain with a free-boundary to a rectangle, where the streamline function, ψ, is an independent variable. The advantages of this transformation were two-fold: we no longer needed to solve for the free boundary, and the streamlines were all parallel lines in the new coordinate system. This latter point facilitated integration of the microscale along the particle paths.

We then applied this method in a number of scenarios to help us better understand extrusion. We first tested this method by considering the incompressible stick–slip problem, for which there is an analytic solution. We found that by decreasing the slip-length, which was introduced to make finding numerical solutions easier, we recovered the solution for the no-slip case. We then considered the full microscale–macroscale model of Chapter 2 in 2D, which corresponds to extrusion through a slit. We observed the same qualitative features that were obsered in Chapter 4, namely, an expanding flow profile, a drop in density, and an axial acceleration. We then made a quantitative comparison between the numerical solution and the asymptotic solution, and found them to be in good agreement. A key observation from the numerical solution, which cannot be deduced through the asymptotic solution, is the density variation in the cross-section induced by the fluid's interaction with the die. We found that the density at the edge of the fluid was less than the density at the centre, and that this discrepancy could be magnified by reducing the slip length.

A significant difference between the fluid at the centre and the fluid at the edge of the product is exposure to the pressure singularity where the fluid detaches from the die. Decreasing the slip length is one mechanism by which this singularity can be strengthened. We studied this singularity in more detail in Section 5.7 by discussing related corner-flow literature, performing numerical simulations, and considering the weakly compressible limit. Using numerical simulations, we found the form of the pressure singularity to be given by $p \sim \ln(r)$; the same as the form predicted for the incompressible case by Salamon *et al.* [63]. We rationalised this comparison between the nature of compressible and incompressible fluids by considering the weakly compressible limit, where the volume fraction ratio of gas to liquid at the point of nucleation, $\tilde{\eta}$, is small. Analysis of the weakly compressible limit suggested that, to leading order in $\tilde{\eta}$, the conservation-of-mass and conservation-of-momentum equations reduced to those of an incompressible fluid, namely, Stokes equations. This means

that the local dynamics of this compressible fluid near the point of detachment will be the same as those of an incompressible fluid, and we would therefore expect the form of the pressure singularity to be unchanged from the incompressible case for small $\tilde{\eta}$.

Finally, in Chapter 5, we presented the formulation of this method in the axisymmetric case. A notable difference between the formulations in 2D and in the axisymmetric case is the prevalence of one of the previously independent variables, r, in the governing equations after performing the partial hodograph in the axisymmetric case. This meant that for the axisymmetric case, unlike the 2D case, the inverse map from ψ to r must be determined as part of the solution.

6.2 Future work

In this section we discuss, for each chapter, opportunities to extend or improve the work in this thesis. The model presented in Chapter 2 can be extended to include different types of bubble interactions that may be important to extrusion; namely, bubble coalescence, Otswald ripening, and bubble break-up. Furthermore, this model can be extended by incorporating a more realistic model for nucleation. We have, in general, assumed that the material parameters (*e.g.* μ, λ, c_P *etc.*) were constant, which is consistent with the dispersed-limit assumption in which the mixture is mostly composed of the liquid phase. Capturing the relationship between these parameters and the state of the mixture would help improve the overall model. For much of the analysis contained in this thesis, we make no assumptions about the form of these parameters, so our analysis should still hold if these parameters can vary. An exception is the analysis of Chapter 4, in which we assume that the viscosity is uniform in the cross-section. Given that the same assumption is made about the density, a viscosity that depends on the density will still allow for the subsequent analysis to hold.

In Chapter 3 we presented a number of reduced microscale models. Finding solutions to each of these models was much simpler than finding solutions to the full model. The most complicated of these models involved solving a coupled system of two ODEs and an algebraic equation. This simplicity can be exploited, for example, by searching for other cases that admit analytic solutions (beyond the analytic solution presented for Case III when the external pressure is constant). With the reduction in complexity of the governing equations, methods of studying dynamical

systems of ODEs, such as phase-field analysis, can be used to study the reduced systems in each case.

The Trouton-like macroscale model derived in Chapter 4 offers a computationally cheaper way of performing sweeps over a high-dimensional parameter space compared to solving the full equations. The ability to efficiently consider a wide range of parameters allows for optimum final properties to be determined in a simulated framework before resorting to experiment or higher fidelity numerical simulations. Moreover, the axial-direction in this model, coupled to any of the reduced microscale models presented in Chapter 3, can be reversed. Thus, these reduced models allow for the investigation of the inverse problem, where the final state is prescribed and the appropriate initial state is determined. Solving the inverse problem directly is not possible using the full model as the microscale model includes the heat equation, which is ill-posed backwards in time.

We can extend the Trouton-like model in Chapter 4 by considering generalisations of the Trouton model for an incompressible fluid. We considered one such extension, using the analysis of Stokes *et al.* [66, 67] to include a viscosity that varies along the axis of flow. Further extensions include solving for the centre-line of the fluid, accounting for twisting of irregular cross-section shapes (both of these problems are discussed for the incompressible case by Howell [38]), or considering the extrusion of a thin-walled hollow fibre (the incompressible case is considered by Griffiths and Howell [34, 35]). The utility of this model would be improved if the conditions for which it performs well are better understood. We have demonstrated agreement between numerical simulations and these reduced models; however, comparison to experiment is still required before the predictions of these reduced models can be used effectively.

The numerical scheme presented in Chapter 5 can be used to perform high-resolution simulations of extrusion. With this capability, we can study dependence of the final properties of an extruded product on the initial conditions and the state of the extruder. We can also use this scheme, with different microscale closures, to study the pressure singularity at the point of separation for different fluids. Moreover, by modifying the constitutive law for the stress in the fluid, this method can be used to study the extrusion of a viscoelastic fluid, or other fluids with history-dependent properties.

Although the numerical method described in Chapter 5 can be extended to account for different physical processes, it is inherently limited to considering 2D and axisymmetric geometries. While these cases are of industrial importance, the construction of a fully 3D method would allow for more complex die geometries to be investigated. Two options for solving the full 3D problem include using a phase-field method, or using an Arbitrary-Lagrangian-Eulerian scheme to update the position of the free boundary. Both of these methods are significantly more computationally expensive than the methods we have used.

6.3 Discussion

After a review of the relevant literature, we first expressed the classical models for extrusion, found in literature, in a more general mathematical framework. In this framework, there was greater opportunity for both asymptotic and numerical analysis. The asymptotic analysis of Chapters 3 and 4 are examples of this. Through this analysis, we were able to construct reduced representations of the macroscale and microscale models that are much easier to solve, and more readily offer insight into the physics of extrusion.

To complement this asymptotic analysis we detailed some numerical methods for finding solutions to different parts of this model. The solutions obtained using these methods can either be used to verify the predictions of the asymptotic methods, or to study features of the problem that cannot be studied using the asymptotic methods (*e.g.* cross-sectional density variation). An industrialist wishing to perform simulation can choose how to proceed: find a quick approximation to the solution using the reduced models derived from asymptotic analysis, or perform more time-consuming, but more detailed numerical simulations. The modularity of this problem suggests a third, intermediate option that we did not discuss: use either a reduced macroscale or microscale model coupled to the full model for its counterpart. This alternative option provides the opportunity to perform more detailed studies of particular components of the model, without unnecessary resources being spent on the rest of the problem.

The work contained in this thesis details a number of methods by which extrusion can be simulated. The choice of method depends on the questions one wishes to answer. For example, to study the change in shape of the product, the reduced model

of Chapter 4 can be used. Alternatively, to study the texture variation within the cross-section of the product, given by the bubble size, the numerical method of Chapter 5 can be used. While there is plenty of scope for further development, the work contained in this thesis provides new tools in the understanding of extrusion and the development of extruded products.

Bibliography

[1] Polyflow brochure. Available from: https://www.ansys.com/-/media/ansys/corporate/resourcelibrary/brochure/ansys-polyflow-brochure-140.pdf.

[2] Extruded snack food market—global industry trends, share, size, growth, opportunity and forecast 2019-2024. Available from: https://www.researchandmarkets.com/research/pgqx82/global_extruded?w=5, 2019.

[3] S. H. Alavi, S. S. H. Rizvi, and P. Harriott. Process dynamics of starch-based microcellular foams produced by supercritical fluid extrusion I: model development. *Food Research International*, 36(4):309–319, 2003.

[4] S. H. Alavi, S. S. H. Rizvi, and P. Harriott. Process dynamics of starch-based microcellular foams produced by supercritical fluid extrusion II: numerical simulation and experimental evaluation. *Food Research International*, 36(4):321–330, 2003.

[5] M. Amon and C. D. Denson. A study of the dynamics of foam growth: analysis of the growth of closely spaced spherical bubbles. *Polymer Engineering & Science*, 24(13):1026–1034, 1984.

[6] K. Ando, T. Colonius, and C. E. Brennen. Improvement of acoustic theory of ultrasonic waves in dilute bubbly liquids. *Journal of the Acoustical Society of America*, 126(3), 2009.

[7] A. Arefmanesh, S. G. Advani, and E. E. Michaelides. A numerical study of bubble growth during low pressure structural foam molding process. *Polymer Engineering & Science*, 30(20):1330–1337, 1990.

[8] P. Atkins and J. De Paula. *Atkins' Physical Chemistry*. Oxford University Press, 9th edition, 2010.

[9] G. Barbosa-Cánovas, A. Fontana Jr., S. Schmidt, and T. Labuza. *Water Activity in Foods, Fundamentals and Applications*. Blackwell Publishing, 2007.

[10] E. Barlow, A. M. Bradley, A. J. Mulholland, and C. Torres-Sanchez. A weak-inertia mathematical model of bubble growth in a polymer foam. *Journal of Non-Newtonian Fluid Mechanics*, 244:1–14, 2017.

[11] G. K. Batchelor. *An Introduction to Fluid Dynamics*. Cambridge Mathematical Library. Cambridge University Press, 2000.

[12] A. Bejan. *Convection Heat Transfer*. John Wiley & Sons, Somerset, 2013.

[13] T. B. Benjamin and A. T. Ellis. The collapse of cavitation bubbles and the pressures thereby produced against solid boundaries. *Philosophical Transactions of the Royal Society of London. Series A, Mathematical and Physical Sciences*, 260(1110):221–240, 1966.

[14] C. E. Brennen. *Cavitation and Bubble Dynamics*. Cambridge University Press, 2013.

[15] C.E. Brennen. *Fundamentals of Multiphase Flow*. Cambridge University Press, 2005.

[16] K. W. Commander and A. Prosperetti. Linear pressure waves in bubbly liquids: comparison between theory and experiments. *Journal of the Acoustical Society of America*, 85(2):732–746, 1989.

[17] L. J. Cummings and P. D. Howell. On the evolution of non-axisymmetric viscous fibres with surface tension, inertia and gravity. *Journal of Fluid Mechanics*, 389:361–389, 1999.

[18] B. de Cindio and S. Correra. Mathematical modelling of leavened cereal goods. *Journal of Food Engineering*, 24(3):379–403, 1995.

[19] J. N. Dewynne, P. D. Howell, and P. Wilmott. Slender viscous fibres with inertia and gravity. *The Quarterly Journal of Mechanics and Applied Mathematics*, 47(4):541–555, 11 1994.

[20] J. N. Dewynne, J. R. Ockendon, and P. Wilmott. A systematic derivation of the leading-order equations for extensional flows in slender geometries. *Journal of Fluid Mechanics*, 244:323–338, 1992.

[21] D. A. Drew. Mathematical modeling of two-phase flow. *Annual Review of Fluid Mechanics*, 15(1):261–291, 1983.

[22] D. A. Drew and S. L. Passman. *Theory of Multicomponent Fluids*. Applied Mathematical Sciences. Springer-Verlag New York, 1 edition, 1998.

[23] R. Elshereef, J. Vlachopoulos, and A. Elkamel. Comparison and analysis of bubble growth and foam formation models. *Engineering Computations*, 27(3):387–408, 2010.

[24] P. S. Epstein and M. S. Plesset. On the stability of gas bubbles in liquid–gas solutions. *Journal of Chemical Physics*, 18(11):1505–1509, 1950.

[25] N. Fadai, C. Please, and R. Van Gorder. Asymptotic analysis of a multiphase drying model motivated by coffee bean roasting. *SIAM Journal on Applied Mathematics*, 78(1):418–436, 2018.

[26] B. Fornberg. Calculation of weights in finite difference formulas. *SIAM Review*, 40, 2002.

[27] A. Fowler. *Mathematical Geoscience*. Springer-Verlag London, 1 edition, 2011.

[28] D. F. Gaitan, L. A. Crum, C. C. Church, and R. A. Roy. Sonoluminescence and bubble dynamics for a single, stable, cavitation bubble. *Journal of the Acoustical Society of America*, 91(6):3166–3183, 1992.

[29] G. C. Georgiou. The compressible Newtonian extrudate swell problem. *International Journal for Numerical Methods in Fluids*, 20(3):255–261, 1995.

[30] G. C. Georgiou. The time-dependent, compressible Poiseuille and extrudate-swell flows of a Carreau fluid with slip at the wall. *Journal of Non-Newtonian Fluid Mechanics*, 109(2):93–114, 2003.

[31] G. C. Georgiou and M. J. Crochet. Compressible viscous flow in slits with slip at the wall. *Journal of Rheology*, 38(3):639–654, 1994.

[32] H. M. Gonnermann and M. Manga. The fluid mechanics inside a volcano. *Annual Review of Fluid Mechanics*, 39(1):321–356, 2007.

[33] I. M. Griffiths and P. D. Howell. The surface-tension-driven evolution of a two-dimensional annular viscous tube. *Journal of Fluid Mechanics*, 593:181–208, 2007.

[34] I. M. Griffiths and P. D. Howell. Mathematical modelling of non-axisymmetric capillary tube drawing. *Journal of Fluid Mechanics*, 605:181–206, 2008.

[35] I. M. Griffiths and P. D. Howell. The surface-tension-driven retraction of a viscida. *SIAM Journal on Applied Mathematics*, 70(5):1453–1487, 2010.

[36] E. J. Hinch. *Perturbation Methods*. Cambridge Texts in Applied Mathematics. Cambridge University Press, 1991.

[37] P. D. Howell. Models for thin viscous sheets. *European Journal of Applied Mathematics*, 7(4):321–343, 1996.

[38] P. D. Howell. *Extensional Thin Layer Flows*. PhD thesis, University of Oxford, University of Oxford, 2006.

[39] M. Ishii and T. Hibiki. *Thermo-Fluid Dynamics of Two-Phase Flow*. Springer-Verlag New York, 2006.

[40] A. M. Jellinek and D. Bercovici. Seismic tremors and magma wagging during explosive volcanism. *Nature*, 470(7335):522–525, 2011.

[41] A. Karpinska Portela and J. Bridgeman. CFD-aided modelling of activated sludge systems—a critical review. *Water Research*, 88, 2015.

[42] L. Lach. *Modelling Vapour Expansion of Extruded Cereals*. PhD thesis, La Faculté Sciences et Techniques De L'ingénieur, École Polytechnique Fédérale De Laussanne, 2006.

[43] E. Lauga and H. A. Stone. Effective slip in pressure-driven Stokes flow. *Journal of Fluid Mechanics*, 489:55–77, 2003.

[44] P. H. Manepalli, H. Dogan, J. M. Mathew, and S. Alavi. Mathematical modeling of flow behavior and cell structure formation during extrusion of starchy melts. *Journal of Food Engineering*, 198:7–16, 2017.

[45] B. Melka, M. Gracka, W. Adamczyk, M. Rojczyk, A. Golda, A. J. Nowak, R. A. Białecki, and Z. Ostrowski. Multiphase simulation of blood flow within main thoracic arteries of 8-year-old child with coarctation of the aorta. *Heat and Mass Transfer*, 54(8):2405–2413, 2018.

[46] D. H. Michael. The separation of a viscous liquid at a straight edge. *Mathematika*, 5(1):82–84, 1958.

[47] E. Mitsoulis and S. G. Hatzikiriakos. Steady flow simulations of compressible PTFE paste extrusion under severe wall slip. *Journal of Non-Newtonian Fluid Mechanics*, 157(1):26–33, 2009.

[48] H. K. Moffatt. Viscous and resistive eddies near a sharp corner. *Journal of Fluid Mechanics*, 18(1):1–18, 1964.

[49] R. R. Myers, C. J. Knauss, and R. D. Hoffman. Dynamic rheology of modified starches. *Journal of Applied Polymer Science*, 6(24):659–666, 1962.

[50] J. R. Ockendon, S. D. Howison, A. A. Lacey, and A. B. Movchan. *Applied Partial Differential Equations*. Oxford Texts in Applied and Engineering Mathematics. Oxford University Press, 2003.

[51] D. O'Kiely, C. J. W. Breward, I. M. Griffiths, P. D. Howell, and U. Lange. Edge behaviour in the glass sheet redraw process. *Journal of Fluid Mechanics*, 785:248–269, 2015.

[52] D. O'Kiely, C. J. W. Breward, I. M. Griffiths, P. D. Howell, and U. Lange. Glass sheet redraw through a long heater zone. *IMA Journal of Applied Mathematics*, 83(5):799–820, 05 2018.

[53] R. D. Patel. Bubble growth in a viscous Newtonian liquid. *Chemical Engineering Science*, 35(11):2352–2356, 1980.

[54] M. S. Plesset and A. Prosperetti. Bubble dynamics and cavitation. *Annual Review of Fluid Mechanics*, 9(1):145–185, 1977.

[55] A. T. Preston. *Modelling heat and mass transfer in bubbly cavitating flows and shock waves in cavitating nozzles*. PhD thesis, California Institute of Technology, 2003.

[56] A. Prosperetti. The speed of sound in a gas–vapour bubbly liquid. *Interface Focus*, 5(5):20150024, 2015.

[57] O. M. Rayleigh. On the pressure developed in a liquid during the collapse of a spherical cavity. *Philosophical Magazine*, 34(200):94–98, 1917.

[58] M. Renardy. *Mathematical Analysis of Viscoelastic Flows*. CBMS-NSF Regional Conference Series in Applied Mathematics. Society for Industrial and Applied Mathematics, 2000.

[59] S. Richardson. A 'stick–slip' problem related to the motion of a free jet at low Reynolds numbers. *Mathematical Proceedings of the Cambridge Philosophical Society*, 67(2):477–489, 1970.

[60] D. E. Rosner and M. Epstein. Effects of interface kinetics, capillarity and solute diffusion on bubble growth rates in highly supersaturated liquids. *Chemical Engineering Science*, 27(1):69–88, 1972.

[61] S. Z. Rouhani and S. Sohal, M. Two-phase flow patterns: a review of research results. *Progress in Nuclear Energy*, 11(3):219–259, 1983.

[62] T. R. Salamon, D. E. Bornside, R. C. Armstrong, and R. Brown. Local similarity solutions in the presence of a slip boundary condition. *Physics of Fluids*, 9, 1997.

[63] T. R. Salamon, D. E. Bornside, R. C. Armstrong, and R. A. Brown. Local similarity solutions for the stress field of an Oldroyd-B fluid in the partial-slip/slip flow. *Physics of Fluids*, 9(8):2191–2209, 1997.

[64] L. E. Scriven. On the dynamics of phase growth. *Chemical Engineering Science*, 10(1):1–13, 1959.

[65] E. Silberman. Sound velocity and attenuation in bubbly mixtures measured in standing wave tubes. *Journal of the Acoustical Society of America*, 29(8):925–933, 1957.

[66] Y. M. Stokes, P. Buchak, D. G. Crowdy, and H. Ebendorff-Heidepriem. Drawing of micro-structured fibres: circular and non-circular tubes. *Journal of Fluid Mechanics*, 755:176–203, 2014.

[67] Y. M. Stokes, J. J. Wylie, and M. J. Chen. Coupled fluid and energy flow in fabrication of microstructured optical fibres. *Journal of Fluid Mechanics*, 874:548–572, 2019.

[68] J. R. Street, A. L. Fricke, and L. P. Reiss. Dynamics of phase growth in viscous, non-Newtonian liquids. initial stages of growth. *Industrial & Engineering Chemistry Fundamentals*, 10(1):54–64, 1971.

[69] E. Süli. A brief excursion into the mathematical theory of mixed finite element methods. Lecture notes.

[70] E. Süli and D. F. Mayers. *An Introduction to Numerical Analysis*. Cambridge University Press, 2003.

[71] E. Taliadorou, G. C. Georgiou, and E. Mitsoulis. Numerical simulation of the extrusion of strongly compressible Newtonian liquids. *Rheologica Acta*, 47(1):49–62, 2008.

[72] I. Tani. History of boundary layer theory. *Annual Review of Fluid Mechanics*, 9:87–111, 2003.

[73] R. I. Tanner. A theory of die-swell. *Journal of Polymer Science Part A-2: Polymer Physics*, 8(12):2067–2078, 1970.

[74] M. Taroni, C. J. W. Breward, L. J. Cummings, and I. M. Griffiths. Asymptotic solutions of glass temperature profiles during steady optical fibre drawing. *Journal of Engineering Mathematics*, 80(1):1–20, 2013.

[75] G. Toth, G. Nagy, A. Bata, and K. Belina. Determination of polymer melts flow-activation energy a function of wide range shear rate. *Journal of Physics: Conference Series*, 1045:012040, 2018.

[76] F. T. Trouton. On the coefficient of viscous traction and its relation to that of viscosity. *Proceedings of the Royal Society of London A: Mathematical, Physical and Engineering Sciences*, 77(519):426–440, 1906.

[77] D. L. Turcotte, H. Ockendon, J. R. Ockendon, and S. J. Cowley. A mathematical model of vulcanian eruptions. *Geophysical Journal International*, 103(1):211–217, 1990.

[78] R. G. M. van der Sman and J. Broeze. Effects of salt on the expansion of starchy snacks: a multiscale analysis. *Food and Function*, 5:3076–3082, 2014.

[79] D. Venerus. Diffusion-induced bubble growth and collapse in yield stress fluids. *Journal of Non-Newtonian Fluid Mechanics*, 215:53–59, 2015.

[80] M. F. Webster, I. J. Keshtiban, and F. Belblidia. Computation of weakly compressible highly viscous liquid flows. *Engineering Computations*, 21(7):777–804, 2004.

[81] L. V. Wijngaarden. One-dimensional flow of liquids containing small gas bubbles. *Annual Review of Fluid Mechanics*, 4(1):369–396, 1972.

[82] J. Zhang and A.K. Datta. Mathematical modeling of bread baking process. *Journal of Food Engineering*, 75(1):78–89, 2006.

Appendix A

Analytic solution to the stick–slip problem

As a way of providing insight into the behaviour of a viscous fluid emerging from a pipe or channel, Richardson [59] studied the stick–slip problem. He considers an infinite strip of an incompressible fluid, illustrated in figure A.1, bounded by two parallel planes at $y = \pm 1$. For two-dimensional (2D) flow in the (z, y)-plane, incompressiblity implies the existence of a streamline function, $\psi(z, y)$, such that

$$w = \frac{\partial \psi}{\partial y}, \qquad v = -\frac{\partial \psi}{\partial z}, \tag{A.1}$$

where (w, v) are the velocity components. For zero Reynolds number, the conservation-of-momentum equations reduce to the biharmonic equation, given by

$$\nabla^4 \psi = 0, \tag{A.2}$$

in $-1 \leq y \leq 1$. For $z < 0$, no-slip boundary conditions are imposed on the planes at $y = \pm 1$, and for $z > 0$ full-slip boundary conditions are imposed. So, on $y = \pm 1$ for $z < 0$ we impose

$$\psi = \pm 1, \qquad \frac{\partial \psi}{\partial y} = 0, \tag{A.3}$$

and on $y = \pm 1$ for $z > 0$ we impose that

$$\psi = \pm 1, \qquad \frac{\partial^2 \psi}{\partial y^2} = 0. \tag{A.4}$$

The difference between this problem and the problem we consider in Section 5.5 of Chapter 5 is the no-slip boundary condition for $z < 0$; we instead impose a Navier-slip law. For $z > 0$, the streamfunction is given by

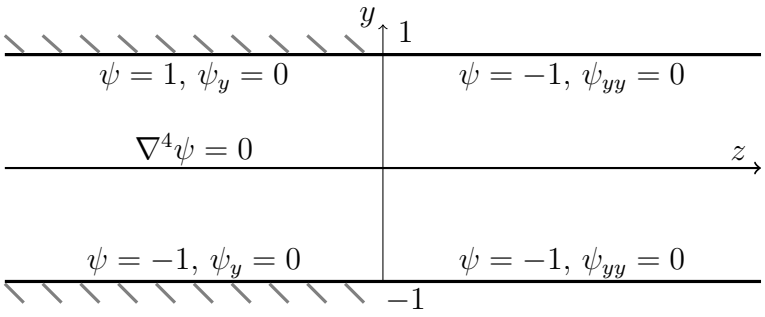

Figure A.1: *A schematic representation of the stick–slip problem. A subscript denotes a partial derivative.*

$$\psi(z,y) = y - \frac{3}{2\pi^2}\sum_{n=1}^{\infty}\frac{(-1)^n}{n^2 B_-(-in\pi)} z\mathrm{e}^{-n\pi z}\sin(n\pi y) + \frac{3}{2}\sum_{n=1}^{\infty}(-1)^n \lim_{\omega\to -in\pi}\left[\frac{\mathrm{d}}{\mathrm{d}\omega}\left\{\frac{i}{\omega^2 B_-(\omega)}\right\}\right]\mathrm{e}^{-n\pi z}\sin(n\pi y), \tag{A.5}$$

where $i = \sqrt{-1}$; and

$$B_-(\omega) = \prod_{n=1}^{\infty}\frac{\left(1-\dfrac{2\omega}{\alpha_n}\right)\left(1+\dfrac{2\omega}{\bar{\alpha}_n}\right)}{\left(1-\dfrac{\omega}{in\pi}\right)^2}, \tag{A.6}$$

where α_n are the non-zero roots of $\alpha = \sinh(\alpha)$ in the first quadrant $0 < \arg(\alpha_n) < \pi/2$, and $\bar{\alpha}_n$ is the complex conjugate of α_n.

For $z < 0$, the streamfunction is given by

$$\psi(z,y) = \frac{1}{2}y(3-y^2) - 3\sum_{n=1}^{\infty}\Re\left\{\frac{B_+(\alpha_n/2)}{\sinh^2(\alpha_n/2)}\left[\frac{\sinh(\alpha_n y/2)}{\sinh(\alpha_n/2)} - \frac{y\cosh(\alpha_n y/2)}{\cosh(\alpha_n/2)}\right]\mathrm{e}^{-i\alpha_n z/2}\right\}, \tag{A.7}$$

where $\Re\{x\}$ denotes the real part of x; and

$$B_+(\omega) = \prod_{n=1}^{\infty}\frac{\left(1+\dfrac{2\omega}{\alpha_n}\right)\left(1-\dfrac{2\omega}{\bar{\alpha}_n}\right)}{\left(1+\dfrac{\omega}{in\pi}\right)^2}. \tag{A.8}$$

In practice, when comparing this solution to the numerical solution of Chapter 5, we truncate both the sum required to determine ψ and the product required to determine $B_\pm(\omega)$ at 200 terms.

Appendix B

Partial hodograph and weak form of axisymmetric compressible-flow problem

In this appendix we present the details of the algebra required to derive the weak formulation for the axisymmetric extrusion of a compressible fluid. For a fluid of density ρ and velocity w, on the domain Ω' illustrated in figure B.1, we define the streamline coordinate, ψ, by

$$\frac{1}{r}\frac{\partial \psi}{\partial r} = \rho w, \qquad \frac{1}{r}\frac{\partial \psi}{\partial z} = -\rho u. \tag{B.1a,b}$$

We will assume that ρ is a prescribed scalar field as, when the following method is used in Section 5.8 of Chapter 5, we determine ρ by integrating the microscale model along streamlines. We can perform a partial hodograph transformation—from (z, r) coordinates to (ϕ, ψ) coordinates, where $\phi = z$—so that we only need to solve our equations on a rectangular domain. Consider the transformation

$$w(z,r) = \hat{w}(\phi,\psi), \quad u(z,r) = \hat{u}(\phi,\psi), \quad \rho(z,r) = \hat{\rho}(\phi,\psi), \quad p(z,r) = \hat{p}(\phi,\psi).$$

Using the chain rule, the z and r derivatives are given by

$$\frac{\partial(\cdot)}{\partial z} = \frac{\partial(\cdot)}{\partial \phi} - r\hat{\rho}\hat{u}\frac{\partial(\cdot)}{\partial \psi}, \qquad \frac{\partial(\cdot)}{\partial r} = r\hat{\rho}\hat{w}\frac{\partial(\cdot)}{\partial \psi}. \tag{B.2}$$

By transforming from (r, z) coordinates to (ψ, ϕ) coordinates, the fluid domain will change from Ω' to Ω, which is shown in figure B.2. After performing this transformation, and dropping all hats, the conservation-of-mass equation, (5.66), is given by

$$\frac{\partial}{\partial \phi}(\rho w) - r\rho u\frac{\partial}{\partial \psi}(\rho w) + \rho w\frac{\partial}{\partial \psi}(r\rho u) = 0, \tag{B.3}$$

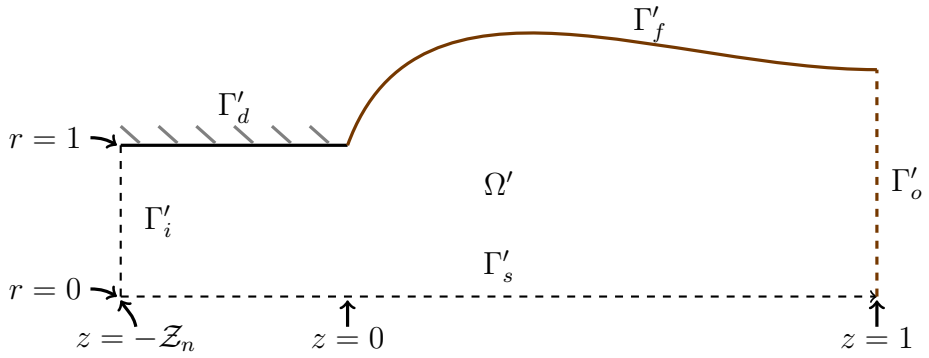

Figure B.1: *Solution domain, Ω' in cylindrical coordinates. The boundaries are denoted by Γ'_d for the die, Γ'_i for the inlet, Γ'_s for the line of symmetry, Γ'_o for the outlet, and Γ'_f for the free boundary. The inlet, Γ'_i, is at $\mathcal{Z}_n = -\ell/L$, where ℓ is the distance from the end of the die at which bubbles nucleate, and L is the characteristic length scale for bubble growth.*

in Ω. The conservation-of-r-momentum equation, (5.67), is transformed to

$$\frac{\partial}{\partial\phi}\left(\mu\left(\epsilon^2\frac{\partial u}{\partial\phi} - \epsilon^2 r\rho u\frac{\partial u}{\partial\psi} + r\rho w\frac{\partial w}{\partial\psi}\right)\right) - r\rho u\frac{\partial}{\partial\psi}\left(\mu\left(\epsilon^2\frac{\partial u}{\partial\phi} - \epsilon^2 r\rho u\frac{\partial u}{\partial\psi} + r\rho w\frac{\partial w}{\partial\psi}\right)\right)$$
$$+ \rho w\frac{\partial}{\partial\psi}\left(r\left(-p + \lambda\left(\rho w\frac{\partial}{\partial\psi}(ru) + \frac{\partial w}{\partial\phi} - \rho ru\frac{\partial w}{\partial\psi}\right) + 2\mu r\rho w\frac{\partial u}{\partial\psi}\right)\right) = 0, \qquad \text{(B.4)}$$

in Ω, and the conservation-of-z-momentum equation, (5.68), is transformed to

$$\epsilon^2\frac{\partial}{\partial\phi}\left(-p + \lambda\left(\rho w\frac{\partial}{\partial\psi}(ru) + \frac{\partial w}{\partial\phi} - \rho ru\frac{\partial w}{\partial\psi}\right) + 2\mu\frac{\partial w}{\partial\phi} - 2\mu r\rho u\frac{\partial w}{\partial\psi}\right)$$
$$- \epsilon^2 r\rho u\frac{\partial}{\partial\psi}\left(-p + \lambda\left(\rho w\frac{\partial}{\partial\psi}(ru) + \frac{\partial w}{\partial\phi} - \rho ru\frac{\partial w}{\partial\psi}\right) + 2\mu\frac{\partial w}{\partial\phi} - 2\mu r\rho u\frac{\partial w}{\partial\psi}\right)$$
$$+ \rho w\frac{\partial}{\partial\psi}\left(r\mu\left(\epsilon^2\frac{\partial u}{\partial\phi} - \epsilon^2 r\rho u\frac{\partial u}{\partial\psi} + r\rho w\frac{\partial w}{\partial\psi}\right)\right) = 0, \qquad \text{(B.5)}$$

in Ω.

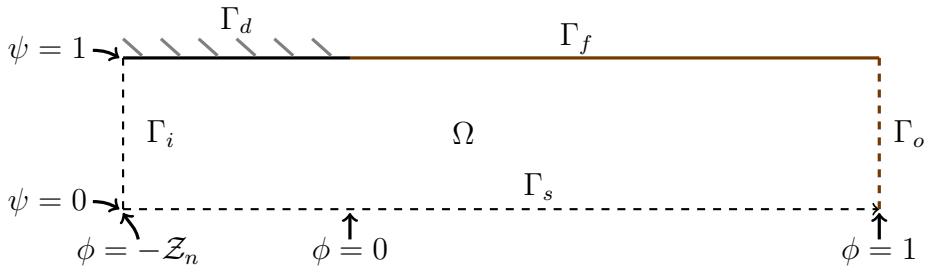

Figure B.2: *Solution domain, Ω in the streamline coordinates. The boundaries are denoted by Γ_d for the die, Γ_i for the inlet, Γ_s for the line of symmetry, Γ_o for the outlet, and Γ_f for the free boundary (which is fixed in ϕ in the (ϕ, ψ) plane).*

The boundary conditions on the free surface, (5.70b), are respectively transformed to

$$-\left(2\mu r\rho w\frac{\partial u}{\partial \psi}-p+\lambda\left(\frac{\partial w}{\partial \phi}-r\rho u\frac{\partial w}{\partial \psi}+\rho w\frac{\partial}{\partial \psi}\left(ru\right)\right)\right)u + \mu\left(\frac{\partial u}{\partial \phi}-r\rho u\frac{\partial u}{\partial \psi}+r\rho w\frac{\partial w}{\partial \psi}\right)w=0, \quad \text{(B.6)}$$

$$-\mu\left(\frac{\partial u}{\partial \phi}-r\rho u\frac{\partial u}{\partial \psi}+r\rho w\frac{\partial w}{\partial \psi}\right)u + \left(2\mu r\rho w\frac{\partial u}{\partial \psi}-p+\lambda\left(\frac{\partial w}{\partial \phi}-r\rho u\frac{\partial w}{\partial \psi}+\rho w\frac{\partial}{\partial \psi}\left(ru\right)\right)\right)w=0, \quad \text{(B.7)}$$

on Γ_f. The inlet flow profile, (5.69), is given by

$$u=0, \qquad w=w(\psi) \quad \text{on} \quad \Gamma_i. \quad \text{(B.8)}$$

The symmetry boundary conditions, (5.71), are given by

$$\frac{\partial w}{\partial \psi}=0, \qquad u=0 \quad \text{on} \quad \Gamma_s, \quad \text{(B.9)}$$

and the stress boundary conditions on the outlet, (5.72), are given by

$$-p+\lambda\left(\rho w\frac{\partial}{\partial r}\left(ru\right)+\frac{\partial w}{\partial \phi}-r\rho u\frac{\partial w}{\partial \psi}\right)+2\mu\left(\frac{\partial w}{\partial \phi}-r\rho u\frac{\partial w}{\partial \psi}\right)=0, \quad \text{(B.10)}$$

$$\left(\frac{\partial u}{\partial \phi}-r\rho u\frac{\partial u}{\partial \psi}+r\rho w\frac{\partial w}{\partial \psi}\right)=0, \quad \text{(B.11)}$$

on Γ_o. The tangential-slip boundary condition, (5.73), is given by

$$w=-\beta r\rho w\frac{\partial w}{\partial \psi} \quad \text{on} \quad \Gamma_d, \quad \text{(B.12)}$$

and the impermeability boundary condition, (5.74), is given by

$$u = 0 \qquad \text{on} \quad \Gamma_d. \tag{B.13}$$

The presence of r in this system means that the inverse mapping from ψ to r must be determined as part of the solution to the system of equations. This map is deduced by considering (B.1a), and using the relationship given by

$$\frac{\partial r}{\partial \psi} = \left(\frac{\partial \psi}{\partial r}\right)^{-1}, \tag{B.14}$$

resulting in the PDE for $r(\phi, \psi)$ given by

$$1 - r\rho w \frac{\partial r}{\partial \psi} = 0, \tag{B.15}$$

in Ω, where $r(\phi, 0) = 0$. This PDE is singular as $r \to 0$, which corresponds to $\psi \to 0$ in Ω, so one might consider defining $s = r^2$ and solving for s which, by (B.15), is given by

$$1 - \frac{\rho w}{2} \frac{\partial s}{\partial \psi} = 0. \tag{B.16}$$

B.1 Weak formulation

In this section we present the weak formulation of the system of partial differential equations (PDEs) presented in this appendix. We let $H^1(\Omega)$ be the space of square-integrable functions with square-integrable derivatives, and let $L^2(\Omega)$ be the space of square-integrable functions. We make use of the following function spaces, from which our solutions will be given:

$$W = \left\{ w \in H^1(\Omega) : w|_{\Gamma_i} = w(\psi) \right\}, \tag{B.17}$$

$$V = \left\{ v \in H^1(\Omega) : v|_{\Gamma_i \cup \Gamma_d \cup \Gamma_s} = 0 \right\}, \tag{B.18}$$

$$Q = \left\{ q \in L^2(\Omega) \right\}, \tag{B.19}$$

$$K = \left\{ k \in H^1(\Omega) : k|_{\Gamma_s} = 0 \right\}, \tag{B.20}$$

where $k|_\Gamma$ denotes the value of k on the boundary Γ. In addition, we define the following function spaces, from which we will take our test functions:

$$W^T = \left\{ w \in H^1(\Omega) : w|_{\Gamma_i} = 0 \right\}, \tag{B.21}$$

$$V^T = V = \left\{ v \in H^1(\Omega) : v|_{\Gamma_i \cup \Gamma_d \cup \Gamma_s} = 0 \right\}, \tag{B.22}$$

$$Q^T = Q = \left\{ q \in L^2(\Omega) \right\}, \tag{B.23}$$

$$K^T = K = \left\{ k \in H^1(\Omega) : k|_{\Gamma_s} = 0 \right\}. \tag{B.24}$$

Multiplying the transformed conservation-of-mass equation, (B.3), by $q \in Q^T$, and integrating over Ω yields

$$\iint_\Omega \left(\frac{\partial(\rho w)}{\partial \phi} - r\rho u \frac{\partial(\rho w)}{\partial \psi} + \rho w \frac{\partial(r\rho u)}{\partial \psi} \right) q \, \mathrm{d}\phi \mathrm{d}\psi = 0. \tag{B.25}$$

Similarly, we multiply (B.4) and (B.5) by $h \in V^T$ and $g \in W^T$ respectively. Integrating the results over Ω, and then integrating by parts, gives

$$\begin{aligned}
&\iint_\Omega - \left(\mu \left(\epsilon^2 \frac{\partial u}{\partial \phi} - \epsilon^2 r\rho u \frac{\partial u}{\partial \psi} + r\rho w \frac{\partial w}{\partial \psi} \right) \right) \frac{\partial h}{\partial \phi} \\
&+ \left(\mu \left(\epsilon^2 \frac{\partial u}{\partial \phi} - \epsilon^2 r\rho u \frac{\partial u}{\partial \psi} + r\rho w \frac{\partial w}{\partial \psi} \right) \right) \frac{\partial}{\partial \psi} (hr\rho u) \\
&- \left(r \left(-p + \lambda \left(\rho w \frac{\partial}{\partial \psi} (ru) + \frac{\partial w}{\partial \phi} - \rho r u \frac{\partial w}{\partial \psi} \right) + 2\mu r \rho w \frac{\partial u}{\partial \psi} \right) \right) \frac{\partial}{\partial \psi} (h\rho w) \, \mathrm{d}\phi \mathrm{d}\psi \\
&+ \oint_{\partial\Omega} \left(\mu \left(\epsilon^2 \frac{\partial u}{\partial \phi} - \epsilon^2 r\rho u \frac{\partial u}{\partial \psi} + r\rho w \frac{\partial w}{\partial \psi} \right) \right) h \, \mathrm{d}\psi \\
&+ \left(\mu \left(\epsilon^2 \frac{\partial u}{\partial \phi} - \epsilon^2 r\rho u \frac{\partial u}{\partial \psi} + r\rho w \frac{\partial w}{\partial \psi} \right) \right) hr\rho u \\
&- \left(r \left(-p + \lambda \left(\rho w \frac{\partial}{\partial \psi} (ru) + \frac{\partial w}{\partial \phi} - \rho r u \frac{\partial w}{\partial \psi} \right) + 2\mu r \rho w \frac{\partial u}{\partial \psi} \right) \right) h\rho w \, \mathrm{d}\phi = 0,
\end{aligned} \tag{B.26}$$

and

$$\begin{aligned}
&\iint_\Omega -\epsilon^2 \left(-p + \lambda \left(\rho w \frac{\partial}{\partial \psi} (ru) + \frac{\partial w}{\partial \phi} - \rho r u \frac{\partial w}{\partial \psi} \right) + 2\mu \frac{\partial w}{\partial \phi} - 2\mu r \rho u \frac{\partial w}{\partial \psi} \right) \frac{\partial g}{\partial \phi} \\
&+ \epsilon^2 \left(-p + \lambda \left(\rho w \frac{\partial}{\partial \psi} (ru) + \frac{\partial w}{\partial \phi} - \rho r u \frac{\partial w}{\partial \psi} \right) + 2\mu \frac{\partial w}{\partial \phi} - 2\mu r \rho u \frac{\partial w}{\partial \psi} \right) \frac{\partial}{\partial \psi} (r\rho u g) \\
&- \left(r\mu \left(\epsilon^2 \frac{\partial u}{\partial \phi} - \epsilon^2 r\rho u \frac{\partial u}{\partial \psi} + r\rho w \frac{\partial w}{\partial \psi} \right) \right) \frac{\partial}{\partial \psi} (\rho w g) \, \mathrm{d}\phi \mathrm{d}\psi \\
&+ \oint_{\partial\Omega} \epsilon^2 \left(-p + \lambda \left(\rho w \frac{\partial}{\partial \psi} (ru) + \frac{\partial w}{\partial \phi} - \rho r u \frac{\partial w}{\partial \psi} \right) + 2\mu \frac{\partial w}{\partial \phi} - 2\mu r \rho u \frac{\partial w}{\partial \psi} \right) g \, \mathrm{d}\psi \\
&\epsilon^2 \left(-p + \lambda \left(\rho w \frac{\partial}{\partial \psi} (ru) + \frac{\partial w}{\partial \phi} - \rho r u \frac{\partial w}{\partial \psi} \right) + 2\mu \frac{\partial w}{\partial \phi} - 2\mu r \rho u \frac{\partial w}{\partial \psi} \right) g \\
&\qquad - \left(r\mu \left(\epsilon^2 \frac{\partial u}{\partial \phi} - \epsilon^2 r\rho u \frac{\partial u}{\partial \psi} + r\rho w \frac{\partial w}{\partial \psi} \right) \right) \rho w g \, \mathrm{d}\phi = 0,
\end{aligned} \tag{B.27}$$

respectively. Finally, we multiply (B.15) by $k \in K^T$ and integrate by parts to give

$$\iint_\Omega k \left(1 - r\rho w \frac{\partial r}{\partial \psi} \right) \mathrm{d}\phi \mathrm{d}\psi = 0. \tag{B.28}$$

We can therefore express the weak formulation of this problem as follows: find $(w, u, p, r) \in W \times V \times Q \times K$ such that (B.25), (B.27), (B.26), and (B.28) are satisfied for all $q \in Q^T$, $g \in W^T$, $h \in V^T$, and $k \in K^T$. Here we assume that ρ is a prescribed scalar field.